Cocrystallization of Energetic Materials

by

Kira Beth Landenberger

A dissertation submitted in partial fulfillment
of the requirements for the degree of
Doctor of Philosophy
(Chemistry)
in The University of Michigan
2013

Doctoral Committee:

Professor Adam J. Matzger, Chair
Professor Mark M. Banaszak Holl
Assistant Professor Anne J. McNeil
Associate Professor Naír Rodríguez-Hornedo

Acknowledgements

My first and foremost thanks are to God, without whom none of this would have been possible. Whether times were good or bad, He was always there, providing a firm foundation. I am deeply thankful for His love, providence, care and support. He is the author of all and I am glad to have had a chance to discover just a little bit more about His creation.

I am also very thankful for my advisor, Professor Matzger. I have always deeply appreciated his honesty, forthrightness and his sense of humor as well as his willingness to assist his students. His vast knowledge and keen insight truly furthered the research endeavors of everyone in his group. I am thankful for his helpful attitude and the autonomy he has allowed all of his students in their projects that has helped us to grow into capable, independent researchers. I am also forever indebted to him for his kindness in allowing me to take Japanese language classes during my time here at the University of Michigan. Accomplishing my future dreams would not have been possible without this opportunity.

Further thanks are due to my fellow partner in crime in the cocrystallization of energetic materials, Dr. Onas Bolton. Words cannot express my appreciation for his help and assistance on this project and moreover his kind and generous attitude that truly made this a successful collaboration. I can never thank him enough for his good advice, willingness to synthesize energetic materials and generosity in assisting in any way possible with this project. I will truly miss his good sense of humor and kindness. I am so glad we could work together as a team.

I am also deeply grateful for Dr. Antek Wong-Foy. His expertise with all the lab equipment and willingness to help truly keep the Matzger lab going. I am very thankful for his kindness and his continual willingness to help and provide whatever suggestions he can for any problems we face in the lab.

I am also so very thankful for my deskmate and friend Rachel. Every day her love and kind support in the lab enabled me to persevere. I am also thankful for her diligent efforts as safety officer for the lab and her organization to make sure that things

get done. Further thanks for all of her encouragement through my thesis work and her assistance with thinking about scientific problems and writing about them.

Dr. Vilmalí López-Mejías was a true role model for me, showing me both how to be a successful graduate student, while also enjoying life to its fullest. I am forever indebted to her for her mentorship and her sage advice. I am so very glad I could know her and be her friend.

I am also very thankful for all members of the Matzger lab, both past and present. In particular I am thankful for Dr. William Porter III, better known as Trey, for his friendliness and guidance to me as an incoming graduate student and for really helping me to get started on my project of cocrystallizing energetic materials. Without his hard efforts none of this would have been possible. I am also thankful for Leila for her inspirational pep talks. I am thankful for Jacob Lucido and Pedro Cooper, undergraduate students who worked with me on this project through the UROP at the University of Michigan. I am also thankful for Dr. Saikat Roy for all his helpful advice on crystallizations. Further thanks are due to Jeremy who kindly offered advice on many of my projects and volunteered to proofread my writing. I am also thankful for Laura who is a great friend, always willing to discuss research ideas. She is inheriting from me the job of being master of instruments in the lab. Thanks to all the members who went before: Austin, John, Koh, Tae Hong, Jenny, Seakhoon, Katie, Eranda, Rosalynn, Rashid, Hara-san, Yoshio-san and for all members who will follow: Ping, Ananya, Brendan, Li Zi, Leah, and Brianna.

I am also very thankful for my committee members. I was very appreciative of their guidance and support as I started my thesis work on the cocrystallization of energetic materials and have benefited from their insight.

I am also so thankful for my dear friends who have supported me through my time here. My best friend Jessie Hughes kindly listened to my report on graduate life every week. Liz Lyons has been a faithful friend no matter how busy things get. Many thanks to my college friends who were always supporting and praying for me even though we have become spread out all over the world: Jessica, Brenna, Emily, Angy, Tessa, Kara, and Meg. The members of my Bible study Liz F., Lee, Mary Margaret, Mary, Liz J., Stacy, Rachel and Larissa were always supportive. I am also thankful for

my friends Di, Ming, Joanna, Colleen, Sara-Marie, Nicole, Jenn M, Sarah A., Jen K., Becky, Amanda, Miho, Cheryl and more people than I could possibly name right now who were also incredibly supportive to me during this time.

And last but certainly not least I am so thankful and indebted to my family. Their constant love, support and concern have been my backbone through this entire process. I never would have made it without their support. I love you and your love has made all the difference in the world.

Table of Contents

List of Figures

List of Tables

List of Appendices

Abstract

Here cocrystallization, the formation of crystals containing two or more neutral molecular components in a defined ratio within a crystal lattice, is explored as a means to alter and improve the properties of energetic materials, including explosives, propellants and pyrotechnics. To develop cocrystal engineering principles for energetic materials, model cocrystal systems between energetic and non-energetic materials were studied. Series of cocrystals were formed with 2,4,6-trinitrotoluene (TNT) and 1,3,5,7-tetranitro-1,3,5,7-tetrazacyclooctane (HMX) to investigate cocrystallization of aromatic and aliphatic energetic materials respectively. These model systems demonstrated the ability to cocrystallize energetic materials and provided insight on favorable interactions for the formations of these cocrystals. TNT formed cocrystals exclusively with electron-rich aromatic compounds through donor acceptor π-π interactions, while HMX formed cocrystals with a wide variety of cocrystal formers primarily through electrostatic interactions. The structures of these cocrystals were dictated by the size, shape and electronic character of the cocrystal formers. Properties relevant to energetic materials were altered through cocrystallization including the melting point, decomposition temperature, density, oxygen balance and impact sensitivity. The principles developed from these two model energetic cocrystal systems led to the formation of novel energetic-energetic cocrystals between diacetone diperoxide (DADP) and a series of halogenated trinitrobenzenes: 1,3,5-trichloro-2,4,6-trinitrobenzene (TCTNB), 1,3,5-tribromo-2,4,6-trinitrobenzene (TBTNB) and 1,3,5-triiodo-2,4,6-trinitrobenzene (TITNB). Like the TNT and HMX cocrystals, the DADP cocrystals showed altered materials properties. Unlike the previously discovered energetic cocrystals, impact sensitivity was not improved with respect to the most sensitive component, DADP, even after cocrystallization, suggesting that the peroxide moiety is inherently unstable. This result suggests that cocrystallization can be used as an experimental means to probe causes of sensitivity for energetic materials. Finally, the DADP/TBTNB cocrystal was discovered

to be a kinetic cocrystal. The existence of a kinetic cocrystal is relevant for the development of cocrystallization because it highlights the need to ensure that potential kinetic cocrystals are not overlooked during the cocrystal screening process by employing methods that only favor thermodynamically stable forms.

Chapter 1 Introduction

1.1 What Are Energetic Materials?

Energetic materials is a broad term used to describe a class of compounds and polymers that rapidly release energy through a chemical reaction or change of state, often accompanied by the expansion of gas. This class of materials is further distinguished from purely combustible materials by the incorporation of oxygen into the compounds, the result of which is that an external oxygen supply is not needed for the explosion reaction to proceed. The term energetic materials encompasses three materials classes: explosives, propellants, and pyrotechnics. Explosives and propellants are differentiated by the speed, duration and quality of energy release after an initiating event. Explosives should provide destructive power, while propellants serve to supply thrust for rockets and engines. Pyrotechnics can include both explosives and propellants and are used to produce various effects, including light, color, production of smoke, and generation of sound. While energetic materials are generally classified as either being explosives or propellants, many compounds can serve as both depending on the shape, size, packing and arrangement of the compound in the munition.

Explosives, also termed "high explosives," are characterized by their ability to release energy solely through detonation. Detonation is distinct from deflagration, a self-propagated form of burning, and combustion, in that the former is propagated at very high speed by the compression-induced heat of a shock wave. After the explosive reaction is initiated, either through thermal ignition, electric shock or mechanical pressure, a shock and heat wave are both produced. In detonation the shock wave is faster than the speed of sound, supersonic, and it is this wave, not the thermal wave, that propagates the explosive chemical reaction. Even compounds that have the potential to detonate may simply deflagrate or burn instead if the conditions for detonation are not met. Whether a compound detonates or not is dependent on the force of the initiation and

the compression of the material. Detonation is key to providing good brisance, or shattering ability, that is required for an explosive to be effective. Brisance scales with detonation power as well as the volume of gas produced. Therefore, there is great interest in developing explosives with greater detonation power and larger volumes of gas generation.

Within explosives, however, there is another important classification: primary and secondary explosives. Primary explosives are more sensitive to shock, whether thermal, impact, static or friction, and are predominantly used to initiate secondary explosives. The detonation velocity and power of primary explosives is typically lower than that of secondary explosives, with detonation velocities ranging from 3500-5500 m/s.[1] Due to their sensitivity, the amount of primary explosives included in any charge is usually limited to what is needed to initiate the secondary explosive. Secondary explosives are less sensitive and more powerful than primary explosives. Typical detonation velocities for secondary explosives are 5500-9000 m/s.[1] Most of the well-known energetic materials are usually classified as secondary explosives and current research efforts focus largely on producing secondary explosives with lower sensitivity and great explosive power.

In contrast to explosives, propellants, also called "low explosives," react through deflagration to provide the sustained thrust necessary for this class of materials. Deflagration can be considered a form of burning, but in contrast to pure combustion, it is self-propagating and does not require an external source of oxygen. Compared to detonation, deflagration is slower and more prolonged. The reaction is propagated through a subsonic thermal wave rather than the shock wave. The longer reaction and massive generation of gases produces the necessary thrust to propel objects such as rockets or missiles forward, hence the term propellants. Burn rates of a propellant can be accelerated or regulated by the addition of inorganic salts such as copper chromate ($CuCr_2O_4$) or ferrocene.[2] In designing propellants, materials that burn longer and produce larger volumes of gas are generally favored.

The term pyrotechnics includes both explosives and propellants and is primarily a distinction of the intended use for these compounds. Fireworks are a common example of pyrotechnics, but even smoke bombs or whistling rockets can be classified this way.

The desired properties for pyrotechnics differ significantly from explosives or propellants intended for weapons or mining. For instance, increasing the explosive power or thrust is less important than controlling the size of the explosion or the timing of a rocket. Furthermore, since pyrotechnics are often used in outdoor public places or in enclosed theaters in close proximity to crowds there is an acute need to produce pyrotechnics that produce little if any toxic gaseous products or solid byproducts. Therefore, significant effort is being expended to develop to produce energetic materials that produce little or no toxic gases and leave no toxic residues.[3-10]

1.2 Key Properties for Energetic Materials

The main challenge in designing new energetic materials lies in the large number critical properties that must be addressed for these materials to be safe and effective. Energetic materials must meet several stringent requirements to be viable for fielding, so although new materials are being synthesized,[7,11-13] the failure to meet one or more requirements has limited their implementation. One of the primary properties to consider is the explosive power of energetic materials, which is affected by density, enthalpy of detonation, oxygen balance and gas formation upon detonation or deflagration. Another factor to consider is the safety of these materials, which includes not only the sensitivity of these materials to shock so they are safe to handle but the nature of the gases and other compounds produced after combustion. Finally, the ability to produce and effectively use these materials in the field, including the cost, processability, water solubility and chemical stability in extreme conditions is critical to consider in designing energetic materials.

Explosive power is typically described in terms of detonation velocity and pressure. These two properties of explosives are related to the density, number of moles of gas produced and detonation enthalpy as seen in the Kamlet-Jacobs equations:

$$v_d = 1.01(1+1.30\rho)\sqrt{N_g\sqrt{M_gQ}} \quad (1.1)$$

$$P_d = 15.58\rho^2 N_g\sqrt{M_gQ} \quad (1.2)$$

where, v_d is the detonation velocity, ρ is the loading density, N_g is the number of moles of gas produced per gram of explosive, M_g is the average molar mass of the gases produced, Q is the enthalpy of detonation for the explosive and P_d is the detonation pressure of the explosive.[14] Since the loading density is in part dependent on the crystallographic density of these materials, it is common practice in the literature to discuss crystallographic densities compared to relative detonation velocities and pressures. For an explosive, a higher density usually correlates with higher explosive power. Unsurprisingly, explosives that produce greater volumes of gas will have higher power, therefore the number of moles of gas, as well as their molecular weight is also important. Finally, in the Kamlet-Jacobs equations, the enthalpy of detonation is shown to be key for improving explosive power: the more heat that can be released, the greater the power.

Oxygen balance is another critical property to consider for energetic materials. Not only does it affect a compound's explosive or propulsive power but also determines, in part, what chemical products might be produced upon detonation or deflagration. The oxygen balance is a weight percent of how much oxygen is either in excess or lacking for an ideal combustion reaction of an energetic material. In a perfect combustion reaction, there is enough oxygen to completely react with all the hydrogen, carbon, sulfur, and metal atoms present to form H_2O, CO_2, SO_2 and metal oxides. Based on the products from an ideal combustion reaction of an organic energetic material $C_aH_bN_cO_dX_eS_f$:

$$C_aH_bN_cO_dX_eS_f \rightarrow aCO_2 + \tfrac{1}{2}(b-e)H_2O + {}^{c}/_{2}N_2 + eHX + fSO_2 - (a+f+\tfrac{1}{4}(b-e) - {}^{d}/_{2})O_2 \quad (1.3)$$

the oxygen balance can be calculated using the following equation:[15]

$$-\frac{32(a+f+\tfrac{1}{4}(b-e)-d/2)}{MW} \quad (1.4)$$

where a, b, d, e, and f represent the number of carbon, hydrogen, oxygen, halogen and sulfur atoms present respectively. For explosives containing metals, this equation can be modified to reflect the amount of oxygen required to fully oxidize the metal atom present, an amount that varies by metal. If the oxygen balance is close to zero, then the heat of detonation will be high, and consequently, the explosive or propulsive power will be higher than materials with less ideal oxygen balances. In the case of a positive oxygen balance, even though more gases are present, the oxidation reaction cannot proceed fully and therefore less energy than a pure combustion reaction is produced. Furthermore, if

the oxygen balance is negative, less desirable products are formed. For example, in the case of carbon, if there is not enough oxygen present, then carbon monoxide, which is less stable and more toxic than carbon dioxide, will be produced and in some cases, solid carbon will be produced, which reduces the moles of gas produced, and ultimately the power of the energetic material. Very few energetic materials have a zero oxygen balance (Figure 1.1). Often inorganic energetic materials have a positive oxygen balance, meaning there is excess oxygen present after detonation or deflagration, while organic energetic materials have a negative oxygen balance, meaning full oxidation cannot be realized in detonation or deflagration. For this reason, a very common strategy to improve the oxygen balance of energetic materials is to blend inorganic and organic compounds together to compensate for the imbalance. But there still exists a need to correct this imbalance more on the molecular scale than at the level of a physical mixture.

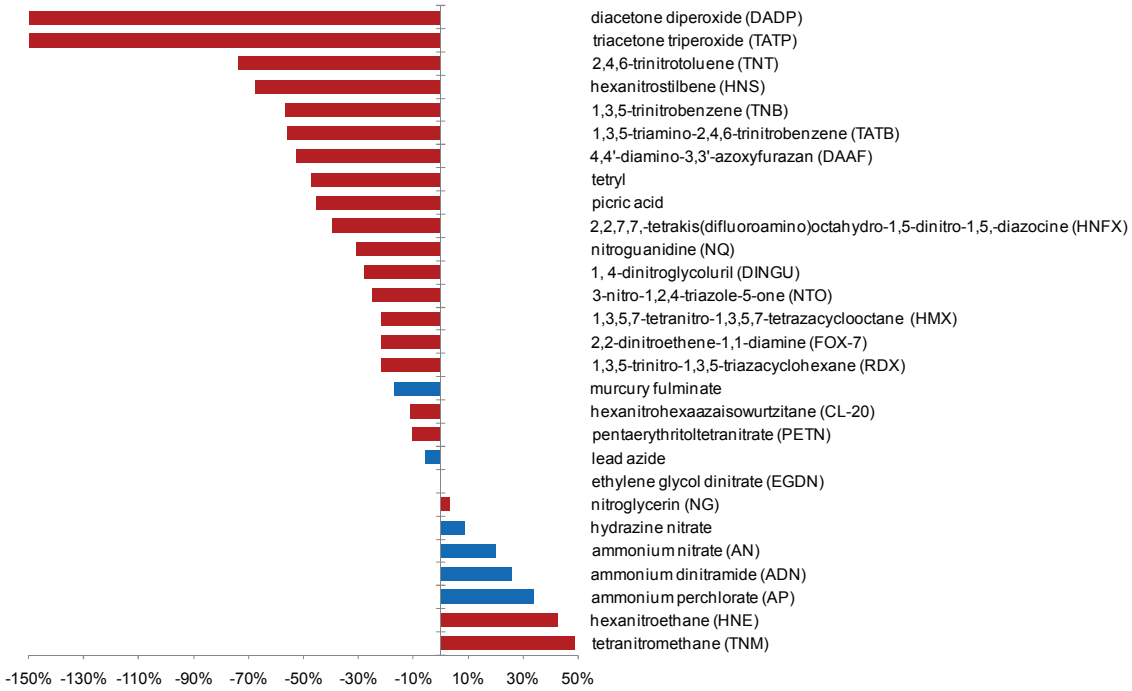

Figure 1.1 Oxygen balance for common energetic materials, including organic (red) and inorganic (blue) energetic materials.

Sensitivity of energetic materials to various forms of shock is another important property to consider. Energetic materials can be sensitive to physical impact, electrical shock, thermal shock and friction. It is valuable to note that the various forms of shock

do not necessarily proceed through the same mechanism. A compound that is relatively insensitive to one form of shock, such as impact shock, could still exhibit heightened sensitivity to another form of shock, such as electric shock.[1] Since most commercially available sensitivity testing equipment requires significant amounts of sample to obtain reliable information, broad sensitivity data for laboratory-scale materials are uncommon. Impact shock sensitivity is perhaps the most straightforward characteristic to measure as it can be assessed via the dropweight test. Other sensitivity tests include friction and static shock tests and gap tests.[16]

Even though the sensitivity of energetic materials to various forms of shock has long been recognized, the cause for sensitivity is still a subject of much research and discussion today. Indubitably, it is recognized that small imperfections in the crystals (e.g. fractures, cracks or holes) serve as hot spots and the initiating point for the explosive reaction. Therefore with lower quality crystals, higher sensitivity is often observed. Nevertheless, it is also recognized that presence of defects to generate hot spots is common to all energetic materials and is hardly the only distinguishing feature as to why some energetic materials are more sensitive than others.[16] An early theory on the cause of sensitivity for energetic materials proposed that energetic materials with an oxygen balance closer to zero were more sensitive and, indeed, for nitroglycerin this would seem to be the case.[17,18] Other theories have focused on the weakest bonds in the energetic material as being the limiting factor, citing the fact the that the nitro group seems to add instability to these materials.[16,19-21] In a modification on this theory, it was proposed that the distribution of electrostatic potential around the weakest bond is responsible for sensitivity.[22,23] This has led to the idea that compounds that have stronger intermolecular bonds are less sensitive, as in the case of TATB.[24,25] An alternative theory focused on the presence of slip planes in molecules as being responsible for a reduction in sensitivity.[26,27] One theory also proposed the correlation of impact sensitivity with the existence of void volume in these crystals.[28] And even the decomposition temperature has been correlated with sensitivity.[17] Many of these factors likely contribute to the overall sensitivity of an energetic material and in more recent literature this concept has been presented. But still there is a need for clarity to be brought to this area of energetic materials research.

Thermal properties of energetic materials are also important to consider as these influence the stability, processability, and ultimately the usability of energetic materials. Among important thermal properties to consider are the melting point, if any, and the decomposition temperature of the energetic materials. Another critical property to consider is the volatility of energetic materials. If energetic materials are excessively volatile this adds undesirable instability into munitions. And finally, chemical stability in hot conditions and sensitivity to thermal shocks are important to understand as unstable materials cannot be safely used.

The melting point of an energetic material in relation to its decomposition temperature determines how an energetic material can be processed and how it can be used. Very few energetic materials can be used in their molten state since most melt at a point only a few degrees below which they explode by autoignition. A few energetic materials, such as 2,4,6-trinitrotoluene (TNT) or 1,3,5-trinitrobenzene (TNB) can be used in their molten state, as the melting point is sufficiently lower than the decomposition temperature.[29] This allows for melt-casting, which is a convenient means of loading and energetic material into a munition by pouring when the energetic material is in a molten state. This easy processibility makes melt-castable explosives very attractive.

The decomposition temperature of an energetic material influences the stability as well. How readily an energetic material can be detonated is in part dependent on the decomposition temperature. When an explosive material is impacted by a shock wave, the compound will compress due to this wave and this gives rise to adiabatic heating. If temperatures above the decomposition temperature are reached, then detonation will occur. Therefore, materials with lower decomposition temperatures are more susceptible to detonation. Ultimately this determines whether a material functions as primary or secondary explosive.

1.3 Examples of Energetic Materials

Energetic materials have been developed in variety of forms. Broad classes include inorganic compounds, organic molecules and polymers. While inorganic energetics are highly dense and often have a positive oxygen balance, these compounds

are frequently more sensitive to shock and susceptible to water damage. Perhaps the mostly widely known energetic materials, organic energetic materials, are generally insoluble in water in their neutral forms and often much less sensitive to shock. Organic energetic materials generally have lower densities and negative oxygen balances. Since the pros and cons of inorganic and organic explosives are complimentary, mixtures of these compounds are often made. Explosive polymers are the third class of energetic materials and are similar to organic energetic materials in their properties, generally non-water soluble and having a negative oxygen balance. Like organic energetic materials, explosive polymers are often mixed with other energetic materials.

Inorganic energetic materials can be considered the first energetic materials discovered with the invention of black powder, a mixture of potassium nitrate, sulfur and solid carbon.[1] Examples of inorganic explosives include mercury fulminate, lead azide, ammonium nitrate and ammonium perchlorate (Figure 1.2). Mercury fulminate, while a very reliable primary explosive, is very sensitive to shock, decomposes in sunlight and produces undesirable explosive products including carbon monoxide and mercury. Lead azide, one of the densest primary explosives available and often used as a replacement for mercury fulminate, still produces toxic byproducts and is relatively sensitive to shock. Ammonium nitrate, also used as a fertilizer, was not initially considered an explosive, despite several incidents that occurred in the shipping of this material. It was not until 1947 that the true explosive power of this material was realized. While these common inorganic energetic materials function very effectively, the presence of toxic metals and halogens in many of them and the high sensitivity of others, in particular ammonium nitrate which does not contain metals or halogens, make them less than desirable. Therefore current research on inorganic energetic materials focuses not only on reducing sensitivity of these materials and susceptibility to water, but also in reducing toxic metal and halogen content.[6]

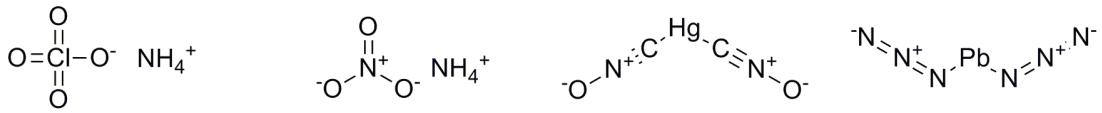

Figure 1.2 Examples of common inorganic energetic materials.

Organic energetic materials represent a second major group of energetic materials and include some of the most iconic explosives, such as 2,4,6-trinitrotoluene (TNT) and nitroglycerin (NG). Indeed, nitroglycerin was among the first organic energetic materials discovered in 1846 by Professor Ascanio Sobrero through the nitration of glycerine.[1] Although dangerously sensitive, this compound initiated interest in other organic explosives. Based on the success with nitroglycerin and due to the assumed explosive capability imparted by the presence of a nitro functional group, one of the earliest strategies for forming energetic materials was to nitrate various compounds. While, the nitro group is relatively unstable and provides a ready source of nitrogen and oxygen, which are key in forming explosives gases for the explosive reaction, the mere process of adding nitro functional groups does not make a compound explosive. Nevertheless, many energetic materials containing nitro functional groups were developed. These include nitroguanidine (NQ) developed in 1877 by Jousselin, TNT in 1880 by Hepp, 2,4,6-triamino-1,3,5-trinitrobenzene (TATB) in 1888 by Jackson and Wing, and pentaerythritol (PETN) in 1894.[1] Even though picric acid was first discovered in 1742 by Glauber, it was not developed as an explosive materials until 1885 in an attempt by Turpin to replace black powder.[1] Other nitro-group rich compounds include 1,3,5-trinitro-1,3,5-triazacyclohexane (RDX), first developed in 1899 for medicinal use by Hennings but not recognized as an explosive until 1920 by Herz, and 1,3,5,7-tetranitro-1,3,5,7-tetrazacyclooctane (HMX), which was discovered as an impurity in the Bachmann process synthesis of RDX during World War I. More recent examples of highly nitrated energetic materials include 2,4,6,8,10,12-hexanitro-2,4,6,8,10,12-hexaazaisowurtzitane (CL-20) developed in 1987 by Nielsen and octanitrocubane (ONC) developed in 1997 by Eaton et al.[30] Today the most commonly used explosives include TNT, RDX, HMX and PETN.

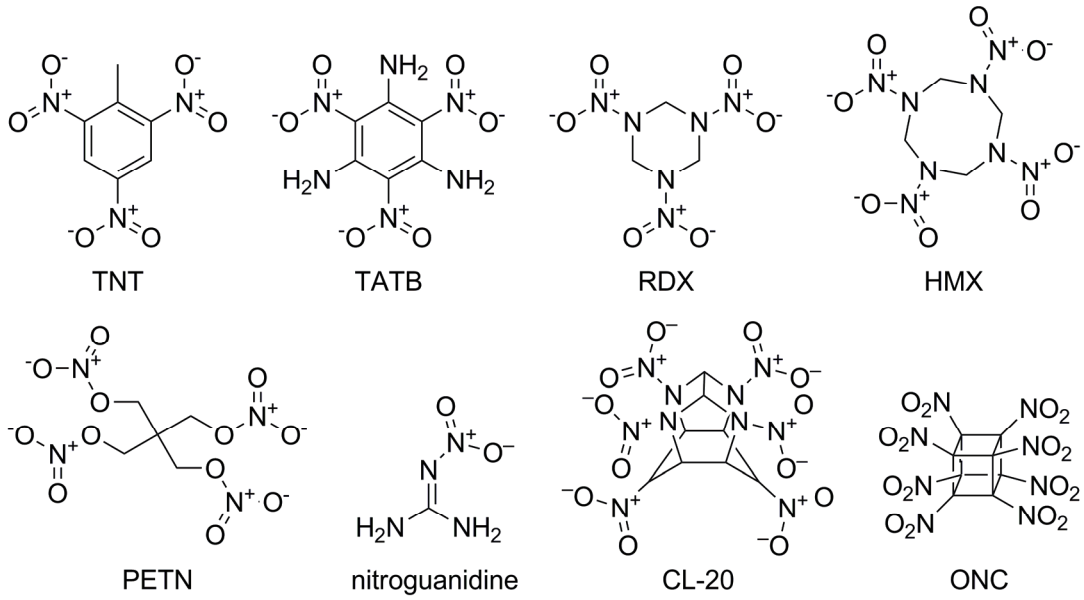

Figure 1.3 Examples of common organic energetic materials.

Current synthesis strategies for the production of organic energetic materials have shifted from incorporating nitro groups to synthesizing nitrogen rich heterocycles. Perhaps the most well known energetic material of this type is 3-nitro-1,2,4-triazole-5-one (NTO). Even though it was first synthesized in 1905, it was not until 1987 that the explosive properties of this material were reported by Chapman, Lee and Coburn.[31] Since NTO shows remarkable explosive power while showing little shock sensitivity, this has inspired research of other nitrogen rich heterocycles.[13] This includes 4,4'-diamino-3,3'-azoxyfurazan (DAAF), and 3,6-bis(1H-1,2,3,4-tetrazol-5-amino)-s-tetrazine (BTATz) and triaminoguanidinium azotetrazolate (TAGzT).[32]

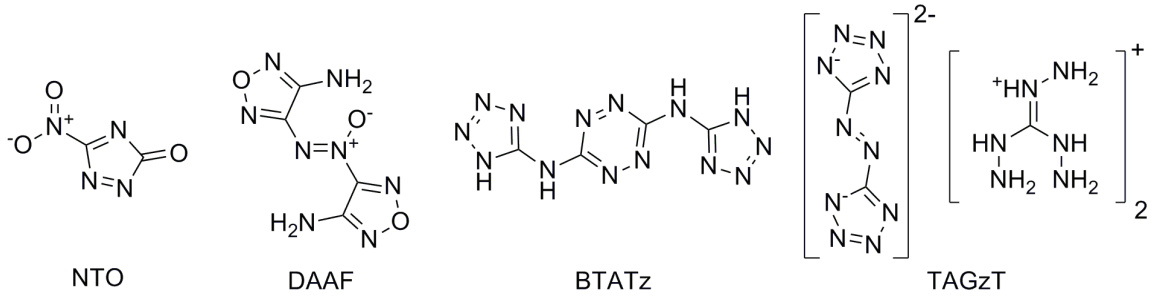

Figure 1.4 Examples of nitrogen rich energetic materials.

Explosive polymers are a third class of energetic materials. While a common strategy to stabilize organic and inorganic explosive is to mix non-explosive polymers

with these compounds, inherently explosive polymers and plasticizers have also been developed. Perhaps the first most well-known explosive polymer is nitrocellulose (gun cotton) in which cellulose is nitrated. Energetic polymers can be highly sensitive to impact shock and therefore are not necessarily safer to handle than other energetic materials. In the case of nitrocellulose, in particular, it is only safe to handle when wet. This led to the idea by Alfred Nobel in 1875 of mixing nitrocellulose and nitroglycerin, which forms a gel. This gel is used either as a blasting gel or gelatin dynamite. Other examples of explosive polymers include poly(glycidyl nitrate) (polyGLYN), glycidyl azide polymer (GAP), poly(3-nitromethyl-3-methyl oxetane) (polyNIMMO), poly(3-azidomethyl-3-methyl-oxetane) (polyAMMO), and poly(3,3'-bis-azidomethyloxetane) (polyBAMO) (Figure 1.5).[1] The development of inherently explosive polymers has seen very little development in comparison to inorganic and organic energetic materials.

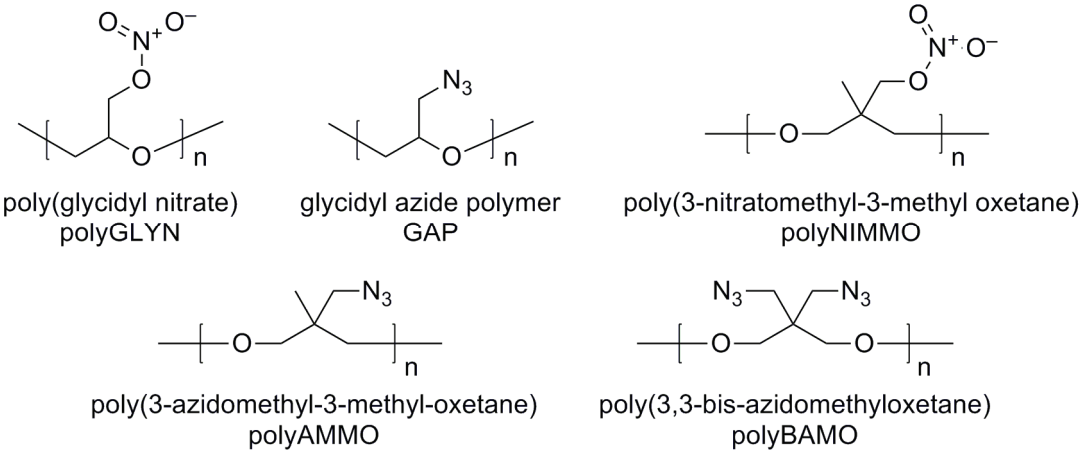

Figure 1.5 Examples of energetic polymers.

1.4 Strategies to Improve Energetic Materials

A significant amount of effort has been expended in developing energetic materials with improved explosive power and safety. In fact, only a very small number of energetic materials have been fielded as high explosives in military applications because of the need for cost effective production methods as well as rigid performance targets. The search for new energetic formulations has employed three different strategies. Currently there is still much effort to synthesize new energetic materials. A second strategy focuses on optimizing existing chemical entities and their solid form, the

polymorph employed, to obtain the best properties, including shock sensitivity, density, melting point, stability, and reactivity. And a third strategy has been to make physical mixtures of two or more energetic materials to create composites with the target properties. Examples include Pentolite, which is a mixture of TNT and PETN, and Composition B, which is a melt mixture of TNT and RDX. Notably absent from the energetics literature is the use of a strategy commonly used in pharmaceutical solid form engineering: cocrystallization.

1.5 What is cocrystallization?

Cocrystallization is the formation of a crystal consisting of two or more neutral molecular components in a defined ratio within a crystal lattice. Cocrystals are distinct from salts, which require ionizable groups that can donate or accept protons to form charged components. Because they remain uncharged, cocrystals provide a way to form multicomponent materials while still maintaining the integrity of the original molecular components. Cocrystals are similar to salts, however, in that two or more distinct species can be combined to form a novel crystalline material. Cocrystals have been called by a wide variety of terms, including multi-component complexes, molecular complexes, adducts, heteromolecular crystals, solid state complexes, pseudopolymorphs, inclusion compounds and non-covalent derivatives. While many of these terms can still be found in older literature, an effort to streamline the terminology to cocrystal (or co-crystal) is being made. Even still, some debate over the term is present. For the purposes of this work, cocrystals will include any neutral molecular components that interact in a defined way within the crystal lattice, whether solid, liquid or gas in its native state. Therefore the term cocrystal includes solvates, which are crystalline materials of two or more neutral molecular compounds where one or more of the compounds is a liquid at room temperature and standard pressure. Some definitions distinguish cocrystals as only forming from components that are solids at room temperature, therefore considering solvates as a distinct species.[33-35]

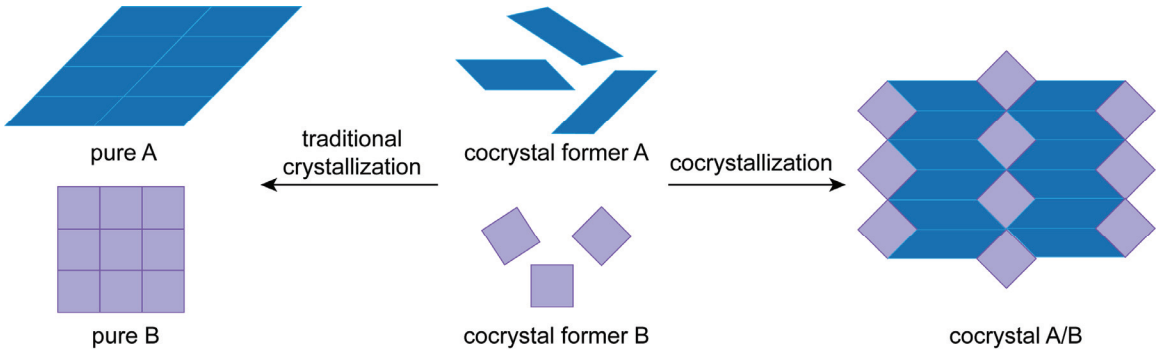

Figure 1.6 Cocrystallization combines two or more neutral molecular components in a defined ratio within a crystal lattice. This produces a material distinct from the pure cocrystal formers.

1.6 Strategies for Designing Cocrystals

While cocrystals often seem to be discovered serendipitously, there has been great effort expended to provide design strategies and principles for the formation of cocrystals. This includes discovering and cataloguing robust and reliable intermolecular interactions, called supramolecular synthons, for the formation of cocrystals. Even single component systems can provide information on favorable supramolecular synthons. Another approach has been to determine the thermodynamic and kinetic factors that govern cocrystallization. From this knowledge, more rational cocrystal experiments can be employed. Both knowledge of favorable interactions and crystallization conditions are needed to more judiciously search for cocrystals.

Understanding favorable supramolecular synthons is key for cocrystal design. Hydrogen bonding is one of the most robust intermolecular interactions available and figures significantly in most cocrystal engineering. There are a variety of interactions that fit into this classification (Figure 1.7).[36-38] In addition to being relatively strong,

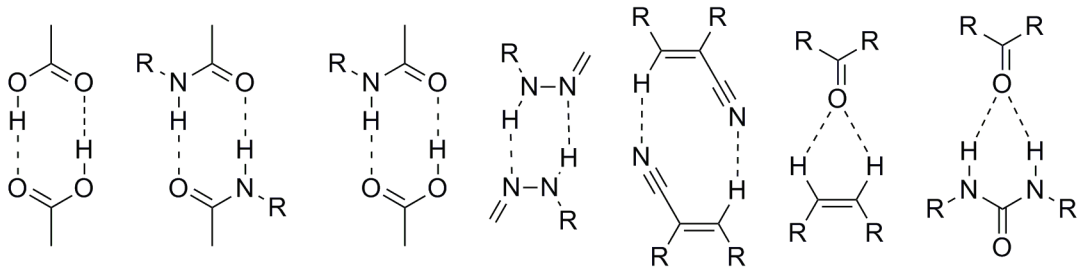

Figure 1.7 Examples of hydrogen bonding synthons

hydrogen bonds are short and directional. Interactions between benzene rings, π-interactions, are also significant. In a homogeneous system, observed interactions are usually edge-to-face or slipped as this maximizes the electrostatic interaction (Figure 1.8). If an electron rich and electron poor aromatic ring are combined, however, then a face-to-face interaction, a donor-acceptor π-π interaction, is observed instead.[39-41] This intermolecular interaction is very strong and is comparable in reliability to hydrogen bonding.

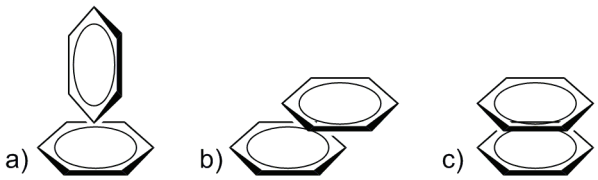

Figure 1.8 Interactions for aromatic rings include a) face-to-edge b) slipped and c) face-to-face

Another strong intermolecular interaction to consider is halogen bonding. A halogen bond is an intermolecular interaction between a nucleophile and the positive electron hole (sigma hole) of a halogen atom (Figure 1.9), typically chlorine, bromine or iodine, although it has been shown that fluorine can form this sigma hole in certain cases.[42-44] As the formation of a halogen bond is dependent on the interaction with the positive electron hole, halogen bonding is by nature very directional, much like hydrogen bonding. The strength of the interaction and the freedom of the angles allowed for the interaction are dependent on the polarization of the halogen atom.[45] In general, iodine is the most polarizable, followed by bromine and then chlorine. Indeed it is the lack of polarizability that limits fluorine from being a halogen bond acceptor. But the polarization, and thus strength and direction of the interaction are also influenced by the presence of neighboring functional groups. Electron-donating groups will decrease the size of the electron hole, decreasing the allowed angle of interaction and the strength of interaction, while, electron-withdrawing groups will increase the size of the electron hole and thus broaden the allowed angles of interaction and increase the strength of interaction.[45-49]

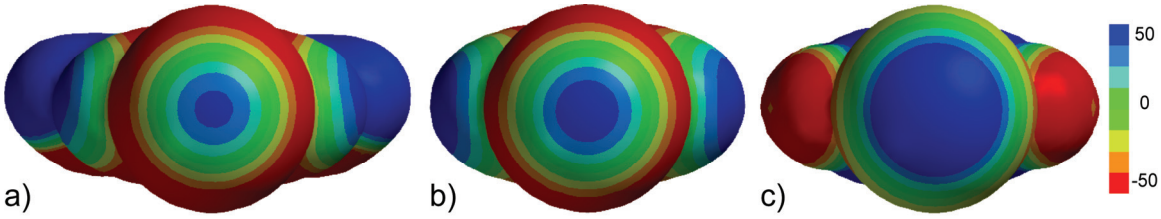

Figure 1.9 Electrostatic potential density surface maps showing the electron hole (sigma hole) of an iodine atom on a benzene ring with a) electron donating groups (5-iodobenzene-1,3-diamine) b) no electron donating or withdrawing groups (iodobenzene) and b) electron withdrawing groups (1,2,3,4,5-pentafluoro-6-iodobenzene). Surfaces were calculated using the semi-empirical method and the AM1 model. Red and blue surfaces represent electron rich and poor regions, respectively, with colors representing values between -50 and 50 kJ/mol.

For energetic materials, however, many of the common and robust synthons relied on for most cocrystal engineering are simply not available. Instead, most energetic materials often have copious amounts of nitro groups and little else in the way of traditional hydrogen bonding functional groups. While some favorable nitro interactions are known, these are limited. These include halogen-nitro interactions, amine-nitro interactions, and hydrogen-nitro interactions (Figure 1.10).[37,38,50-55] Even though these interactions are known to exist, it still does not guarantee cocrystal formation. Among other things there must be a favorable fit between the molecules. Crystal forms that minimize free space are generally more favorable.[56-58] Strong intermolecular interactions, such as hydrogen bonding, can allow for the formation of structures that introduce void space. The study of energetic materials, therefore, provides an ideal opportunity to study less well-known and potentially weaker intermolecular interactions.

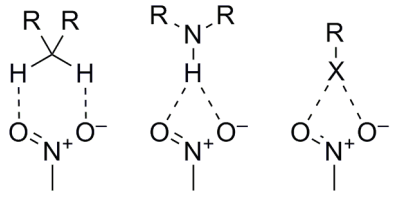

Figure 1.10 Examples of nitro interactions reported in the literature.

A second key to designing cocrystals is to understand favorable crystallization methods and conditions for their formation. In a large part this means understanding the thermodynamics and kinetics of the cocrystals and therefore the conditions that favor

formation. Most of the cocrystals discovered are more thermodynamically stable than the pure components. Therefore, producing these cocrystals generally necessitates accessing thermodynamically favorable conditions for cocrystal formation. This does not always mean employing a 1:1 molar ratio in setting up the crystallization, however. Cocrystals can be overlooked if a simplistic approach in cocrystal screening is applied.[59-61] For example in the case of carbamazepine/succinic acid cocrystal a 1:40 ratio was required to access the 1:1 cocrystal.[61] Phase diagrams can be helpful in understanding what conditions are favorable for cocrystal formation (Figure 1.11). One method that takes advantage of knowledge gained from the phase diagram for accessing cocrystals employs the reaction cocrystallization method (RCM).[62] In this method, a saturated or near saturated solution of the more soluble of the two components, and the second cocrystal former is added to selectively form the cocrystal. In this way, supersaturation is achieved with respect to the cocrystal, but not for either cocrystal former.

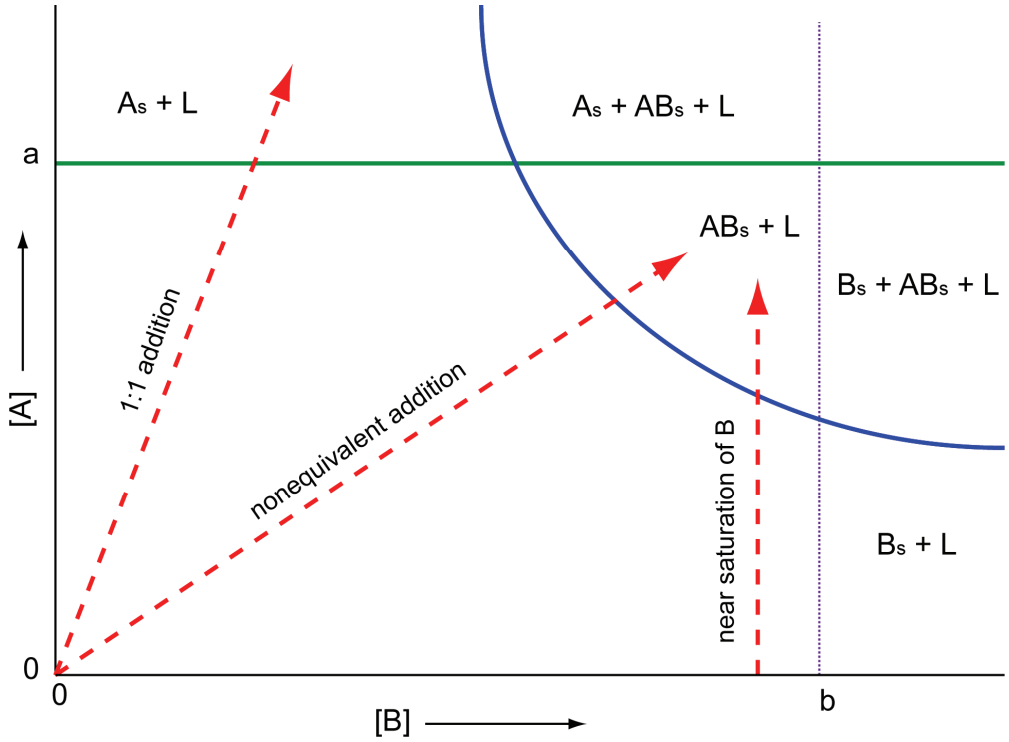

Figure 1.11 Solubility phase diagram for a hypothetical cocrystal AB in liquid L. In this case, a 1:1 ratio of cocrystal formers will not lead to cocrystal formation, while a nonequivalent ratio will. Another approach for cocrystal formation, employing the reaction cocrystallization method (RCM), starts with a saturated or near saturated solution of the more soluble compound (B), and cocrystal is exclusively formed by the careful addition of A.

Cocrystallization can be more complex than the scenario described above. For instance, while 1:1 cocrystals are very common, other cocrystal ratios are possible, even for the same system. In such a system, there will be a thermodynamically stable region for each cocrystal form.[60] Additionally, cocrystals, like pure compounds can form polymorphs.[63] At a given temperature and pressure, one polymorph will be the most stable form. Another factor that will alter the conditions favoring cocrystal formation is if the cocrystal formers complex in solution. This is more likely in solvents that are poor for the cocrystal formers. If solution complexation occurs, apparent solubility of a cocrystal former will increase as the concentration of the other cocrystal former increases. It will also appear to make the cocrystal more soluble, altering the conditions for optimal cocrystal formation.[64]

From a consideration of the thermodynamics of cocrystallization a few cocrystallization strategies become clear. First, cocrystal screens that only utilize 1:1 ratios can miss conditions that would favor cocrystal growth. And second, utilizing different solvent can be key as this will alter the difference in solubility between two components and may make cocrystallization more feasible.[60,61,64,65] Furthermore, while these conditions consider thermodynamically stable forms, kinetic cocrystallization methods should also be considered. Therefore, to thoroughly search for cocrystals a range of conditions and ratios should be tested.

1.7 Cocrystallization to Improve Energetic Materials

In this thesis, cocrystallization is explored as a method to improve properties critical to energetic materials. Due to the potential to greatly alter the properties of target materials while maintaining the integrity of the molecules cocrystallization offers great possibilities for providing enhanced energetic materials. Properties for broad classes of materials that can be altered through cocrystallization include density, solubility, bioavailability, morphology, color, and melting point.[66] Cocrystallization has seen application in many fields including the research of pharmaceutical materials, [67-74] optoelectronic materials,[75,76] and non-linear optical materials.[77-80] Cocrystals have also been used to provide unique and "green" solutions to various materials problems, as in

the case of the work of John Warner that used cocrystallization of hydroquinone with terephthalamide to control the dissolution rate of hydroquinone in water.[81] Likewise, cocrystallization provides a means to alter and improve existing energetic materials without synthesizing new materials. This includes not only commonly employed energetic materials, but also the surfeit of energetic materials that have been synthesized but never fielded due to one or more unfavorable properties. Through cocrystallization, such materials could be stabilized allowing for their common use.

1.8 Previously Reported Energetic Cocrystals

What would today be termed cocrystals, were not entirely unknown for energetic materials. For example, the HMX/*N*,*N*-dimethylformamide cocrystal was discovered serendipitously when recrystallizing HMX.[82-86] This cocrystal sparked a study of over a hundred solvates for HMX,[86-92] but little was done for most of these cocrystals beyond a report of their existence and a brief characterization, with the exception of two cocrystals: HMX/*N*-methyl-2-pyrrolidone and HMX/2,4,-dinitro-2,4-diaazapentane.[93-95] In the case of TNT, this explosive was often employed to form donor acceptor complexes due to its electron-poor nature. Though complexes were reported,[96-103] these were not always necessarily crystalline materials, the characterization was far from thorough, and only the TNT/pyrene cocrystal was ever structurally characterized.[104] Other reported cocrystals include HNS/tetrathiavulane[105] and RDX[106] with various solvents. In all cases, very few crystalline structures are available and the data on the interactions driving the formation of these complexes was speculative.

Though these cocrystals were known, this area of research has remained virtually untouched for almost 20 years and the intentional use of cocrystallization specifically for improving and enhancing energetic materials was never clearly stated in these works. The work in this thesis marks a determined effort to study cocrystallization of energetic materials in a systematic way. To establish cocrystal engineering principles and favorable intermolecular interactions for energetic materials commonly employed prototype aromatic and aliphatic energetic materials were cocrystallized with non-energetic materials. These principles were then successfully applied to the design of

cocrystals composed of two energetic materials. From these principles, the groundwork is laid for the development of many more energetic cocrystals.

1.9 References

(1) Akhavan, J. *The Chemistry of Explosives*; 2nd ed.; The Royal Society of Chemistry: Cambridge, 2004.

(2) Folly, P.; Mader, P. *Chimia* **2004**, *58*, 374-382.

(3) Moretti, J. D.; Sabatini, J. J.; Chen, G. *Angew. Chem., Int. Ed.* **2012**, *51*, 6981-6983.

(4) Sabatini, J. J.; Poret, J. C.; Broad, R. N. *Angew. Chem., Int. Ed.* **2011**, *50*, 4624-4626.

(5) Rahm, M.; Brinck, T. *Chem.-Eur. J.* **2010**, *16*, 6590-6600.

(6) Talawar, M. B.; Sivabalan, R.; Mukundan, T.; Muthurajan, H.; Sikder, A. K.; Gandhe, B. R.; Rao, A. S. *J. Hazard. Mater.* **2009**, *161*, 589-607.

(7) Steinhauser, G.; Klapötke, T. M. *Angew. Chem., Int. Ed.* **2008**, *47*, 3330-3347.

(8) Huynh, M. H. V.; Hiskey, M. A.; Meyer, T. J.; Wetzler, M. *Proc. Natl. Acad. Sci. U. S. A.* **2006**, *103*, 5409-5412.

(9) Ding, Y. H.; Inagaki, S. *Eur. J. Inorg. Chem.* **2005**, 3131-3134.

(10) Klapötke, T. M.; Mayer, P.; Schulz, A.; Weigand, J. J. *Propellants, Explos., Pyrotech.* **2004**, *29*, 325-332.

(11) Göbel, M.; Klapötke, T. M. *Adv. Funct. Mater.* **2009**, *19*, 347-365.

(12) Badgujar, D. M.; Talawar, M. B.; Asthana, S. N.; Mahulikar, P. P. *J. Hazard. Mater.* **2008**, *151*, 289-305.

(13) Singh, R. P.; Ga, H.; Meshri, D. T.; Shreeve, J. M. In *High Energy Density Materials*; Klapötke, T. M., Ed.; Springer-Verlag Berlin: Berlin, 2007; Vol. 125, p 35-83.

(14) Kamlet, M. J.; Jacobs, S. J. *J. Chem. Phys.* **1968**, *48*, 23-35.

(15) Kubota, N. In *Propellants and Explosives*; 2nd ed.; Wiley-VCH: Darmstadt, Germany, 2007, p 23-39.

(16) Mathieu, D. *J. Phys. Chem. A* **2012**, *116*, 1794-1800.

(17) Wang, Q.; Ma, H. X.; Li, J. Z.; Wei, H. J.; Fan, X. Z. *Acta Chim. Sin.* **2012**, *70*, 629-634.

(18) Kamlet, M. J.; Adolph, H. G. *Propellants Explos.* **1979**, *4*, 30-34.

(19) Tan, B. S.; Long, X. P.; Peng, R. F.; Li, H. B.; Jin, B.; Chu, S. J.; Dong, H. S. *J. Hazard. Mater.* **2010**, *183*, 908-912.

(20) Owens, F. J.; Jayasuriya, K.; Abrahmsen, L.; Politzer, P. *Chem. Phys. Lett.* **1985**, *116*, 434-438.

(21) Li, J. S. *J. Hazard. Mater.* **2010**, *174*, 728-733.

(22) Liu, Y.; Wang, L. J.; Wang, G. X.; Du, H. C.; Gong, X. D. *J. Mol. Model.* **2012**, *18*, 1561-1572.

(23) Rice, B. M.; Hare, J. J. *J. Phys. Chem. A* **2002**, *106*, 1770-1783.

(24) Du, S.; Wang, Y.; Chen, L. Z.; Shi, W. J.; Ren, F. D.; Li, Y. X.; Wang, J. L.; Cao, D. L. *J. Mol. Model.* **2012**, *18*, 2105-2115.

(25) Zhang, C. Y. *J. Phys. Chem. A* **2006**, *110*, 14029-14035.

(26) Zhang, C. Y.; Wang, X. C.; Huang, H. *J. Am. Chem. Soc.* **2008**, *130*, 8359-8365.

(27) McNesby, K. L.; Coffey, C. S. *J. Phys. Chem. B* **1997**, *101*, 3097-3104.

(28) Pospísil, M.; Vávra, P.; Concha, M. C.; Murray, J. S.; Politzer, P. *J. Mol. Model.* **2010**, *16*, 895-901.

(29) Mathieu, J.; Stucki, H. *Chimia* **2004**, *58*, 383-389.

(30) Eaton, P. E.; Gilardi, R. L.; Zhang, M. X. *Adv. Mat.* **2000**, *12*, 1143–1148.

(31) Lee, K.-Y.; Chapman, L. B.; Cobura, M. D. *J. Energ. Mater.* **1987**, *5*, 27-33.

(32) Tremblay, M. *Can. J. Chem.* **1965**, *43*, 1230.

(33) Aitipamula, S.; Banerjee, R.; Bansal, A. K.; Biradha, K.; Cheney, M. L.; Choudhury, A. R.; Desiraju, G. R.; Dikundwar, A. G.; Dubey, R.; Duggirala, N.; Ghogale, P. P.; Ghosh, S.; Goswami, P. K.; Goud, N. R.; Jetti, R. R. K. R.; Karpinski, P.; Kaushik, P.; Kumar, D.; Kumar, V.; Moulton, B.; Mukherjee, A.; Mukherjee, G.; Myerson, A. S.; Puri, V.; Ramanan, A.; Rajamannar, T.; Reddy, C. M.; Rodríguez-Hornedo, N.; Rogers, R. D.; Row, T. N. G.; Sanphui, P.; Shan, N.; Shete, G.; Singh, A.; Sun, C. C.; Swift, J. A.; Thaimattam, R.; Thakur, T. S.; Thaper, R. K.; Thomas, S. P.; Tothadi, S.; Vangala, V. R.; Variankaval, N.; Vishweshwar, P.; Weyna, D. R.; Zaworotko, M. J. *Cryst. Growth Des.* **2012**, *12*, 2147-2152.

(34) Stahly, G. P. *Cryst. Growth Des.* **2009**, *9*, 4212-4229.

(35) Bond, A. D. *CrystEngComm* **2007**, *9*, 833-834.

(36) Steiner, T. *Angew. Chem., Int. Ed.* **2002**, *41*, 48-76.

(37) Desiraju, G. R. *Angew. Chem., Int. Ed. Engl.* **1995**, *34*, 2311-2327.

(38) Etter, M. C. *J. Phys. Chem.* **1991**, *95*, 4601-4610.

(39) Headen, T. F.; Howard, C. A.; Skipper, N. T.; Wilkinson, M. A.; Bowron, D. T.; Soper, A. K. *J. Am. Chem. Soc.* **2010**, *132*, 5735-5742.

(40) Hunter, C. A.; Singh, J.; Thornton, J. M. *J. Mol. Biol.* **1991**, *218*, 837-846.

(41) Hunter, C. A.; Sanders, J. K. M. *J. Am. Chem. Soc.* **1990**, *112*, 5525-5534.

(42) Chopra, D. *Cryst. Growth Des.* **2012**, *12*, 541-546.

(43) Metrangolo, P.; Murray, J. S.; Pilati, T.; Politzer, P.; Resnati, G.; Terraneo, G. *CrystEngComm* **2011**, *13*, 6593-6596.

(44) Berger, R.; Resnati, G.; Metrangolo, P.; Weber, E.; Hulliger, J. *Chem. Soc. Rev.* **2011**, *40*, 3496-3508.

(45) Lommerse, J. P. M.; Stone, A. J.; Taylor, R.; Allen, F. H. *J. Am. Chem. Soc.* **1996**, *118*, 3108-3116.

(46) Kapadia, P. P.; Swenson, D. C.; Pigge, F. C. *Cryst. Growth Des.* **2012**, *12*, 698-706.

(47) Politzer, P.; Murray, J. S.; Clark, T. *Phys. Chem. Chem. Phys.* **2010**, *12*, 7748-7757.

(48) Metrangolo, P.; Resnati, G.; Pilati, T.; Biella, S. In *Halogen Bonding: Fundamentals and Applications*; Metrangolo, P., Resnati, G., Eds.; Springer-Verlag Berlin: Berlin, 2008; Vol. 126, p 105-136.

(49) Ramasubbu, N.; Parthasarathy, R.; Murrayrust, P. *J. Am. Chem. Soc.* **1986**, *108*, 4308-4314.

(50) Reddy, L. S.; Chandran, S. K.; George, S.; Babu, N. J.; Nangia, A. *Cryst. Growth Des.* **2007**, *7*, 2675-2690.

(51) Saha, B. K.; Nangia, A.; Jaskolski, M. *CrystEngComm* **2005**, *7*, 355-358.

(52) George, S.; Nangia, A.; Lam, C. K.; Mak, T. C. W.; Nicoud, J. F. *Chem. Commun.* **2004**, 1202-1203.

(53) Robinson, J. M. A.; Philp, D.; Harris, K. D. M.; Kariuki, B. M. *New J. Chem.* **2000**, *24*, 799-806.

(54) Allen, F. H.; Lommerse, J. P. M.; Hoy, V. J.; Howard, J. A. K.; Desiraju, G. R. *Acta Crystallogr., Sect. B: Struct. Sci.* **1997**, *53*, 1006-1016.

(55) Biradha, K.; Nangia, A.; Desiraju, G. R.; Carrell, C. J.; Carrell, H. L. *J. Mat. Chem.* **1997**, *7*, 1111-1122.

(56) Brock, C. P.; Dunitz, J. D. *Chem. Mater.* **1994**, *6*, 1118-1127.

(57) Perlstein, J. *J. Am. Chem. Soc.* **1994**, *116*, 11420-11432.

(58) Kitajgorodskij, A. I. *Acta Cryst.* **1965**, *18*, 585-590.

(59) ter Horst, J. H.; Deij, M. A.; Cains, P. W. *Cryst. Growth Des.* **2009**, *9*, 1531-1537.

(60) Jayasankar, A.; Reddy, L. S.; Bethune, S. J.; Rodriguez-Hornedo, N. *Cryst. Growth Des.* **2009**, *9*, 889-897.

(61) Childs, S. L.; Rodríguez-Hornedo, N.; Reddy, L. S.; Jayasankar, A.; Maheshwari, C.; McCausland, L.; Shipplett, R.; Stahly, B. C. *CrystEngComm* **2008**, *10*, 856-864.

(62) Rodríguez-Hornedo, N.; Nehru, S. J.; Seefeldt, K. F.; Pagan-Torres, Y.; Falkiewicz, C. J. *Molecular Pharmaceutics* **2006**, *3*, 362-367.

(63) Porter, W. W.; Elie, S. C.; Matzger, A. J. *Cryst. Growth Des.* **2008**, *8*, 14-16.

(64) Nehm, S. J.; Rodríguez-Spong, B.; Rodríguez-Hornedo, N. *Cryst. Growth Des.* **2006**, *6*, 592-600.

(65) Leyssens, T.; Springuel, G.; Montis, R.; Candoni, N.; Veesler, S. *Cryst. Growth Des.* **2012**, *12*, 1520-1530.

(66) Schultheiss, N.; Newman, A. *Cryst. Growth Des.* **2009**, *9*, 2950-2967.

(67) Brittain, H. G. *Cryst. Growth Des.* **2012**, *12*, 5823-5832.

(68) Qiao, N.; Li, M. Z.; Schlindwein, W.; Malek, N.; Davies, A.; Trappitt, G. *Int. J. Pharm.* **2011**, *419*, 1-11.

(69) Good, D. J.; Rodríguez-Hornedo, N. *Cryst. Growth Des.* **2009**, *9*, 2252-2264.

(70) Schultheiss, N.; Newman, A. *Cryst. Growth Des.* **2009**, *9*, 2950-2967.

(71) Shan, N.; Zaworotko, M. J. *Drug Discov. Today* **2008**, *13*, 440-446.

(72) Trask, A. V.; Motherwell, W. D. S.; Jones, W. *Int. J. Pharm.* **2006**, *320*, 114-123.

(73) McNamara, D. P.; Childs, S. L.; Giordano, J.; Iarriccio, A.; Cassidy, J.; Shet, M. S.; Mannion, R.; O'Donnell, E.; Park, A. *Pharm. Res.* **2006**, *23*, 1888-1897.

(74) Trask, A. V.; Motherwell, W. D. S.; Jones, W. *Cryst. Growth Des.* **2005**, *5*, 1013-1021.

(75) Bolton, O.; Kim, J. *J. Mater. Chem.* **2007**, *17*, 1981-1988.

(76) Del Mauro, A. D. G.; Carotenuto, M.; Venditto, V.; Petraccone, V.; Scoponi, M.; Guerra, G. *Chem. Mat.* **2007**, *19*, 6041-6046.

(77) Choi, E. Y.; Jazbinsek, M.; Lee, S. H.; Günter, P.; Yun, H.; Lee, S. W.; Kwon, O. P. *CrystEngComm* **2012**, *14*, 4306-4311.

(78) Koshima, H.; Nagano, M.; Asahi, T. *J. Am. Chem. Soc.* **2005**, *127*, 2455-2463.

(79) Pan, F.; Wong, M. S.; Gramlich, V.; Bosshard, C.; Günter, P. *J. Am. Chem. Soc.* **1996**, *118*, 6315-6316.

(80) Frankenbach, G. M.; Etter, M. C. *Chem. Mat.* **1992**, *4*, 272-278.

(81) Cannon, A. S.; Warner, J. C. *Cryst. Growth Des.* **2002**, *2*, 255-257.

(82) Bedard, M.; Myers, J. L.; Wright, G. F.; Huber, H. *Can. J. Chem.-Rev. Can. Chim.* **1962**, *40*, 2278-2299.

(83) Scullion, H. J.; Lewis, J. *Talanta* **1966**, *13*, 1201-1202.

(84) Cobbledick, R. E.; Small, R. W. H. *Acta Crystallogr., Sect. B: Struct. Sci.* **1975**, *31*, 2805-2808.

(85) Haller, T. M.; Rheingold, A. L.; Brill, T. B. *Acta Crystallogr., Sect. C: Cryst. Struct. Commun.* **1983**, *39*, 1559-1563.

(86) George, R. S.; Cady, H. H.; Rogers, R. N.; Rohwer, R. K. *Industrial & Engineering Chemistry Product Research and Development* **1965**, *4*, 209-210.

(87) Selig, W. *Some 1:1 Complexes of Cyclomethylenetetranitramine (HMX) and Their Application to the Estimation of HMX in Admixture with RDX* Lawrence Radiation Laboratory, Livermore, California, 1964.

(88) Selig, W. *Explosivstoffe* **1966**, *14*, 174-177.

(89) Selig, W. *Explosivstoffe* **1967**, *15*, 76-87.

(90) Selig, W. *Explosivstoffe* **1969**, *17*, 73-86.

(91) Levinthal, M. L.; Patent, U. S., Ed.; Thiokol Corporation: United States, 1978; Vol. 4086110.

(92) Selig, W. *Propellants, Explos., Pyrotech.* **1982**, *7*, 70-77.

(93) Michaud, C.; Merx, H.; Poulain, G.; Lepage, S. *C.R. Hebd. Seances Acad. Sci. Ser. C* **1968**, *267*, 652-654.

(94) Selig, W. *Explosivstoffe* **1969**, *4*, 73-86.

(95) Selig, W. *Explosivstoffe* **1966**, *8*, 174-177.

(96) Hoffman, R. E.; Rabinovitz, M. *Magn. Reson. Chem.* **1993**, *31*, 1031-1033.

(97) Kotula, I.; Rabczuk, A. *Thermochim. Acta* **1988**, *126*, 61-66.

(98) Kotula, I.; Rabczuk, A. *Thermochim. Acta* **1988**, *126*, 67-73.

(99) Leibler, K.; Graczyk, A. *J. Chim. Phys. Phys.- Chim. Biol.* **1970**, *67*, 740-742.

(100) Foster, R.; Hanson, P. *Biochim. Biophys. Acta* **1966**, *112*, 482-489.

(101) Burkardt, L. A. *Anal. Chem.* **1956**, *28*, 1271-1273.

(102) Hammick, D. L.; Hutchison, H. P. *J. Chem. Soc.* **1955**, 89-91.

(103) Skraup, S.; Eismann, M. *Liebigs Ann.* **1926**, *449*, 1-14.

(104) Barnes, J. C.; Golnazarians, W. *Acta Crystallogr., Sect. C: Cryst. Struct. Commun.* **1987**, *43*, 549-552.

(105) Fourmigué, M.; Boubekeur, K.; Batail, P.; Renouard, J.; Jacob, G. *New J. Chem.* **1998**, *22*, 845-850.

(106) Selig, W. *Propellants, Explos., Pyrotech.* **1981**, *6*, 1-4.

Chapter 2 Cocrystal Engineering of a Prototype Energetic Material: Supramolecular Chemistry of 2,4,6-Trinitrotoluene

Published in *Crystal Growth & Design* **2010**, *10*, 5341-5347

2.1 Introduction

To rationally design energetic cocrystals, and energetic-energetic cocrystals in particular, cocrystallization principles for energetic materials first had to be developed. This includes not only a thorough understanding of favorable intermolecular interactions, supramolecular synthons, for cocrystallizing energetic materials, but also an understanding of what and to what extent properties relevant to energetic materials can be altered through cocrystallization. Therefore, despite the known existence of some multi-component complexes and cocrystals with energetic materials,[1-26] very little in the way of rational cocrystallization principles could be derived from these reports. In particular, there was a lack of single crystal structures, which offer clearest insight into favorable supramolecular synthons for energetic materials. Consequently, more systematic and thorough exploration of energetic materials was required. For organic energetic materials, two broad classes can be considered: aromatic and aliphatic energetic materials. Therefore, cocrystallization principles should be developed for both classes of materials. This chapter focuses on the aromatic class of energetic materials whereas Chapter 3 will focus on aliphatic energetic materials.

Electron-poor aromatic energetic materials represent a significant portion of the energetic materials available today. Starting with picric acid, first prepared in 1742 and used as an explosive in 1830, a plethora of energetic materials containing electron poor aromatic rings were developed, including 2,4,6-trinitrophenyl-N-methylnitramine (tetryl), 2,4,6-trinitrotoluene (TNT), 1,3,5-trinitrobenzene, and 1,3,5-triamino-2,4,6-trinitrobenzene (TATB).[27] Perhaps the most notable among these is TNT. First developed in 1863, TNT is still among the most commonly employed energetic materials,

in part for its low cost and easy manufacture, but also for its ability to be safely melt-cast into munitions and its relative insensitivity to detonation by physical shock. Unfortunately, TNT has a comparatively lower density, and thus explosive power, and has a relatively negative oxygen balance, and therefore produces too much carbon monoxide and soot. For both of these reasons TNT is a less than ideal explosive and improvements are still desirable. Multicomponent complexes, both in solution and in the solid state, are reported for some aromatic energetic materials including TNT and hexanitrostilbene (HNS).[1,2,4-8] Despite this work there was only one crystal structure of a TNT cocrystal reported in the Cambridge Structural Database (CSD): TNT/pyrene.[26] This cocrystal features donor-acceptor π-π interactions leading to a 1:1 complex of the two components. Here the generality of TNT cocrystallization was scrutinized for a wide range of cocrystal formers (ccf) and the alteration of structural, chemical, and spectroscopic properties, especially as they are relevant to energetic materials, was elucidated. The principles developed from this study can be applied to cocrystallization of other aromatic energetic materials.

2.2 Results and Discussion

2.2.1 Structure of TNT Cocrystals

A wide variety of potential cocrystal formers were screened for cocrystal formation with TNT. This resulted in the discovery of seventeen unique cocrystals with TNT from fifteen cocrystal formers, all of which were electron-rich aromatic compounds. The following compounds form cocrystals with TNT: naphthalene (**1**), 1-bromonaphthalene (**2**), anthracene (**3**), 9-bromoanthracene (**4**), phenanthrene (**5**), perylene (**6**), tetrathiafulvalene (**7**), thieno[3,2-*b*]thiophene (**8**), phenothiazine (**9**), dibenzothiophene (**10**), 4,6-dimethyldibenzothiophene (**11**), 1,2-phenylenediamine (**12**), 1,4-dimethoxybenzene (**13**), 4-aminobenzoic acid (**14**, **15**), and anthranilic acid (**16**, **17**). All of the cocrystals contain a 1:1 ratio of components with the exception of 4-aminobenozoic acid and anthranilic acid, which exist in both a 1:1 and 1:2 ratio with TNT (TNT/ccf). Structural elucidation of these cocrystals provides insight into the structural changes that occur due to cocrystallization as well as favorable interactions for

cocrystal formation. The crystallographic data of the TNT cocrystals obtained are presented in Table 2.1 and a discussion of the structures of these cocrystals follows.

Table 2.1 Crystallographic information for the seventeen cocrystals of TNT. All structures were collected at 95 K.

	1	**2**	**3**	**4**	**5**	**6**	**7**	**8**	**9**
formula	$C_{17}H_{13}N_3O_6$	$C_{17}H_{12}BrN_3O_6$	$C_{21}H_{15}N_3O_6$	$C_{21}H_{14}BrN_3O_6$	$C_{21}H_{15}N_3O_6$	$C_{27}H_{17}N_3O_6$	$C_{13}H_9N_3O_6S_4$	$C_{13}H_9N_3O_6S_2$	$C_{19}H_{14}N_4O_6S$
MW (g/mol)	355.30	434.21	405.36	484.26	405.36	479.44	431.47	367.35	426.40
stoichiometry	1:1	1:1	1:1	1:1	1:1	1:1	1:1	1:1	1:1
color	colorless	light yellow	orange	yellow	light yellow	red	dark brown	light yellow	dark brown
morphology	blade	blade	blade	blade	blade	needle	prism	blade	blade
solvent	ethanol	neat	THF	THF	ethanol	toluene	THF	ethanol	ethanol
crystal system	triclinic	triclinic	monoclinic	triclinic	orthorhombic	orthorhombic	triclinic	triclinic	orthorhombic
space group	$P\ \bar{1}$	$P\ \bar{1}$	$P2_1/c$	$P\ \bar{1}$	$P2_12_12_1$	$P2_12_12_1$	$P\ \bar{1}$	$P\ \bar{1}$	$P2_12_12_1$
a (Å)	8.6559(6)	7.2538(3)	14.0050(3)	6.7461(2)	7.07587(16)	7.19649(17)	8.39611(15)	6.81044(18)	7.4869(4)
b (Å)	9.8012(5)	7.7969(3)	6.72457(16)	8.61691(19)	9.2294(2)	7.98291(18)	9.42210(19)	9.2640(3)	9.1121(4)
c (Å)	10.0969(6)	14.8572(5)	19.4127(5)	17.3981(4)	27.7299(7	36.206(3)	11.4671(2)	12.7021(4)	26.5398(19)
α (deg)	92.333(3)	91.504(3)	90.00	97.606(2)	90.00	90.00	86.4170(10)	95.909(2)	90.00
β (deg)	111.371(4)	92.976(2)	103.538(2)	100.297(2)	90.00	90.00	69.5530(10)	91.239(2)	90.00
γ (deg)	96.598(4)	98.164(3)	90.00	103.182(2)	90.00	90.00	81.0340(10)	113.853(2)	90.00
cell vol. (Å^3)	789.26(8)	830.17(6)	1777.44(7)	952.90(4)	1810.92(8)	2079.98(16)	839.58(3)	727.29(4)	1810.56(18)
ρ_{calc} (g/cm^3)	1.495	1.737	1.515	1.698	1.487	1.531	1.707	1.677	1.564
Z	2	2	4	2	4	4	2	2	4
data/param.	2479/236	2581/245	3118/272	3075/280	3113/308	3078/296	2682/236	2302/218	2535/307/
R_1/wR_2	3.8/11.0	5.8/17.2	4.6/11.3	3.8/9.6	8.8/22.7	8.5/24.8	2.7/6.9	3.7/12.0	8.9/18.8
GOF	1.109	1.235	1.122	1.073	1.096	1.132	1.056	1.189	1.223

	10	**11**	**12**	**13**	**14**	**15**	**16**	**17**
formula	$C_{19}H_{13}N_3O_6S$	$C_{21}H_{17}N_3O_6S$	$C_{13}H_{13}N_5O_6$	$C_{15}H_{15}N_3O_8$	$C_{14}H_{12}N_4O_8$	$C_{21}H_{19}N_5O_{10}$	$C_{14}H_{12}N_4O_8$	$C_{21}H_{19}N_5O_{10}$
MW (g/mol)	411.38	439.44	335.28	365.30	364.28	501.41	364.28	501.41
stoichiometry	1:1	1:1	1:1	1:1	1:1	1:2	1:1	1:2
color	light yellow	yellow	brown	yellow	yellow	orange	yellow	orange
morphology	blade	blade	blade	blade	blade	prism	blade	prism
solvent	ethanol	ethanol	ethanol	ethanol	ethanol	ethanol	ethanol	melt
crystal system	monoclinic	triclinic	orthorhombic	monoclinic	monoclinic	monoclinic	triclinic	triclinic
space group	$P2_1/c$	$P\ \bar{1}$	$Pna2_1$	$P2_1/n$	$P2_1$	$P2_1/c$	$P\ \bar{1}$	$P\ \bar{1}$
a (Å)	9.09248(16)	7.22567(18)	19.0408(13)	6.6019(8)	6.90525(18)	10.5492(4)	6.68253(12)	10.3188(3)
b (Å)	7.17969(18)	9.3056(2)	6.66738(12)	28.237(3)	14.1124(3)	14.4420(5)	8.67582(16)	13.8350(3)
c (Å)	54.4492(10)	15.1173(3)	11.1188(2)	8.6743(8)	15.7976(11)	14.7554(6)	14.2195(10)	15.3114(11)
α (deg)	90.00	104.5420(10)	90.00	90.00	90.00	90.00	86.507(6)	89.339(6)
β (deg)	95.7200(10)	96.8790(10)	90.00	91.197(7)	93.559(7)	101.061(2)	80.859(6)	85.674(6)
γ (deg)	90.00	91.3760(10)	90.00	90.00	90.00	90.00	68.812(5)	81.667(6)
cell vol. (Å^3)	3536.81(13)	975.28(4)	1411.56(11)	1616.7(3)	1536.50(12)	2206.25(15)	758.90(6)	2156.63(17)
ρ_{calc} (g/cm^3)	1.545	1.496	1.578	1.501	1.575	1.510	1.594	1.544
Z	8	2	4	4	4	4	2	4
data/param.	6058/524	3145/281	2366/233	2511/235	4686/494	3764/351	2557/235	7458/697
R_1/wR_2	5.9/15.2	5.9/15.8	3.4/10.0	6.5/16.9	5.8/12.8	7.5/17.7	5.1/14.3	9.4/25.3
GOF	1.056	1.159	0.981	1.032	1.113	1.154	1.002	1.042

Donor-acceptor π-π interactions drive the formation of these cocrystals. Due to the strong electron-withdrawing effects of the nitro groups, TNT has an electron-poor π-system; conversely, the cocrystal formers all possess relatively electron-rich benzene rings promoting a favorable interaction between the electron-poor and electron-rich aromatic rings. Electrostatic potential surfaces, which show the calculated distribution of electron density on the surface of a molecule, provide a means to visualize areas of charge on a molecule and thereby understand intermolecular interactions. The calculated electrostatic potential surfaces of TNT and the cocrystal formers are shown in Figure 2.1. The introduction of donor-acceptor π-π interactions between aromatic rings has a profound influence on the packing of the molecules in these cocrystals, and consequently on the solid-state properties. Both polymorphs of TNT, as well as most of the cocrystal formers in their pure form, pack in a herringbone motif to facilitate electrostatically favorable edge-to-face interactions.[28-30] Due to the donor-acceptor π-π interactions, face-to-face π-stacking is observed in the cocrystals. Representative examples of both packing motifs are presented in Figure 2.2. All of the TNT cocrystals presented similar face-to-face π-stacking motifs to the TNT/anthracene cocrystal.

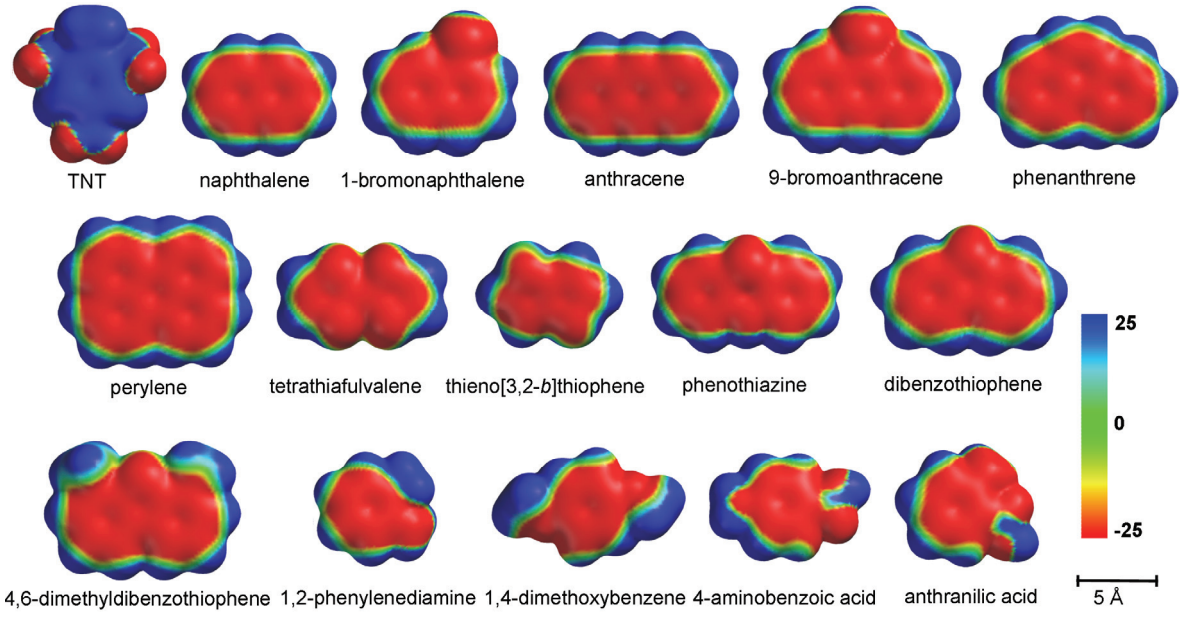

Figure 2.1 Electrostatic potential surfaces of TNT and the cocrystal formers calculated using the semi-empirical method and the AM1 model. Red and blue surfaces represent electron rich and poor regions respectively. Surfaces are normalized between -25 and 25 kJ/mol.

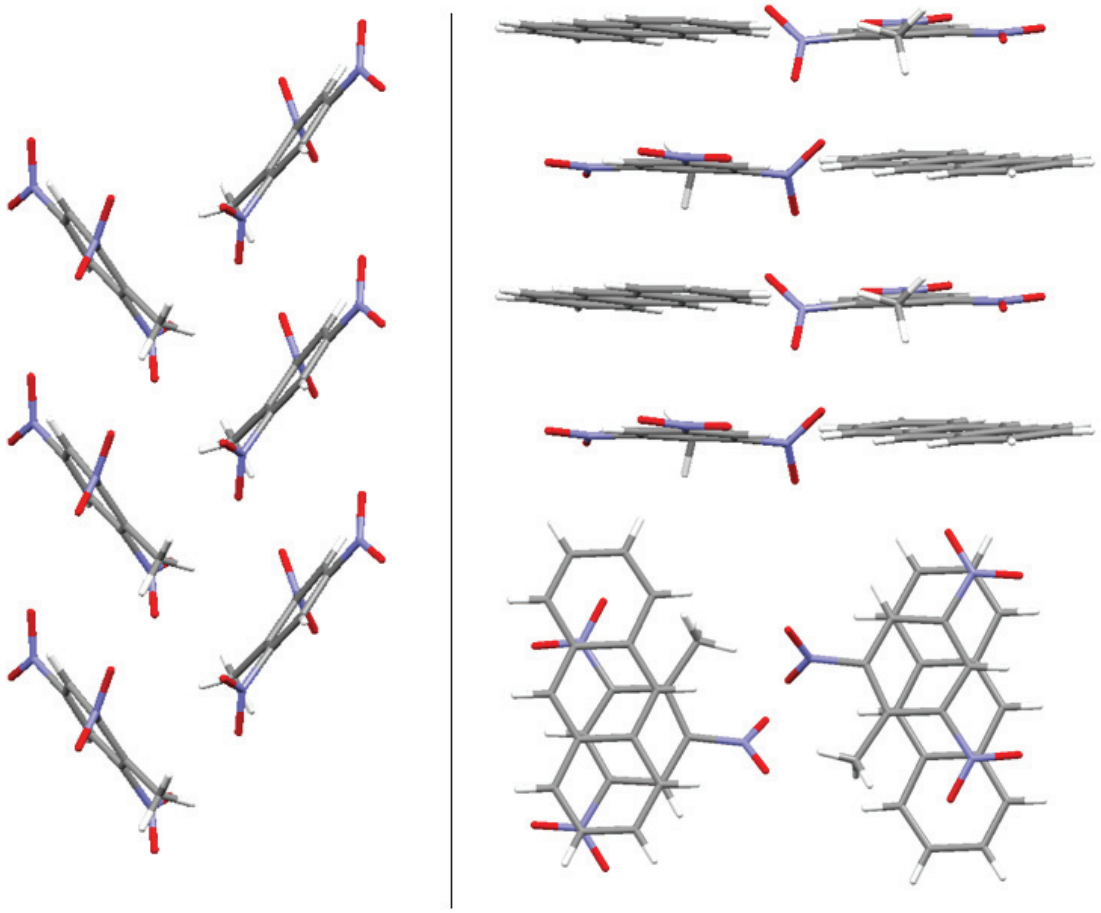

Figure 2.2 A comparison of the herringbone packing of monoclinic TNT (CSD code ZZZMUC08)[30] (left) and a the face-to-face π-stacking of the TNT/anthracene cocrystal (right)

The formation of cocrystals with TNT not only alters the π-stacking motif of the cocrystal formers, but also significantly reorients the nitro groups of the TNT molecule. In particular, there is a notable and consistent change in the angle of the nitro group in the 4 position (*para* to the CH_3) of TNT in the cocrystals. In monoclinic TNT these nitro groups of the inequivalent molecules make angles of 33.8 and 23.7° to the benzene ring, whereas in orthorhombic TNT the corresponding angles are 33.9 and 23.2°.[30] In the TNT cocrystals, these angles range from 1.3 to 14.3° and are 5.0° on average. Torsion angles are presented in Table 2.2.

Table 2.2 Average torsion angles for the 4-nitro group of TNT in the TNT polymorphs and cocrystals. When two inequivalent TNT molecules are present both torsion angles are given.

TNT/TNT cocrystal	TNT A (°)	TNT B (°)
monoclinic TNT	33.8	23.7
orthorhombic TNT	33.9	23.2
naphthalene	5.4	
1-bromonaphthalene	2.1	
anthracene	3.4	
9-bromoanthracene	2.3	
phenanthrene	1.3	
perylene	2.5	
tetrathiafulvalene	3.5	
thieno[3,2-*b*]thiophene	4.8	
phenothiazine	4.1	
dibenzothiophene	1.4	2.3
4,6-dimethyldibenzothiophene	4.5	
1,2-phenylenediamine	1.8	
1,4-dimethoxybenzene	4.7	
4-aminobenzoic acid (1:1)	9.0	14.3
4-aminobenzoic acid (1:2)	6.4	
anthranilic acid (1:1)	6.2	
anthranilic acid (1:2)	4.7	14.6

The change in orientation of the nitro groups influences the properties of TNT within the cocrystals. Indeed, the change in the orientation of nitro groups is significant enough that it results in shifts in the vibrational spectra of these materials. Monoclinic and orthorhombic TNT have an asymmetric nitro stretch (ν_{as}) at 1537.4 and 1535.7 cm^{-1} and a symmetric nitro stretch (ν_s) at 1368.7 and 1358.7 cm^{-1} respectively. In the TNT cocrystals, the asymmetric nitro stretch generally increases in energy with respect to both forms of TNT, 6.7 and 8.4 cm^{-1} on average for monoclinic and orthorhombic TNT respectively. In contrast to this, the symmetric nitro stretch in the TNT cocrystals decreases in energy, 8.7 cm^{-1} on average, with respect to monoclinic TNT, while remaining relatively unchanged with respect to orthorhombic TNT.[31]

Although the donor-acceptor π-π interactions are dominant in the formation of the TNT cocrystals reported herein, the secondary interactions within these cocrystals provide valuable insight into favorable interactions that can be applied in the formation of cocrystals with other nitrated energetic materials. The amine-nitro interaction is expected to be among the strongest of the interactions found in the TNT cocrystals and indeed is present in all of the cocrystals containing amine functional groups, including the cocrystals of TNT with 1,2-phenylenediamine, 4-aminobenzoic acid, anthranilic acid and phenothiazine.[32] Monocoordinated amine-nitro interactions are observed in every TNT cocrystal containing an amine functional group (examples shown in Figure 2.3). These interactions are incorporated into a wide variety of motifs in the TNT cocrystals including dimers, chains and rings. Bicoordinated amine-nitro interactions occur only in the TNT/anthranilic acid 1:2, TNT/1,2-phenylenediamine and TNT/phenothiazine cocrystals (Figures 2.3 and 2.4).

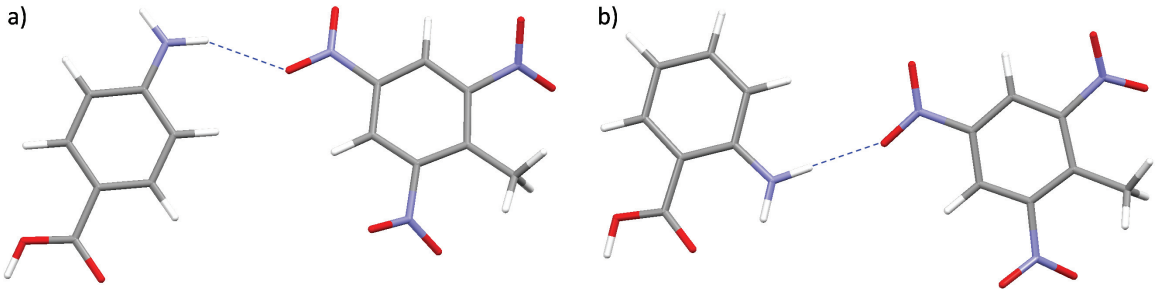

Figure 2.3 Example of a monocoordinated amine-nitro interaction in the a) TNT-4/aminobenzoic acid 1:1 cocrystal and the b) TNT/anthranilic acid 1:1 cocrystal.

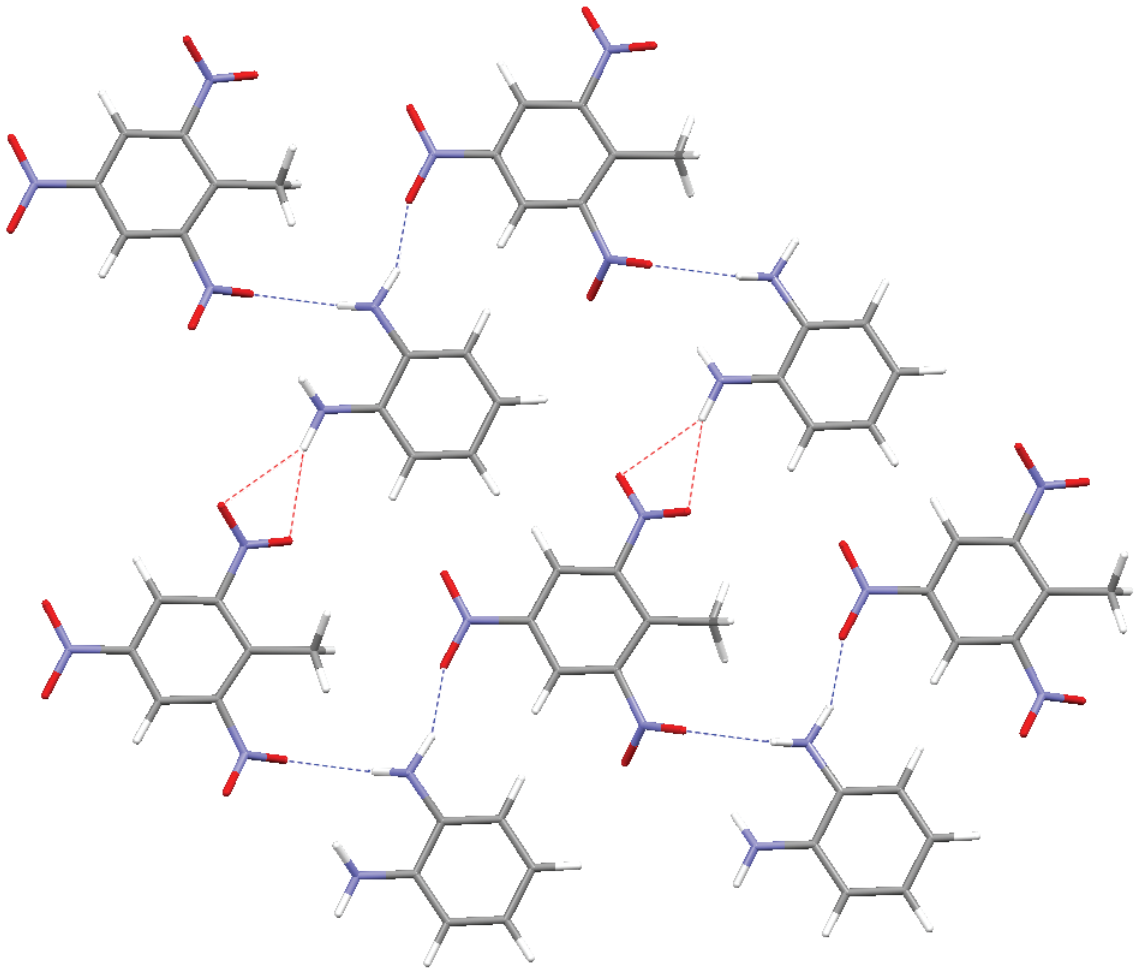

Figure 2.4 Amine-nitro interactions in the TNT/1,2-phenylenediamine cocrystal. Both monocoordinated (blue) and bicoordinated (red) amine-nitro interactions are observed.

The monocoordinated amine-nitro interactions in the TNT/1,2-phenylenediamine cocrystal form a chain ($C_2^2(10)$) that generates sheets of alternating TNT and 1,2-phenylenediamine molecules when linked through the bicoordinated (2.376 and 2.450 Å) amine-nitro interaction ($R_1^2(4)$). In the TNT/anthranilic 1:2 cocrystal the bicoordinated amine-nitro interaction (2.221 and 2.397 Å) forms a dimer between anthranilic acid and TNT ($R_1^2(4)$). In a similar fashion, the amine of the TNT/phenothiazine cocrystal is bicoordinated to a nitro group of TNT, though asymmetrically (2.381 and 2.754 Å), to form a dimer ($R_1^2(4)$). In general the TNT cocrystals containing amines do not preferentially form bicoordinated (three-centered) amine-nitro interactions, as might be expected based on interactions of nitroanilines reported in the literature.[33,34]

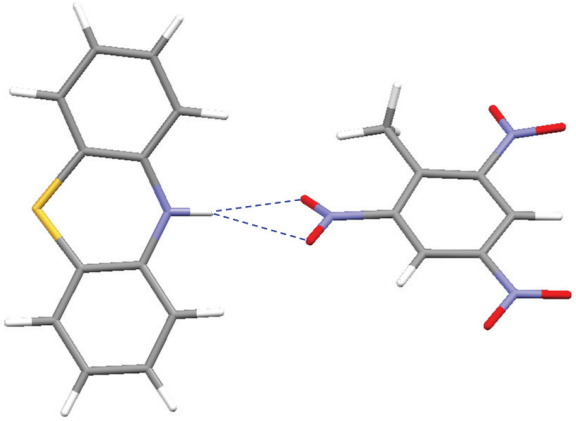

Figure 2.5 The bicoordinated amine-nitro interaction in the major conformer of the TNT/phenothiazine cocrystal.

2.2.2 Properties of TNT Cocrystals.

One significant result of cocrystallizing TNT is that a relatively dramatic change in the density of this material can be accomplished. Density is often used as a very general guide to predict properties, including the detonation velocity and detonation pressure, of explosives.[35] More dense energetic materials have the potential to have larger detonation velocities and therefore are preferred. A comparison of the densities of the TNT cocrystals to that of the cocrystal formers is presented in Table 2.3. As might be expected, many of these cocrystals have a density in between that of both components. This is not always the case, however; the TNT/tetrathiafulvalene cocrystal has a density higher than two of the reported forms of tetrathiafulvalene and the orthorhombic form of TNT. Perhaps more notable is the TNT/1-bromonaphthalene cocrystal in which the density is higher than both forms of TNT as well as pure 1-bromonaphthalene. This latter cocrystal in particular demonstrates the effectiveness of cocrystallization in achieving higher density materials. It should be noted, however, when cocrystallizing an energetic material with a non-energetic material that even the approximate relationship of density to the detonation properties no longer applies. In the case of the TNT/1-bromonaphthalene cocrystal, even though the overall density of 1.737 g/cm^3 is greater than that of monoclinic TNT (1.713 g/cm^3), the effective density of TNT is reduced to 0.909 g/cm^3. While TNT is diluted in this case, these results still raise the intriguing possibility that by cocrystallizing two energetic materials together higher density explosives with enhanced performance could be achieved.

Table 2.3 A comparison of the densities of the TNT cocrystals to the available polymorphs of the cocrystal formers (ccf).[36-55] All densities reported are for crystals at 95 K unless otherwise specified.

compound	TNT cocrystal (g/cm^3)	ccf form I (g/cm^3)	ccf form II (g/cm^3)	ccf form III (g/cm^3)
phenanthrene	1.487	1.222[c]		
naphthalene	1.495	1.239[l]		
4,6-dimethyldibenzothiophene	1.496	1.299[c]		
1,4-dimethoxybenzene	1.501	1.231[f]		
4-aminobenzoic acid (1:2)	1.509	1.373[c]	1.389[b,c]	
anthracene	1.515	1.297[k]	1.250[c]	
perylene	1.531	1.388[f]	1.394[e]	
anthranilic acid (1:2)	1.544	1.369[c]	1.409[c]	1.388[c]
dibenzothiophene	1.545	1.418[i]		
phenothiazine	1.561	1.387[c]	1.417[h]	
4-aminobenzoic acid (1:1)	1.575	1.373[c]	1.389[b,c]	
1,2-phenylenediamine	1.578	1.214[c]		
anthranilic acid (1:1)	1.594	1.369[c]	1.409[c]	1.388[c]
thieno[3,2-*b*]thiophene	1.677	1.542[c]		
9-bromoanthracene	1.698	1.592[c]	1.622[c]	
TNT	–	1.713[i]	1.704[g]	
tetrathiafulvalene	1.707	1.686[d]	1.750[j]	1.676[i]
1-bromonaphthalene	1.737	1.489[a]		

[a]liquid at room temperature, no crystal structure available [b]designated form beta IV
[c]room temperature [d]290 K [e]200 K [f]150 K [g]123 K [h]120 K [i]100 K [j]98 K [k]94 K [l]90 K

In the case of TNT/1-bromonaphthalene, not only has the density increased relative to the pure components, but multifunctionality has been added to this material as well. Through cocrystallization a halogen, bromine, is effectively added to TNT. The production of reactive halogen species within the explosion plume provides a means of annihilating biological and chemical warfare agents (BWA and CWA) remotely.[56,57] Much effort has been exerted to synthetically introduce halogens into energetics to create effective anti-BWA and anti-CWA munitions. Here cocrystallization is shown to provide a straightforward means to add halogens to existing energetic materials. By selecting

appropriately halogenated cocrystal formers, cocrystallization offers the opportunity to modify energetics as needed without necessitating new chemical synthesis.

In addition to density, cocrystallization also changes the packing coefficient. As evidenced from the packing coefficients of the TNT cocrystals and cocrystal formers in Table 2.4, all of the packing coefficients are altered with respect to the cocrystal formers. Packing coefficients were calculated by using the following equation: $C_k = ZV_{mol}V_{cell}^{-1}$, where C_k is the packing coefficient, Z is the number of molecules in the unit cell, V_{mol} is the molecular volume (Å^3), and V_{cell} is the volume of the unit cell. While many of the TNT cocrystals do not possess higher density with respect to TNT, the packing coefficient of TNT improves by as much as 3.6% through cocrystallization. Indeed, the packing coefficients of more than half of cocrystals formed are higher than those of either polymorph of TNT, indicating a strong complementary relationship between the molecules. Although there is a reduction of the packing coefficient of the cocrystals with respect to the solid forms of many of the aromatic compounds without functional groups, these compounds provide a means to improve the packing coefficient with respect to the solid forms of TNT by minimizing empty space within the crystal lattice of this energetic material.[58,59] These cocrystals highlight the potential to minimize the free volume in solid forms with TNT and other energetic materials and provide insights into the size and shapes of molecules that can improve the packing coefficient.

Table 2.4 A comparison of the packing coefficients of the TNT cocrystals to the available polymorphs of the cocrystal formers (ccf).[36-55] All packing coefficients reported are for crystal forms at 95 K unless otherwise specified.

compound	TNT cocrystal	ccf form I	ccf form II	ccf form III
1,4-dimethoxybenzene	81.6%	82.2%[f]		
anthranilic acid (1:2)	82.0%	81.2%[c]	83.8%[c]	82.3%[c]
4-aminobenzoic acid (1:1)	82.2%	82.1%[c]	83.2%[b,c]	
4-aminobenzoic acid (1:2)	82.2%	82.1%[c]	83.2%[b,c]	
TNT	–	82.4%[i]	81.9%[g]	
anthranilic acid (1:1)	82.6%	81.2%[c]	83.8%[c]	82.3%[c]
phenanthrene	82.7%	82.1%[c]		
4,6-dimethyldibenzothiophene	82.7%	83.1%[c]		
phenothiazine	82.8%	84.3%[c]	86.1%[h]	
9-bromoanthracene	83.1%	81.8%[c]	86.1%[c]	
dibenzothiophene	83.2%	87.4%[i]		
thieno[3,2-*b*]thiophene	83.4%	82.9%[c]		
1-bromonaphthalene[a]	83.5%	–		
naphthalene	84.0%	87.5%[l]		
anthracene	85.0%	88.1%[k]	85.0%[c]	
1,2-phenylenediamine	85.4%	80.7%[c]		
tetrathiafulvalene	85.4%	80.4%[d]	83.8%[j]	79.9%[i]
perylene	86.6%	89.6%[f]	90.0%[e]	

[a]liquid at room temperature, no crystal structure available [b]designated form beta IV
[c]room temperature [d]290 K [e]200 K [f]150 K [g]123K [h]120 K [i]100 K [j]98 K [k]94 K [l]90 K

Cocrystallization forms unique compounds and therefore, drastically altered melting points can be achieved. A summary of the melting points for the TNT cocrystals are presented in Table 2.5. The TNT cocrystals formed exhibit a wide range of melting points. Through cocrystallization the melting point with respect to TNT can be lowered by as much as 36 °C or increased by 94 °C. While many of the melting points of the cocrystals formed are between that of both cocrystal formers, this is not always the case. Two notable exceptions to this trend are the TNT cocrystals with 1,4-dimethoxybenzene and 1,2-phenylenediamine where the cocrystal exhibits a lower melting point than either of the pure components. By contrast, the cocrystals of TNT with thieno[3,2-*b*]thiophene,

naphthalene, dibenzothiophene, and anthranilic acid all exhibit melting points higher than either cocrystal former. Through cocrystallization therefore, it is possible to manipulate the melting point of energetic materials as needed. For example, decreasing the melting point can be desirable to form energetic materials that can be easily melt-processed. Conversely, increasing the melting point can be advantageous when creating munitions that resist deformation prior to detonation. The range of temperatures available through this technique is notably broader than that achievable through polymorphic modification.

Table 2.5 Melting points of TNT cocrystals as compared to the most stable polymorph of the cocrystal formers (ccf) measured using differential scanning calorimetry (DSC) at a ramp rate of 10 °C/min.

TNT/TNT cocrystal	ccf (°C)	cocrystal (°C)
1,4-dimethoxybenzene	56.6	45.2
1-bromonaphthalene	-1.0	73.3
1,2-phenylenediamine	101.8	73.8
orthorhombic TNT	81.1	–
monoclinic TNT	81.9	–
thieno[3,2-*b*]thiophene	56.0	83.7
naphthalene	81.5	95.9
phenanthrene	99.7	100.2
9-bromoanthracene	102.9	101.0
phenothiazine	186.4	107.2
anthracene	217.1	108.5
tetrathiafulvalene	119.2	108.8
4,6-dimethyldibenzothiophene	154.6	116.3
4-aminobenzoic acid (1:1)	188.1	117.6
dibenzothiophene	99.0	118.8
anthranilic acid (1:2)	99.0	139.3
perylene	276.0	151.5
anthranilic acid (1:1)	99.0	151.7
4-aminobenzoic acid (1:2)	188.1	175.2

Cocrystallization also can produce significant changes in another critical thermal property for energetic materials: the decomposition temperature. Ideally this value is high for energetic materials to ease processing as well as to increase their detonation

temperature and thus allow for deeper penetration of the energetic material into a target. The decomposition temperature data are summarized in Table 2.6.

Table 2.6 Decomposition temperature and enthalpy of TNT and TNT cocrystals as measured by DSC at a ramp rate of 10 °C/min.

TNT/TNT cocrystal	$T_{decomp.}$ (°C)	ΔH_{decomp} (kJ/g)
tetrathiafulvalene	202.9	0.95
phenothiazine	237.3	1.1
4-aminobenzoic acid (1:2)	251.8	0.34
4-aminobenzoic acid (1:1)	256.7	1.0
anthranilic acid (1:2)	258.4	0.45
anthranilic acid (1:1)	266.2	1.0
1,2-phenylenediamine	267.3	0.91
perylene	268.6	0.91
9-bromoanthracene	288.2	1.5
1,4-dimethoxybenzene	289.5	0.89
thieno[3,2-*b*]thiophene	291.9	1.3
anthracene	293.5	1.4
1-bromonaphthalene	296.4	0.84
monoclinic TNT	298.0	1.7
4,6-dimethyldibenzothiophene	299.1	1.4
orthorhombic TNT	299.6	2.0
naphthalene	304.2	0.71
phenanthrene	307.0	1.3
dibenzothiophene	312.8	1.2

In almost every case, the decomposition temperature of cocrystals is altered with respect to TNT. Even in the liquid state the interactions driving the formation of the cocrystals are significant enough to change the decomposition temperature by as much as 95 °C. It is notable that in some of the cocrystals formed, the decomposition temperature can be increased with respect to TNT. This is observed in TNT cocrystals with phenanthrene, naphthalene, dibenzothiophene, and 4,6-dimethyldibenzothiophene. By selecting the appropriate cocrystal former, therefore, cocrystallization provides a means

of increasing the decomposition temperature and therefore improving this aspect of a common energetic material.

Although the TNT cocrystals presented here are diluted through cocrystallization with non-energetic materials, violent decomposition is still achievable (Figures 2.6 and 2.7). In all DSC thermograms a substantial heat of decomposition was observed. Qualitative tests of a subset of cocrystals confirm that violent decomposition is still achievable in these TNT cocrystals with non-energetics, thus validating the approach of making new multifunctional energetic compositions based on a single energetic component.

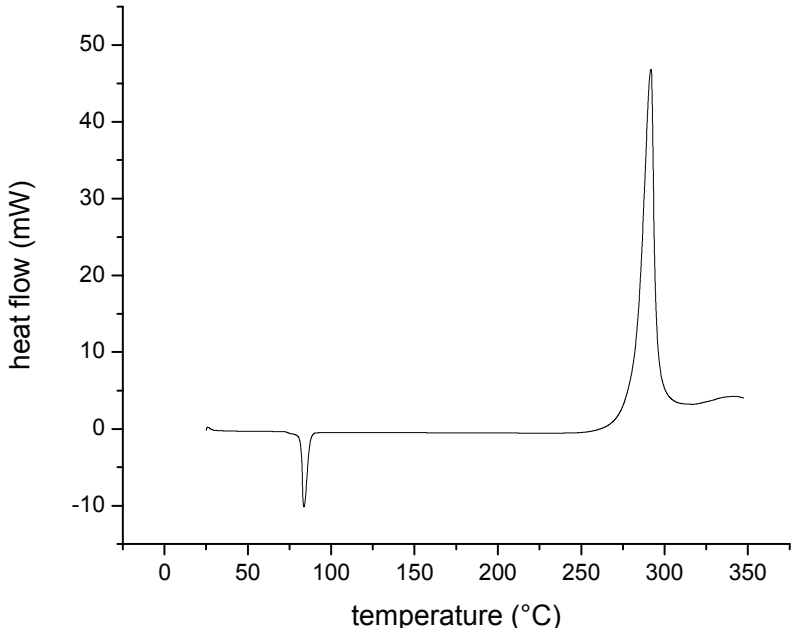

Figure 2.6 DSC thermal trace for the TNT/thieno[3,2-*b*]thiophene cocrystal (exothermic direction up). The endothermic peak shows the melting point of the cocrystal (83.7 °C) and the exothermic peak is the decomposition of the cocrystal (291.9 °C).

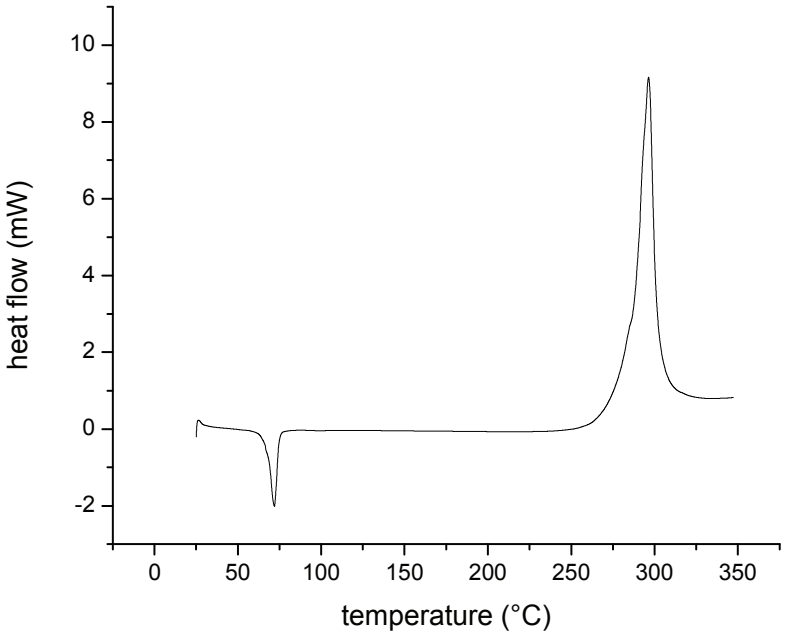

Figure 2.7 DSC thermal trace for the TNT/1-bromonaphthalene cocrystal (exothermic direction up). The endothermic peak shows the melting point of the cocrystal (73.3 °C) and the exothermic peak is the decomposition of the cocrystal (296.4 °C).

2.3 Conclusions

A wide range of aromatic compounds successfully form cocrystals with TNT mediated by donor-acceptor π-π interactions. These interactions direct the cocrystal structure, giving preference to face-to-face over edge-to-face stacking. When present, amine-nitro interactions also guide the cocrystal structure. The alterations in structure ultimately produce unique properties in the cocrystals, with respect to the pure components. Properties vital to energetic materials, including the density, packing coefficient, melting point and decomposition temperature are successfully modified through cocrystallization. Indeed, this technique allows for wider variations in the properties of energetic materials than is achievable through polymorphic modification. Although the interactions mediating cocrystal formation discussed here are applicable primarily to the aromatic family of energetic compounds, the concept of cocrystallizing energetic materials to improve their properties can be applied broadly. Indeed, as will be shown in Chapters 3 and 4, favorable electrostatic interactions are often key in the formation of energetic cocrystals.

2.4 Experimental

2.4.1 Materials

Naphthalene (98%), anthracene (99%), 9-bromoanthracene (94%), phenanthrene (98+%), dibenzothiophene (98%), 2-amino-4,5-dimethoxybenzoic acid (98%) and perylene (99%) were obtained from Aldrich (Milwaukee, WI). Tetrathiafulvalene (97%), 4,6-dimethyldibenzothiophene (97%), 1,4-dimethoxybenzene (99%) and 1,2-phenylenediamine (99.5%) were obtained from Aldrich, (St. Louis, MO). Phenothiazine and 1-bromonaphthalene (97%) were obtained from Sigma (St. Louis, MO). Anthranilic acid (puriss, >99.5%) was obtained from Fluka (Steinheim, Switzerland). 2,4,6-Trinitrotoluene[60] and thieno[3,2-*b*]thiophene[61] were synthesized and purified according to the published procedures. *Caution! 2,4,6-Trinitrotoluene is an explosive material and care should be exercised in avoiding excessive heat, static electricity and mechanical shock!*

2.4.2 Cocrystal Formation

High throughput screening (HTS) experiments were performed in 96 well polypropylene plates. Solutions were dispensed into the plates using either a Gilson 215 liquid handler or an Eppendorf EpMotion 5070 liquid handling robot. A 10 mg/mL (0.044 M) solution of TNT in ethanol (Decon Labs, Inc., 200 Proof, USP) was dispensed throughout the plate; the volumes dispensed across each row were 0, 2, 2, 3, 4, 3, 4, 4, 6, 6, 6, and 4 μL. A different cocrystal former solution (0.044 M) was dispensed for every row; the volumes dispensed across each row were 6, 8, 6, 6, 6, 4, 4, 3, 4, 3, 2, and 0 μL. Cocrystal formers screened were dissolved in ethanol when possible. Cocrystal formers anthracene, 9-bromoanthracene, and tetrathiafulvalene were dissolved in inhibitor free tetrahydrofuran (Fisher Chemical, HPLC Grade). Other solvents used for the screening process include methanol (Fisher Chemical, Certified ACS), dimethylsulfoxide (Fisher Chemical, HPLC Grade), and toluene (Fisher Chemical, Certified ACS). The solutions were mixed, covered and allowed to evaporate at room temperature over a period of three days. The resulting ratios of cocrystal former to TNT were 1:4, 1:3, 1:2, 2:3, 3:4, 1:1, 4:3, 3:2, 2:1, and 3:1.

2.4.3 Additional Crystallizations

Additional crystallizations were performed to produce cocrystals for powder X-ray diffraction (PXRD), thermal analysis and single crystal X-ray diffraction. **TNT/naphthalene (1)** 1.380 mg TNT and 0.779 mg naphthalene in 1 mL ethanol, 6.1 mg TNT and 3.7 mg naphthalene in 0.7 mL ethanol, 0.604 mg TNT and 0.232 mg naphthalene in acetone; **TNT/anthracene (3)** 0.367 mg TNT and 0.401 mg anthracene in 0.5 mL tetrahydrofuran (THF), 0.845 mg TNT and 0.798 mg anthracene in 0.5 mL THF; **TNT/9-bromoanthracene (4)** 0.442 mg TNT and 0.506 mg of 9-bromoanthracene in 0.5 mL acetonitrile, 10.4 mg TNT and 11.8 mg 9-bromoanthracene in 1 mL THF; **TNT/phenanthrene (5)** 0.651 mg TNT and 0.532 mg phenanthrane in 0.5 mL ethanol; **TNT/tetrathiafulvalene (7)** 0.582 mg TNT and 0.522 mg tetrathiafulvalene in 0.5 mL THF; **TNT/thieno[3,2-*b*]thiophene (8)** 6.7 mg TNT and 4.6 mg thieno[3,2-*b*]thiophene in 0.7 mL ethanol, 1.373 mg TNT and 0.623 mg thieno[3,2-*b*]thiophene in acetone, 1.240 mg TNT and 0.747 mg thieno[3,2-*b*]thiophene in ethanol; **TNT/phenothiazine (9)** 0.853 mg TNT and 0.795 mg phenothiazine in 0.5 mL ethanol; 0.372 mg TNT and 0.342 mg phenothiazine in ethanol; **TNT/dibenzothiophene (10)** 0.657 mg TNT and 0.629 mg dibenzothiophene in 0.5 mL ethanol; **TNT/4,6-dimethyldibenzothiophene (11)** 2.0 mg TNT and 1.9 mg 4,6-dimethyldibenzothiophene in 0.4 mL of ethanol; **TNT/1,2-phenylenediamine (12)** 5.903 mg TNT and 2.775 mg 1,2-phenylenediamine in 1 mL of methanol; 0.967 mg TNT and 0.503 mg 1,2-phenylenediamine in a 1:1 mixture by volume of THF and ethanol; **TNT/1,4-dimethoxybenzene (13)** 13.399 mg TNT and 8.216 mg 1,4-dimethoxybenzene in 1.6 mL ethanol; **TNT/4-aminobenzoic acid 1:1 (14)** 12.128 mg TNT and 7.384 mg 4-aminobenzoic acid in 1.4 mL ethanol; **TNT/anthranilic acid 1:1 (16)** 7.473 mg TNT and 4.750 mg anthranilic acid in 1 mL ethanol.

2.4.4 Thermomicroscopy

Thermomicroscopy was performed with a Linkham LTS 350 hot stage connected to a Linkham TMS 94 processor and controlled using Linksys32 Version 1.9.3 software, viewed under polarized light with a Nikon Eclipse E600 microscope. For initial observation, samples were heated from room temperature up to temperatures ranging from 50 to 200 °C at a rate of 1 °C/min. Fused samples were cooled and identified using Raman spectroscopy. Thermomicroscopy was used to form three TNT cocrystals:

TNT/1-bromonaphthalene (2) 1 mg of TNT in excess 1-bromonaphthalene was heated at a rate of 1 ºC/min to 50 ºC and held for 15 minutes, cooled and allowed to sit for 24 hours; **TNT/4-aminobenzoic acid 1:2 (15)** 1 mg of the 1:1 TNT-4-aminobenzoic acid cocrystal was heated at 10 ºC/min to 107 ºC and held there for 15 minutes; **TNT/anthranilic acid 1:2 (17)** 1 mg of both TNT and anthranilic were mixed, placed on a microscope slide under cover slip, heated up to 120 °C at 1 °C/min, and held at this temperature for 1 hour.

2.4.5 Raman Spectroscopy

Raman spectra were obtained using a Renishaw inVia Raman microscope equipped with a 633 nm He-Ne laser and a 514 nm argon laser with 1800 lines/mm grating and a RenCam CCD detector. Spectra were collected and analyzed using the WiRE 3.1 software package. Calibration was performed using a silicon standard. Spectra were collected using an Olympus SLMPlan 20 × objective (numerical aperture = 0.35) and 50 μm slit in extended scan mode with a range of 100-3600 cm^{-1}.

2.4.6 Powder X-Ray Diffraction

Powder X-ray diffraction (PXRD) patterns were collected at 95 K using a Rigaku R-Axis Spider diffractometer with an image plate detector and graphite monochromated Cu-Kα radiation (1.5419 Å). Samples were mounted on a CryoLoop™ and images were collected for ten minutes while rotating the sample about the φ-axis at 10°/sec, oscillating ω between 120° and 180° at 1°/sec with χ fixed at 45°. Images were integrated from 3° to 70° with a 0.05° step size using AreaMax 2 software. Powder patterns were processed in Jade Plus.

2.4.7 Single Crystal X-ray Diffraction

All measurements were made on a Rigaku R-Axis Spider diffractometer with an image plate area detector using graphite monochromated Cu-Kα radiation (1.5419 Å). All collections were carried out at 95 K with the sample mounted on a MiTeGen MicroMount™. The structures were solved by direct methods[62,63] and expanded using Fourier techniques.[64] The non-hydrogen atoms were refined anisotropically and the hydrogen atoms were refined using the riding model. The final cycle of full-matrix least-

squares refinement was made on F^2. An empirical absorption correction was applied to the structure. All calculations were performed using the CrystalStructure 3.8[65] crystallographic software package except for refinement, which was performed using SHELXL-97.[66] For determination of inter- and intramolecular distances, all carbon-hydrogen bond lengths were normalized to 1.083 Å, all nitrogen-hydrogen bond lengths were normalized to 1.008 Å and all oxygen-hydrogen bond lengths were normalized to 0.983 Å. Structures **1**, **2**, **4**, **7**, **8**, **10**, **11**, and **16** all exhibit low completeness due to the triclinic space group and the copper X-ray radiation source employed; data collection strategies to achieve the maximum possible completeness were used. Structure **17** has a relatively high R factor (0.0944). The method for the formation of this 1:2 cocrystal introduces disorder within the bulk of the crystal and therefore good quality crystals of adequate size for single crystal X-ray diffraction could not be grown. In structures **6** and **9** large C-C bond uncertainties (>0.01 Å) were observed (0.011 and 0.015 Å respectively). Quality crystals of **6** were not obtainable; this cocrystal exhibits a significant amount of disorder in the nitro groups of the TNT, and the best crystal selected still diffracted weakly. Despite considerable effort, high quality crystals, without twinning, of **9** were not obtainable; this cocrystal structure exhibits a significant amount of disorder, particularly in two of the nitro groups of TNT as a result of the various conformations possible for these groups. Due to poor crystal quality large C-C bond uncertainties were observed. The disorder in the nitro groups also contributed significantly to increasing the ADP values of two oxygen atoms, O1B and O5B.

2.4.8 Differential Scanning Calorimetry

Thermograms of the samples were recorded on a TA Instruments Q10 differential scanning calorimeter and programmed using Thermal Advantage for Q Series Version 2.5. Samples (0.5-2 mg weighed to a precision of 0.005 mg) were placed in aluminum pans and the lids were crimped using a TA-Instruments hermetic sealing press. Thermal behavior of the samples was studied under a nitrogen purge of 50.0 mL/min at a heating rate of 10 °C/min, over a temperature range of 25-360 °C. The instrument was calibrated with an indium standard. Data were analyzed using Universal Analysis Version 4.3 Thermal Advantage Software.

2.4.9 Calculations

Packing coefficients were calculated by using the following equation: $C_k = ZV_{mol}V_{cell}^{-1}$, where C_k is the packing coefficient, Z is the number of molecules in the unit cell, V_{mol} is the molecular volume (Å^3), and V_{cell} is the volume of the unit cell. Molecular volume was calculated with Spartan '08 version 1.2.0 (Wavefunction, Inc.), which employs van der Waals radii of 1.89 Å for bromine, 1.92 Å for carbon, 1.20 Å for hydrogen, 1.55 Å for nitrogen, 1.52 Å for oxygen, and 1.82 Å for sulfur.

Torsion angles were determined using Mercury 1.4.2. Torsion angles were calculated by measuring the angle between the plane of the benzene ring and the plane formed by the nitrogen and two oxygen atoms of the nitro group.

Calculations of the electrostatic potential energy density maps were performed using semi-empirical methods with the AM1 model available in Spartan '08 version 1.2.0 (Wavefunction, Inc.). All maps were normalized between -25 and 25 kJ/mol.

2.5 References

(1) Kotula, I.; Rabczuk, A. *Thermochim. Acta* **1988**, *126*, 61-66.

(2) Kotula, I.; Rabczuk, A. *Thermochim. Acta* **1988**, *126*, 67-73.

(3) Leibler, K.; Graczyk, A. *J. Chim. Phys. Phys.- Chim. Biol.* **1970**, *67*, 740-742.

(4) Hammick, D. L.; Hutchison, H. P. *J. Chem. Soc.* **1955**, 89-91.

(5) Foster, R.; Hanson, P. *Biochim. Biophys. Acta* **1966**, *112*, 482-489.

(6) Skraup, S.; Eismann, M. *Liebigs Ann.* **1926**, *449*, 1-14.

(7) Hoffman, R. E.; Rabinovitz, M. *Magn. Reson. Chem.* **1993**, *31*, 1031-1033.

(8) Burkardt, L. A. *Anal. Chem.* **1956**, *28*, 1271-1273.

(9) Fourmigué, M.; Boubekeur, K.; Batail, P.; Renouard, J.; Jacob, G. *New J. Chem.* **1998**, *22*, 845-850.

(10) Bedard, M.; Myers, J. L.; Wright, G. F.; Huber, H. *Can. J. Chem.-Rev. Can. Chim.* **1962**, *40*, 2278-2299.

(11) Scullion, H. J.; Lewis, J. *Talanta* **1966**, *13*, 1201-1202.

(12) Cobbledick, R. E.; Small, R. W. H. *Acta Crystallogr., Sect. B: Struct. Sci.* **1975**, *31*, 2805-2808.

(13) Haller, T. M.; Rheingold, A. L.; Brill, T. B. *Acta Crystallogr., Sect. C: Cryst. Struct. Commun.* **1983**, *39*, 1559-1563.

(14) Haller, T. M.; Rheingold, A. L.; Brill, T. B. *Acta Crystallogr., Sect. C: Cryst. Struct. Commun.* **1985**, *41*, 963-965.

(15) George, R. S.; Cady, H. H.; Rogers, R. N.; Rohwer, R. K. *Ind. Eng. Chem. Prod. Res. Dev.* **1965**, *4*, 209-210.

(16) Selig, W. *Some 1:1 Complexes of Cyclomethylenetetranitramine (HMX) and Their Application to the Estimation of HMX in Admixture with RDX* Lawrence Radiation Laboratory, Livermore, California, 1964.

(17) Selig, W. *Explosivstoffe* **1966**, *14*, 174-177.

(18) Selig, W. *Explosivstoffe* **1966**, *8*, 174-177.

(19) Selig, W. *Explosivstoffe* **1967**, *15*, 76-87.

(20) Selig, W. *Explosivstoffe* **1969**, *17*, 73-86.

(21) Selig, W. *Explosivstoffe* **1969**, *4*, 73-86.

(22) Selig, W. *Propellants, Explos., Pyrotech.* **1981**, *6*, 1-4.

(23) Selig, W. *Propellants, Explos., Pyrotech.* **1982**, *7*, 70-77.

(24) Levinthal, M. L.; Patent, U. S., Ed.; Thiokol Corporation: United States, 1978; Vol. 4086110.

(25) Levakova, I. V.; Korobko, A. P.; Krasheninnikov, S. V.; Zavodnik, V. E. *Crystallogr. Rep.* **1996**, *41*, 963-965.

(26) Barnes, J. C.; Golnazarians, W. *Acta Crystallogr., Sect. C: Cryst. Struct. Commun.* **1987**, *43*, 549-552.

(27) Akhavan, J. *The Chemistry of Explosives*; 2nd ed.; The Royal Society of Chemistry: Cambridge, 2004.

(28) Hunter, C. A.; Sanders, J. K. M. *J. Am. Chem. Soc.* **1990**, *112*, 5525-5534.

(29) Hunter, C. A.; Singh, J.; Thornton, J. M. *J. Mol. Biol.* **1991**, *218*, 837-846.

(30) Vrcelj, R. M.; Sherwood, J. N.; Kennedy, A. R.; Gallagher, H. G.; Gelbrich, T. *Cryst. Growth Des.* **2003**, *3*, 1027-1032.

(31) A summary of relevant peaks and their shifts in the cocrystals are available in Appendix 1.

(32) In the TNT cocrystals formed, other possible secondary interactions were not clearly observable and therefore will not be discussed.

(33) Etter, M. C. *J. Phys. Chem.* **1991**, *95*, 4601-4610.

(34) Panunto, T. W.; Urbánczyk-Lipkowska, Z.; Johnson, R.; Etter, M. C. *J. Am. Chem. Soc.* **1987**, *109*, 7786-7797.

(35) Kamlet, M. J.; Jacobs, S. J. *J. Chem. Phys.* **1968**, *48*, 23-35.

(36) Capelli, S. C.; Albinati, A.; Mason, S. A.; Willis, B. T. M. *J. Phys. Chem. A* **2006**, *110*, 11695-11703.

(37) Brock, C. P.; Dunitz, J. D. *Acta Crystallogr., Sect. B: Struct. Sci.* **1990**, *46*, 795-806.

(38) Marciniak, B.; Pavlyuk, V. *Mol. Cryst. Liq. Cryst.* **2002**, *373*, 237-250.

(39) Heller, E.; Schmidt, G. M. J. *Isr. J. Chem.* **1971**, *9*, 449-462.

(40) Petricek, V.; Cisarova, I.; Hummel, L.; Kroupa, J.; Brezina, B. *Acta Crystallogr., Sect. B: Struct. Sci.* **1990**, *46*, 830-832.

(41) Botoshansky, M.; Herbstein, R. H.; Kapon, M. *Helv. Chim. Acta* **2003**, *86*, 1113-1128.

(42) Batsanov, A. S. *Acta Crystallogr., Sect. C: Cryst. Struct. Commun.* **2006**, *62*, O501-O504.

(43) García, P.; Dahaoui, S.; Katan, C.; Souhassou, M.; Lecomte, C. *Faraday Discuss.* **2007**, *135*, 217-235.

(44) Cox, E. G.; Gillot, R.; Jeffrey, G. A. *Acta Crystallogr.* **1949**, *2*, 356-363.

(45) Bell, J. D.; Blount, J. F.; Briscoe, O. V.; Freeman, H. C. *Chem. Commun.* **1968**, 1656-1657.

(46) Van De Waal, B. W.; Feil, D. *Acta Crystallogr., Sect. B: Struct. Sci.* **1977**, *33*, 314-315.

(47) Yamazaki, D.; Nishinaga, T.; Komatsu, K. *Org. Lett.* **2004**, *6*, 4179-4182.

(48) Meille, V.; Schulz, E.; Lemaire, M.; Faure, R.; Vrinat, M. *Tetrahedron* **1996**, *52*, 3953-3960.

(49) Stalhandske, C. *Acta Crystallogr., Sect. C: Cryst. Struct. Commun.* **1981**, *10*, 1081-1086.

(50) Iuliucci, R.; Hoop, C. L.; Arif, A. M.; Harper, J. K.; Pugmire, R. J.; Grant, D. M. *Acta Crystallogr., Sect. E: Struct. Rep. Online* **2009**, *65*, O251.

(51) Athimoolam, S.; Natarajan, S. *Acta Crystallogr., Sect. C: Cryst. Struct. Commun.* **2007**, *63*, O514-O517.

(52) Gracin, S.; Rasmuson, Å. C. *Cryst. Growth Des.* **2004**, *4*, 1013-1023.

(53) Hardy, G. E.; Kaska, W. C.; Chandra, B. P.; Zink, J. I. *J. Am. Chem. Soc.* **1981**, *103*, 1074-1079.

(54) Brown, C. J.; Ehrenberg, M. *Acta Crystallogr., Sect. C: Cryst. Struct. Commun.* **1985**, *41*, 441-443.

(55) Takazawa, H.; Ohba, S.; Saito, Y. *Acta Crystallogr., Sect. C: Cryst. Struct. Commun.* **1986**, *42*, 1880-1881.

(56) Yang, Y. C.; Baker, J. A.; Ward, J. R. *Chem. Rev.* **1992**, *92*, 1729-1743.

(57) Wilcox, J. L.; Bacon, D. P. In *Annual Conference on Explosives and Blasting Technique* U.S. Army West Desert Test Center, Dugway, UT, USA, 1996; Vol. 22, p 209-216.

(58) Perlstein, J. *J. Am. Chem. Soc.* **1994**, *116*, 11420-11432.

(59) Brock, C. P.; Dunitz, J. D. *Chem. Mater.* **1994**, *6*, 1118-1127.

(60) Dorey, R. C.; Carper, W. R. *J. Chem. Eng. Data* **1987**, *29*, 93-97.

(61) Henssler, J. T.; Matzger, A. J. *Org. Lett.* **2009**, *11*, 3144-3147.

(62) Altomare, A.; Cascarano, G.; Giacovazzo, C.; Guagliardi, A. *J. Appl. Crystallogr.* **1994**, *27*, 1045-1050.

(63) Burla, M. C.; Caliandro, R.; Camalli, M.; Carrozzini, B.; Cascarano, G. L.; De Caro, L.; Giacovazzo, C.; Polidori, G.; Spagna, R. *J. Appl. Crystallogr.* **2005**, *38*, 381-388.

(64) Beurskens, P. T.; Admiraal, G.; Beurskens, G.; Bosman, W. P.; de Gelder, R.; Israel, R.; Smits, J. M. M. *DIRDIF99*, University of Nijmegen, 1999.

(65) In *Crystal Structure Analysis Package*; 4.0 ed.; Rigaku and Rigaku Americas: 9009 New Trails Dr., The Woodlands, TX 77381 USA, 2000-2007.

(66) Sheldrick, G. M.; Schneider, T. R. *Macromol. Crystallogr., Pt A* **1997**, *277*, 319-343.

Chapter 3 Cocrystals of 1,3,5,7-Tetranitro-1,3,5,7-tetrazacyclooctane (HMX)

Published in *Crystal Growth & Design* **2012**, *12*, 3603-3609

3.1 Introduction

While cocrystallization offers great potential to address many of the materials properties concerns for energetics, including chemical stability, sensitivity to shock and oxygen balance, the lack of information on supramolecular synthons suitable for energetics has hindered the rational design of energetic cocrystals. Cocrystals are generally difficult to design *a priori*; for the case of energetics, where most of the functional groups traditionally relied upon for cocrystal engineering are notably absent, the problem is compounded. For this reason, models for engineering energetic cocrystals would prove invaluable for successfully designing novel and effective energetic materials. Previously, donor-acceptor π-π interactions were shown to be highly effective in cocrystallizing 2,4,6-trinitrotoluene (TNT).[1] From these results, rational design strategies for cocrystallizing other electron poor aromatic energetic materials can be devised. In an effort to address an archetypal example from the broader class of aliphatic energetics, this work explored one of the most widely deployed energetics: 1,3,5,7-tetranitro-1,3,5,7-tetrazacyclooctane (HMX).

First discovered as a byproduct in the synthesis of 1,3,5-trinitro-1,3,5-triazacyclohexane (RDX) in 1930, HMX is among the most commonly used energetic materials in explosive applications today and is noted for its high melting point, superb detonation power and moderate sensitivity. HMX exhibits three distinct polymorphic forms:[2] α,[3] β[3-5] and δ[6,7] as well as one hemi-hydrate, γ,[8] that can also exist in its dehydrated form. In these forms, two conformations of the HMX molecule are observed: the *chair-chair* and *chair* conformations (Figure 3.1). The most energetically favorable molecular conformation is the *chair* conformation, which is observed in the most stable

room temperature form of HMX: β-HMX.[2,5,9,10] The opposing position of the nitro groups reduces internal repulsions and allows for closer intermolecular interactions making β-HMX the densest observed form. By contrast, in the *chair-chair* conformation adopted in α-, δ-, and γ-HMX, the repulsion between the four nitro groups that are closely-spaced makes this conformation less stable.[9] β-HMX is the form of choice in energetics applications due to its stability and density.

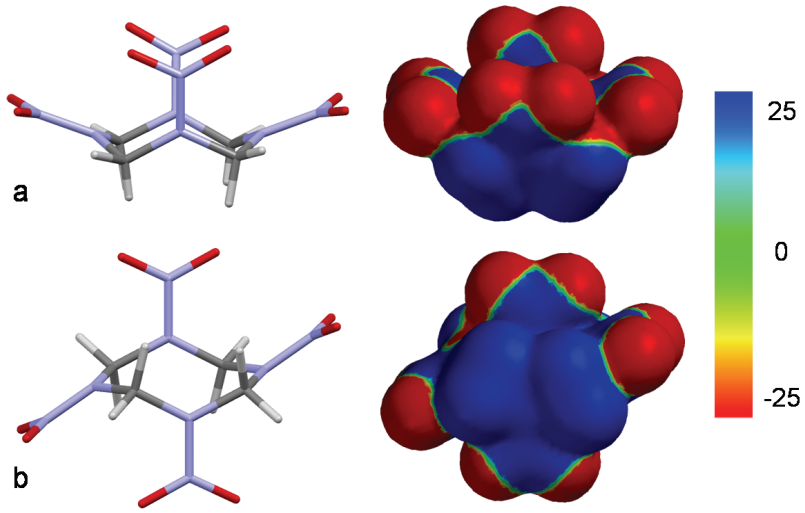

Figure 3.1 HMX exhibits two conformations: the a) *chair-chair* and b) *chair* conformation. *Ab initio* electrostatic potential surfaces (right) were calculated using the semi-empirical method and the AM1 model. Red and blue surfaces represent electron rich and poor regions, respectively, with colors representing values between -25 and 25 kJ/mol.

In 1962, a solvate of HMX with *N*,*N*-dimethylformamide (DMF) was discovered.[11-15] This spurred extensive research on potential solvate former candidates for HMX, and to date almost one hundred HMX solvates and cocrystals, hereafter referred to collectively as cocrystals, have been claimed.[15-21] Despite this level of activity, very few crystal structures have been reported. In addition to HMX/DMF, the only structurally characterized HMX cocrystals available from the Cambridge Structural Database (CSD) are HMX/*N*-methyl-2-pyrrolidone[22] and HMX/2,4-dinitro-2,4-diazapentane.[23] In order to effectively engineer novel cocrystals of HMX and other aliphatic energetic materials, knowledge of the interactions driving the formation of these cocrystals must be understood. Crystal structures provide an unambiguous means to observe these intermolecular interactions. Here we present seven new HMX cocrystal

structures. These, along with the previously reported structures of HMX/DMF, HMX/*N*-methyl-2-pyrrolidone and HMX/2,4-dinitro-2,4-diazapentane, are used to compare the structures and properties of HMX cocrystals. From this study we determined that HMX cocrystallizes in three distinct motifs, as dictated by the cocrystal former, with each motif exerting a predictable effect on materials properties. These structures offer the first steps to rational HMX cocrystal design and provide insight into cocrystal design for aliphatic energetics.

3.2 Results and Discussion.

3.2.1 Structure of HMX Cocrystals

Crystal structures were elucidated for the following cocrystals: HMX/1,2-phenylenediamine (**1**), HMX/3,4-diamintoluene (**3**), HMX/4-fluoroaniline (**4**), HMX/thieno[3,2-*b*]thiophene (**5**), HMX/2-pyrrolidone (**6**), HMX/1,4-piperazinedicarboxaldehyde (**8**), and HMX/2-picoline-*N*-oxide (**9**). Cocrystals of HMX/2-bromoaniline (**2**) and HMX/4-picoline-*N*-oxide (**7**) were also studied and structurally examined, but single-crystal X-ray diffraction data were inadequate for precise structural elucidation. The existence of all but the HMX/thieno[3,2-*b*]thiophene cocrystal were previously reported in the literature although in all cases without crystal structures.[18,19,21] The crystallographic data are presented in Table 3.1. The structures observed in these HMX cocrystals fit into three well-defined structural motifs herein termed *chair-chair/layered*, *chair-chair/pocket*, and *chair/layered*.

Table 3.1 Crystallographic data for HMX cocrystals (collected at 95 K unless otherwise noted).

HMX cocrystal	*chair-chair/layered*					*chair-chair/pocket*		*chair/layered*	
	1	**2**	**3**	**4**	**5**	**6**	**7**	**8**	**9**
stoichiometry	1:1	1:1	1:1	1:1	1:1	1:1	1:1	1:1	1:2
morphology	prism	prism	prism	prism	prism	needle	needle	block prism	block prism
space group	*Pnma*	$P2_12_12_1$	*Pnma*	$P2_12_12_1$	*Pnma*	$P6_3/m$	$P6_3/m$	$P2_1/c$	$P\bar{1}$
a (Å)	11.4153(8)	7.7484(5)	11.4367(10)	7.7156(5)	11.1402(5)	15.8469(6)	15.765(4)	13.8386(9)	6.0611(16)
b (Å)	18.4825(18)	11.1996(8)	18.7309(15)	11.2114(6)	19.1745(14)	15.8469(6)	15.765(4)	6.4188(5)	7.818(2)
c (Å)	7.7116(6)	19.2710(14)	7.8305(7)	18.5392(12)	7.6902(6)	10.5371(7)	10.730(2)	20.7476(16	12.154(3)
α (deg)	90	90	90	90	90	90	90	90	71.604(13)
β (deg)	90	90	90	90	90	90	90	104.246(7)	80.885(14)
γ (deg)	90	90	90	90	90	120	120	90	86.334(14)
vol. (Å^3)	1627.0(2)	1672.32(19)	1677.4(2)	1603.68(17)	1642.69(15)	2291.6(2)	2309.5(9)	1786.3(2)	539.5(3)
Z	4	4	4	4	4	6	6	4	1
ρ_{calc} (g/cm^3)	1.651	1.860	1.657	1.687	1.765	1.657	1.749	1.630	1.583
data/param.	1478/158	–	1413/168	2903/310	1490/133	1342/148	–	2882/272	1730/164
R_1/wR_2	6.36/15.00	–	4.94/12.35	2.37/5.84	3.56/9.77	6.27/17.44	–	9.37/24.84	15.4/35.97
GOF	1.155	–	1.164	1.077	1.096	1.007	–	1.199	1.083

[a]Collected at 85 K

3.2.1.1 Chair-chair/Layered

The *chair-chair/layered* motif is observed with cocrystal formers consisting of electron-rich aromatic rings, including 1,2-phenylenediamine, 2-bromoaniline, 3,4-diamintoluene, 4-fluoroaniline, and thieno[3,2-*b*]thiophene. Homogeneous layers of HMX alternate with layers of cocrystal former (Figure 3.2). The HMX molecule displays the less stable *chair-chair* conformation, as is found in α-, δ-, and γ-HMX. The electrostatic potential surfaces reveal considerable similarity among the cocrystal formers leading to this motif (Figure 3.3). When considering the electron poor nature of the HMX molecule (Figure 3.1) the main driving force for the cocrystallization of HMX with electron rich aromatic rings becomes apparent. Indeed, the presence of electron-rich aromatic rings appears to drive the formation of this motif. Short contacts within the van der Waals radii between hydrogen atoms of HMX and the carbon atoms of the benzene

rings, or the sulfur atoms in the case of the thieno[3,2-*b*]thiophene, in these cocrystal formers were observed for all structures in this motif.

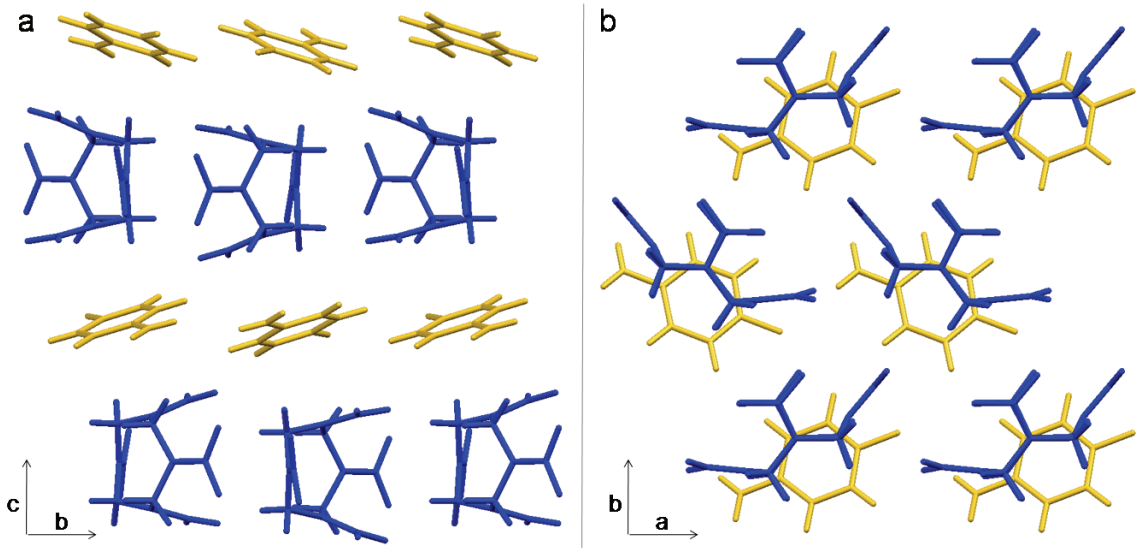

Figure 3.2 The *chair-chair/layered* motif as demonstrated by HMX/4-flouroaniline viewed down a) the *a*-axis and b) the *c*-axis.

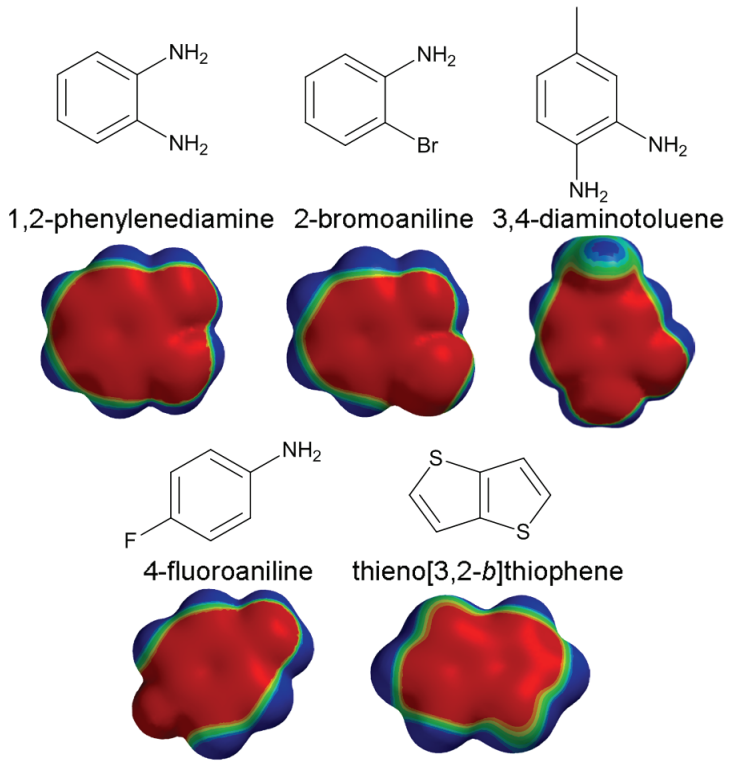

Figure 3.3 Electrostatic potential surfaces for the cocrystal formers of the *chair-chair/layered* motif. *Ab initio* electrostatic potential surfaces (right) were calculated using the semi-empirical method and the AM1 model. Red and blue surfaces represent

electron rich and poor regions, respectively, with colors representing values between -25 and 25 kJ/mol.

In addition to the electrostatic interactions between HMX and the electron-rich aromatic rings, interactions between the nitro groups of HMX and various functional groups of the cocrystal formers were also observed (Figure 3.4). As expected, when amines are present, amine-nitro interactions are observed.[24-28] In the HMX/thieno[3,2-*b*]thiophene cocrystal, the closest nitro interactions exist between an equatorial nitro group and a hydrogen atom from the thiophene ring. These interactions in combination with the general electrostatic interactions provide the cohesive force between the layers.

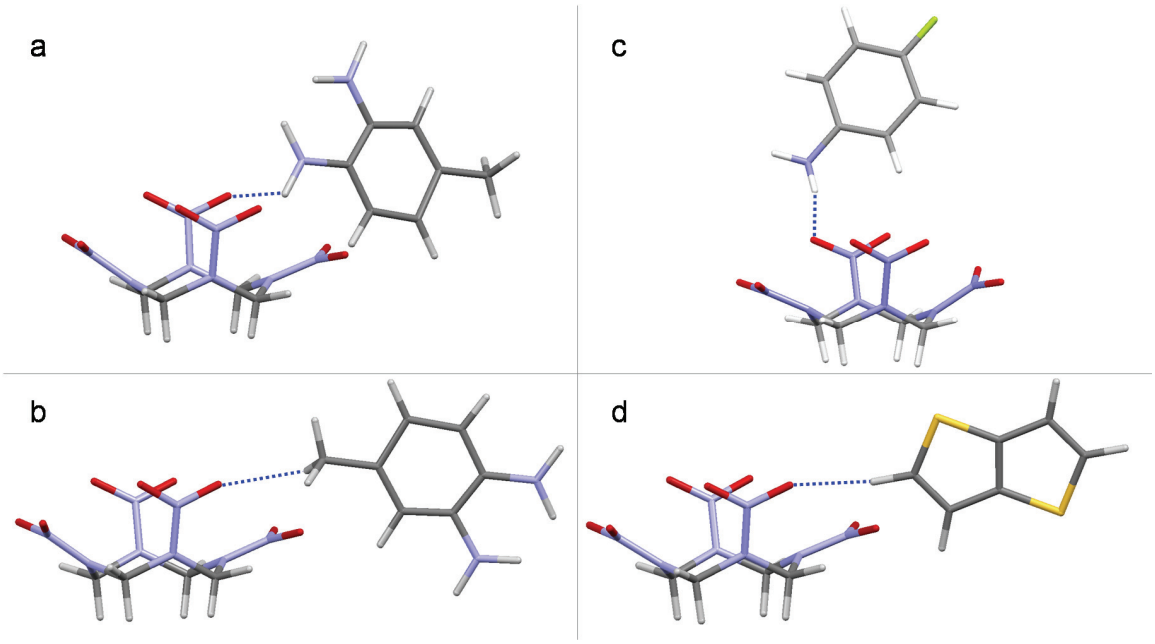

Figure 3.4 HMX-cocrystal former interactions for *chair-chair/layered* cocrystals: a) N-H···O-NO interaction (2.412 Å) and b) C-H···O-NO interaction (2.411 and 2.420 Å) of HMX/3,4-diaminotoluene (rotational disorder omitted for clarity); c) N-H···O-NO interaction (2.202 Å) of HMX/4-fluoroaniline; and d) C-H···O-NO interaction (2.397 Å) of HMX/thieno[3,2-*b*]thiophene.

Within the single-component layers of the *chair-chair/layered* motif, significant interactions are observed as well. Most notably, neighboring HMX molecules form chains ($C_2^2(7)[R_2^2(8)]$) through donation of electron density from the axial nitro group to the hydrogen atoms on the neighboring HMX molecule (Figure 3.5). These HMX-HMX interactions are consistent for all of the HMX cocrystals in this motif. This regularity is

emphasized in the unit cell lengths of these cocrystals, which are similar to within 0.8 Å or less of each other (7.7-7.8 Å × 11.1-11.4 Å × 18.5-19.2 Å). Interactions between the cocrystal formers provide further stability within the cocrystal, but vary among each cocrystal former. The consistency displayed by the HMX-HMX interactions in this motif allows for the accommodation of an assortment of electron-rich aromatic materials, suggesting the possibility of many more HMX cocrystals.

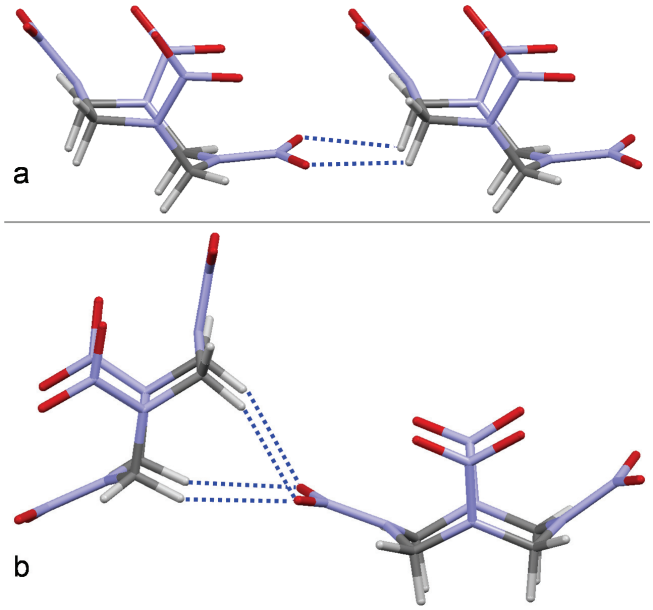

Figure 3.5. a) HMX-HMX interactions propagating a chain (2.40 Å) and b) HMX-HMX interactions between chains (2.43 and 2.61 Å).

3.2.1.2 Chair-chair/Pocket

The *chair-chair/pocket* motif is observed for HMX/*N*-methyl-2-pyrrolidone,[22] HMX/2-pyrrolidone, HMX/4-picoline-*N*-oxide, and HMX/DMF.[13,14,22] Despite the structural variety of the cocrystal formers observed in this motif, the solid-state packing is remarkably consistent. In all of the cocrystals of this motif HMX again adopts the *chair-chair* conformation. Layers consist of three cocrystal former molecules surrounded by six HMX molecules, three HMX molecules with nitro groups facing towards the cocrystal former and three with nitro groups facing away (Figure 3.6). As in the previous motif, the HMX molecules form chains with electron-rich nitro groups of one HMX molecule interacting with the electron-poor hydrogen atoms of the adjacent molecule. The differences lie in the relative orientation of adjacent HMX molecules and the fact

that these chains form in three directions resulting in a kagome-like structure. Alternating layers are offset from one another so that a cluster of three cocrystal formers are sandwiched by a cluster of three HMX molecules both above and below.

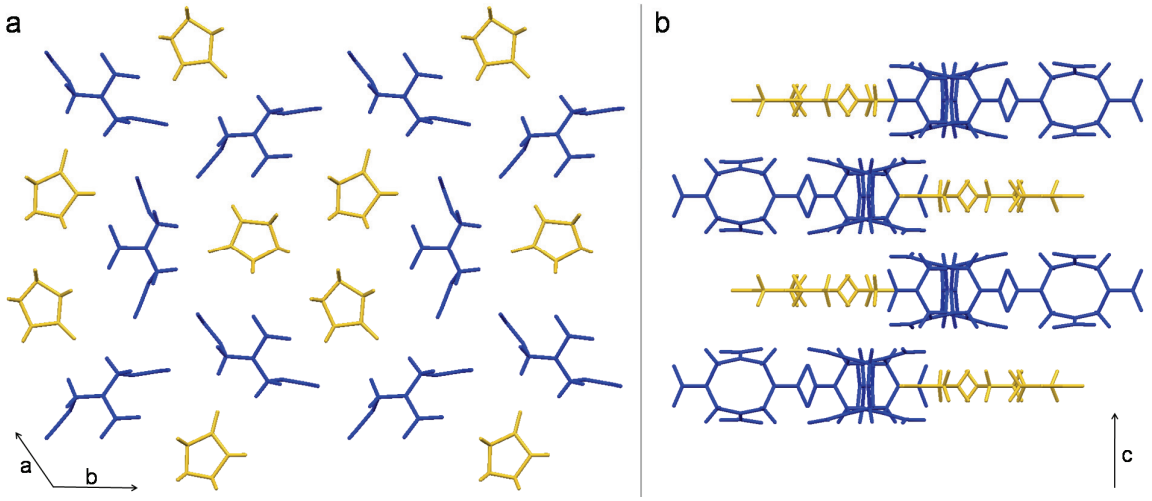

Figure 3.6 HMX/2-pyrrolidone viewed a) down the *c*-axis and b) perpendicular to the (110) plane. For clarity only one set of disordered atoms is shown for 2-pyrrolidone.

The HMX molecules form a network that is constant among all of the cocrystals adopting the *chair-chair/pocket* motif, with less than 1 Å difference in the spacing between the HMX molecules. Cocrystal formers serve as interchangeable guest molecules to stabilize this network of HMX molecules. The consistency of the arrangement of the HMX network and the cocrystal formers suggests that the HMX interactions drive the formation of this motif and cocrystal formers need only fulfill size, shape and electronic character requirements to fill the interstitial spaces and stabilize the crystal. Due to this effect and the pocket-like nature of this motif there is a high propensity for the cocrystal formers to be disordered. This has hindered, both historically and presently, an accurate understanding of the specific interactions between HMX and the cocrystal formers. However, despite the disorder it is clear that all of the cocrystal formers possess a highly polarized oxygen atom that can interact with the hydrogen atoms of the HMX ring through hydrogen bonding (Figure 3.7). The electrostatic potential surfaces for these compounds (Figure 3.8) highlight the polarization of the oxygen atom containing functional groups. Indeed, the uneven electron density and small cocrystal former size seem to promote the formation of this structural motif.

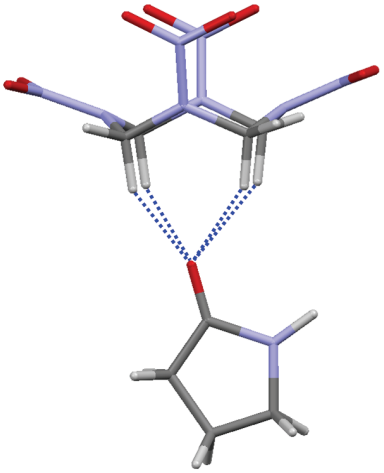

Figure 3.7 Hydrogen bonding between the carbonyl of 2-pyrrolidone and the HMX ring of HMX/2-pyrrolidone (2.260 and 2.426 Å). For clarity only one set of disordered atoms is shown for 2-pyrrolidone.

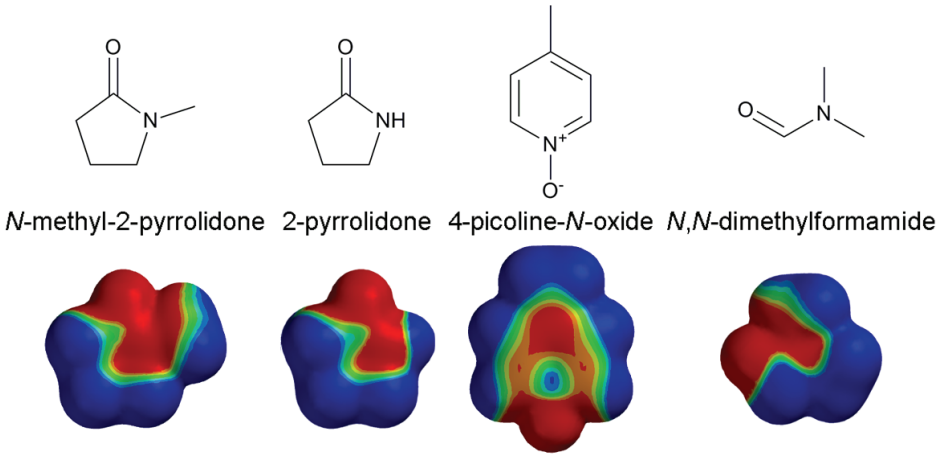

Figure 3.8 Electrostatic potential surfaces for the cocrystal formers of the *chair-chair/pocket* motif calculated. *Ab initio* electrostatic potential surfaces (right) were calculated using the semi-empirical method and the AM1 model. Red and blue surfaces represent electron rich and poor regions, respectively, with colors representing values between -25 and 25 kJ/mol.

In contrast to the other two motifs, the *chair-chair/pocket* motif often produces long thin needles due to preferential growth in the layer-stacking direction. Only HMX/DMF and HMX/*N*-methyl-2-pyrrolidone, *chair-chair/pocket* cocrystals that both form prisms, are exceptions while all other HMX cocrystals of this motif produce thin needles. This common morphology, combined with the regularity of this cocrystal motif, suggests that many structurally uncharacterized HMX cocrystals[29] also appear to cocrystallize in this motif based on their powder X-ray diffraction (PXRD) patterns

(Figure 3.9). Indeed, it is their propensity to form long, thin needles that has prevented the structural elucidation of these cocrystals as it is difficult to grow an adequately thick sample. Furthermore, in the manufacturing of explosives, prisms are preferred over needles as they are easier to handle and load consistently.[30] Cocrystals that adopt the *chair-chair/pocket* motif are, thus, expected to be less favorable in this respect. Still, the *chair-chair/pocket* motif offers a unique means of packing HMX: in non-continuous layers, different from any other solid form of HMX.

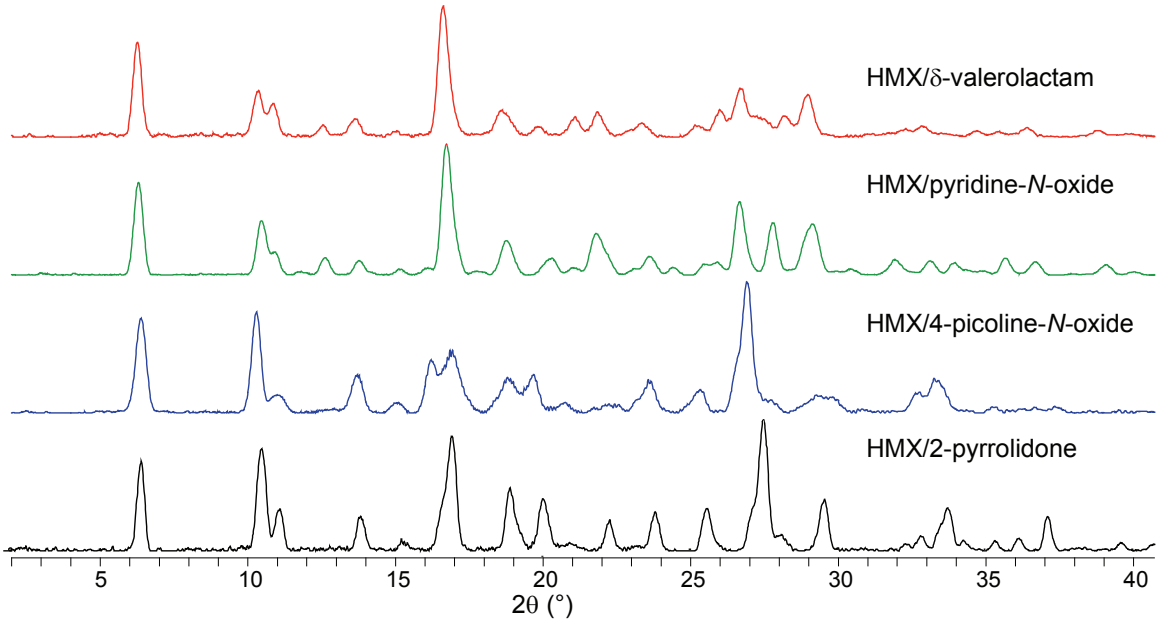

Figure 3.9. PXRD pattern comparison of two HMX cocrystals in the *chair-chair/pocket* motif (HMX/2-pyrrolidone and HMX/4-picoline-*N*-oxide) and two HMX cocrystals that seem likely to adopt this motif (HMX/pyridine-*N*-oxide and HMX/δ-valerolactam) but were not structurally elucidated.

3.2.1.3 Chair/Layered

The *chair/layered* motif contains layers of *chair* conformation HMX alternating with layers of cocrystal former (Figure 3.10). This is the only motif in which the HMX molecule adopts its most stable conformation, the *chair* conformation, like that of β-HMX. Though the *chair* conformation is the most energetically stable, this conformation was the least commonly observed in the HMX cocrystals studied. HMX cocrystals exhibiting this structure include HMX/1,4-piperazinedicarboxaldehye, HMX/2-picoline-*N*-oxide and HMX/2,4-dinitro-2,4-diazapentane.[23]

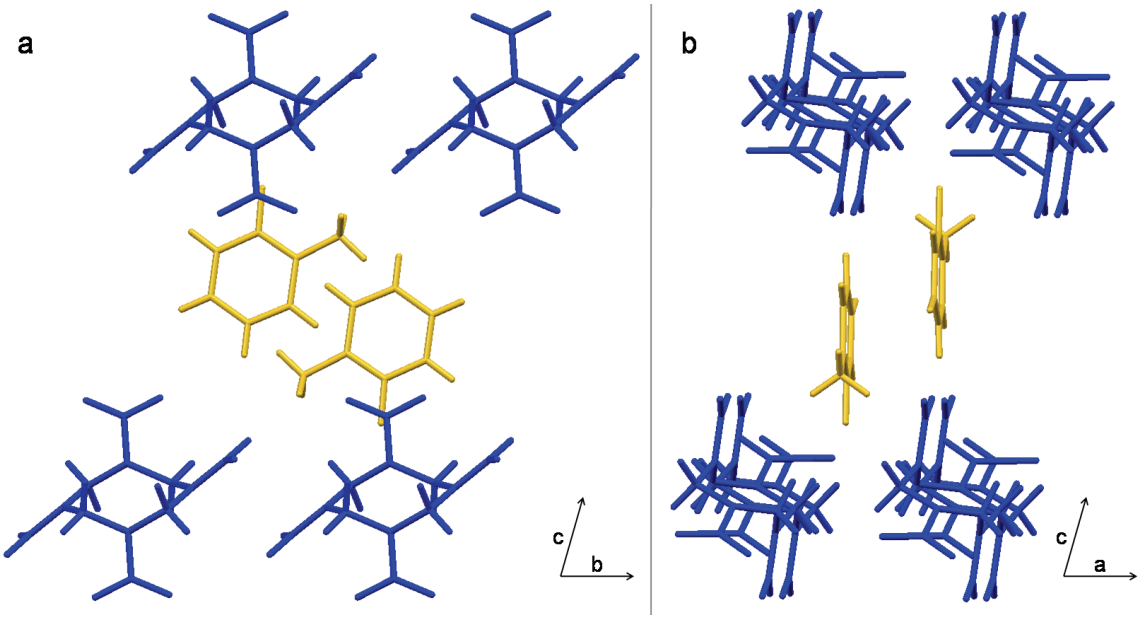

Figure 3.10 HMX/2-picoline-*N*-oxide viewed down a) the *a*-axis and b) the *b*-axis

In contrast to the other motifs, the HMX-HMX interactions are relatively distant and the interactions between HMX and the various cocrystal formers in this motif are shorter and more numerous (Figure 3.11). In general, the cocrystal formers generating this motif display greater variation in size and functionality than those producing either the *chair-chair/layered* or *chair-chair/pocket* motifs. This variety is seen in both the functional groups and size of these cocrystal formers. The electrostatic potential surfaces reveal the unique electronic character of these cocrystal formers and indicate areas of electron density that can interact favorably with the HMX molecule (Figure 3.12). The diversity in the functionality, electron density and size of these cocrystal formers highlights the great adaptability offered by this motif. Since greater variations in both size and functionality of the cocrystal former are permitted, this motif holds the greatest promise for accommodating other energetic compounds.

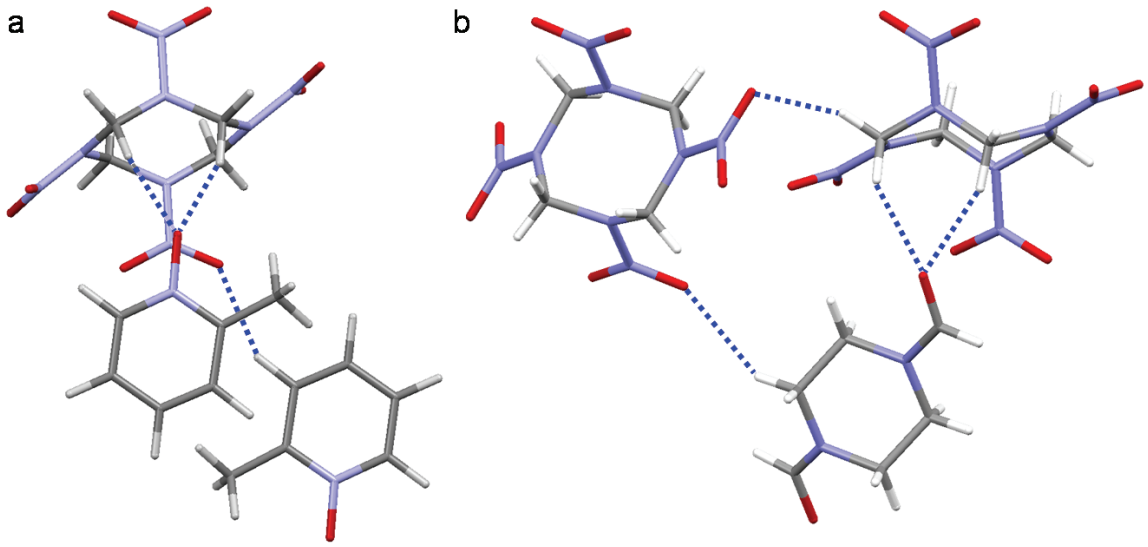

Figure 3.11 HMX-cocrystal former interactions for a) HMX/2-picoline-*N*-oxide, with a N^{+}-O^{-}···H-C interaction (2.151 and 2.157 Å) and a C-H···O-NO interaction (2.335 Å), and b) HMX/1,4-piperazinedicarboxaldehyde, with a C=O···H-C interaction (2.210 and 2.237 Å) and a C-H···O-NO interaction (2.450 Å).

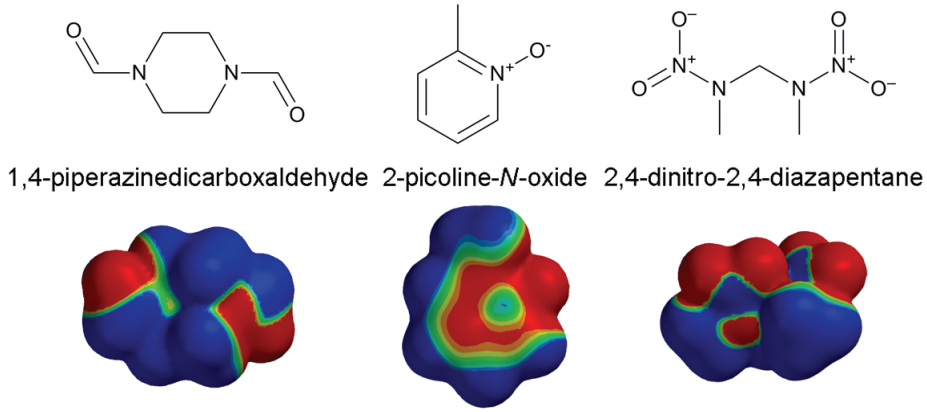

Figure 3.12 Electrostatic potential density surfaces for the cocrystal formers of the *chair/layered* motif calculated. *Ab initio* electrostatic potential surfaces (right) were calculated using the semi-empirical method and the AM1 model. Red and blue surfaces represent electron rich and poor regions, respectively, with colors representing values between -25 and 25 kJ/mol.

3.2.2 Structural Influence on HMX Cocrystal Properties

The correlation between the motifs formed and the observed materials properties is an important consideration for engineering novel HMX cocrystals. Properties considered in this work include density, packing coefficient, and thermal properties. While many more properties are altered through cocrystallization, these properties are particularly relevant when considering energetic materials.

3.2.2.1 Density and Packing Coefficient Comparisons

The density, and by extension packing coefficient, of energetics correlates with their performance. Ideal energetic materials have high densities and packing coefficients. Therefore, in designing novel HMX cocrystals, optimizing these parameters is crucial. Overall, a slight loss in density was observed for HMX cocrystals with non-energetic cocrystal formers relative to pure HMX (Table 3.2). This is different than what was observed for previously studied TNT cocrystals, where some cocrystals demonstrated higher density upon cocrystallization.[1] In contrast to density, the packing coefficient of the HMX cocrystals is approximately the same as HMX or better. Packing coefficients were calculated using the equation $C_k = ZV_{mol}V_{cell}^{-1}$, where V_{mol} is the molecular volume (Å^3), V_{cell} is the volume of the unit cell (Å^3), and Z is the number of molecules in the unit cell. The minimal difference in the packing coefficient of the HMX cocrystals as compared to the pure forms of HMX accounts for their favorable formation and suggests that losses in density are due to the higher ratio of hydrogen atoms in the cocrystal formers rather than poorer packing. In comparing the motifs, some differences are apparent. In particular, the density and packing coefficient of the crystals in the *chair-chair/layered* motif is generally greater than those of the *chair-chair/pocket* motif. Consistent with the structural variety observed in the *chair/layered* motif, a range of densities and packing coefficients are observed.

Table 3.2 Density (ρ) and packing coefficient (PC) data for HMX cocrystals and pure HMX.[a]

cocrystal or polymorph	ρ_{calc} (g/cm^3)	PC
chair-chair/layered		
HMX/1,2-phenylenediamine	1.651	82.7%
HMX/3,4-diaminotoluene	1.657	84.6%
HMX/4-fluoroaniline	1.687	82.5%
HMX/thieno[3,2-*b*]thiophene	1.765	83.2%
HMX/2-bromoaniline	1.859	82.3%
chair-chair/pocket		
HMX/*N*-methyl-2-pyrrolidone[b]	1.570	78.4%
HMX/*N*,*N*-dimethylformamide[b]	1.612	79.7%
HMX/2-pyrrolidone[c]	1.657	80.6%
chair/layered		
HMX/2,4-dinitro-2,4-diazapentane (1:2)[b]	1.570	77.8%
HMX/2-picoline-*N*-oxide (1:2)	1.583	83.8%
HMX/1,4-piperazinedicarboxaldehyde	1.630	80.2%
pure HMX		
δ-HMX[b]	1.759	77.5%
γ-HMX[b,d]	1.780	82.4%
α-HMX[b]	1.839	81.0%
β-HMX[b]	1.903	82.3%

[a]Calculated for structures at 95 K except where specified [b]room temperature [c]85 K [d]hemihydrate

3.2.2.2 Morphology of HMX Cocrystals

The morphology of the HMX cocrystals was also remarkably consistent within each of the motifs and relatively distinct from each other (Table 3.3). In the *chair-chair/layered* motif cocrystals growth within a layer is favored over the addition of layers producing diamond-shaped plates. In contrast to this, the *chair-chair/pocket* motif often produces long thin needles due to preferential growth in the layer-stacking direction. While HMX/DMF and HMX/1-methyl-2-pyrrolidone, *chair-chair/pocket* cocrystals that both form prisms, are exceptions to this, a large number of uncharacterized HMX cocrystals seem to cocrystallize in this motif, based on their needle morphology, PXRD

patterns and Raman spectra. The *chair/layered* motif cocrystals formed as rectangular block prisms.

Table 3.3 HMX cocrystal morphology information (*pictured cocrystal).

motif	observed morphology	picture	cocrystal
chair-chair/layered	diamond plates	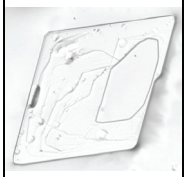	HMX/1,2-phenylenediamine HMX/2-bromoaniline HMX/3,4-diaminotoluene HMX/4-fluoroaniline* HMX/thieno[3,2-*b*]thiophene
chair-chair/pocket	long, thin needles	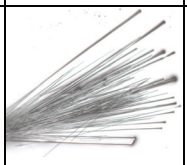	HMX/2-pyrrolidone* HMX/4-picoline-*N*-oxide
	prisms	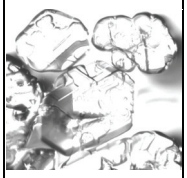	HMX/*N*,*N*-dimethylformamide HMX/*N*-methyl-2-pyrrolidone*
chair/layered	rectangular block prisms		HMX/1,4-piperazinedicarboxaldehyde HMX/2- picoline-*N*-oxide*

Morphology has important implications in the processing of explosives. Since the morphology of the HMX cocrystals often follows a predictable pattern based on the motif formed, which is based on the characteristics of the cocrystal former, this information can be applied in engineering novel HMX cocrystals amenable for bulk processing. In manufacturing ordnances, prisms are preferred over needles as they are easier to handle and load consistently.[30] From this perspective, therefore, engineering HMX cocrystals from cocrystal formers that are more likely to produce either the *chair-chair/layered* or *chair/layered* motifs is favorable.

3.2.2.3 Thermal Properties of the HMX Cocrystals

While all pure forms of HMX convert to δ-HMX at temperatures above 149 °C,[2,10] the thermal behavior of the HMX cocrystals is more complex and appears to be correlated to the structural motif. In all HMX cocrystals studied, the cocrystal former

separates from HMX at a temperature far below the decomposition temperature of HMX (279 °C at a heating rate of 10 °C/min), resulting in the formation of δ-HMX, as confirmed via Raman spectroscopy and powder X-ray diffraction (PXRD). The phase separation temperatures vary depending on the cocrystal former and the structural motif (Table 3.4). Cocrystals with HMX in the *chair-chair* conformation display a range of phase separation temperatures, from 125 to 179 °C. The phase separation occurs as a gradual release of the cocrystal former, with the rate depending on the size of the crystal. Crystal growth was not apparent during the phase separation, though the resulting multi-crystalline material was identified as δ-HMX via Raman spectroscopy and PXRD. These samples were consistently tan-colored, indicating the presence of impurities. In contrast to this, the two cocrystals studied with HMX in the *chair* conformation show a phase change near 150 °C, which is within the reported temperature range at which pure β-HMX transforms into δ-HMX (reported values range from 149 to 200 °C).[10,31,32] Furthermore, as observed using hotstage microscopy, there is a regular transformation in which the cocrystal appears to become partially liquefied and well-defined crystals of δ-HMX grow within this liquid (Figure 3.13). For example, when held isothermally at temperatures above the phase separation temperature, at 170 °C, large needles of δ-HMX of up to 2 mm can be grown from HMX/2-picoline-*N*-oxide. Though any correlation is only hypothetical, it is an intriguing coincidence that the *chair/layered* cocrystals, within the β to δ transformation temperature range, convert so cleanly δ-HMX while the conversion with the *chair-chair* conformation HMX containing cocrystals are not so well defined. In any case, HMX cocrystals in the *chair/layered* motif, as opposed to the other two motifs, provide a reliable means to grow high quality δ-HMX crystals, which can be difficult to obtain by other methods.

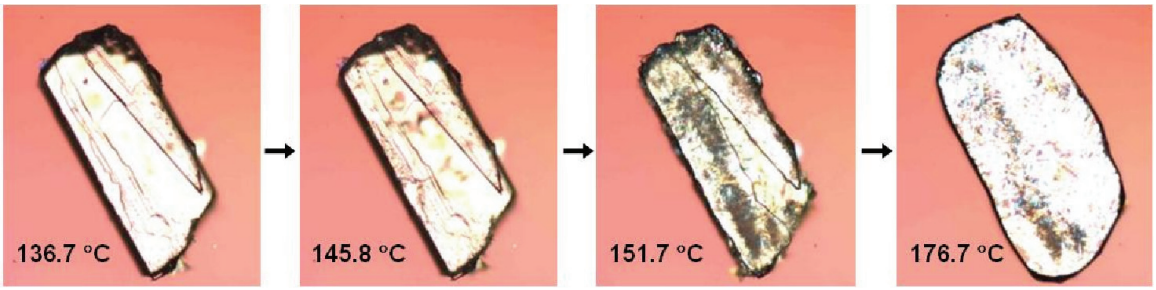

Figure 3.13 Phase separation of HMX/1,4-piperazinedicarboxaldehyde, with crystals of δ-HMX growing from the liquid.

Table 3.4 HMX cocrystal phase separation temperature (T_{ps}) and pure cocrystal former (ccf) melting points.

cocrystal	**T_{ps} (°C)**	**ccf mp (°C)**
chair-chair/layered		
HMX/1,2-phenylenediamine	170	102.1
HMX/2-bromoaniline	156	30.8
HMX/3,4-diaminotoluene	148	88.7
HMX/4-fluoroaniline	128	-1.9
HMX/thieno[3,2-*b*]thiophene	179	56
chair-chair/pocket		
HMX/*N*-methyl-2-pyrrolidone	125	-24
HMX/2-pyrrolidone	163	12.2
HMX/4-picoline-*N*-oxide	125	182
HMX/*N,N*-dimethylformamide	166	-61
chair/layered		
HMX/2-picoline-*N*-oxide (1:2)	153	46-50
HMX/1,4-piperazinedicarboxaldehyde	151	129.1

3.2.2.4 Impact Sensitivity

Through cocrystallization a notable reduction in impact sensitivity relative to pure HMX is observed. Impact sensitivity was tested for representative cocrystals from each of the observed motifs through the means of an in-house constructed drop-weight test (Table 3.5).[33] While β– and δ–HMX detonated when impacted from a height of 45 cm and 27 cm respectively, detonation was not observed for HMX cocrystals, even at heights of 145 cm, the limit for the apparatus, indicating a significant decrease in impact

sensitivity. These cocrystals not only possess inert partners for HMX, but the alteration in the packing of HMX has great potential to assist in reducing the sensitivity. The layered structures found in all of these motifs introduce slip planes, which are hypothesized to reduce the mechanical shock sensitivity of explosives.[34,35]

Table 3.5 Drop-weight impact sensitivity test data for β-HMX, δ-HMX, HMX cocrystals and phase-separated HMX cocrystals. The drop height for the pure forms of HMX represent the $h_{50\%}$, or the height at which samples exhibited a 50% likelihood of detonation. Due to sample size limitations, the drop height of the cocrystals represents the lowest height from which a detonation was observed.

sample	**drop height (cm)**
β-HMX	47
δ-HMX	27
HMX/*N*,*N*-dimethylformamide	>145
HMX/thieno[3,2-*b*]thiophene	>145
HMX/2-bromoaniline	>145
HMX/2-picoline-*N*-oxide	>145
HMX/*N*,*N*-dimethylformamide, after phase separation	29
HMX/thieno[3,2-*b*]thiophene, after phase separation	27
HMX/2-picoline-*N*-oxide, after phase separation	27

Considering both the increased insensitivity of HMX cocrystals and the aforementioned phase separation of the cocrystals at a temperature safely below the detonation temperature, these cocrystals are viable candidates for smart energetic materials. In the energetic/non-energetic cocrystal form, these energetic materials can be handled and transported in a form that is insensitive to shock. However, by a process of gentle heating above the phase separation temperature, but well below the decomposition temperature of HMX, the cocrystal former can be selectively removed, with δ-HMX, the most sensitive HMX form, remaining. To achieve phase separation of representative cocrystals, HMX/thieno[3,2-*b*]thiophene, HMX/DMF, and HMX/2-picoline-*N*-oxide cocrystals were heated at 10 °C/min to 210 °C, 240 °C and 170 °C respectively, and held isothermally for 60 minutes to ensure removal of the cocrystal former from the crystal. These samples were then immediately tested for impact sensitivity. After phase separation impact sensitivity for all of the cocrystals was similar to that of δ-HMX, as

demonstrated by a drop height of 29 cm for HMX/DMF, 27 cm for HMX/ thieno[3,2-*b*]thiophene and 27 cm for HMX/2-picoline-*N*-oxide. By exploiting both the insensitivity of the cocrystal form and the ease of regeneration to δ-HMX these cocrystals provide a means to safely transport HMX and then selectively prepare the energetic for use.

3.3 Conclusions

HMX forms cocrystals with a wide variety of cocrystal formers in three distinct motifs: *chair-chair/layered*, *chair-chair/pocket* and *chair/layered*. These motifs are a direct result of the electronic character of the cocrystal formers, their specific interactions with HMX and their size. The regularity with which these patterns form suggests consistent driving forces for their formation that can be exploited in further cocrystal engineering of HMX.

The properties of these cocrystals are influenced by the structural motif adopted. In particular, trends in the density and packing coefficient as well as the thermal properties of the cocrystals correlate with the structural motif present. Additionally, the HMX cocrystals afford a tremendous reduction in sensitivity in comparison to pure HMX. Coupled with the ability to selectively remove the cocrystal formers, these cocrystals serve well to provide safer energetics that can be selectively "activated." From these findings, novel HMX cocrystals can be designed by searching for cocrystal formers likely to produce the desired structure and properties.

3.4 Experimental

3.4.1 Materials

2-Bromoaniline (98%), 2-pyrrolidone (98%), 1,4-piperazinedicarboxaldehyde (98%), and 2-picoline-*N*-oxide (98%) were obtained from Acros Organics (New Jersey, USA). 1,2-Phenylenediamine (99.5%), 3,4-diaminotoluene (97%), and 4-picoline-*N*-oxide (98%) were obtained from Aldrich, (St. Louis, MO). 4-Fluoroaniline (98%) was obtained from Aldrich (Milwaukee, WI). *N*,*N*-Dimethylformamide (Synthesis, Fisher BioReagent) and *N*-methyl-2-pyrrolidone (Fisher BioReagents) were obtained from

Fisher Scientific. Thieno[3,2-*b*]thiophene was synthesized and purified according to the published procedure.[36] 1,3,5,7-Tetranitro-1,3,5,7-tetrazacyclooctane (HMX) was obtained from both the China Lake Naval Air Weapons Station and the Indian Head Naval Surface Warfare Center. *Caution! 1,3,5,7-Tetranitro-1,3,5,7-tetrazacyclooctane (HMX) is an explosive material and care should be exercised in avoiding excessive heat, static electricity and mechanical shock!*

3.4.2 Cocrystal Formation

HMX/1,4-Piperazinedicarboxaldehyde, HMX/2-bromoaniline, and HMX/thieno[3,2-*b*]thiophene were prepared in a 1:1 molar ratio, while HMX/2-pyrrolidone and HMX/4-fluoroaniline were prepared in 1:10 molar ratio. HMX/4-Picoline-*N*-oxide was prepared in a 2:3 ratio and HMX/2-picoline-*N*-oxide in a 1:2 ratio. In all of these samples HMX and the cocrystal former were dissolved in acetonitrile (Fisher Chemical, HPLC Grade), in a sufficient amount to ensure full dissolution, placed in 4 mL glass vials and left to evaporate at room temperature. In the case of HMX/1,2-phenylenediamine and HMX/3,4-diaminotoluene, cocrystals were prepared in a 3:4 ratio, dissolved in a sufficient volume of acetonitrile, deposited in a polypropylene 96 well plate and left to evaporate at room temperature. To achieve larger, pure sample quantities of HMX/1,4-piperazinedicarboxaldehyde, samples in both a 1:1 and 1:3 ratio were prepared, dissolved in acetonitrile, placed in a 96 well polypropylene plate and left to evaporate at room temperature. The mass of HMX employed for HMX cocrystal formation ranged from 0.5 to 20 mg as measured on a Sartorius ME36S microbalance (± 0.005 mg).

3.4.3 Raman Spectroscopy

Raman spectra were obtained using a Renishaw inVia Raman Microscope equipped with a 514 nm argon ion laser, a 785 nm diode laser and a RenCam CCD detector. The 514 nm argon ion laser employed an 1800 lines/mm grating and a 50 μm slit while the 785 nm diode laser employed a 1200 lines/mm grating and a 65 μm slit. Spectra were collected and analyzed using the WiRE 3.1 software package (Renishaw). Calibration was performed using a silicon standard. Spectra were collected using an Olympus SLMPlan 20× objective (numerical aperture = 0.35) in extended scan mode

with a range of 100-3800 cm^{-1}. Spectra were further analyzed using ACD/SpecManager Version 12.01 software (ACD/Labs).

3.4.4 Powder X-Ray Diffraction

Powder X-ray diffraction (PXRD) patterns were collected at room temperature using a Rigaku R-Axis Spider diffractometer with an image plate detector and graphite monochromated Cu-Kα radiation (λ = 1.54187 Å). Samples were mounted on a CryoLoop™ and images were collected for ten minutes while rotating the sample about the φ-axis at 10°/sec, oscillating ω between 120° and 180° at 1°/sec with χ fixed at 45°. Images were integrated from 2 to 70° with a 0.01° step size using AreaMax 2.0 software (Rigaku). Powder patterns were processed using Jade 8 XRD Pattern Processing, Identification & Quantification analysis software (Materials Data, Inc).

3.4.5 Single Crystal X-ray Diffraction

Single crystal diffraction data for HMX/1,2-phenylenediamine, HMX/3,4-diamintoluene, HMX/4-fluoroaniline, HMX/thieno[3,2-*b*]thiophene, HMX/1,4-piperazinedicarboxaldehyde, and HMX/2-picoline-*N*-oxide were collected using a Rigaku R-Axis Spider diffractometer with an image plate area detector using graphite monochromated Cu-Kα radiation (λ = 1.54187 Å) operated at 2.0 kW power (50 kV, 40 mA) with the sample mounted on a MiTeGen MicroMount™. The X-ray intensities were measured at 95(2) K with the detector at a distance 127.00 mm from the crystal. Single crystal diffraction data for HMX/2-pyrrolidone was collected using a Rigaku AFC10K Saturn 944+ CCD-based X-ray diffractometer equipped with a low temperature device and Micromax-007HF Cu-target micro-focus rotating anode (λ = 1.54187 Å) operated at 1.2 kW power (40 kV, 30 mA). The X-ray intensities were measured at 85(1) K with the detector placed at a distance 42.00 mm from the crystal. All data were processed with CrystalClear 2.0 (Rigaku) and corrected for absorption using an empirical absorption correction. HMX/4-fluoroaniline crystallizes as a 50/50 racemic twin (refined twin scale factor 0.49(18)). Therefore for this data set, the scaling and absorption correction routines treated Friedel opposites as independent reflections so that any small anomalous signal in the intensities was preserved. Structures were solved by direct methods[37,38] refined and expanded using the CrystalStructure 4.0[39] crystallographic software package (Rigaku).

Non-hydrogen atoms were refined anisotropically. Hydrogen atoms were placed using the riding model, with the exception of the hydrogen atoms in HMX/4-fluoroaniline and hydrogen atoms participating in hydrogen bonding in HMX/1,2-phenylenediamine and HMX/3,4-diaminotoluene, which were refined isotropically. Full-matrix least-squares refinement was made on F^2. For determination of intermolecular distances all carbon-hydrogen, nitrogen-hydrogen and oxygen-hydrogen bond lengths were normalized to 1.083 Å, 1.008 Å and 0.983 Å respectively. HMX/1,2-phenylenediamine and HMX/3,4-diamintoluene can be modeled in both the P*na2*$_1$ and the P*nma* space groups. When considering the P*na2*$_1$ model, mirror symmetry was observed for both cocrystals, favoring the choice of P*nma*. Furthermore, in comparison to the P*nma* models, the P*na2*$_1$ models display more significantly distorted thermal ellipsoids in the cocrystal former. For these reasons, P*nma* was used for these cocrystals. The HMX/2-pyrrolidone cocrystal was modeled in the P*6*$_3$*/m* space group with disorder of the 2-pyrrolidone over a mirror plane. This disorder is present in the P*6*$_3$ model as well, so the highest symmetry space group was selected. HMX/2-picoline-*N*-oxide could only be grown as small, marginal quality crystals, and therefore, despite considerable effort using multiple crystals on at least two X-ray diffractometers, the values of R_1 = 0.1541 and wR_2 = 0.3597 were the best that could be obtained.

3.4.6 Differential Scanning Calorimetry

Thermograms of the samples were recorded on a TA Instruments Q10 differential scanning calorimeter and programmed using Thermal Advantage for Q Series Version 2.5. Samples (0.3-1.5 mg, weighed to a precision of ± 0.005 mg) were placed in hermetic aluminum pans and the lids were crimped using a TA-Instruments hermetic sealing press. Thermal behavior of the samples from 25 to 360 °C was studied under a nitrogen purge of 50.0 mL/min at a heating rate of 10 °C/min. The instrument was calibrated with an indium standard. Data were analyzed using Universal Analysis 2000 4.3 software (TA-Instruments-Waters LLC).

3.4.7 Thermomicroscopy

Thermomicroscopy was performed with a Linkham LTS 350 hot stage connected to a Linkham TMS 94 processor and controlled using Linksys32 Version 1.9.3 software,

viewed under polarized light with a Nikon Eclipse E600 microscope. Thermal transitions were observed optically for comparison with DSC data. Samples were heated from room temperature at a rate of 10 °C/min to temperatures ranging from 200 to 350 °C. Temperatures both before and past the detonation temperature were tested for all samples. Sample heated to a point prior the detonation temperature were immediately probed using Raman spectroscopy.

3.4.8 Calculations

Packing coefficients were calculated by using the following equation: $C_k = ZV_{mol}V_{cell}^{-1}$, where C_k is the packing coefficient, Z is the number of molecules in the unit cell, V_{mol} is the molecular volume (Å^3), and V_{cell} is the volume of the unit cell. Molecular volume was calculated with Spartan '10 version 1.0.1 (Wavefunction, Inc.), which employs van der Waals radii of 1.8855 Å for bromine, 1.5138 Å for fluorine, 1.9200 Å for carbon, 1.2000 Å for hydrogen, 1.5500 Å for nitrogen, 1.5200 Å for oxygen, and 1.8153 Å for sulfur.

Calculations of the electrostatic potential energy density surfaces for HMX and the cocrystal formers were performed using semi-empirical methods with the AM1 model available in Spartan '10 version 1.0.1 (Wavefunction, Inc.). All surfaces were normalized between -25 and 25 kJ/mol.

3.4.9 Drop Weight Impact Sensitivity Tests

Sensitivities of the cocrystals were determined using an in-house-constructed drop-weight test. Samples of 0.50 ± 0.05 mg were enclosed in aluminum pans and impacted with a 5 lb weight. β-HMX and δ-HMX were used as benchmarks for sensitivity and demonstrated a 50% probability to detonate ($h_{50\%}$) when impacted from heights of 45 cm and 27 cm respectively.

HMX cocrystals were phase separated through gentle heating. HMX/thieno[3,2-*b*]thiophene samples were heated at 10 °C/min to 210 °C and held isothermally for 60 minutes. HMX/DMF samples were heated at 10 °C/min to 240 °C and held isothermally for 60 minutes. HMX/2-picoline-*N*-oxide samples were heated at 10 °C/min to 170 °C and held isothermally for 60 minutes. Phase separation of these cocrystals was monitored using both DSC (see above) and thermogravimetric analysis (TGA) using a TGA Q50

instrument from TA-Instruments-Waters LLC; these data were analyzed using Universal Analysis 2000 4.3 software (TA-Instruments-Waters LLC). Sample masses for the phase-separation drop tests were designed so that either 0.5 or 1.0 mg of HMX (in the δ form) would remain. In the case of HMX/thieno[3,2-*b*]thiophene and HMX/2-picoline-*N*-oxide, 0.5 mg HMX equivalent samples detonated at 27 cm. In the case of HMX/DMF the 1.0 mg HMX equivalent sample was found to detonate at 29 cm.

3.5 References

(1) Landenberger, K. B.; Matzger, A. J. *Cryst. Growth Des.* **2010**, *10*, 5341-5347.

(2) McCrone, W. C. *Anal. Chem.* **1950**, *22*, 1225-1226.

(3) Cady, H. H.; Cromer, D. T.; Larson, A. C. *Acta Cryst.* **1963**, *16*, 617-623.

(4) Choi, C. S.; Boutin, H. P. *Acta Crystallogr., Sect. B: Struct. Sci.* **1970**, *26*, 1235-1240.

(5) Zhurova, E. A.; Zhurov, V. V.; Pinkerton, A. A. *J. Am. Chem. Soc.* **2007**, *129*, 13887-13893.

(6) Cobbledick, R. E.; Small, R. W. H. *Acta Crystallogr. Sect. B-Struct. Sci.* **1974**, *30*, 1918-1922.

(7) Selig, W. *Explosivstoffe* **1969**, *9*, 201-202.

(8) Main, P.; Cobbledick, R. E.; Small, R. W. H. *Acta Crystallogr., Sect. C: Cryst. Struct. Commun.* **1985**, *41*, 1351-1354.

(9) Brill, T. B.; Reese, C. O. *J. Phys. Chem.* **1980**, *84*, 1376-1380.

(10) Cady, H. H.; Smith, L. C. *Studies on the Polymorphs of HMX*, Los Alamos Scientific Laboratory, University of California, 1962.

(11) Bedard, M.; Myers, J. L.; Wright, G. F.; Huber, H. *Can. J. Chem.-Rev. Can. Chim.* **1962**, *40*, 2278-2299.

(12) Scullion, H. J.; Lewis, J. *Talanta* **1966**, *13*, 1201-1202.

(13) Cobbledick, R. E.; Small, R. W. H. *Acta Crystallogr., Sect. B: Struct. Sci.* **1975**, *31*, 2805-2808.

(14) Haller, T. M.; Rheingold, A. L.; Brill, T. B. *Acta Crystallogr., Sect. C: Cryst. Struct. Commun.* **1983**, *39*, 1559-1563.

(15) George, R. S.; Cady, H. H.; Rogers, R. N.; Rohwer, R. K. *Ind. Eng. Chem. Prod. Res. Dev.* **1965**, *4*, 209-210.

(16) Selig, W. *Some 1:1 Complexes of Cyclomethylenetetranitramine (HMX) and Their Application to the Estimation of HMX in Admixture with RDX* Lawrence Radiation Laboratory, Livermore, California, 1964.

(17) Selig, W. *Explosivstoffe* **1966**, *14*, 174-177.

(18) Selig, W. *Explosivstoffe* **1967**, *15*, 76-87.

(19) Selig, W. *Explosivstoffe* **1969**, *17*, 73-86.

(20) Levinthal, M. L.; Patent, U. S., Ed.; Thiokol Corporation: United States, 1978; Vol. 4086110.

(21) Selig, W. *Propellants, Explos., Pyrotech.* **1982**, *7*, 70-77.

(22) Haller, T. M.; Rheingold, A. L.; Brill, T. B. *Acta Crystallogr., Sect. C: Cryst. Struct. Commun.* **1985**, *41*, 963-965.

(23) Levakova, I. V.; Korobko, A. P.; Krasheninnikov, S. V.; Zavodnik, V. E. *Crystallogr. Rep.* **1996**, *41*, 963-965.

(24) Robinson, J. M. A.; Philp, D.; Harris, K. D. M.; Kariuki, B. M. *New J. Chem.* **2000**, *24*, 799-806.

(25) Desiraju, G. R. *Angew. Chem., Int. Ed. Engl.* **1995**, *34*, 2311-2327.

(26) Etter, M. C. *Acc. Chem. Res.* **1990**, *23*, 120-126.

(27) Etter, M. C. *J. Phys. Chem.* **1991**, *95*, 4601-4610.

(28) Panunto, T. W.; Urbánczyk-Lipkowska, Z.; Johnson, R.; Etter, M. C. *J. Am. Chem. Soc.* **1987**, *109*, 7786-7797.

(29) These cocrystals include HMX/δ-valerolactam, HMX/*N*-methyl-2-piperidone and HMX/pyridine-*N*-oxide.

(30) Heijden, A. v. d.; ter Horst, J.; Kendrick, J.; Kim, K.-J.; Kröber, H.; Simon, F.; Teipel, U. In *Energetic Materials*; Teipel, U., Ed.; Wiley-VCH Verlag GmbH & Co. KGaA: Weinheim, Germany, 2005, p 53-157.

(31) Weese, R. K.; Burnham, A. K. *Propellants, Explos., Pyrotech.* **2005**, *30*, 344-350.

(32) Karpowicz, R. J.; Brill, T. B. *AIAA J.* **1982**, *20*, 1586-1591.

(33) Bolton, O.; Matzger, A. J. *Angew. Chem., Int. Ed.* **2011**, *50*, 8960-8963.

(34) Zhang, C. Y.; Wang, X. C.; Huang, H. *J. Am. Chem. Soc.* **2008**, *130*, 8359-8365.

(35) Walley, S. M.; Field, J. E.; Greenaway, M. W. *Mater. Sci. Technol.* **2006**, *22*, 402-413.

(36) Henssler, J. T.; Matzger, A. J. *Org. Lett.* **2009**, *11*, 3144-3147.

(37) Altomare, A.; Cascarano, G.; Giacovazzo, C.; Guagliardi, A. *J. Appl. Crystallogr.* **1994**, *27*, 1045-1050.

(38) Burla, M. C.; Caliandro, R.; Camalli, M.; Carrozzini, B.; Cascarano, G. L.; De Caro, L.; Giacovazzo, C.; Polidori, G.; Spagna, R. *J. Appl. Crystallogr.* **2005**, *38*, 381-388.

(39) In *Crystal Structure Analysis Package*; 4.0 ed.; Rigaku and Rigaku Americas: 9009 New Trails Dr., The Woodlands, TX 77381 USA, 2000-2007.

Chapter 4 Energetic-Energetic Cocrystals of Diacetone Diperoxide

Unpublished work

4.1 Introduction

In the previous two chapters, the focus was exclusively on nitro-containing energetics. While this comprises a significant portion of known organic energetic materials, many viable energetic materials that do not contain these functional groups exist as attractive targets for cocrystal formation. In particular, the acetone peroxides, first discovered in 1895 by Wolffenstein et al.,[1] are desirable potential cocrystal formers not only for their cheap and facile synthesis, but also for the electron-rich peroxide moieties that compliment the electron-poor rings found in most known energetic materials. The two most common molecules of this class of energetics are triacetone triperoxide (TATP) and diacetone diperoxide (DADP) (Figure 4.1). Of the two, TATP is far more common and infamous, having a more facile synthetic route and has been utilized by terrorists. Less common is DADP, which is more thermodynamically stable than TATP[2] and, due to the strain of the six-membered ring, features electron-rich peroxide oxygen atoms that are accessible for non-covalent interactions. Based on this feature and the favorable electrostatic interactions postulated above, three novel energetic-energetic cocrystals were designed to include DADP and are presented here: DADP/1,3,5-trichloro-2,4,6-trinitrobenzene (TCTNB), DADP/1,3,5-tribromo-2,4,6-trinitrobenzene (TBTNB), and DADP/1,3,5-triiodo-2,4,6-trinitrobenzene (TITNB). These cocrystals represent a successful application of cocrystal engineering theory.

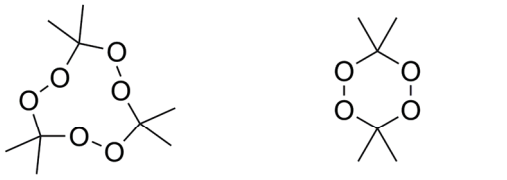

Figure 4.1 Chemical structures of TATP and DADP

These cocrystals further understanding for the cocrystallization of energetic materials. The halogenated trinitrobenzene cocrystal formers are very similar in structure, exchanging only the identity of the halogen atom present, and this allows for an investigation of the delicate balance of energy in cocrystal formation and the differences that atom size and polarizability can have on the final crystalline structure. This series of cocrystals also, in contrast to earlier reports, demonstrates the possibility of energetic-energetic cocrystals that do not reduce the sensitivity with respect to the most sensitive component. They provide an interesting case study on the poorly understood interplay of chemical and solid state factors that influence energetic material sensitivity. The cocrystals presented here retain the high sensitivity of DADP while adding the power of the trihalotrinitrobenzenes, making these attractive as cocrystalline primary explosives. Additionally, cocrystallization is shown for the first time to provide an experimental means to probe mechanisms for sensitivity observed in energetic materials.

4.2 Results and Discussion

DADP forms energetic-energetic cocrystals with TCTNB, TBTNB and TITNB. To better understand the interactions promoting cocrystal formation, these cocrystals were structurally elucidated by single crystal X-ray diffraction. Materials properties were also examined to determine the effect of halogen substitution as well as the extent of improvement in explosive power with respect to DADP that is possible through cocrystallization. While many of the results follow logically from earlier findings about energetic cocrystallization, the DADP cocrystals presented a few unique results that have

wider implications not only for the study of energetic cocrystallization, but for cocrystallization in general.

4.2.1 Structure of DADP Cocrystals

High quality single crystals of each cocrystal, DADP/TCTNB, DADP/TBNTB and DADP/TITNB, were grown and structurally elucidated by X-ray diffractometry. While DADP/TCTNB and DADP/TBNTB are nearly isostructural (Table 4.1), the DADP/TITNB cocrystal exhibits unique packing (Figure 4.2). Even though all of the cocrystals have molecular layers, those of DADP/TCTNB and DADP/TBTNB could roughly be described as face-to-face whereas the layers in DADP/TITNB are more aptly described as edge-to-face. This difference in the orientation of the molecules with respect to each other is in part due to a difference in intermolecular interactions. Thus differences in the steric environment and strength of interactions between the cocrystal formers translate to differences in the observed crystal structures.

Table 4.1 Crystal structure information for DADP cocrystals and pure TBTNB and TITNB.

	DADP/TCTNB	DADP/TBTNB	DADP/TITNB	TBTNB	TITNB
MW (g/mol)	464.60	597.98	738.95	449.82	590.79
color	colorless	colorless	colorless	colorless	colorless
morphology	prism	needle	block needle	prism	prism
crystal system	monoclinic	monoclinic	monoclinic	monoclinic	monoclinic
space group	C 2/*c*	C 2/*c*	C 2/*c*	P 2_1/*c*	I 2/*a*
a (Å)	14.4125(10)	14.6110(15)	25.909(2)	10.0427(4)	10.9062(8)
b (Å)	15.2577(2)	15.4570(14)	10.0061(7)	9.6251(4)	9.9510(6)
c (Å)	9.0616(2)	9.0938(8)	8.2501(8)	12.5715(9)	12.8568(19)
α (°)	90	90	90	90	90
β (°)	91.429(6)	92.496(6)	97.684(7)	94.829(7)	92.754(10)
γ (°)	90	90	90	90	90
volume (Å^3)	1992.04(15)	2051.8(3)	2119.6(3)	1210.87(11)	1393.7(2)
ρ_{calc} (g/cm^3)	1.549	1.936	2.316	2.467	2.816
Z	4	4	4	4	4
data/param	1829/166	1793/166	1851/148	2121/163	1232/84
R_1/wR_2	5.43/12.71	5.23/10.08	6.46/15.26	4.09/12.27	4.22/10.62
GOF	1.158	1.025	1.228	1.222	1.194
crystal size (mm)	0.22 × 0.17 × 0.07	0.29 × 0.03 × 0.02	0.18 × 0.06 × 0.03	0.26 × 0.09 × 0.07	0.13 × 0.10 × 0.09
temperature	rt	rt	95 K	95 K	rt

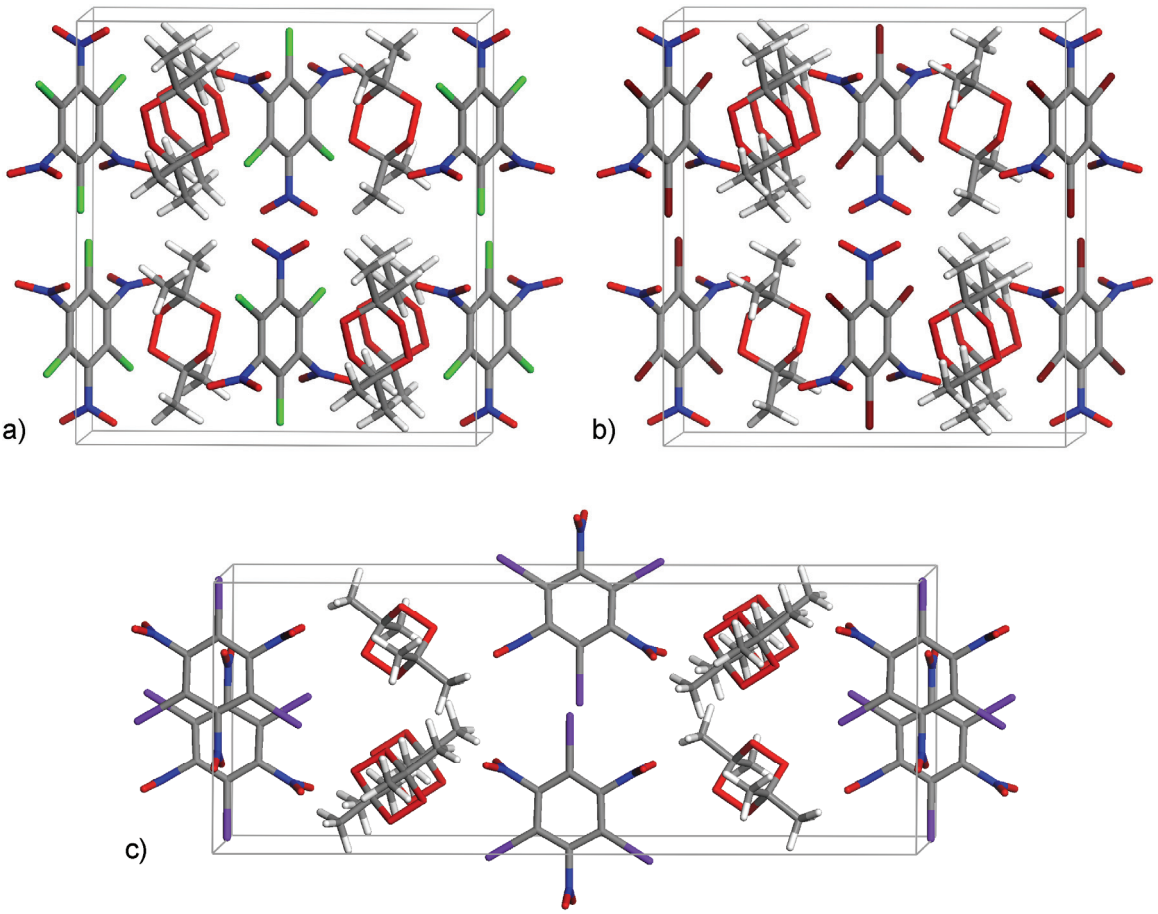

Figure 4.2. Crystal packing for the DADP cocrystals with a) TCTNB b) TBTNB c) TITNB. Disorder of the DADP ring has been omitted for clarity.

4.2.1.1 Interactions in DADP Cocrystals

In many of the energetic cocrystals previously discovered it has been noted that favorable electrostatic interactions make a significant contribution in the formation of cocrystals.[3] Indeed, it was the supposed favorable interaction between the electron-rich peroxide moieties of DADP and the electron-poor aromatic rings of aromatic energetic materials that prompted the search for these cocrystals. The general interaction can be well understood when considering the distribution of electrostatic potential density for these materials (Figure 4.3). Certainly, in the DADP/TCTNB and DADP/TBTNB cocrystals an interaction between oxygen atoms of DADP and the halogenated trinitrobenzene rings is clearly observed (Figure 4.4). This interaction is analogous to those previously discovered for energetic cocrystals with electron-rich cocrystal formers, including most TNT cocrystals and the *chair-chair/layered* motif cocrystals of HMX.[3,4]

While this electrostatic interaction with the peroxide of DADP seems to be important in driving the cocrystallization of DADP/TCTNB and DADP/TBTNB, it is not present in the DADP/TITNB cocrystal. Instead, the electron-rich peroxide moiety of DADP very clearly donates into the sigma hole of the iodine atoms of TITNB (Figure 4.4). While crystal structures do not necessarily provide information about the strength of intermolecular interactions, it is significant to note that the I···O interaction in DADP/TITNB is the shortest interaction observed for all of the cocrystals. At 2.95 Å it was 0.55 Å shorter than the combined van der Waals radii of oxygen and iodine: 3.5 Å.

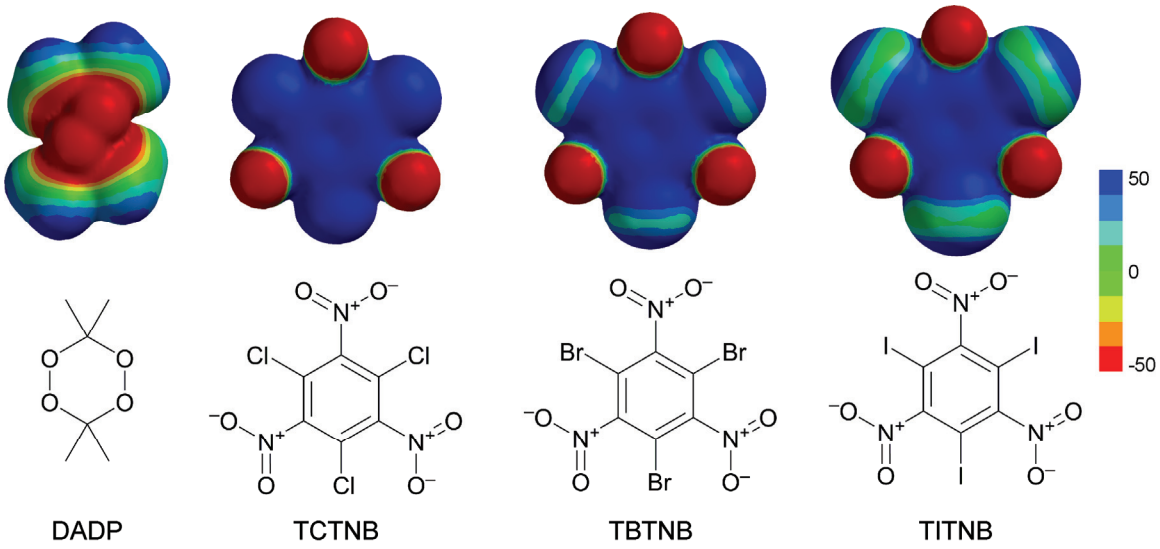

Figure 4.3 Electrostatic potential surfaces were calculated using the semi-empirical method and the AM1 model for DADP and all three halogenated trinitrobenzenes. Red and blue surfaces represent electron rich and poor regions, respectively, with colors representing values between -50 and 50 kJ/mol.

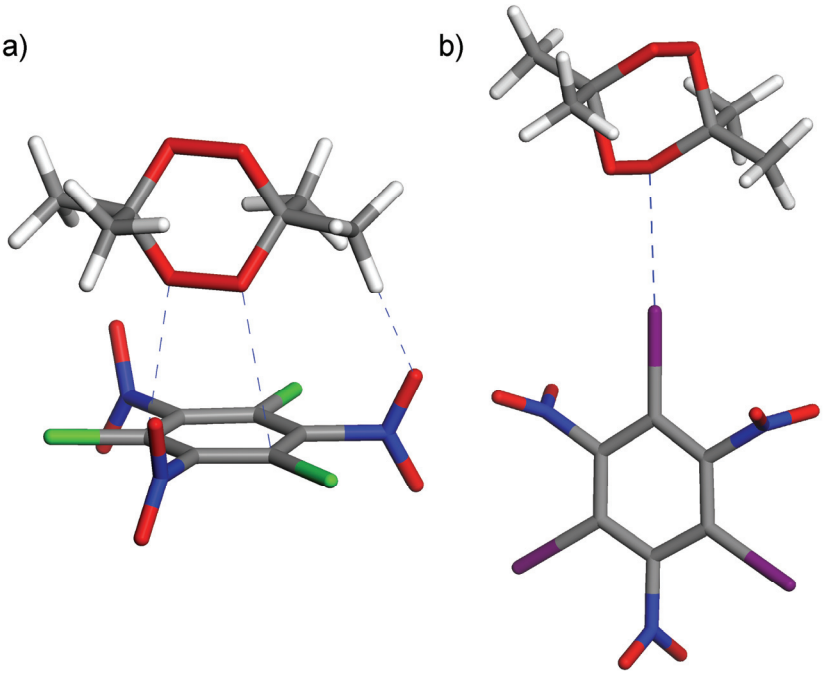

Figure 4.4 Intermolecular interaction of the peroxide oxygen atoms of DADP with a) the benzene ring of TCTNB observed in both the DADP/TCTNB and DADP/TBTNB and b) the iodine atom of TITNB in the DADP/TITNB cocrystal. Disorder of the DADP ring is omitted for clarity.

Halogen bonding interactions feature significantly in all of the DADP cocrystals. While halogen-nitro interactions are reported in the literature,[5-11] the DADP cocrystals are the first known energetic cocrystals to exhibit this interaction. In the case of the DADP/TITNB cocrystal the I···O interaction is not the only halogen bonding interaction observed; iodo-nitro interactions are also present and allow for the formation of infinite chains of TITNB ($C_1^2(8)[R_1^2(4)]$). These interactions are exclusively mono-dentate bi-coordinated interactions (Figure 4.5). Halogen-nitro interactions also appear prominently in both DADP/TCTNB and DADP/TBTNB as well. Like DADP/TITNB, infinite chains of halogenated trinitrobenzene are observed. However in contrast to DADP/TITNB, two distinct infinite chains of halogenated trinitrobenzene are formed through bi-dentate and mono-coordinated interactions ($C_1^1(8)[R_1^1(10)]$) (Figure 4.5). Given the presence of these halogen interactions, it is hypothesized that these may be significant in promoting the formation of these cocrystals.

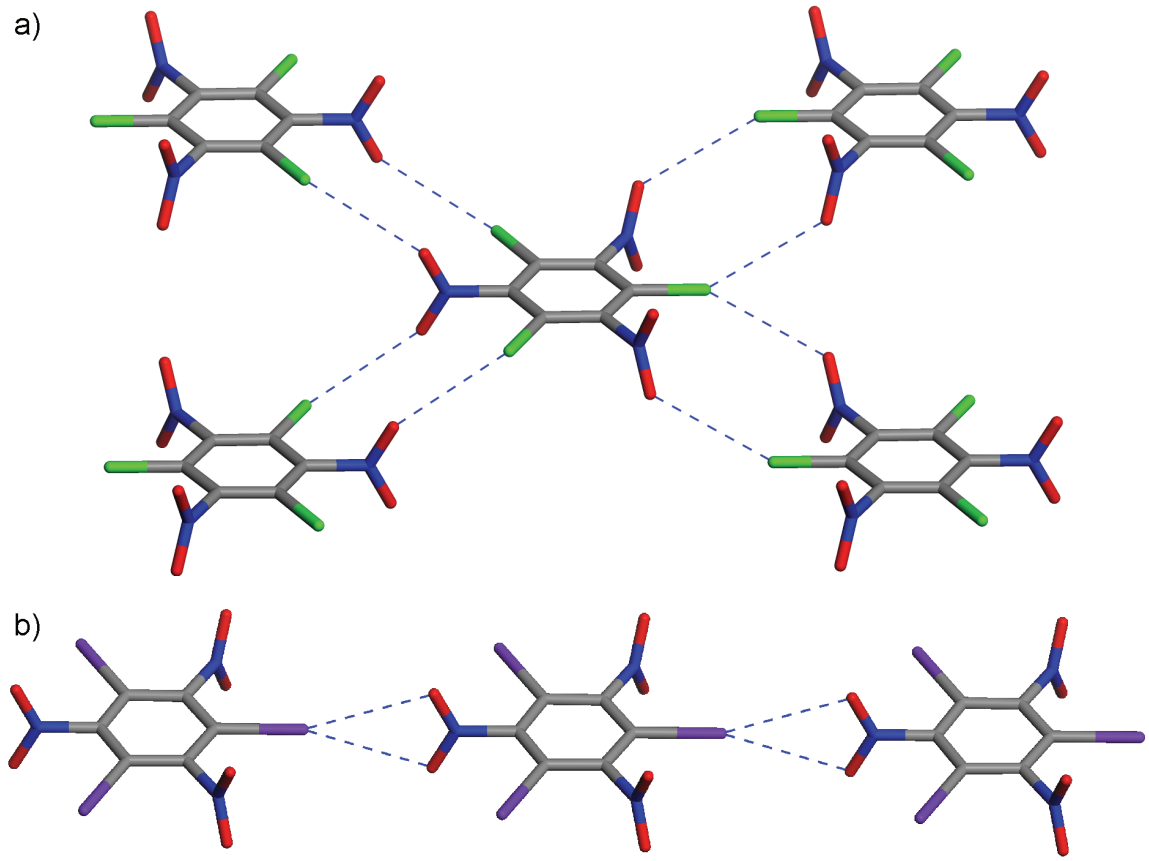

Figure 4.5 Halogen-nitro interactions (DADP not pictured) for a) the DADP/TCTNB cocrystal showing the bidentate, monocoordinated interaction found in the DADP/TCTNB and DADP/TBTNB cocrystal and b) the DADP/TITNB cocrystal exhibiting the monodentate bicoordinated interaction.

The differences in the crystal packing between the DADP/TITNB cocrystal and both the DADP/TCTNB and DADP/TBTNB cocrystals reveal the collective effects of steric hindrance, distribution of electron density, and intermolecular interactions due to halogen substitution. With each increase in atomic radius, from chlorine to bromine to iodine, steric interference increases prohibiting potential interactions between the peroxide moiety of DADP and the electron-poor ring of the halogenated trinitrobenzene. Distribution of electron density influences the observed interactions as well. In particular, the polarizability of the halogen atoms influences the size of the sigma hole responsible for halogen bonding. The iodine atom is also most polarizable, followed by the bromine atom and then the chlorine atom.[12-16] The polarizability of the iodine atom may allow for the I···O interaction with the DADP ring, where this interaction is not

observed for DADP cocrystals with TCTNB or TBTNB. Notably, even though the bromine atom also shows more polarization than the chlorine atom, this polarization is not sufficient for bromine to interact with DADP in the DADP/TBTNB cocrystal in the same way that iodine does in TITNB.

4.2.1.2 Hirshfeld Surface Calculations

A comprehensive examination of the interactions within the DADP cocrystals through Hirshfeld surface calculations reinforces the similarity between the DADP/TCTNB and DADP/TBTNB cocrystals and the differences in the DADP/TITNB cocrystal compared to the other two. By measuring the closest point of contact from the center of each atom of a molecule to surrounding molecules, Hirshfeld surfaces allow for a comprehensive consideration of all the close contact in a crystal structure.[17] A summary of observed close contacts from Hirshfeld surface calculations is shown in Figure 4.6. All of the DADP cocrystals have similar amounts of halogen-oxygen interactions, despite the different halogen interactions observed in these cocrystals. In considering the other interactions, the DADP/TITNB cocrystal is noticeably different. For instance, the DADP/TITNB cocrystal has halogen-halogen interactions which are not observed in the other cocrystals but are featured in the pure halogenated trinitrobenzenes. The Hirshfeld surfaces very clearly reinforce the differences of the DADP/TITNB cocrystal.

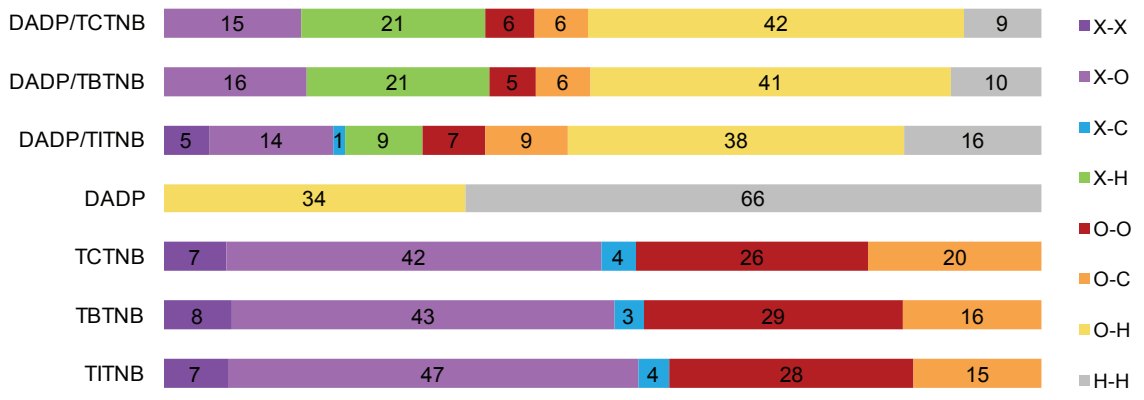

Figure 4.6 A summary of total close contacts for the DADP cocrystals and pure cocrystal formers as calculated using Hirshfeld surfaces.[17] X is used to symbolize either chlorine, bromine or iodine depending on the identity of the cocrystal or cocrystal former.

4.2.2 A Kinetic Cocrystal: DADP/TBTNB

While the DADP/TITNB cocrystal is clearly unique in structure, it is also critical to note that the thermodynamic stability of the nearly isostructural DADP/TCTNB and DADP/TBTNB cocrystals is very different. The DADP/TCTNB cocrystal is thermodynamically stable compared to its cocrystal formers. In contrast to this the DADP/TBTNB cocrystal can only be accessed as a kinetic form and is thermodynamically unstable compared to DADP and TBTNB. It is a kinetic cocrystal.

Kinetic cocrystals are cocrystals that, when placed in a thermodynamic equilibrium, are unstable relative to their own pure components. Though kinetic forms are a well-known phenomenon in single component crystals systems, to date, kinetic cocrystals are unknown in the literature. Similar kinetic forms must exist for cocrystal systems, however, though with more complex thermodynamic relationships, as multiple chemical species and solid forms are involved. For cocrystals, the potential for kinetic forms is largely unconsidered as the common model of discovery often reveals only cocrystals that are more thermodynamically favorable than the pure constituents.[18-23] Even in cases where metastable polymorphs of cocrystals exist these forms are always thermodynamically favored with respect to the cocrystal formers (thermodynamic forms).[22,24-26] Because researchers fail to consider kinetic cocrystals they may miss a large and unexplored phase space for cocrystal discovery.

The DADP/TBTNB cocrystal was initially discovered through solvent evaporation from acetonitrile, but it was produced in very low yield and amid the concomitant growth of large portions of pure DADP and TBTNB. In attempts to scale up the cocrystal for further analysis, it was observed that this cocrystal could not be formed via most commonly employed crystallization methods, such as solvent mediated transformation, and could not even be reliably reproduced from solvent evaporation in ways similar to that in which the cocrystal was discovered. One of the few reliable methods of formation was to cool solutions supersaturated with both DADP and TBTNB in a solvent that was poor for both compounds. The lack of cocrystal formation in a wide screen of crystallization conditions inspired careful examination of the possibility that DADP/TBTNB is a kinetic cocrystal.

4.2.2.1 Solvent-mediated Thermodynamic Experiments

When solid forms are in equilibrium with a solution, the system allows for the transformation of a solid into its most thermodynamically stable form. This technique provides an unambiguous means to determine the most stable form of a compound by providing equilibrium conditions. If a solvent is poor for a particular material, the transformation could take longer, but the direction of the equilibrium is inherent for the materials and should not change at a given temperature and pressure. To compare the stability of the DADP/TBTNB cocrystal to its pure components, slurries of DADP with TBTNB at room temperature were made. To consider possible kinetic factors or differences in solubility that might influence the kinetics a wide range of solvents were tested. Even after allowing the cocrystal formers to be in contact with solution for one week at room temperature, with all solvents employed no cocrystal formation was observed. This indicated that the DADP/TBTNB cocrystal could be less thermodynamically stable than the pure components at room temperature.

It is possible in solvent-mediated transformation, however, that a more thermodynamically stable form may not be accessed if the potential kinetic barrier is too high for this transformation to occur. To reduce the potential kinetic barrier at room temperature, cocrystal seeds were added to saturated solutions of DADP and TBTNB. Still, no cocrystal formation was observed; rather, the disappearance of the cocrystal seed was observed. To investigate this further and to provide as much cocrystal seed as possible, solutions saturated with DADP and TBTNB were added to vials containing the cocrystal. In all cases dissolution of the cocrystal was observed. In good solvents for DADP and TBTNB this dissolution took significantly less than 30 seconds (see Appendix 3). Even in cyclohexane, which is a poor solvent for both compounds, dissolution occurred in less than an hour. Only in the case of water, in which neither DADP nor TBTNB is substantially soluble, did dissolution take more than one hour. In all cases, the DADP/TBTNB cocrystal was shown to be less thermodynamically stable than saturated solutions of DADP and TBTNB at room temperature, thus validating the hypothesis that DADP/TBTNB is a kinetic cocrystal at room temperature.

To the best of our knowledge the DADP/TBTNB cocrystal represents the first reported case of a kinetic cocrystal. When placed in equilibrium with a saturated solution

of both cocrystal formers, the cocrystal spontaneously converts to the pure components, indicating that the cocrystal is more soluble than the pure forms of its components. Due to this thermodynamic instability, this cocrystal can only be accessed through kinetic growth conditions. Once formed, the cocrystal is metastable and can be stored in a sealed environment saturated with DADP vapor to prevent sublimation of DADP from the cocrystal. The discovery and characterization of this cocrystal holds considerable implications for the field of cocrystallization as it indicates that possible cocrystals may remain undiscovered due to the widespread use of cocrystallization methods that favor thermodynamic forms. Moreover, the fact that potential cocrystals might only be accessible using kinetic crystallization methods has significant implications for areas in which cocrystals are being applied, including the development of pharmaceutical compounds,[27-34] non-linear optical[35-38] and opto-electronic materials.[39,40]

4.2.2.2 Halogen Substitution and the Stability of the DADP Cocrystals

The thermodynamic instability of the DADP/TBTNB cocrystal with respect to its pure components, the fact that the DADP/TBTNB cocrystal is nearly isostructural with the DADP/TCTNB cocrystal (which is thermodynamically stable compared to its cocrystal formers), and that DADP/TITNB forms a completely distinct structure suggests that the halogen substitution influences the stabilities of these materials. The increase of steric interference by the substitution from chlorine to bromine may be partly responsible for the loss in stability. It is very likely that a DADP/TITNB cocrystal isostructural with the DADP/TCTNB and DADP/TBTNB cocrystals would be similarly thermodynamically unstable. In the case of TITNB, however, the I···O interaction is sufficiently strong to allow for an alternative cocrystal structure. The fact that DADP and TBTNB do not form an isostructural cocrystal with the DADP/TITNB cocrystal suggests that the Br···O interaction with the peroxide oxygen atoms is not sufficiently strong. The DADP/TBNTB cocrystal appears to be caught in the middle between two thermodynamic minima and adopts the DADP/TCTNB structure rather than the DADP/TITNB structure. These cocrystals show the influence that slight substitutions can have in resulting cocrystal forms and demonstrate the care that must be taken in screening for cocrystals.

4.2.3 Properties of DADP Cocrystals

Cocrystallization of DADP with halogenated trinitrobenzenes generally affords substantial improvements with respect to DADP for many key performance metrics for explosives. While the alteration and improvement of explosive properties through cocrystallization is known in the literature,[3,4,41-43] it is significant to note that cocrystallization effectively transforms an energetic material with unfavorable properties that limit its application into an energetic material with properties comparable to or better than commonly used explosives.

4.2.3.1 Density

Since density has significant influence over the power of detonation, specifically the detonation velocity and pressure, high density is desirable for energetic materials. All of the DADP cocrystals show improved density with respect to DADP (Table 4.2). The density of DADP/TCTNB is increased to 1.549 g/cm^3, which is significantly greater than that of DADP (1.330 g/cm^3). In the cases of DADP/TBTNB and DADP/TITNB the densities are even more significantly improved to 1.950 and 2.259 g/cm^3, respectively. For the DADP/TBTNB and DADP/TITNB cocrystals these densities are greater than most commonly employed organic energetic materials such as pentaerythritol tetranitrate (PETN, 1.778 g/cm^3), 1,3,5-trinitro-1,3,5-trinitroazacyclohexane (RDX, 1.840 g/cm^3), 1,3,5,7-tetranitro-1,3,5,7-tetraazacyclooctane (HMX, 1.903 g/cm^3), and 3-nitro-1,2,4-triazole-5-one (NTO, 1.916 g/cm^3). Perhaps even more remarkable, the density for the DADP/TITNB cocrystal far surpasses even that of 2,4,6,8,10,12-hexanitro-2,4,6,8,10,12-hexaazaisowurtzitane (CL-20, 2.044 g/cm^3), which is the densest organic energetic material utilized. The cocrystal densities are in between the densities of both cocrystal formers (Table 4.2). However, the pure halogenated trinitrobenzenes are difficult to detonate by impact, so despite some loss in density with respect to these materials through cocrystallization, the ability to detonate is greatly improved. Therefore cocrystallization provides an opportunity to improve the properties of both energetic materials. Density is improved with respect to DADP and the halogenated trinitrobenzenes become more effective secondary and primary explosives.

Table 4.2 Room temperature crystallographic density and calculated packing coefficient for DADP, DADP cocrystals and halogenated trinitrobenzenes.

	density (g/cm^3)	PC (%)
DADP	1.309	79.6%
DADP/TCTNB cc	1.549	72.8%
TCTNB	1.915	74.7%
DADP/TBTNB cc	1.936	74.8%
DADP/TITNB cc	2.259	84.2%
TBTNB	2.402	69.9%
TITNB	2.815	68.4%

4.2.3.2 Packing Coefficient

The packing coefficients of these materials provide insight into another effect of the halogen substitution in packing for the DADP cocrystals (Table 4.2). The packing coefficient for the DADP/TBTNB cocrystal is between that of both cocrystal formers. For the DADP/TCTNB cocrystal, however, the packing coefficient of the cocrystal is lower than that of either cocrystal former. Since the introduction of void space in a crystal is generally not favorable,[44-46] this may indicate the presence of interactions that promote the formation of the DADP/TCTNB cocrystal. As the DADP/TCTNB and DADP/TBTNB cocrystals are nearly isostructural, the difference in the packing coefficients can be explained due to the size of the halogen atoms. The DADP/TITNB cocrystal has a higher packing coefficient than either cocrystal former. Considering the polarizability of the iodine atom and the short interactions present in this cocrystal it seems likely that the high packing coefficient is due in part to the presence of iodine.

4.2.3.3 Oxygen Balance

Oxygen balance is another key concern for energetic materials. This value describes, in terms of weight percent of oxygen, how much oxygen is in excess or lacking for a perfectly balanced explosion reaction to occur. If there is too much oxygen, the power of the explosive will be diminished, while if there is too little oxygen, the far more common case for organic energetic materials, not only will the power be diminished, but instead of reacting cleanly to produce carbon dioxide, water, nitrogen gas or other relatively benign compounds, more toxic gases such as carbon monoxide will be

produced. While mixtures of inorganic over-oxidized explosives are often blended with organic explosives, cocrystallization offers a unique opportunity to balance the oxygen content on a molecular level.

The cocrystallization of DADP with the halogenated trinitrobenzenes greatly improves the oxygen balance with respect to DADP (Table 4.3). The oxygen balance of the DADP/TCTNB cocrystal is comparable with that of TNT, one of the most commonly used explosives. The DADP/TBTNB and DADP/TITNB cocrystals show even more improvement in the oxygen balance. While the addition of heavier halogens appears to improve this property, this is in part an effect of the oxygen comprising a smaller percent of the overall weight, so the effective oxygen deficiency for all of the cocrystals are the same on a molar basis. Nevertheless, DADP is highly oxygen deficient and cocrystallizing with the halogenated trinitrobenzenes provides energetic materials with more oxygen with respect to DADP, therefore lending the cocrystals greater power.

Table 4.3 Oxygen balances (OB) for DADP, DADP cocrystals and pure halogenated trinitrobenzenes.

	OB (%)
TITNB	-12.19%
TBTNB	-16.01%
TCTNB	-22.75%
DADP/TITNB cc	-40.07%
DADP/TBTNB cc	-49.50%
DADP/TCTNB cc	-63.71%
DADP	-151.19%

4.2.3.4 Thermal Properties of DADP Cocrystals

While the acetone peroxides are attractive for their cheap and facile synthesis, these explosives have properties, including a low detonation temperature and excessive volatility, which have hindered their widespread use. Cocrystallization provides an opportunity to alter these properties. The DADP cocrystals demonstrate improved stability with respect to DADP loss and alter the thermal characteristics with respect to both cocrystal formers. This mitigation of some DADP loss demonstrates progress in

transforming energetic materials with one or two characteristic that prevent them from being fielded into viable materials.

DADP sublimes at room temperature.[47-49] Though DADP still sublimes out of the cocrystals, it does so at a reduced rate. This demonstrates the ability to reduce volatility for materials through cocrystallization. Additionally, the rate of DADP loss reveals the comparative strength of interactions between DADP and the halogenated trinitrobenzenes in the cocrystals. To quantitatively study the loss of DADP, the partial vapor pressure of DADP was determined by measuring the mass loss from a vapor effusion cell at a constant temperature of 40 °C. It is interesting to note that the DADP/TCTNB and DADP/TBTNB cocrystals show a similar decrease in DADP vapor pressure (Table 4.4), though DADP is slightly more volatile in the DADP/TBTNB cocrystal. Considering that the DADP/TCTNB and DADP/TBTNB cocrystals are nearly isostructural, this similarity in vapor pressure may suggest that the interactions within these cocrystals are of comparable strength. Remarkably, the DADP/TITNB cocrystal exhibits more than an order of magnitude reduction in the partial vapor pressure of DADP. This is a significantly greater reduction than that observed in either the DADP/TCTNB or DADP/TBTNB cocrystal and could likely be due to the presence of significantly stronger interactions with DADP present in the DADP/TITNB cocrystal. In particular, the I···O interaction could be responsible for reducing DADP loss. These cocrystals demonstrate that cocrystallization can improve the stability of volatile energetic materials like DADP. Cocrystal formers that form strong interactions with the peroxide of the acetone peroxides, therefore, could reduce the vapor pressure of this material to make it useable.

Table 4.4 Partial vapor pressure of DADP for pure DADP and the DADP cocrystals using a vapor effusion cell at 40 °C

compound	partial vapor pressure (Pa)
DADP	0.332
DADP/TCTNB cocrystal	0.153
DADP/TBTNB cocrystal	0.187
DADP/TITNB cocrystal	0.028

Cocrystallization also alters the thermal profile of these materials with respect to their pure components. When heating cocrystals two different phenomena have been observed: a) the cocrystal behaves as one unique compound, as is the case for cocrystals of TNT with aromatic compounds,[4] or b) the components of the cocrystal separate when heated, as is the case for HMX cocrystals[3] CL-20/TNT[41] and CL-20/HMX (2:1).[42] Due to the high volatility of DADP, it is no surprise that when heating these cocrystals, DADP sublimes out of the cocrystal first. In the cocrystals, similar temperatures for DADP loss is observed. This is followed by sublimation of the halogenated trinitrobenzenes, melting and then decomposition. The temperatures for these are similar to those of the pure halogenated trinitrobenzenes. It is also worth noting that TCTNB and TCTNB have clear melting points before decomposition, whereas TITNB, never melts but only decomposes at about 395˚C.

4.2.3.5 Explosive Properties of DADP Cocrystals

The explosive properties of the DADP cocrystals provided surprising results that have significant implications not only for the development of novel energetic materials via cocrystallization, but also for the use of cocrystallization as an original technique to answer fundamental questions about origin of sensitivity for energetic materials. Explosives can be sensitive to various forms of shock, including impact, friction, static electricity and heat. The origin of sensitivity for energetic materials is an oft-debated and much-studied subject in the research of explosives, pyrotechnics and propellants. Theories have been put forth regarding the strength and number of intermolecular interactions present in the explosive,[50-52] the presence of slip planes,[50,53] the bond dissociation energy of the weakest covalent bond present,[54-57] the oxygen balance,[58,59] decomposition temperature,[59] the distribution of electron density,[60,61] and even the volume available within the crystal lattice of energetics.[62] While impact sensitivity is only one of many sensitivity tests, it was incredible to note that sensitivity is fully retained for both the DADP/TCTNB and DADP/TITNB cocrystals despite significant changes in packing, interactions and overall distribution of electronic potential within the cocrystal (Table 4.5). This result is in stark contrast to the impact sensitivity tests performed for all other energetic cocrystals to date, in which cocrystallization reduced sensitivity by more than half the difference between the least and most sensitive energetic

materials.[41,42] The shock sensitivity for these cocrystals points towards the inherent sensitivity of the peroxide moiety which is not stabilized by the interaction with the electron poor ring of TCTNB nor with the iodine atom of TITNB. This is consistent with earlier research that noted that acetone peroxides retain sensitivity even when wetted with liquids, a procedure that generally desensitizes most energetics.[49] Therefore, based on these results, cocrystallization offers a remarkable means to probe the mechanism for sensitivity of energetic materials. By significantly altering the packing and interactions through cocrystallization, the extent to which these factors influence the sensitivity of a particular material becomes clear. In the case of CL-20 cocrystals with TNT or HMX,[41,42] sensitivity can be mitigated through the alteration of structure and the introduction of more interactions and stability within those interactions. In the DADP cocrystals, despite alterations in interactions and packing, the sensitivity is retained. While many other useful tools for probing the sensitivity of explosives exist, cocrystallization offers a unique and powerful tool for determining the mechanism of sensitivity for energetic materials

Table 4.5 Impact sensitivity data for DADP cocrystals and the cocrystal formers represented by the $h_{50\%}$, or the height at which at least 50% of the samples detonated.

	$h_{50\%}$ (cm)
DADP	15
DADP/TCTNB cocrystal	15
DADP/TITNB cocrystal	15
TCTNB	91
TBTNB	135
TITNB	>145

The retained sensitivity of the DADP cocrystals is also important as it demonstrates for the first time the possibility of making cocrystals with improved power that remain unaltered in their sensitivity. While producing less sensitive explosives and propellants is a large focus in energetic materials research, there is also significant interest in developing primary explosives with improved power. As a certain degree of sensitivity is key to the function of these materials, it would be disadvantageous to make primary explosives significantly less sensitive. Improving the oxygen balance and

increasing the density boosts the power of these materials. The ability to create primary explosives with improved power through cocrystallization with energetic materials like DADP has the potential to transform the search for energetic cocrystals as well as broaden their application.

4.3 Conclusions

This chapter reported the formation of energetic-energetic cocrystals with DADP: DADP/TCTNB, DADP/TBTNB, and DADP/TITNB. This work also presents the first reported synthesis and characterization of the cocrystal former TITNB (see Section 4.4.1). These cocrystals represent an advance in the cocrystal engineering of explosives since their formation was predicted based on the distribution of electron density within each of the cocrystal formers. Not only do these cocrystals represent a successful application of cocrystal engineering theory, but the halogen substitution provides rare insight into the delicate balance of energy in crystal formation and the differences that atom size and polarizability can have on the structure of a material. The DADP/TCTNB cocrystal was thermodynamically stable with respect to its cocrystal formers at room temperature, while the DADP/TBTNB cocrystal, though almost isostructural, was shown to be a kinetic form at room temperature. Although a similar crystal structure was expected, the introduction of iodine allowed for a completely different crystal structure in the case of the DADP/TITNB cocrystal. The relative stabilities of these cocrystals reinforce the need for cocrystallization screening methods that allow for both kinetic and thermodynamic forms to be formed. The existence of a kinetic cocrystal, DADP/TBTNB, in particular has significant implications for cocrystal research.

Several results were observed that are of importance for future research. First, cocrystallization and the halogen substitution influence the resulting materials properties with respect to DADP. Improved oxygen balance, higher densities and lower DADP volatility were all achieved through cocrystallization. Indeed, the density is dramatically increased for an energetic cocrystal. In the case of the DADP/TITNB cocrystal, the density is even higher than that of CL-20, the densest organic explosive commonly used. The retention of sensitivity of DADP cocrystals also shows for the first time the

opportunity to use cocrystallization to improve the power of explosives without a loss in sensitivity, which has great promise in cocrystallizing more effective primary explosives.

Finally, this research demonstrates for the first time the potential for cocrystallization to serve as an experimental means to probe the cause of sensitivity in energetic materials. The retention of peroxide-like sensitivity for the DADP/TCTNB and DADP/TITNB cocrystals despite the significant change in interactions and packing afforded through cocrystallization support the conclusion that the peroxide moiety, as an element in energetic materials, is inherently unstable. Functional group sensitivities can, therefore, sometimes be the determining factor in the sensitivity an energetic material and cocrystallization provides a means to examine the influence of packing and intermolecular interactions versus functional group sensitivity experimentally. This result offers a novel application for cocrystallization in future energetics research.

4.4 Experimental

4.4.1 Cocrystal synthesis

4.4.1.1 Synthesis of Cocrystal Formers

Synthesis of DADP was modified from the literature method.[63] In an ice bath, 1 mL of acetone (Fisher, Certified ACS) and 2 mL of 30% hydrogen peroxide (Fisher, Certified ACS) were added to 5 mL of dichloromethane (Fisher, stabilized HPLC Grade). 2 mL of 70% perchloric acid (B&A, Reagent ACS) was then added drop-wise. The reaction stirred for one hour at 0 °C and then stood at room temperature for three days to ensure full conversion to DADP. The precipitate was filtered, washed with water and 5% $NaHCO_3$ to remove any residual acid, and then recrystallized from methanol to afford a white solid. The resulting white solid was analyzed with ^{1}H NMR and the ^{1}H NMR chemical shifts agreed with the literature.[64] The best obtained yield after recrystallization was 54.4%.

Both TCTNB and TBTNB were synthesized according to literature procedures.[65]

TITNB was synthesized by the following procedure. Into a 25 ml 2-neck round bottom flask 12 ml of 100% nitric acid were added to 2 ml of concentrated sulfuric acid. To this acid mixture 0.46 g (1 mmol) of 1,3,5-triiodobenzene, prepared from 1,3,5-

tribromobenzene by the method of Mich,[66] was added in one portion. The reaction turned immediately a red/amber color and was stirred at 60 °C under a condenser for 24 hours. The reaction was poured onto ice and the resultant solids were collected and recrystallized from 9 ml of chloroform. This afforded an off-white powder of 0.266 g (45% yield). ^{13}C NMR (400 MHz, DMSO): δ = 86.9, 161.9. MS (EI): found = 590.69, calculated for $C_6I_3N_3O_6$ = 590.7.

4.4.1.2 Methods for Cocrystal Formation

Cocrystals of DADP/TCTNB were obtained by solvent mediated transformation in a 1:1 molar ratio of DADP and TCTNB at room temperature in acetonitrile (ACN, Fisher, HPLC Grade). Cocrystals of DADP/TITNB were obtained by solvent mediated transformation in a 3:1 molar ratio in acetontrile at room temperature.

Many synthesis conditions were tested before optimizing the best the conditions for the DADP/TBTNB cocrystal synthesis. Though the DADP/TBTNB cocrystal was first obtained by dissolving a 1:1 molar ratio of DADP (1.544 mg) and TBTNB (4.663 mg) in 0.1 mL ACN, and evaporating the solution, the cocrystal formed accounted for less than 10% of the solids obtained as determined by optical microscopy and Raman spectroscopy. In attempts to scale up these previous conditions larger quantities of both cocrystal formers were dissolved in ACN (14.299 mg of TBTNB with 4.738 mg of DADP dissolved in 0.3 mL of ACN, and 11.811 mg of TBTNB and 3.952 mg of DADP in 0.4 mL of ACN) and left to evaporate at room temperature, but little if any cocrystal was formed, indicating unpredictable formation of this cocrystal.

Other attempted methods included solvent inversion, solvent mediated transformation (slurrying), seeding and cooling crystallization. Most methods failed to produce cocrystals. Solvent inversion, accomplished by dissolving a 1:1 mole ratio of DADP and TBTNB in ACN and then adding water produced no cocrystal. Solvent mediated transformation in solutions saturated with and containing both solid DADP and TBTNB were made with water, ethanol, methanol (Fisher, Certified ACS), ethyl acetate (Fisher, HPLC Grade), 1,4-dioxane (Fisher, Certified ACS), tetrahydrofuran (Fisher, Certified, dry), chloroform (Fisher, Certified ACS), *N*,*N*-dimethylformamide (Fisher, Sequencing Grade), cyclohexane (Aldrich, anhydrous), ACN, and diethyl ether (Fisher, Stabilized HPLC Grade) at room temperature. All room temperature slurries produced no

cocrystal. Another method attempted to form this cocrystal involved heating and then cooling solutions containing both cocrystal formers. In cases where one of the cocrystal formers was undersaturated, cocrystal formation usually was not observed and only pure components were produced. Furthermore, saturating solutions of DADP and TBTNB in ACN, methanol, ethanol (Decon Laboratories, Inc., 200 proof), toluene, benzene, propyl alcohol, and isopropyl alcohol never produced cocrystals. Consistent cocrystal formation by rapid cooling was only achieved in solutions supersaturated with both cocrystal formers in solvents that were poor for both cocrystal formers, such as cyclohexane and heptane.

Based on these results, a method to consistently form cocrystal was developed. To obtain larger quantities of the cocrystal, a supersaturated solution of both DADP and TBTNB was created in cyclohexane by heating to 80 °C. This solution was then filtered, while hot, into a clean vial and monitored with optical microscopy as the solution came to room temperature. Cocrystal formed concomitantly with TBTNB and/or DADP depending on the individual nucleation events. The optimized procedure employed 4.0 mg of TBTNB, 28 mg of DADP in 1.0 mL of cyclohexane, sonicated for 30 minutes and heated to in a sealed 4 mL vial at 80 °C for at 10 minutes. Cocrystals were isolated by removing the cyclohexane, allowing residual cyclohexane to dry and then sealing the material in a 4 mL vial.

Solvent mediated transformation with both cocrystal formers could fail to produce a cocrystal if the kinetic potential energy barrier is too high. To reduce this barrier cocrystal was introduced into these systems as a seed. In order to maximize the amount of cocrystal introduced, saturated solutions of DADP and TBTNB in either water, ethanol, methanol, ethyl acetate, 1,4-dioxane, tetrahydrofuran, chloroform, *N*,*N*-dimethylformamide, cyclohexane, ACN, or diethyl ether were added to cocrystal and monitored using optical microscopy. In all cases the cocrystal (needle) became smaller as if it were dissolving and then disappeared while the DADP and TBTNB remained. This dissolution was almost instantaneous in the cases of all but methanol, ethanol, cyclohexane and water and the cocrystal was effectively gone after less than 30 seconds. For the latter four solvents, dissolution times were 2 minutes, 5 minutes, 50 minutes and more than two weeks respectively.

4.4.2 Raman Spectroscopy

Raman spectra were obtained using a Renishaw inVia Raman Microscope equipped with a 514 nm argon ion laser, a 785 nm diode laser and a RenCam CCD detector. The 514 nm argon ion laser employed an 1800 lines/mm grating and a 50 μm slit while the 785 nm diode laser employed a 1200 lines/mm grating and a 65 μm slit. Spectra were collected and analyzed using the WiRE 3.1 software package (Renishaw). Calibration was performed using a silicon standard. Spectra were collected using an Olympus SLMPlan 20× objective (numerical aperture = 0.35) in extended scan mode with a range of 100-3800 cm^{-1}. Spectra were further analyzed using ACD/SpecManager Version 12.01 software (ACD/Labs).

4.4.3 Powder X-Ray Diffraction

Powder X-ray diffraction (PXRD) patterns were collected at room temperature using a Rigaku R-Axis Spider diffractometer with an image plate detector and graphite monochromated Cu-Kα radiation (λ = 1.54187 Å). Samples were mounted on a CryoLoop™ and images were collected for ten minutes while rotating the sample about the φ-axis at 10°/sec, oscillating ω between 120° and 180° at 1°/sec with χ fixed at 45°. Images were integrated from 2 to 70° with a 0.01° step size using AreaMax 2.0 software (Rigaku). Powder patterns were processed using Jade 8 XRD Pattern Processing, Identification & Quantification analysis software (Materials Data, Inc).

4.4.4 Single Crystal Structure Determination

Single crystal diffraction X-ray data for the DADP/TCTNB cocrystal was collected using a Rigaku AFC10K Saturn 944+ CCD-based X-ray diffractometer equipped with a low temperature device and Micromax-007HF Cu-target micro-focus rotating anode (λ = 1.54187 Å) operated at 1.2 kW power (40 kV, 30 mA). The crystal was mounted in a 0.3 mm capillary loaded with DADP to make a DADP saturated atmosphere to stabilize the cocrystal. The X-ray intensities were measured at room temperature with the detector placed at a distance 42.00 mm from the crystal.

Single crystal X-ray diffraction data for the DADP/TBTNB and DADP/TITNB cocrystals and pure TBTNB and TITNB was obtained using a Rigaku R-Axis Spider diffractometer with an image plate area detector using graphite monochromated Cu-Kα

radiation (λ = 1.54187 Å) operated at 2.0 kW power (50 kV, 40 mA). The X-ray intensities were measured with the detector at a distance 127.00 mm from the crystals. The DADP/TBTNB cocrystal was mounted in a 0.3 mm capillary loaded with DADP to make a DADP saturated atmosphere to stabilize the cocrystal; some decay was observed. The DADP/TITNB cocrystal, pure TBTNB and pure TITNB were mounted on a MiTeGen MicroMount™. The DADP/TBTNB cocrystal and TITNB were collected at room temperature and the DADP/TITNB cocrystal and TBTNB were collected at 95(2) K.

All data were processed with CrystalClear 2.0 (Rigaku) and corrected for absorption using an empirical absorption correction. Structures were solved by direct methods[67,68] refined and expanded using the CrystalStructure 4.0[69] crystallographic software package (Rigaku). Non-hydrogen atoms were refined anisotropically. Hydrogen atoms were placed using the riding model. Full-matrix least-squares refinement was made on F^2. Full details are available as supporting information in the CIF file. For determination of intermolecular distances all carbon-hydrogen, nitrogen-hydrogen and oxygen-hydrogen bond lengths were normalized to 1.083 Å, 1.008 Å and 0.983 Å respectively.

4.4.5 Differential Scanning Calorimetry

Thermograms of the samples were recorded on a TA Instruments Q10 differential scanning calorimeter and programmed using Thermal Advantage for Q Series Version 2.5. Samples (weighed to a precision of ± 0.005 mg) were placed in hermetic aluminum pans and the lids were crimped using a TA-Instruments hermetic sealing press. Thermal behavior of the samples from 25 up to 395 °C was studied under a nitrogen purge of 50.0 mL/min at a heating rate of 10 °C/min. Thermal behavior was also measured by cycling the temperature from 20 to -90 °C and back to 20 °C using 1, 5, and 10 °C/min cooling and heating rates. The instrument was calibrated with an indium standard. Data were analyzed using Universal Analysis 2000 4.3 software (TA-Instruments-Waters LLC).

4.4.6 Thermomicroscopy

Thermomicroscopy was performed with a Linkham LTS 350 hot stage connected to a Linkham TMS 94 processor and controlled using Linksys32 Version 1.9.3 software,

viewed under polarized light with a Nikon Eclipse E600 microscope. Thermal transitions were observed optically for comparison with DSC data. Samples were heated from room temperature at a rate of 10 °C/min to temperatures up to 350 °C.

4.4.7 Vapor Pressure Measurements

Vapor pressure experiments were performed by loading DADP or the cocrystals into DSC pans with 50 μm diameter holes from a Perkin-Elmer volatile pan kit on a TA Instruments Thermogravimetric Analysis Instrument. Samples were heated to 40 °C at a rate of 20 °C/min and held isothermally for at least 16 hours under a 30 mL/min flow of nitrogen gas. Partial vapor pressure was calculated using the following equation (4.1):[70]

$$p_j = \frac{d_{mj}}{d_t}\frac{1}{A_0}\sqrt{\frac{2\pi RT}{MW_j}} \tag{4.1}$$

where p_j is the equilibrium partial vapor pressure of the species, d_{mj}/d_t is the rate of mass loss, A_0 is the area of the orifice, R is the gas constant, T is the temperature in K, and MW_j is the molecular weight of the species.

4.4.8 Calculations

4.4.8.1 Hirshfeld Surface Calculations

Hirshfeld surface calculations were performed using CrystalExplorer version 3.0.[71] Hydrogen bond lengths were normalized (O–H to 0.983, N–H to 1.008 and C–H to 1.083 Å) and disorder was removed for all crystallographic information files used. Hirshfeld surfaces are generated by partitioning space in a crystal by considering the electron distribution of the sum of spherical atoms for the molecule (promolecule) to the whole crystal (procrystal). Everywhere this sum that contributes more than twice the electron density to that of procrystal is partitioned into the promolecule. Therefore, from the center of an atom, the electron density is counted as the promolecule until it contributes more to the molecule touching it. This generates a surface describing where and to what extent atoms from different molecules are in proximity to one another. From this Hirshfeld surface a 2D fingerprint, plotting the d_e value, or distance to the surface from the nearest atom from exterior, against the d_i, or distance from the surface to the

nearest atom of the interior, is generated. Specific interactions can be isolated from the plot to reveal their contribution to overall contacts within the crystal structure.

4.4.8.2 Packing Coefficient Calculations

Packing coefficients were calculated by using the following equation: $C_k = ZV_{mol}V_{cell}^{-1}$, where C_k is the packing coefficient, Z is the number of molecules in the unit cell, V_{mol} is the molecular volume (Å^3), and V_{cell} is the volume of the unit cell. Molecular volume was calculated with Spartan '10 version 1.0.1 (Wavefunction, Inc.), which employs van der Waals radii of 1.8855 Å for bromine, 1.5138 Å for fluorine, 1.9200 Å for carbon, 1.2000 Å for hydrogen, 1.5500 Å for nitrogen, and 1.5200 Å for oxygen.

4.4.8.3 Electrostatic Potential Surface Density Map Calculations

Calculations of the electrostatic potential energy density surfaces for the DADP cocrystals, DADP and the halogenated trinitrobenzenes were performed using semi-empirical methods with the AM1 model available in Spartan '10 version 1.0.1 (Wavefunction, Inc.). All surfaces were normalized between -50 and 50 kJ/mol.

4.4.9 Drop Weight Impact Sensitivity Tests

Sensitivities of the DADP cocrystals and the pure cocrystal formers were determined using an in-house-constructed drop-weight test. Samples of 2.0 ± 0.2 mg (except in the case of DADP/TITNB where samples of 2.5 ± 0.25 mg were measured) were enclosed in aluminum pans and impacted with a 5 lb weight. Samples were tested for a 50% probability to detonate ($h_{50\%}$) when impacted from a specified height.

4.5 References

(1) Wolffenstein, R. *Ber. Dtsch. Chem. Ges.* **1895**, *28*, 2265-2269.

(2) Dubnikova, F.; Kosloff, R.; Almog, J.; Zeiri, Y.; Boese, R.; Itzhaky, H.; Alt, A.; Keinan, E. *J. Am. Chem. Soc.* **2005**, *127*, 1146-1159.

(3) Landenberger, K. B.; Matzger, A. J. *Cryst. Growth Des.* **2012**, *12*, 3603-3609.

(4) Landenberger, K. B.; Matzger, A. J. *Cryst. Growth Des.* **2010**, *10*, 5341-5347.

(5) Robinson, J. M. A.; Philp, D.; Harris, K. D. M.; Kariuki, B. M. *New J. Chem.* **2000**, *24*, 799-806.

(6) Allen, F. H.; Lommerse, J. P. M.; Hoy, V. J.; Howard, J. A. K.; Desiraju, G. R. *Acta Crystallogr., Sect. B: Struct. Sci.* **1997**, *53*, 1006-1016.

(7) Desiraju, G. R. *Angew. Chem., Int. Ed. Engl.* **1995**, *34*, 2311-2327.

(8) Desiraju, G. R.; Pedireddi, V. R.; Sarma, J.; Zacharias, D. E. *Acta Chim. Hung.* **1993**, *130*, 451-465.

(9) Espallargas, G. M.; Zordan, F.; Marín, L. A.; Adams, H.; Shankland, K.; van de Streek, J.; Brammer, L. *Chem.-Eur. J.* **2009**, *15*, 7554-7568.

(10) Reddy, L. S.; Chandran, S. K.; George, S.; Babu, N. J.; Nangia, A. *Cryst. Growth Des.* **2007**, *7*, 2675-2690.

(11) Saha, B. K.; Nangia, A.; Jaskolski, M. *CrystEngComm* **2005**, *7*, 355-358.

(12) Metrangolo, P.; Resnati, G.; Pilati, T.; Biella, S. In *Halogen Bonding: Fundamentals and Applications*; Metrangolo, P., Resnati, G., Eds.; Springer-Verlag Berlin: Berlin, 2008; Vol. 126, p 105-136.

(13) Riley, K. E.; Merz, K. M. *J. Phys. Chem. A* **2007**, *111*, 1688-1694.

(14) Gavezzotti, A. *Mol. Phys.* **2008**, *106*, 1473-1485.

(15) Politzer, P.; Murray, J. S.; Clark, T. *Phys. Chem. Chem. Phys.* **2010**, *12*, 7748-7757.

(16) Lommerse, J. P. M.; Stone, A. J.; Taylor, R.; Allen, F. H. *J. Am. Chem. Soc.* **1996**, *118*, 3108-3116.

(17) Spackman, M. A.; Jayatilaka, D. *CrystEngComm* **2009**, *11*, 19-32.

(18) Oliveira, M. A.; Peterson, M. L.; Davey, R. J. *Cryst. Growth Des.* **2011**, *11*, 449-457.

(19) ter Horst, J. H.; Deij, M. A.; Cains, P. W. *Cryst. Growth Des.* **2009**, *9*, 1531-1537.

(20) Schartman, R. R. *Int. J. Pharm.* **2009**, *365*, 77-80.

(21) Karamertzanis, P. G.; Kazantsev, A. V.; Issa, N.; Welch, G. W. A.; Adjiman, C. S.; Pantelides, C. C.; Price, S. L. *J. Chem. Theory Comput.* **2009**, *5*, 1432-1448.

(22) Gagnière, E.; Mangin, D.; Puel, F.; Rivoire, A.; Monnier, O.; Garcia, E.; Klein, J. R. *J. Cryst. Growth* **2009**, *311*, 2689-2695.

(23) Issa, N.; Karamertzanis, P. G.; Welch, G. W. A.; Price, S. L. *Cryst. Growth Des.* **2009**, *9*, 442-453.

(24) Kaur, R.; Row, T. N. G. *Cryst. Growth Des.* **2012**, *12*, 2744-2747.

(25) Aitipamula, S.; Chow, P. S.; Tan, R. B. H. *CrystEngComm* **2009**, *11*, 889-895.

(26) Ueto, T.; Takata, N.; Muroyama, N.; Nedu, A.; Sasaki, A.; Tanida, S.; Terada, K. *Cryst. Growth Des.* **2012**, *12*, 485-494.

(27) Brittain, H. G. *Cryst. Growth Des.* **2012**, *12*, 5823-5832.

(28) Qiao, N.; Li, M. Z.; Schlindwein, W.; Malek, N.; Davies, A.; Trappitt, G. *Int. J. Pharm.* **2011**, *419*, 1-11.

(29) Good, D. J.; Rodríguez-Hornedo, N. *Cryst. Growth Des.* **2009**, *9*, 2252-2264.

(30) Schultheiss, N.; Newman, A. *Cryst. Growth Des.* **2009**, *9*, 2950-2967.

(31) Shan, N.; Zaworotko, M. J. *Drug Discov. Today* **2008**, *13*, 440-446.

(32) Trask, A. V.; Motherwell, W. D. S.; Jones, W. *Int. J. Pharm.* **2006**, *320*, 114-123.

(33) McNamara, D. P.; Childs, S. L.; Giordano, J.; Iarriccio, A.; Cassidy, J.; Shet, M. S.; Mannion, R.; O'Donnell, E.; Park, A. *Pharm. Res.* **2006**, *23*, 1888-1897.

(34) Trask, A. V.; Motherwell, W. D. S.; Jones, W. *Cryst. Growth Des.* **2005**, *5*, 1013-1021.

(35) Choi, E. Y.; Jazbinsek, M.; Lee, S. H.; Günter, P.; Yun, H.; Lee, S. W.; Kwon, O. P. *CrystEngComm* **2012**, *14*, 4306-4311.

(36) Koshima, H.; Nagano, M.; Asahi, T. *J. Am. Chem. Soc.* **2005**, *127*, 2455-2463.

(37) Pan, F.; Wong, M. S.; Gramlich, V.; Bosshard, C.; Günter, P. *J. Am. Chem. Soc.* **1996**, *118*, 6315-6316.

(38) Frankenbach, G. M.; Etter, M. C. *Chem. Mat.* **1992**, *4*, 272-278.

(39) Bolton, O.; Kim, J. *J. Mater. Chem.* **2007**, *17*, 1981-1988.

(40) Del Mauro, A. D. G.; Carotenuto, M.; Venditto, V.; Petraccone, V.; Scoponi, M.; Guerra, G. *Chem. Mat.* **2007**, *19*, 6041-6046.

(41) Bolton, O.; Matzger, A. J. *Angew. Chem., Int. Ed.* **2011**, *50*, 8960-8963.

(42) Bolton, O.; Simke, L. R.; Pagoria, P. F.; Matzger, A. J. *Cryst. Growth Des.* **2012**, *12*, 4311–4314.

(43) Millar, D. I. A.; Maynard-Casely, H. E.; Allan, D. R.; Cumming, A. S.; Lennie, A. R.; Mackay, A. J.; Oswald, I. D. H.; Tang, C. C.; Pulham, C. R. *CrystEngComm* **2012**, *14*, 3742-3749.

(44) Brock, C. P.; Dunitz, J. D. *Chem. Mater.* **1994**, *6*, 1118-1127.

(45) Perlstein, J. *J. Am. Chem. Soc.* **1994**, *116*, 11420-11432.

(46) Kitajgorodskij, A. I. *Acta Cryst.* **1965**, *18*, 585-590.

(47) Ostmark, H.; Wallin, S.; Ang, H. G. *Propellants, Explos., Pyrotech.* **2012**, *37*, 12-23.

(48) Damour, P. L.; Freedman, A.; Wormhoudt, J. *Propellants, Explos., Pyrotech.* **2010**, *35*, 514-520.

(49) Bellamy, A. J. *J. Forensic Sci.* **1999**, *44*, 603-608.

(50) Zhang, C. Y.; Wang, X. C.; Huang, H. *J. Am. Chem. Soc.* **2008**, *130*, 8359-8365.

(51) Zhang, C. Y. *J. Phys. Chem. A* **2006**, *110*, 14029-14035.

(52) Du, S.; Wang, Y.; Chen, L. Z.; Shi, W. J.; Ren, F. D.; Li, Y. X.; Wang, J. L.; Cao, D. L. *J. Mol. Model.* **2012**, *18*, 2105-2115.

(53) McNesby, K. L.; Coffey, C. S. *J. Phys. Chem. B* **1997**, *101*, 3097-3104.

(54) Mathieu, D. *J. Phys. Chem. A* **2012**, *116*, 1794-1800.

(55) Tan, B. S.; Long, X. P.; Peng, R. F.; Li, H. B.; Jin, B.; Chu, S. J.; Dong, H. S. *J. Hazard. Mater.* **2010**, *183*, 908-912.

(56) Owens, F. J.; Jayasuriya, K.; Abrahmsen, L.; Politzer, P. *Chem. Phys. Lett.* **1985**, *116*, 434-438.

(57) Li, J. S. *J. Hazard. Mater.* **2010**, *174*, 728-733.

(58) Kamlet, M. J.; Adolph, H. G. *Propellants Explos.* **1979**, *4*, 30-34.

(59) Wang, Q.; Ma, H. X.; Li, J. Z.; Wei, H. J.; Fan, X. Z. *Acta Chim. Sin.* **2012**, *70*, 629-634.

(60) Liu, Y.; Wang, L. J.; Wang, G. X.; Du, H. C.; Gong, X. D. *J. Mol. Model.* **2012**, *18*, 1561-1572.

(61) Rice, B. M.; Hare, J. J. *J. Phys. Chem. A* **2002**, *106*, 1770-1783.

(62) Pospísil, M.; Vávra, P.; Concha, M. C.; Murray, J. S.; Politzer, P. *J. Mol. Model.* **2010**, *16*, 895-901.

(63) Matyáš, R.; Pachman, J. *Propellants, Explos., Pyrotech.* **2010**, *35*, 31-37.

(64) Peña, Á. J.; Pacheco-Londoño, L.; Figueroa, J.; Rivera-Montalvo, L. A.; Román-Velazquez, F. R.; Hernández-Rivera, S. P. In *Sensors, and Command, Control, Communications, and Intelligence*; Carapezza, E. M., Ed.; Spie-Int Soc Optical Engineering: Bellingham, 2005; Vol. 5778, p 347-358.

(65) Hill, M. E.; Taylor, F. *J. Org. Chem.* **1960**, *25*, 1037-1038.

(66) Schoberl, U.; Magnera, T. F.; Harrison, R. M.; Fleischer, F.; Pflug, J. L.; Schwab, P. F. H.; Meng, X. S.; Lipiak, D.; Noll, B. C.; Allured, V. S.; Rudalevige, T.; Lee, S.; Michl, J. *J. Am. Chem. Soc.* **1997**, *119*, 3907-3917.

(67) Altomare, A.; Cascarano, G.; Giacovazzo, C.; Guagliardi, A. *J. Appl. Crystallogr.* **1994**, *27*, 1045-1050.

(68) Burla, M. C.; Caliandro, R.; Camalli, M.; Carrozzini, B.; Cascarano, G. L.; De Caro, L.; Giacovazzo, C.; Polidori, G.; Spagna, R. *J. Appl. Crystallogr.* **2005**, *38*, 381-388.

(69) In *Crystal Structure Analysis Package*; 4.0 ed.; Rigaku and Rigaku Americas: 9009 New Trails Dr., The Woodlands, TX 77381 USA, 2000-2007.

(70) Wiedemann, H. G. *Thermochim. Acta* **1972**, *3*, 355-366.

(71) Wolff, S. K.; Grimwood, D. J.; McKinnon, J. J.; Turner, M. J.; Jayatilaka, D.; Spackman, M. A.; 3.0 ed.; University of Western Australia: 2012.

Chapter 5 Conclusions and Future Directions

5.1 Summary of Work on Cocrystallization of Energetic Materials

Cocrystallization strategies for both aromatic and aliphatic energetic materials were explored through the cocrystallization of model energetic materials, TNT and HMX, with non-energetic materials. This work showed not only that energetic materials can be cocrystallized but also that there are rational guiding principles for cocrystallizing them. In the case of electron-poor aromatic energetic materials, like TNT, the donor-acceptor π-π interaction is robust enough to regularly produce cocrystals with electron rich aromatic materials. While other interactions are possible, this interaction is so comparatively strong that it overpowers weaker interactions. For aliphatic energetic materials, where this strong donor-acceptor π-π interaction is absent, favorable interactions for cocrystallization rely more on complimentary distribution of electrostatic potential for each of the cocrystal formers. Several cocrystals of HMX were found to form, and the structures obtained are dictated by the size and electrostatic potential of the cocrystal former.

In addition to showing favorable interactions for the formation of energetic cocrystals, these model cocrystal systems have clearly demonstrated that materials properties relevant to energetic materials can be favorably altered via cocrystallization. Most notably, changes in density were observed for both aromatic and aliphatic cocrystal systems. For TNT in particular, it was demonstrated that in a few cases densities higher than those of either cocrystal formers could be obtained from the cocrystal. This is key in supporting the idea that cocrystallization offers a means to obtain improved properties for energetic materials with respect to the original components. The study of the TNT cocrystals also demonstrated that the melting point and decomposition temperature can be altered through cocrystallization, while HMX, in contrast, showed that solid energetic cocrystals can separate into their separate components upon heating. In either case these

thermal properties can be leveraged. For TNT, cocrystallization provides a means to alter the melting point for melt-casting as needed. For HMX, since the sensitivity to impact shock can be greatly reduced by cocrystallization with non-energetic materials, this offers a means to transport HMX in an insensitive form and to return it to its full explosive capacity upon heating.

The study of energetic cocrystallization between energetic and non-energetic materials also led to the discovery and formation of novel cocrystals with diacetone diperoxide (DADP). Indeed, the DADP/1,3,5-trichloro-2,4,6-trinitrobenzene (TCTNB) and DADP/1,3,5-tribromo-2,4,6-trinitrobenzene (TBTNB) cocrystals featured a favorable electrostatic interaction between the electron-poor aromatic halogenated trinitrobenzenes and the electron rich peroxide moieties of the DADP that was reminiscent of the donor-acceptor π-π present in the TNT cocrystals with aromatic compounds. In contrast to these two cocrystals, the DADP/1,3,5-triiodo-2,4,6-trinitrobenzene (TITNB) cocrystal exhibited a unique structure and featured an extremely short I···O interaction between TITNB and the peroxides of DADP. All of these cocrystals showed halogen-nitro interactions, which are the first of such ever reported for an energetic cocrystal

Study of the DADP cocrystals also led to some surprising results that have implications for not only the development of energetic cocrystals, but also for the field of cocrystallization as a whole. First, despite the significant change in structure and interactions afforded through cocrystallization, the DADP cocrystals exhibited the same impact sensitivity as pure DADP. This result is in contrast with all previous energetic cocrystals and suggests that the peroxide moiety is inherently unstable. Considering the difference in the sensitivity results together with the alterations and structure for each of the energetic cocrystals, cocrystallization is shown to as a means to experimentally probe the source of sensitivity in an energetic material. A second result that holds particular relevance for the field of cocrystal design and cocrystallization in general is the discovery of a kinetic cocrystal: DADP/TBTNB. The existence of this kinetic cocrystal suggests that many more kinetic cocrystals could exist that have yet to be discovered. Due to the widespread use of crystallization techniques that favor thermodynamic forms, however, kinetic cocrystals could easily be missed during screening. This result demands that

cocrystal screening methods be carefully reevaluated to ensure that kinetic cocrystals are not missed.

5.2 Current Work in the Field of Cocrystallization of Energetic Materials

While energetic cocrystals were reported prior to this work, the concept of energetic cocrystallization had seen little advancement. The work presented in this thesis, and in particular the TNT and HMX cocrystals, has aroused interest in this field again. Following the publication of the work on TNT, many recent examples of energetic cocrystals, not only with non-energetic materials but also with energetic materials have been published.[1-7] The examples presented here represent the beginning and this field will surely continue to develop.

Very recently, work to show basic cocrystallization principles for CL-20 with non-energetic materials was reported by Millar et al.[3] The structures of four CL-20 cocrystals with *N*,*N*-dimethylformamide (DMF), 1,4-dioxane, hexamethylphosphoramide (HMPA) and γ-butyrolactone were studied.[8] They compared the conformation of CL-20 found in each of the cocrystals and noted that in all but the HMPA cocrystal CL-20 adopted the γ conformation. Upon desolvating the CL-20/HMPA cocrystal they obtained the β-CL-20 polymorph, the conformation of which was observed in the cocrystal. From this perspective, cocrystallization was shown to provide a novel means to access polymorphs of CL-20 selectively. Finally, the authors noted that cocrystallization of CL-20 with non-energetic materials generally decreased the density and thus explosive performance of these materials.

Studies of the underlying principles for cocrystallization of energetic materials with non-energetic materials have recently led to the discovery of several energetic-energetic cocrystals. In these cocrystals, the principles developed for cocrystallization with non-energetic materials are shown to be relevant, supporting the idea that the model systems can guide the search for novel energetic-energetic cocrystals. Indeed, energetic-energetic cocrystals that incorporated TNT, CL-20 or HMX were among the first discovered. Furthermore, the large number of cocrystals that can be formed with non-energetic materials allows for trends in cocrystal formation to be developed, in particular

for the case of TNT and HMX cocrystals. Understanding these trends gives insight into novel energetic-energetic cocrystals that would not be possible without the energetic-non-energetic cocrystal series presented in this work.

Following not long after our report of the TNT cocrystals with non-energetic materials, the first energetic-energetic cocrystal was discovered: 2,4,6,8,10,12-hexanitro-2,4,6,8,10,12-hexaazaisowurtzitane (CL-20)/TNT 1:1.[1] This energetic/energetic cocrystal displayed many interactions similar to those in the model TNT cocrystals.[9] TNT formed layers between CL-20. This cocrystal exhibited a density between both cocrystal formers as is often the case for energetic cocrystals. The sensitivity of this material was also in between that of both TNT and CL-20, indicating the chance for cocrystallization to reduce the sensitivity of materials like CL-20, while still maintaining explosive properties. Unlike the non-energetic cocrystals with TNT, however, this cocrystal separated upon heating so that TNT entered a molten state while solid CL-20 remained. Therefore this cocrystal can be used as a smart material: it can be transported or used in its relatively less sensitive form and then heated to remove the TNT and regain the high sensitivity of CL-20.

Not long after the report of the HMX cocrystals with non-energetic materials a CL-20/HMX 2:1 cocrystal was also reported.[4] This cocrystal forms with HMX in the *chair/layered* motif as suggested by the earlier work with HMX cocrystallization. Indeed based on this motif, the conformation of HMX and the resulting crystal structure are more understandable. As HMX is denser and has a better oxygen balance, this cocrystal has even more favorable properties than the CL-20/TNT cocrystal. Furthermore, this material actually showed better sensitivity than just an average of the two pure components. The alteration in interactions may allow for this reduction in sensitivity. This change in the interactions present was only accessible through cocrystallization, clearly demonstrating the advantage of cocrystallization in producing superior energetic materials.

Very recently a TNT/TNB cocrystal was reported.[6] In contrast to cocrystals of TNT with electron-rich aromatic rings, this cocrystal shows zigzag structures formed through interactions between the nitro group of TNT and the benzene ring of TNB. More importantly, the authors demonstrated that the impact sensitivity of this material was

improved with respect to both TNT and TNB. It should be noted that the flash point is lower for this cocrystal than for either TNT or TNB and the authors hypothesize that this is due to a lower lattice energy. This work represents one among many recent and growing efforts aiming for the cocrystallization of energetic materials.

Cocrystals of newer energetic materials are also being discovered. There have recently been two reports of cocrystals with benzotrifuroxane (BTF), a relatively new energetic material. These include the report of a CL-20/BTF cocrystal[5] and a series of five energetic-energetic cocrystals with BTF.[7] Additionally, in work by Thottempudi et al., a cocrystal of 5,50-bis(trinitromethyl)-3,30-azo-1H-1,2,4-triazole with 3,5-diamino-1,2,4-triazole was found as part of a larger work on synthesizing novel energetic materials and forming salts from these materials.[2] They found that this cocrystal was less impact sensitive than the azo compound alone. This work demonstrates the surfeit of potential cocrystal formers that are available in newly synthesized energetic materials; a potential for cocrystal discovery that is only beginning to be realized. As more energetic materials are considered as cocrystal formers, more model systems will be needed to assist in understanding these materials.

5.3 Future Work for the Cocrystallization of Energetic Materials

The study of energetic cocrystallization is only just beginning. Many of the energetic-energetic cocrystals described above were only reported within the last half year and more are likely to follow shortly. It seems very likely that this field will continue to grow and expand as better understanding of the guiding principles for cocrystallizing this unique class of materials is gained. While this work focused on well-known and traditional energetic materials, the list of energetic materials in-development for use in their pure form that were cast away due to failure to perform in one or more critical parameters is vast. Through cocrystallization there is great potential to resurrect many of these discarded materials. Therefore it seems likely that this field will continue to see tremendous growth.

Nitrogen-rich heterocyclic energetic materials are a relatively new class of energetic materials and represent a significant effort by the energetic community to

produce greener energetic materials.[10-13] While traditional energetic material synthesis focused on nitrating various compounds, it was discovered that nitrogen rich heterocycles could serve as effective energetic materials. Due to the presence of nitrogen, less carbon was used and more nitrogen gas could be produced which is favorable for improving explosive or propulsive power. While some of these materials have shown remarkable stability, others have proven to be excessively sensitive and dangerous.[12,13] Additionally, these materials have some differences from the electron-poor aromatic rings of energetics like TNT and often have potential hydrogen bonding moieties in abundance. Therefore, cocrystallization of prototype nitrogen rich energetic materials should also be performed, to provide cocrystal engineering principles for these materials.

Furthermore, many of the energetic cocrystals, while sometimes improving the oxygen balance, often only improved it minimally due to the limitation of acceptable high-oxygen cocrystal formers. Therefore, energetic-energetic cocrystals, or even energetic-non-energetic cocrystals that incorporate high-oxygen compounds are expected to greatly improve the performance and also reduce the toxicity of the byproducts produced. Examples of oxygen rich, potential cocrystal formers include tetranitromethane (TNM) and hexanitroethane (HNE) (Figure 5.1). Due to the high density of nitro functional groups in these compounds and many of the high-oxygen cocrystal formers, it seems likely that cocrystals with these materials will only form if cocrystal formers can interact well with the nitro group. While some favorable nitro interactions for energetic materials were reported in this thesis, knowledge of even more favorable intermolecular interactions for nitro functional groups will allow for the cocrystallization of these materials.

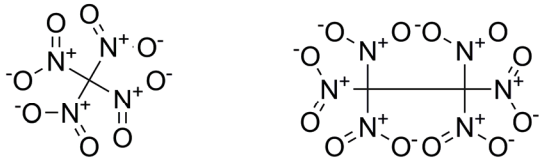

tetranitromethane (TNM) hexanitroethane (HNE)

Figure 5.1 Oxygen rich, potential cocrystal formers include TNM and HNE.

Finally, the cocrystals of DADP reported in Chapter 4 revealed two further areas for study. First, the existence of DADP/TBTNB as a kinetic cocrystal at room

temperature demands that potential cocrystal combinations be reexamined as potential cocrystal forms may have been missed due to a lack of cocrystallization methods that favor kinetic forms. This need applies to not only energetic cocrystals, but cocrystals in general. Secondly, the retention of sensitivity of DADP despite cocrystallization offers the intriguing possibility of using cocrystallization to produce more powerful primary explosives that retain their sensitivity. While energetic-energetic cocrystals are still limited in number, broad generalizations cannot be made, but energetic materials containing peroxide moieties may provide a means to retain sensitivity while increasing power. Energetic materials that contain only nitro functional groups may offer a means to reduce sensitivity without a significant loss in power. To confirm this, more peroxide containing energetic-energetic cocrystals need to be considered.

These are but a few of the unexplored areas in energetic cocrystallization. In addition to the commonly employed energetic materials, there is a seemingly limitless supply of energetic materials that could be screened for energetic cocrystal formation. While study of energetic cocrystals is still in its early stages, it seems certain that study of these materials will continue throughout the world. Due to the advantages of energetic cocrystallization, it is only a matter of time before widespread use of these materials becomes realized.

5.4 References

(1) Bolton, O.; Matzger, A. J. *Angew. Chem., Int. Ed.* **2011**, *50*, 8960-8963.

(2) Thottempudi, V.; Shreeve, J. M. *J. Am. Chem. Soc.* **2011**, *133*, 19982-19992.

(3) Millar, D. I. A.; Maynard-Casely, H. E.; Allan, D. R.; Cumming, A. S.; Lennie, A. R.; Mackay, A. J.; Oswald, I. D. H.; Tang, C. C.; Pulham, C. R. *CrystEngComm* **2012**, *14*, 3742-3749.

(4) Bolton, O.; Simke, L. R.; Pagoria, P. F.; Matzger, A. J. *Cryst. Growth Des.* **2012**, *12*, 4311–4314.

(5) Yang, Z.; Li, H.; Zhou, X.; Zhang, C.; Huang, H.; Li, J.; Nie, F. *Cryst. Growth Des.* **2012**, *12*, 5155–5158.

(6) Guo, C. Y.; Zhang, H. B.; Wang, X. C.; Liu, X. F.; Sun, J. *J. Mater. Sci.* **2012**, 1-7.

(7) Zhang, H.; Guo, C.; Wang, X.; Xu, J.; He, X.; Liu, Y.; Liu, X.; Huang, H.; Sun, J. *Cryst. Growth Des.* [Online early access] DOI: 10.1021/cg301353f. Published online: December 13, 2012. http://pubs.acs.org/doi/abs/10.1021/cg301353f. (acessed Jan. 5, 2013).

(8) The CL-20/DMF cocrystal had been previously been structurally elucidated, but this work presented the structure of the other three CL-20 cocrystals for the first time.

(9) Landenberger, K. B.; Matzger, A. J. *Cryst. Growth Des.* **2010**, *10*, 5341-5347.

(10) Talawar, M. B.; Sivabalan, R.; Mukundan, T.; Muthurajan, H.; Sikder, A. K.; Gandhe, B. R.; Rao, A. S. *J. Hazard. Mater.* **2009**, *161*, 589-607.

(11) Steinhauser, G.; Klapötke, T. M. *Angew. Chem., Int. Ed.* **2008**, *47*, 3330-3347.

(12) Singh, R. P.; Ga, H.; Meshri, D. T.; Shreeve, J. M. In *High Energy Density Materials*; Klapötke, T. M., Ed.; Springer-Verlag Berlin: Berlin, 2007; Vol. 125, p 35-83.

(13) Klapötke, T. M. In *High Energy Density Materials*; Klapötke, T. M., Ed.; Springer-Verlag Berlin: Berlin, 2007; Vol. 125, p 85-121.

Appendix 1 Cocrystal Engineering of a Prototype Energetic Material: Supramolecular Chemistry of 2,4,6-Trinitrotoluene Data

A1.1 Raman Spectra of TNT Cocrystals

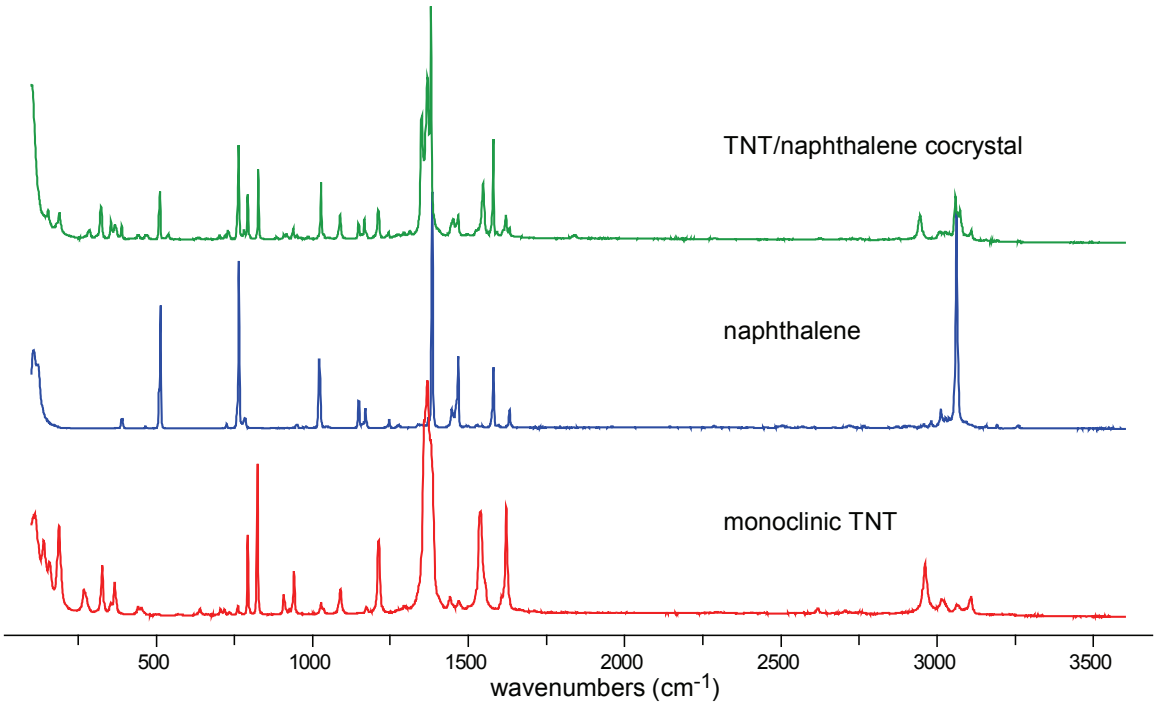

Figure A1.1 Raman spectra of TNT/naphthalene cocrystal, naphthalene and monoclinic TNT

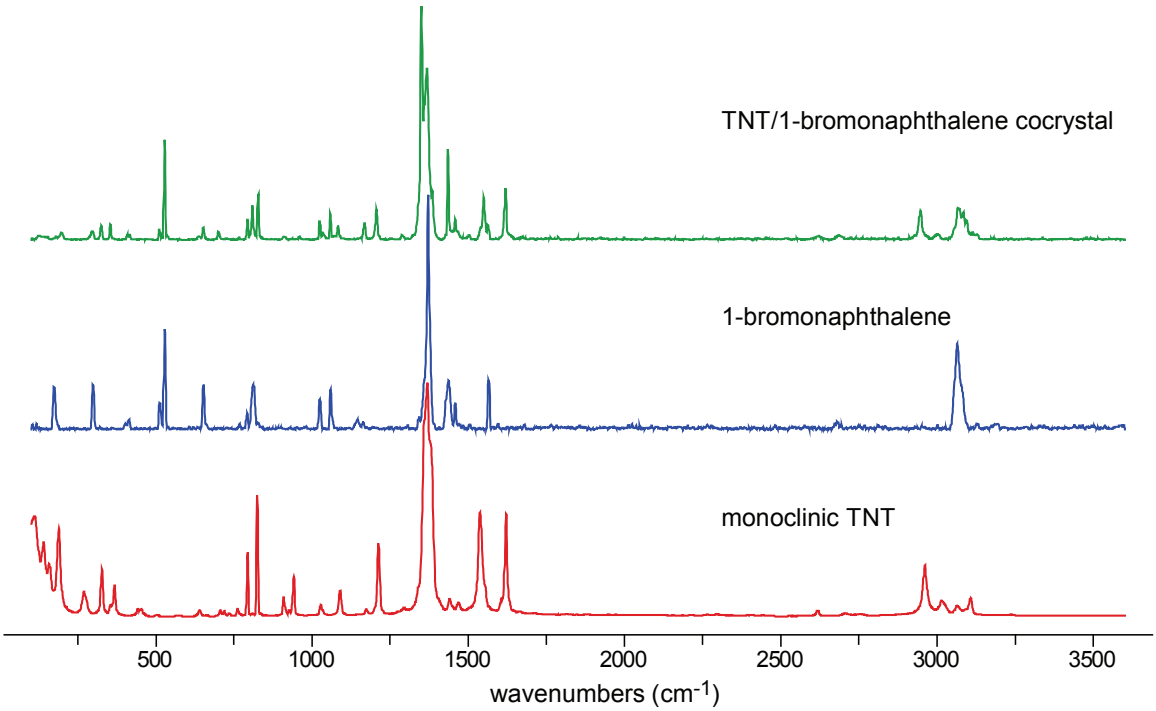

Figure A1.2 Raman spectra of TNT/1-bromonaphthalene cocrystal, 1-bromonaphthalene and monoclinic TNT

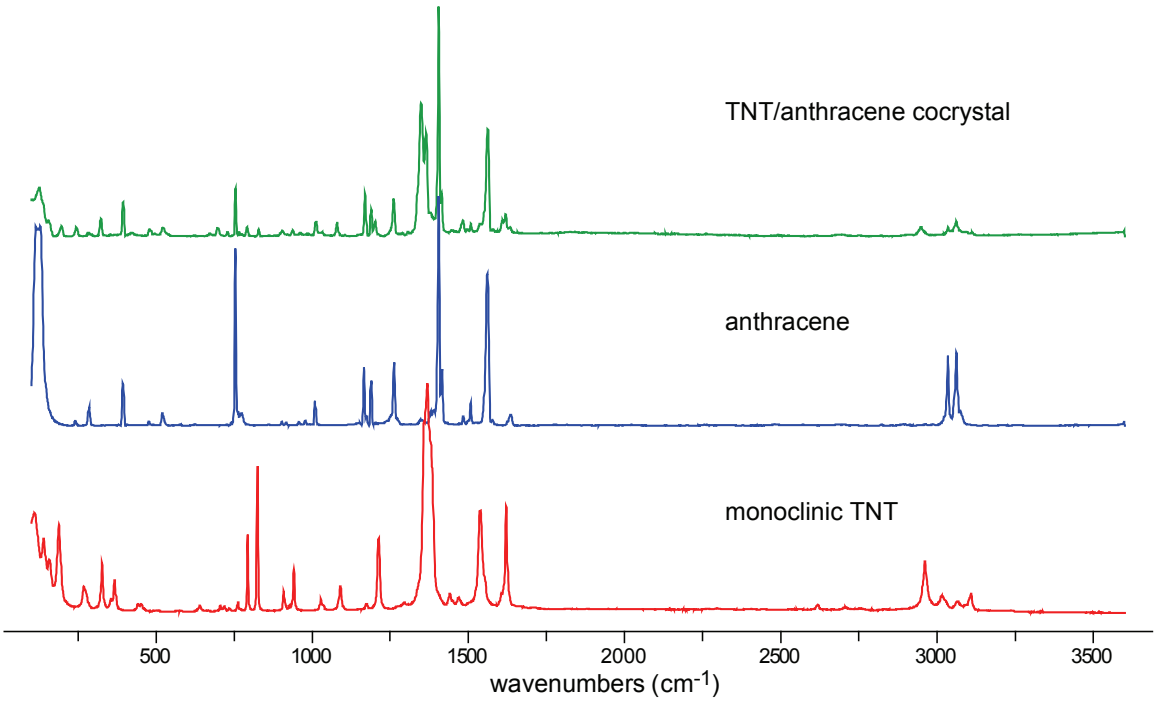

Figure A1.3 Raman spectra of TNT/anthracene cocrystal, anthracene and monoclinic TNT

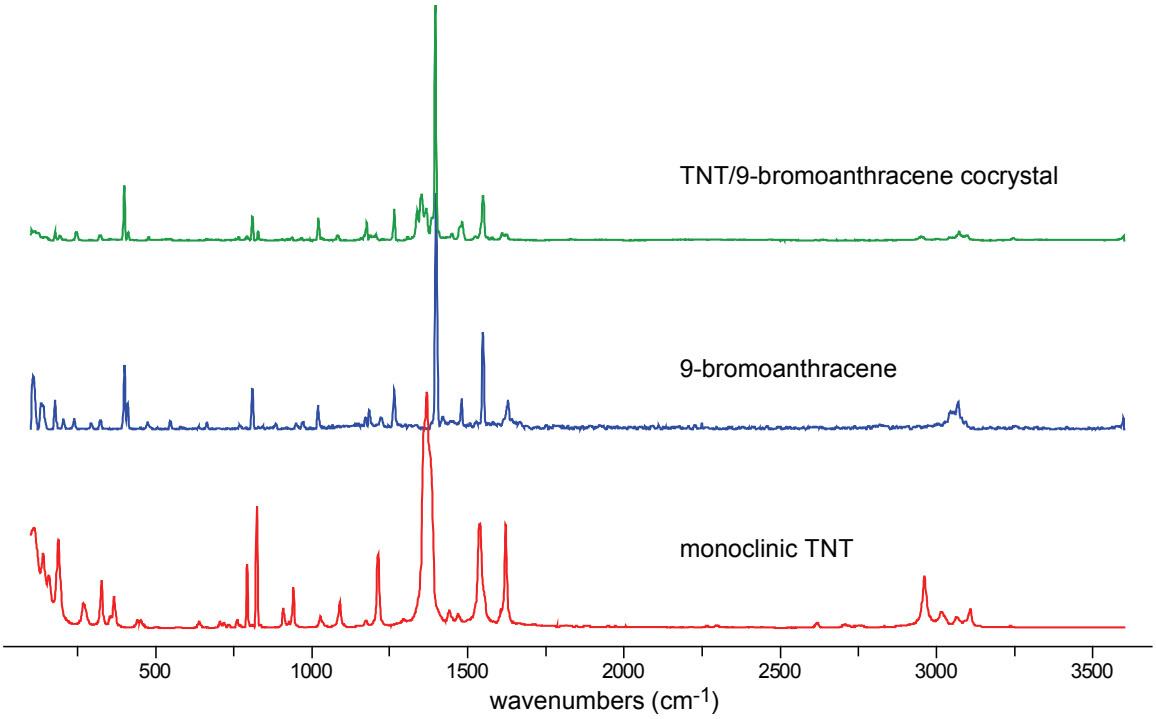

Figure A1.1 Raman spectra of TNT/9-bromoanthracene cocrystal, 9-bromoanthracene and monoclinic TNT

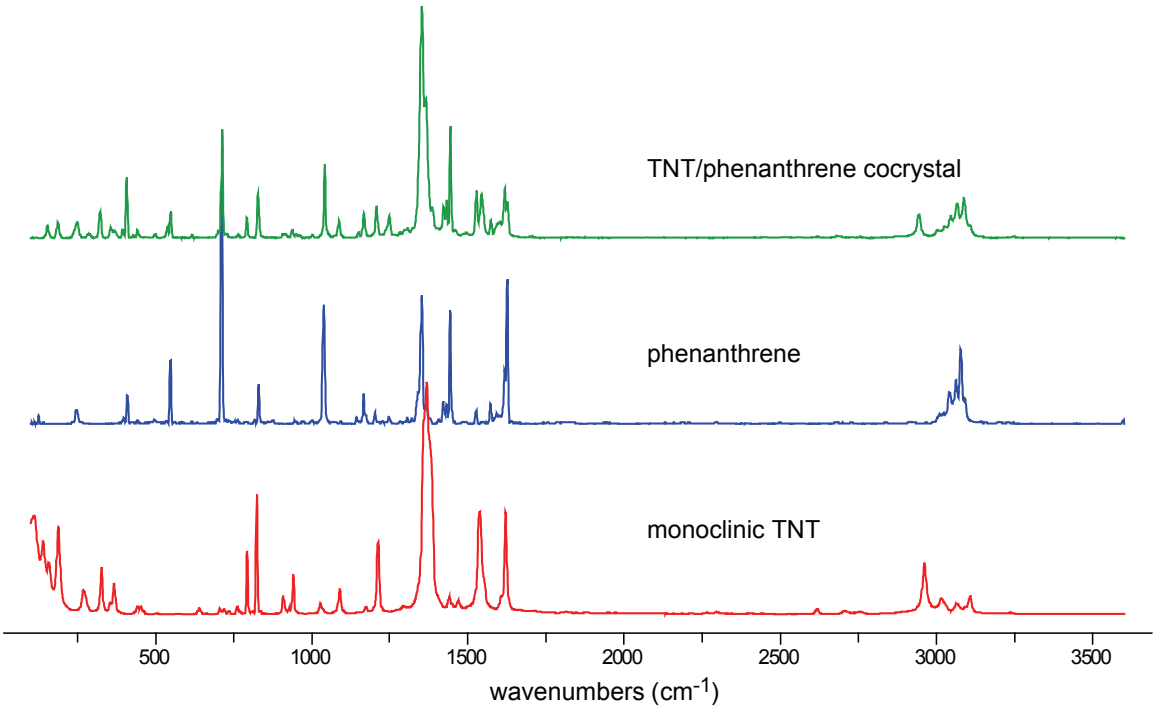

Figure A1.2 Raman spectra of TNT/phenanthrene cocrystal, phenanthrene and monoclinic TNT

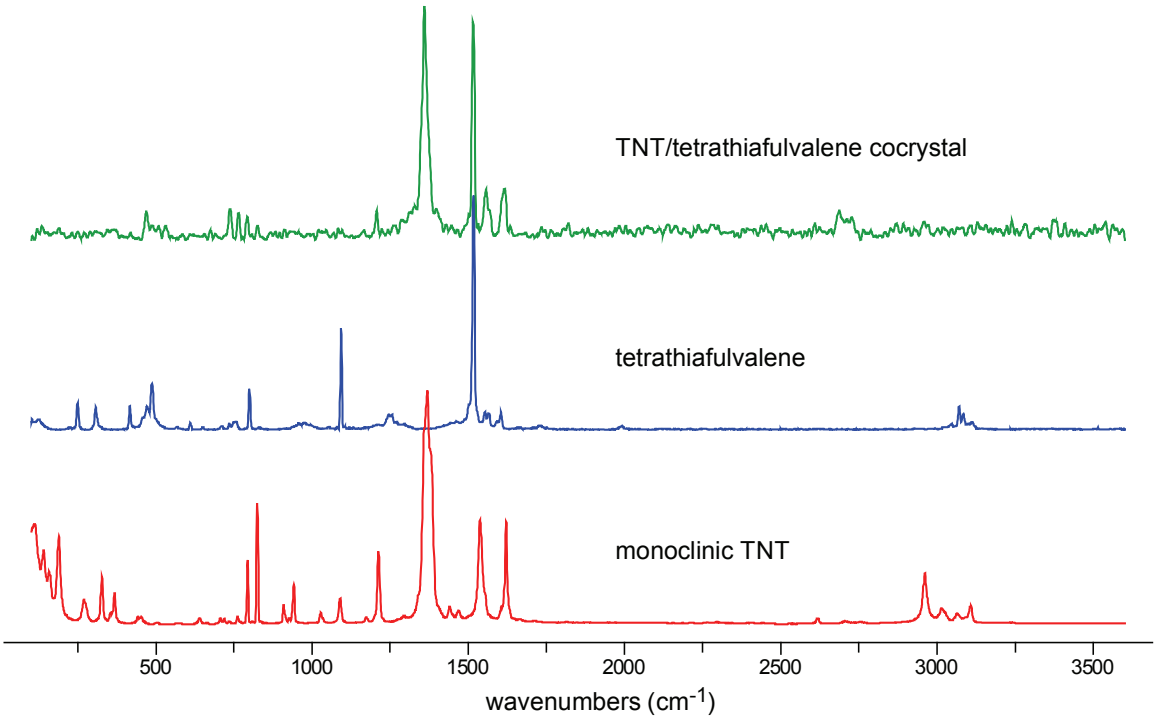

Figure A1.3 Raman spectra of TNT/tetrathiafulvalene cocrystal, tetrathiafulvalene and monoclinic TNT

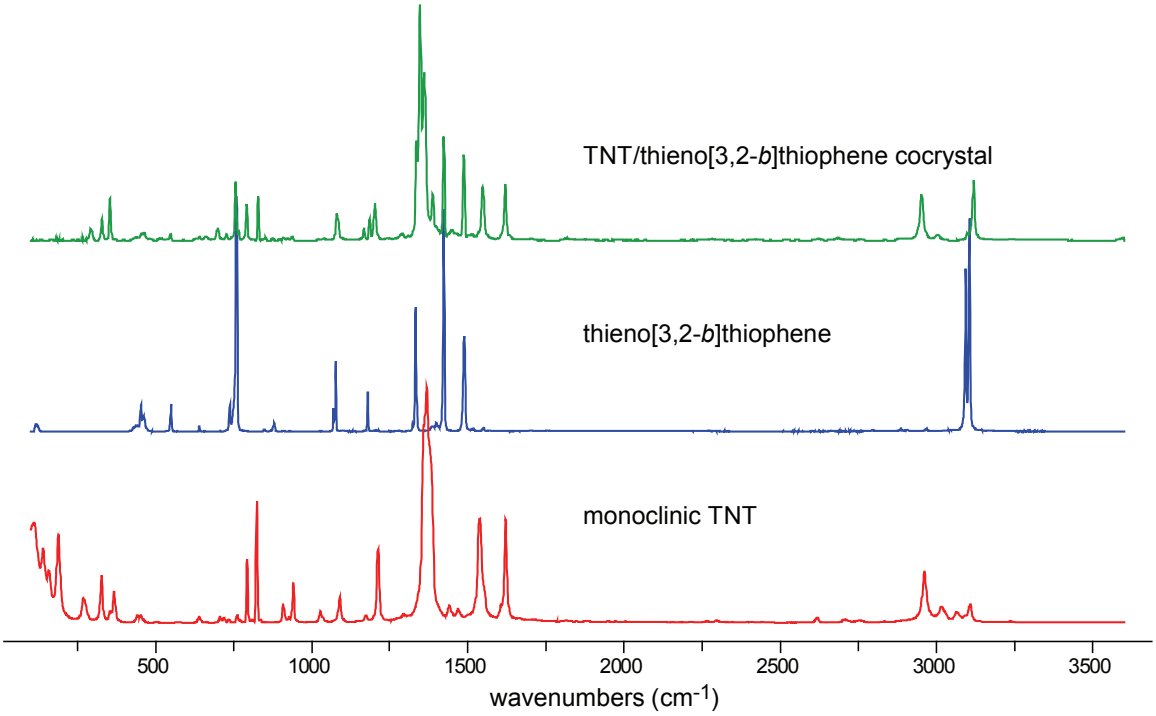

Figure A1.4 Raman spectra of TNT/thieno[3,2-*b*]thiophene cocrystal, thieno[3,2-*b*]thiophene and monoclinic TNT.

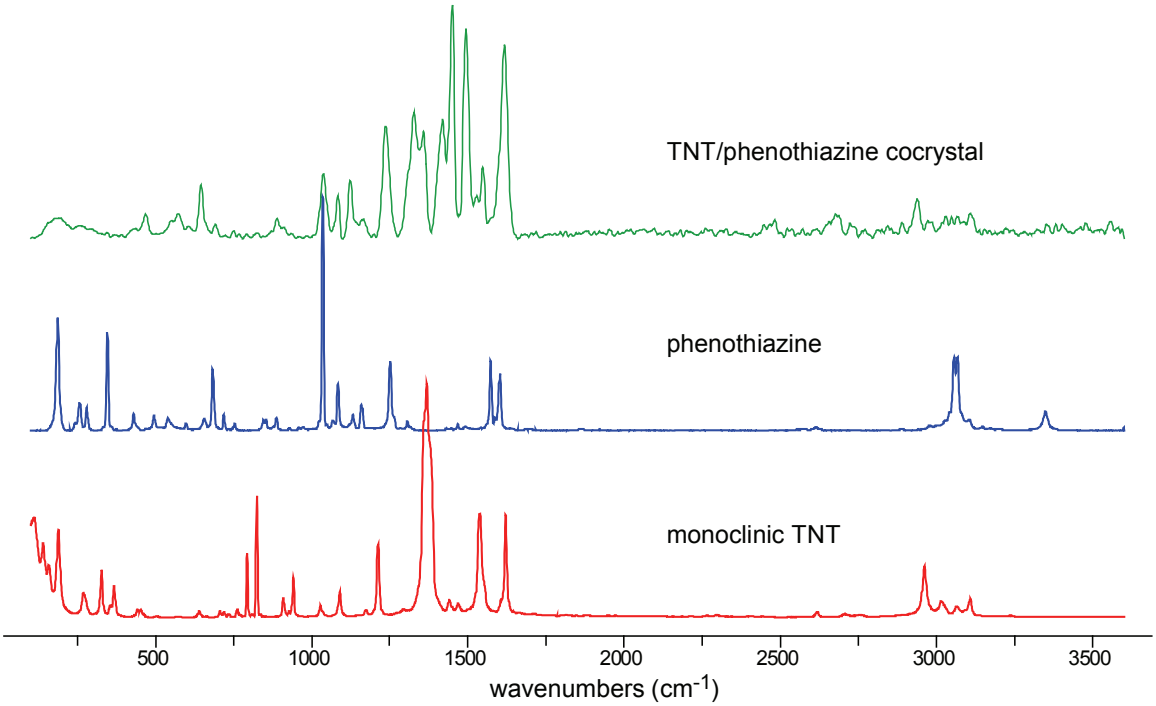

Figure A1.5 Raman spectra of TNT/phenothiazine cocrystal, phenothiazine and monoclinic TNT.

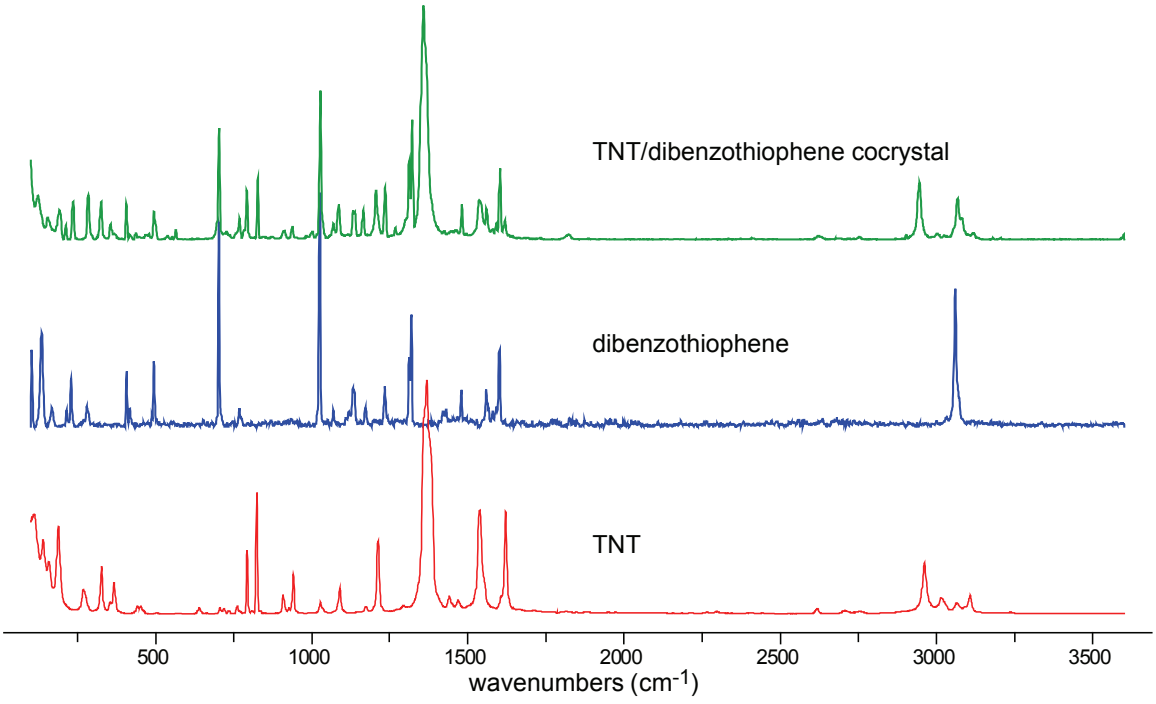

Figure A1.6 Raman spectra of TNT/dibenzothiophene cocrystal, dibenzothiophene and monoclinic TNT.

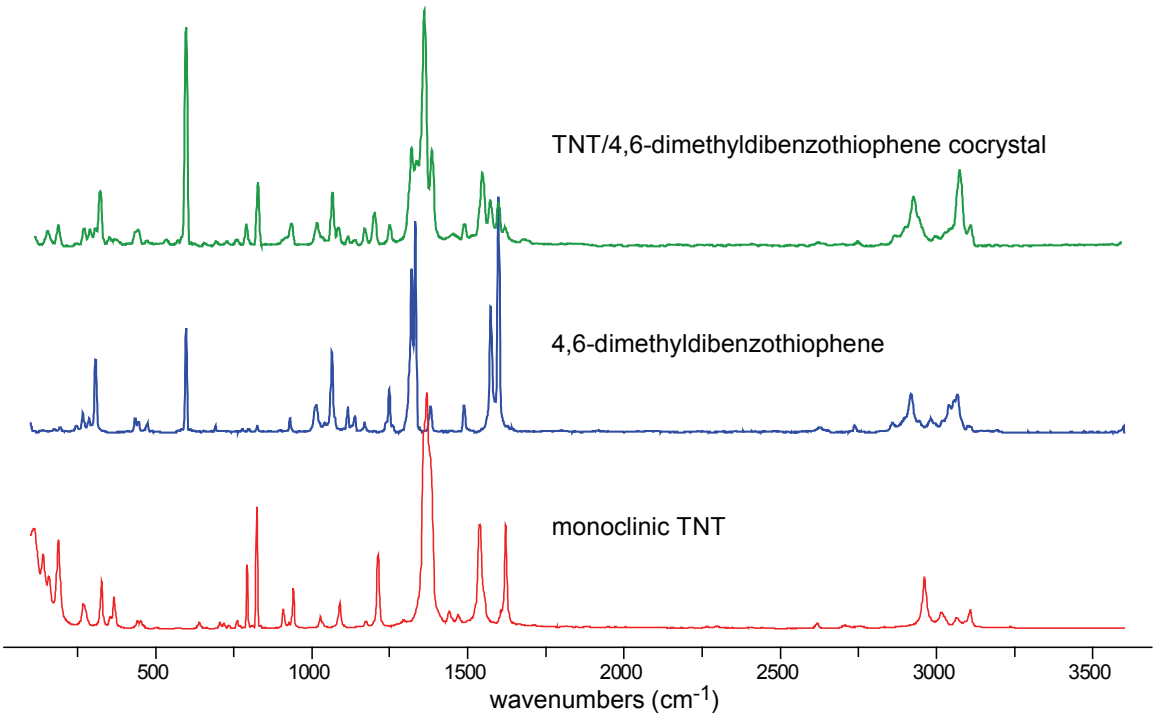

Figure A1.7 Raman spectra of TNT/4,6-dimethyldibenzothiophene cocrystal, 4,6-dimethyldibenzothiophene and monoclinic TNT.

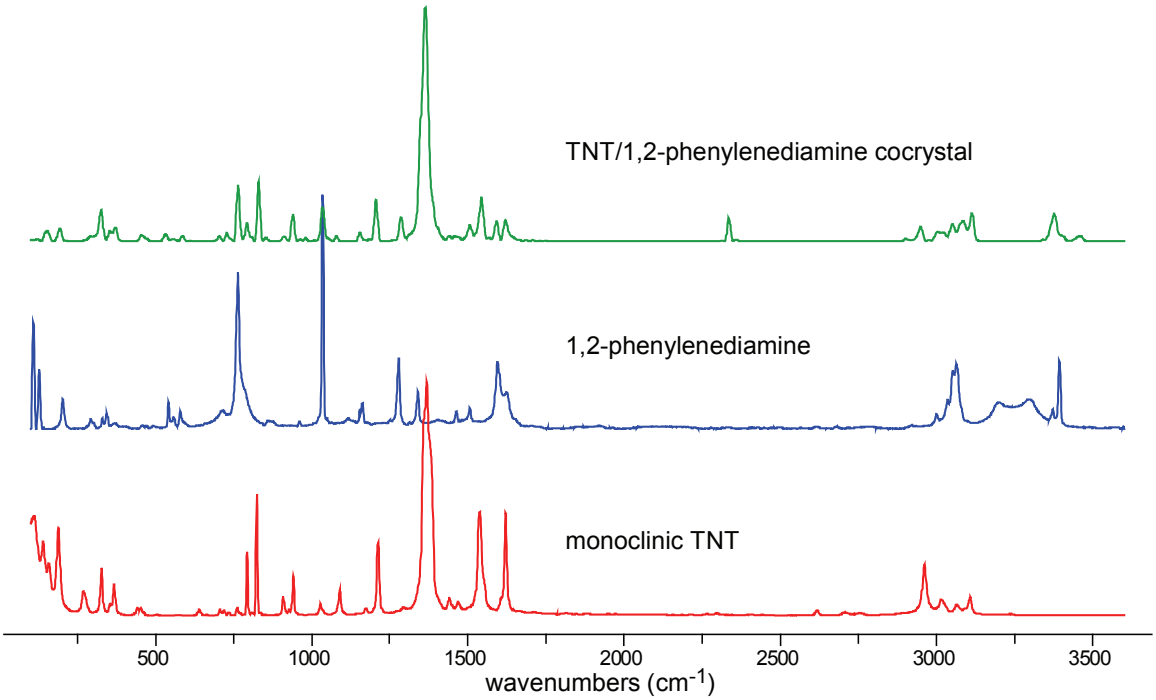

Figure A1.8 Raman spectra of TNT/1,2-phenylenediamine cocrystal, 1,2-phenylenediamine and monoclinic TNT.

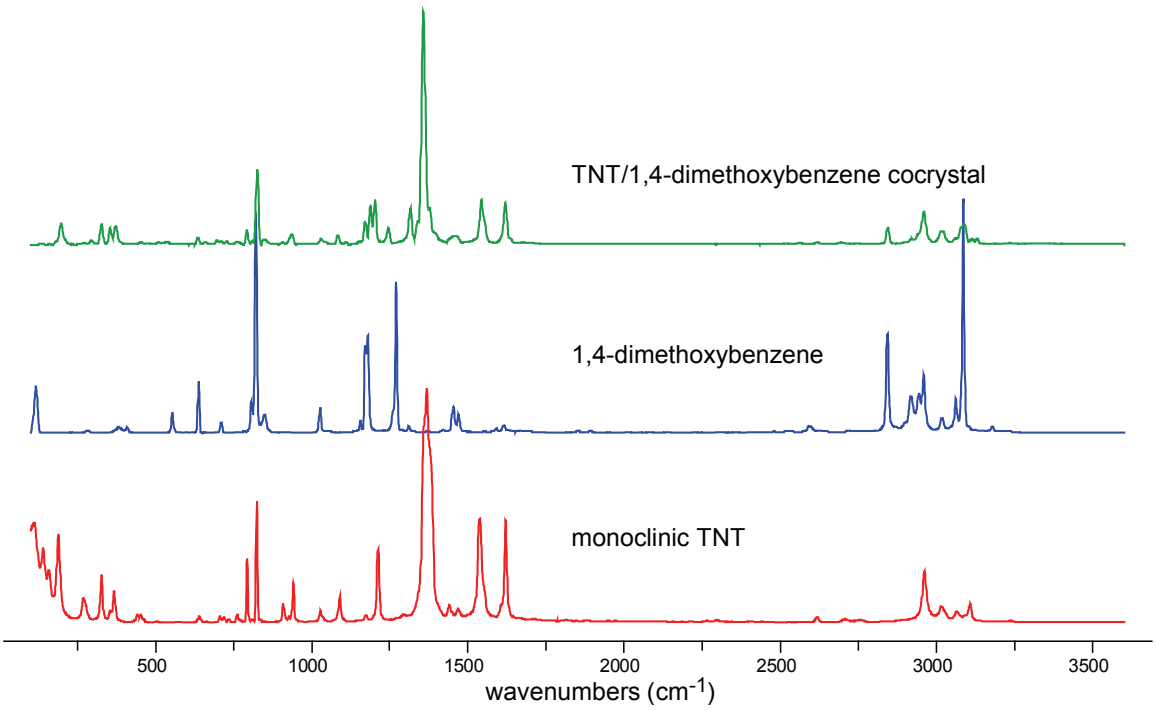

Figure A1.9 Raman spectra of TNT/1,4-dimethoxybenzene cocrystal, 1,4-dimethoxybenzene and monoclinic TNT.

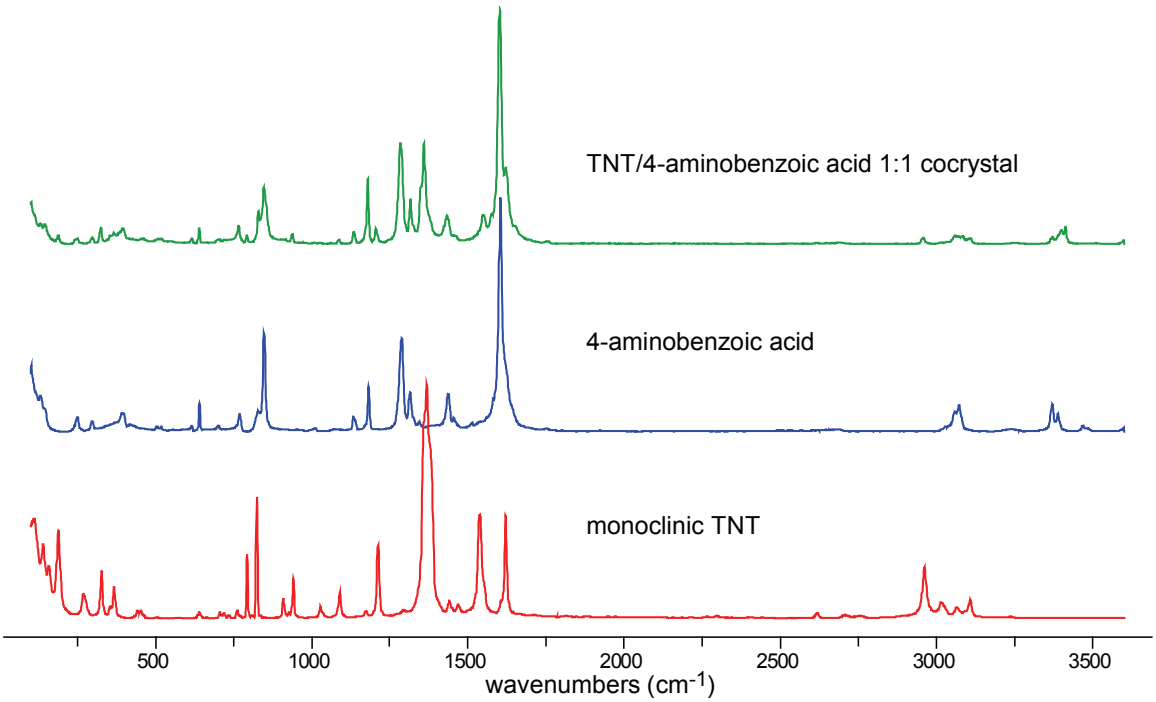

Figure A1.10 Raman spectra of TNT/4-aminobenzoic acid 1:1 cocrystal, 4-aminobenzoic acid and monoclinic TNT.

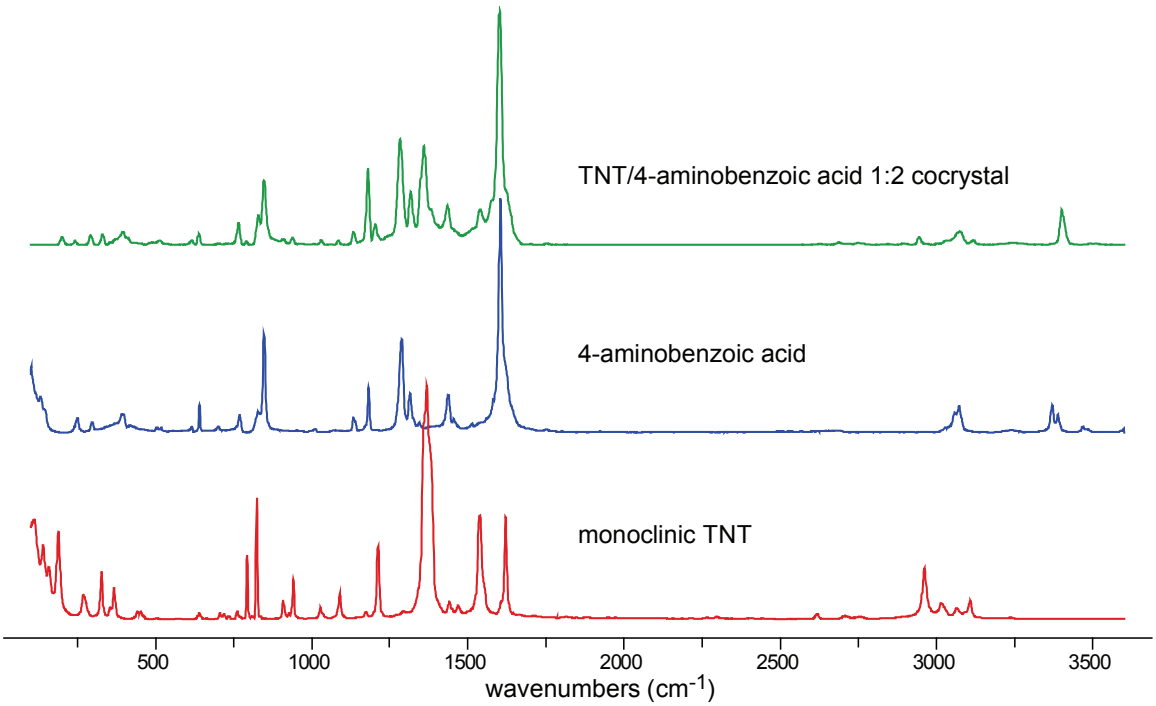

Figure A1.11 Raman spectra of TNT/4-aminobenzoic acid 1:2 cocrystal, 4-aminobenzoic acid and monoclinic TNT.

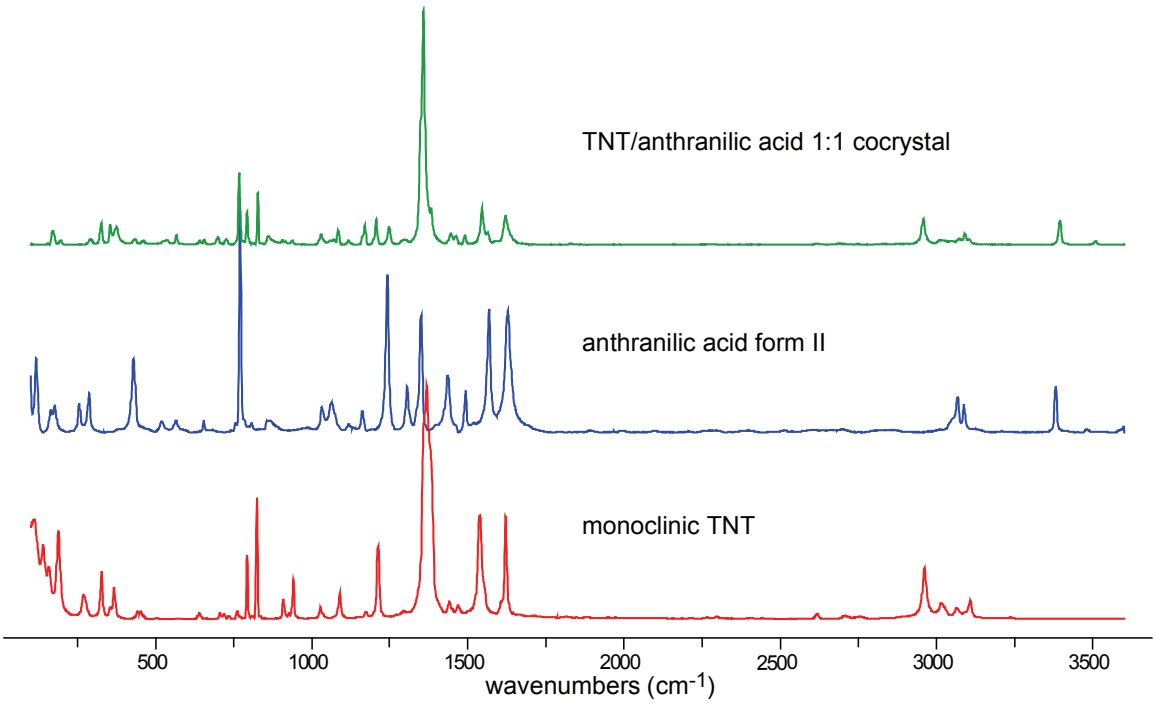

Figure A1.12 Raman spectra of TNT/anthranilic acid 1:1 cocrystal, anthranilic acid form II and monoclinic TNT.

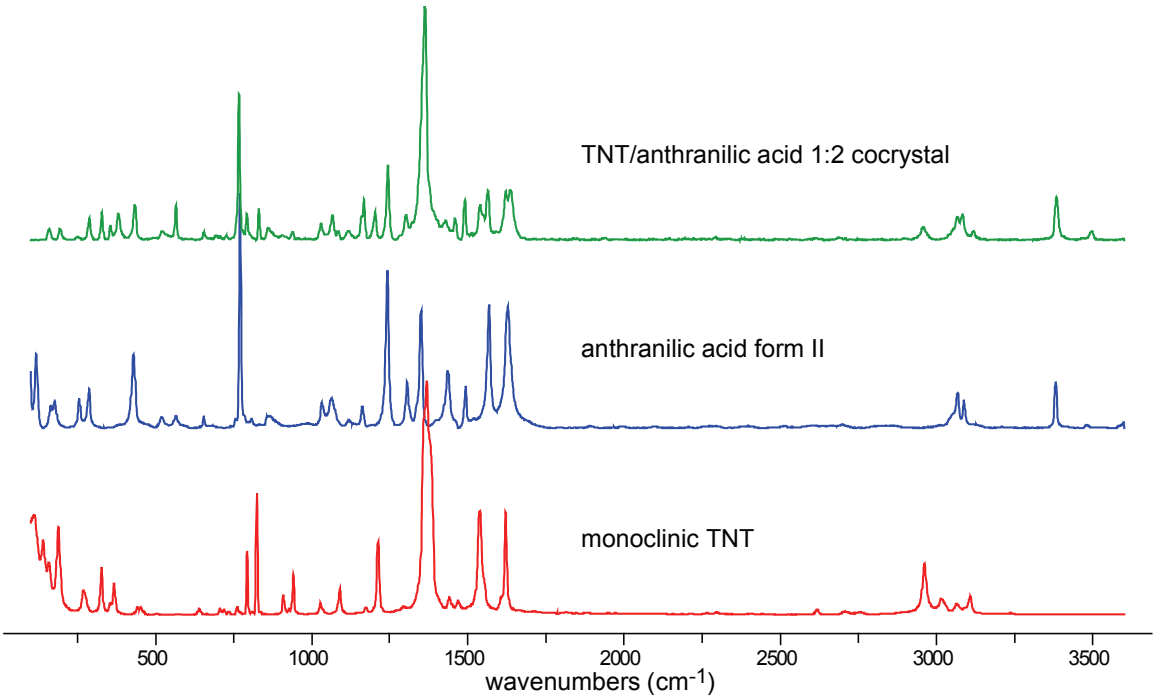

Figure A1.13 Raman spectra of TNT/anthranilic acid 1:2 cocrystal, anthranilic acid form II and monoclinic TNT.

Table A1.1 Frequency of Raman vibrational modes (cm^{-1}) of TNT cocrystals.

1	2	3	4	5	7	8	9	10	11	12	13	14	15	16	17
3108	3114	3112	3245	3245	2959	3598	3557	3117	3108	3460	3129	3598	3401	3508	3495
3073	3084	3093	3097	3088	2727	3118	3477	3066	3074	3377	3113	3412	3118	3395	3383
3058	3067	3062	3072	3066	2687	3098	3352	3001	2997	3113	3089	3369	3075	3090	3118
3008	3003	3034	3043	3045	1616	3003	3107	2945	2927	3085	3015	3108	2945	3073	3082
2945	2946	2948	3003	3026	1556	2951	3029	2751	2866	3051	2959	3058	2750	3048	3066
1840	2682	1634	2952	3003	1516	2758	2972	2621	2748	3023	2920	2956	2688	3011	2957
1631	2624	1619	1622	2944	1360	2685	2938	1822	2621	3004	2843	2690	1752	2957	1636
1620	1619	1579	1610	1626	1263	2621	2844	1618	1678	2948	2692	1753	1602	1830	1564
1579	1564	1561	1578	1618	1207	1815	2676	1602	1619	2900	2618	1602	1539	1620	1538
1547	1550	1508	1548	1603	1083	1703	2481	1591	1597	2335	1620	1549	1435	1563	1490
1497	1503	1483	1481	1574	1021	1620	1617	1560	1572	1620	1543	1433	1360	1545	1459
1467	1458	1449	1449	1528	912	1547	1548	1537	1546	1592	1454	1360	1317	1490	1429
1451	1435	1413	1433	1496	825	1514	1493	1481	1489	1543	1377	1316	1283	1462	1363
1379	1385	1404	1396	1458	793	1487	1449	1461	1453	1506	1357	1285	1203	1445	1302
1369	1367	1365	1366	1444	765	1449	1418	1358	1385	1458	1339	1206	1180	1383	1244
1350	1350	1349	1351	1432	738	1423	1358	1322	1361	1440	1316	1179	1134	1358	1203
1312	1288	1307	1337	1422	675	1388	1327	1312	1336	1364	1246	1135	1085	1291	1167
1293	1206	1261	1307	1386	531	1360	1237	1268	1320	1286	1202	1086	1031	1248	1119
1275	1167	1201	1263	1365	509	1347	1165	1235	1250	1206	1188	938	939	1207	1085
1244	1083	1188	1205	1352	488	1335	1124	1206	1202	1154	1171	847	909	1170	1067
1212	1059	1170	1175	1307	469	1290	1084	1165	1170	1079	1153	793	848	1117	1031
1166	1025	1079	1083	1249	419	1244	1037	1133	1139	1035	1109	766	830	1085	939
1088	961	1032	1021	1208	361	1202	889	1086	1116	980	1083	704	791	1030	905
1027	910	1012	968	1167	345	1185	692	1069	1066	962	1030	640	766	937	861
938	827	985	937	1151		1167	645	1027	1017	940	937	616	640	862	831
827	809	961	829	1087		1081	573	1003	935	912	906	458	617	828	793
793	794	937	810	1042		1040	469	938	828	854	826	396	514	793	767
782	701	904	793	1003		937	193	912	791	830	793	367	395	768	727
764	652	829	766	938		922		827	760	793	761	325	330	725	694
730	528	792	478	916		909		793	728	765	728	298	292	700	655
703	511	766	413	828		876		770	694	728	711	249	243	656	566
635	409	755	400	793		852		728	598	705	697	189	201	641	522
512	354	729	323	765		829		704	533	586	660	147		567	434
470	325	698	247	714		792		565	472	533	636			537	381
442	297	672	194	701		766		496	445	456	538			462	329
390	199	522	179	617		756		408	370	371	454			435	288
369		478	113	549		728		357	353	355	373			356	250
356		422		538		699		326	324	326	328			326	194
324		395		500		663		285	308	194	296			291	160
286		324		442		641		236	291	153	198			197	
191		284		408		548		213	272					171	
155		245		357		517		194	189						
		198		323		463		156	155						
				287		355		124							
				250		328									
				188		293									
				154											

Table A1.2 Observed frequencies (cm^{-1}) for the asymmetric and symmetric nitro stretch of TNT in both pure and the TNT cocrystals

TNT/TNT cocrystal	ν_{as} NO_2	ν_s NO_2
monoclinic TNT	1537.4	1367.9
orthorhombic TNT	1535.7	1358.7
naphthalene	1546.5	1349.8
anthracene	1561.2	1348.9
9-bromoanthracene	1548.1	1366.2
phenanthrene	1544.0	1365.4
tetrathiafulvalene	1528.4	1359.7
thieno[3,2-*b*]thiophene	1547.3	1360.5
phenothiazine	1546.5	1358.0
dibenzothiophene	1536.6	1358.0
4,6-dimethyldibenzothiophene	1546.5	1361.3
1,2-phenylenediamine	1543.2	1363.8
1,4-dimethoxybenzene	1543.2	1357.2
4-aminobenzoic acid 1:1	1538.3	1359.7
4-aminobenzoic acid 1:2	1549.8	1358.9
anthranilic acid 1:1	1544.8	1358.0
anthranilic acid 1:2	1537.4	1363.0

A1.2 ORTEP Diagrams for TNT Cocrystals

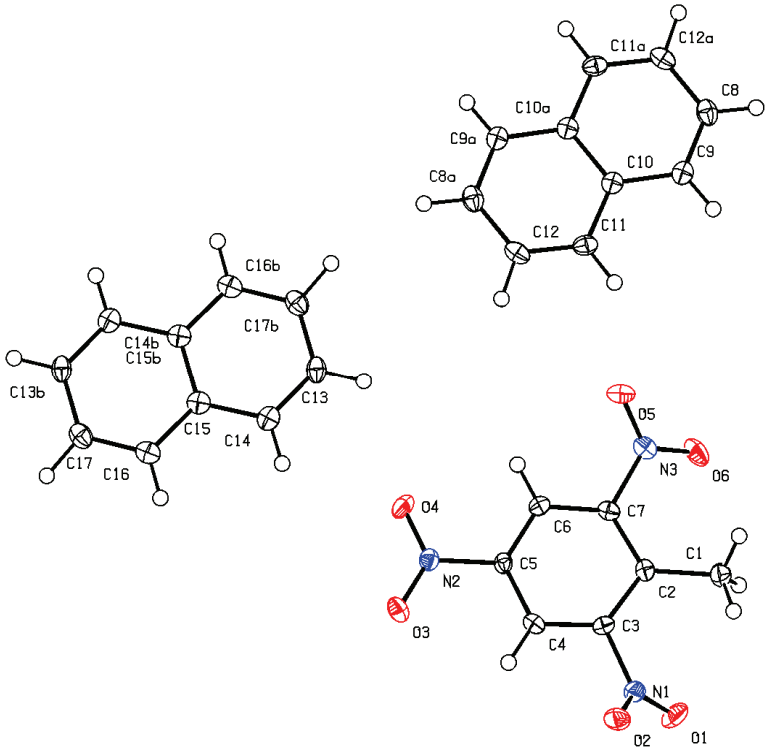

Figure A1.14 ORTEP diagram of TNT/naphthalene cocrystal with thermal ellipsoids of 50% probability.

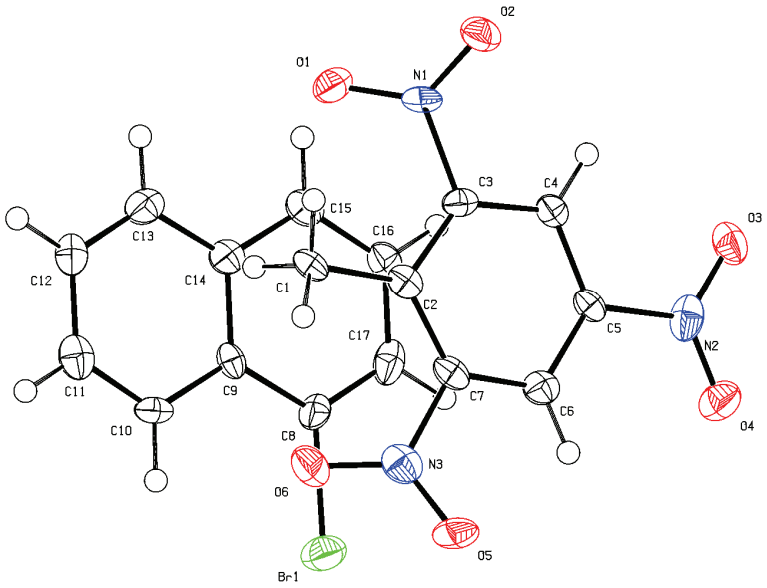

Figure A1.15 ORTEP diagram of TNT/1-bromonaphthalene cocrystal with thermal ellipsoids of 50% probability.

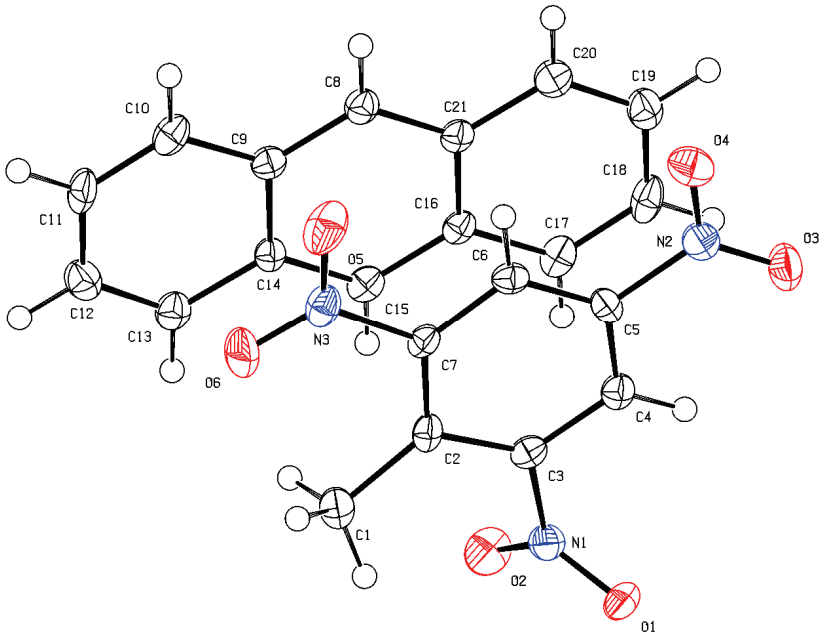

Figure A1.16 ORTEP diagram of TNT/anthracene cocrystal with thermal ellipsoids of 50% probability.

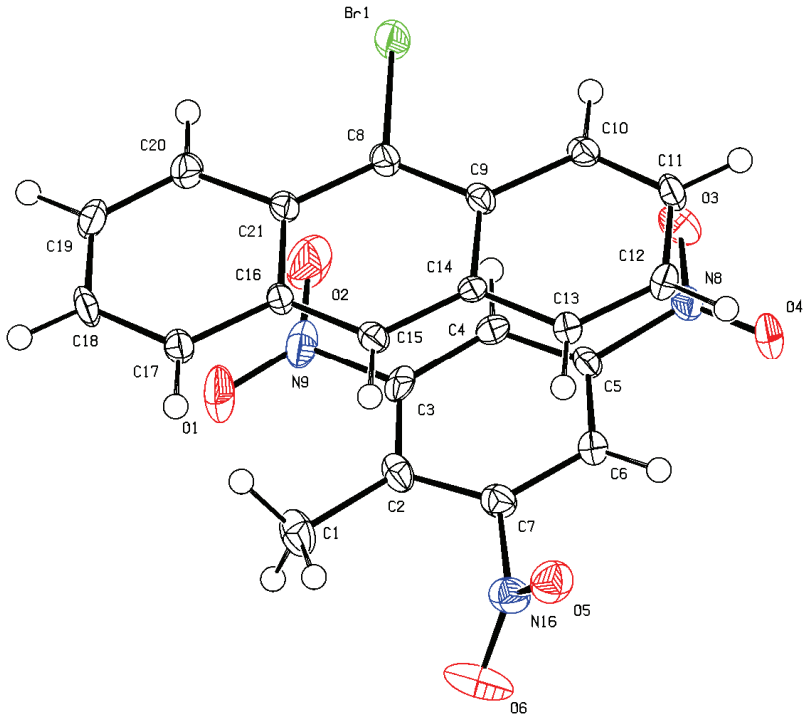

Figure A1.17 ORTEP diagram of TNT/9-bromoanthracene cocrystal with thermal ellipsoids of 50% probability.

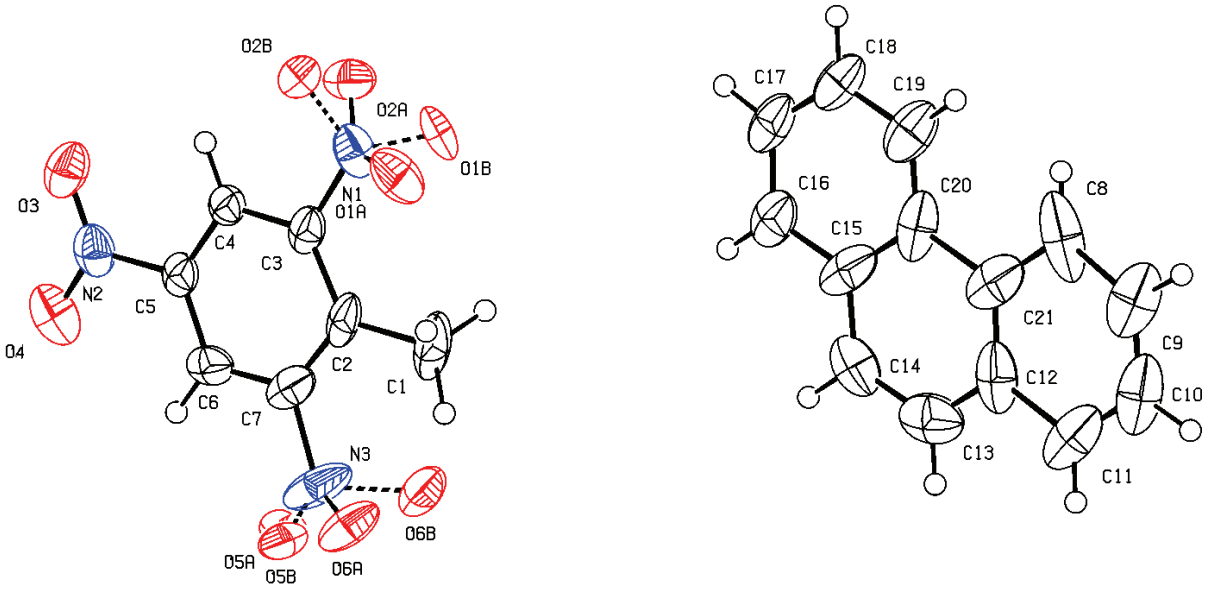

Figure A1.18 ORTEP diagram of TNT/phenanthrene cocrystal with thermal ellipsoids of 50% probability.

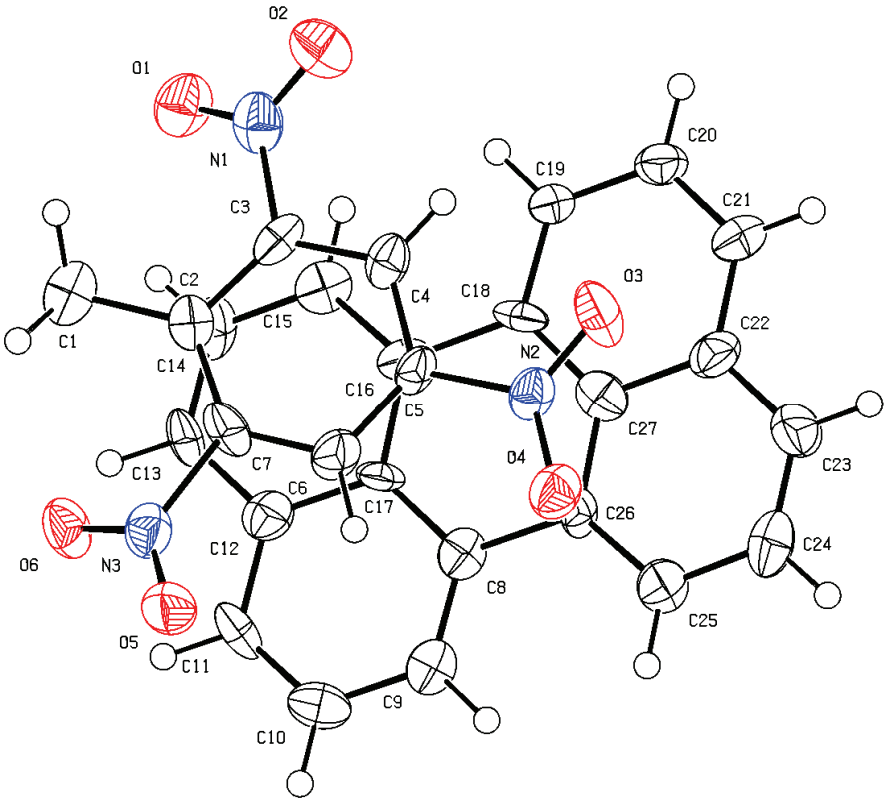

Figure A1.19 ORTEP diagram of TNT/perylene cocrystal with thermal ellipsoids of 50% probability.

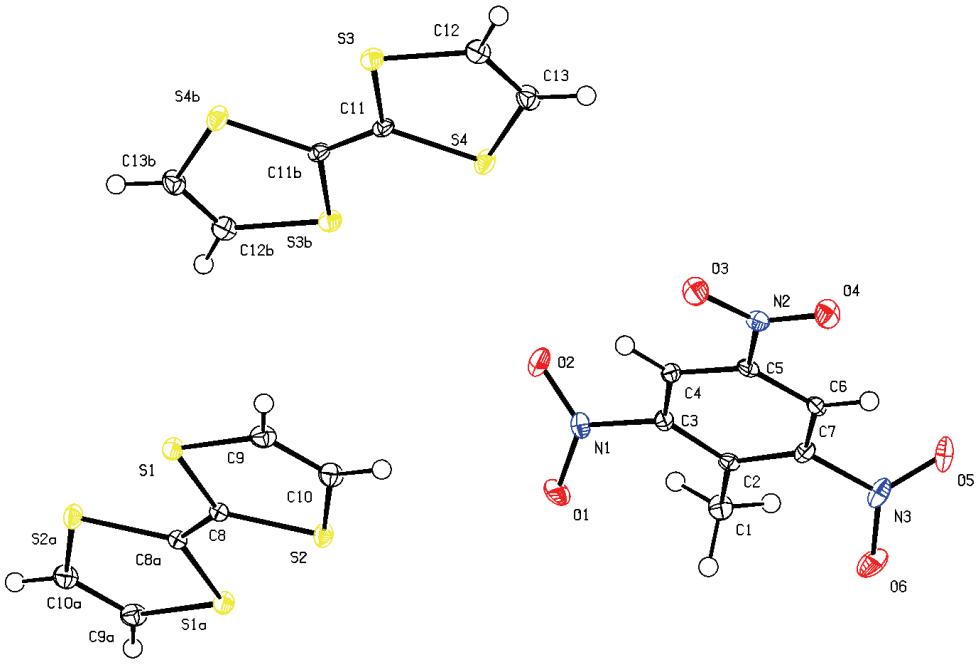

Figure A1.20 ORTEP diagram of TNT/tetrathiafulvalene cocrystal with thermal ellipsoids of 50% probability.

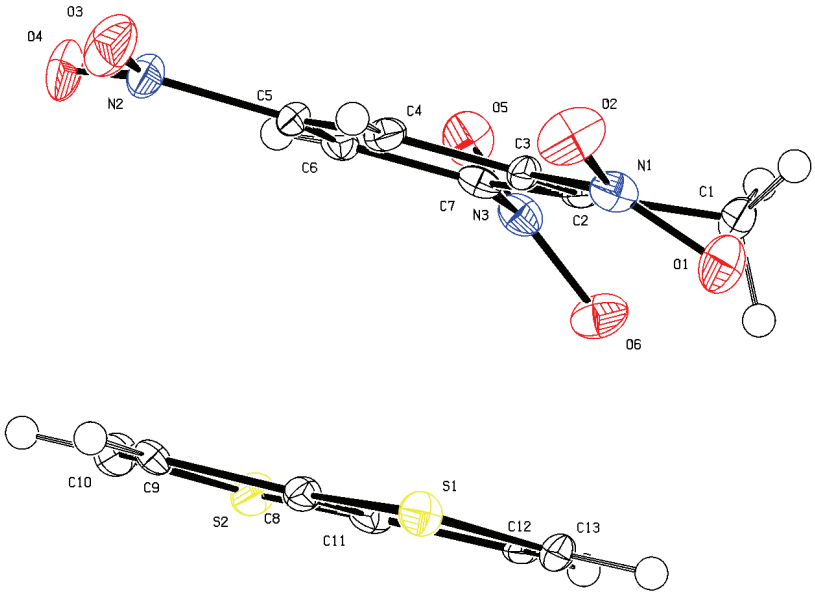

Figure A1.21 ORTEP diagram of TNT/thieno[3,2-*b*]thiophene cocrystal with thermal ellipsoids of 50% probability.

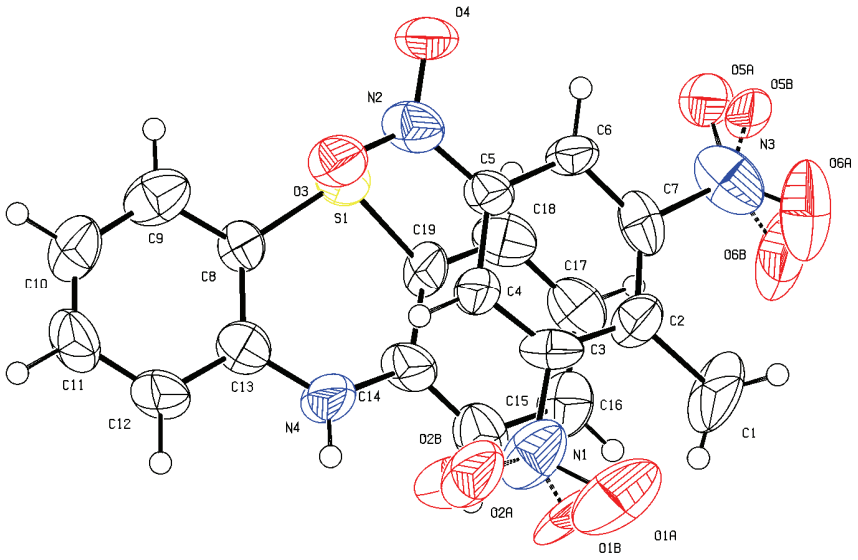

Figure A1.22 ORTEP diagram of TNT/phenothiazine cocrystal with thermal ellipsoids of 50% probability.

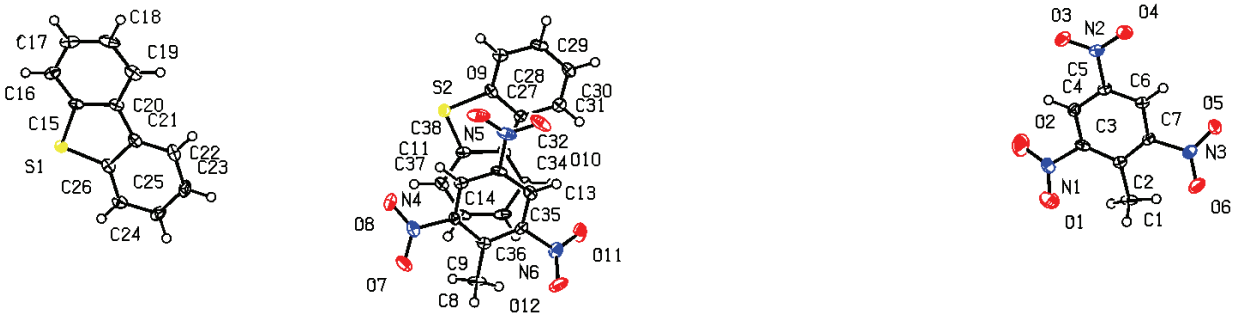

Figure A1.23 ORTEP diagram of TNT/dibenzothiophene cocrystal with thermal ellipsoids of 50% probability.

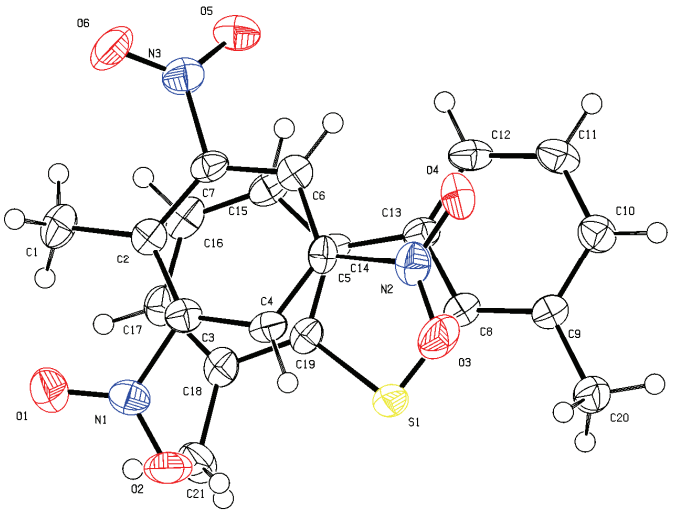

Figure A1.24 ORTEP diagram of TNT/4,6-dimethyldibenzothiophene cocrystal with thermal ellipsoids of 50% probability.

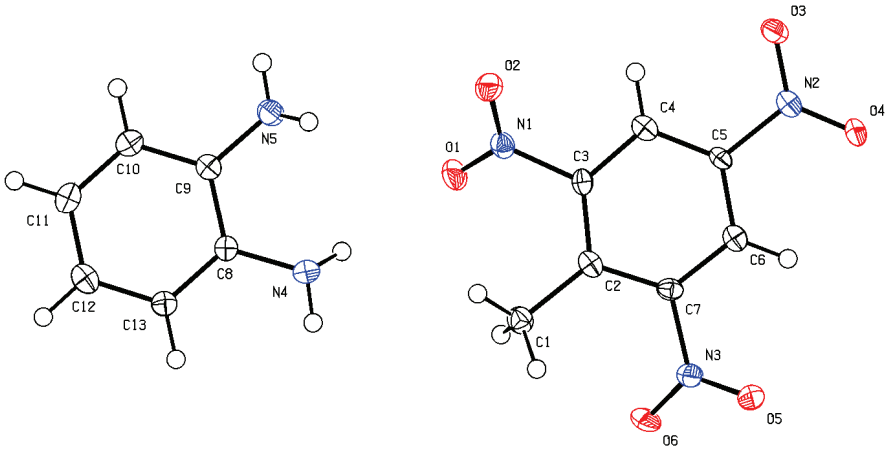

Figure A1.25 ORTEP diagram of TNT/1,2-phenylenediamine cocrystal with thermal ellipsoids of 50% probability.

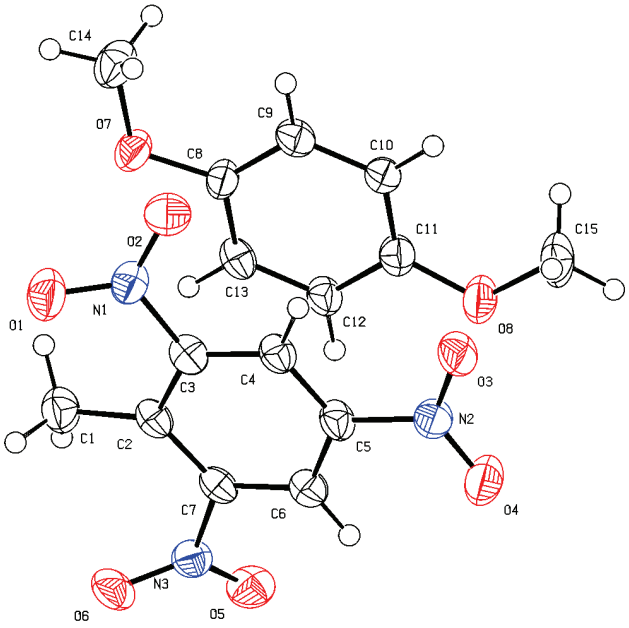

Figure A1.26 ORTEP diagram of TNT/1,4-dimethoxybenzene cocrystal with thermal ellipsoids of 50% probability.

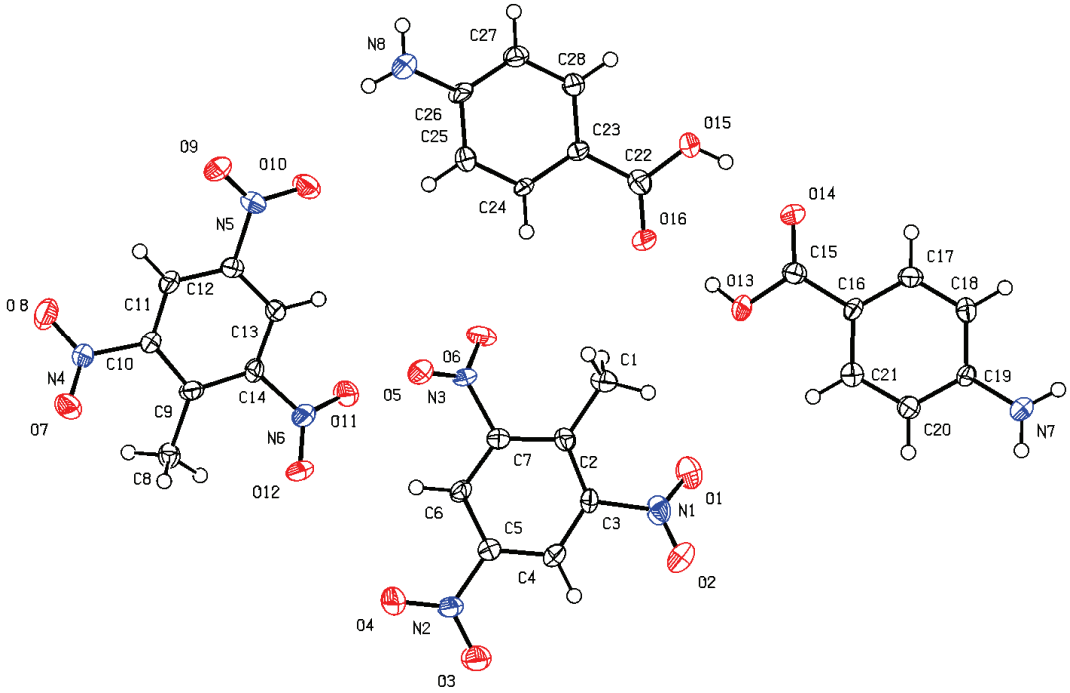

Figure A1.27 ORTEP diagram of TNT/4-aminobenzoic acid 1:1 cocrystal with thermal ellipsoids of 50% probability.

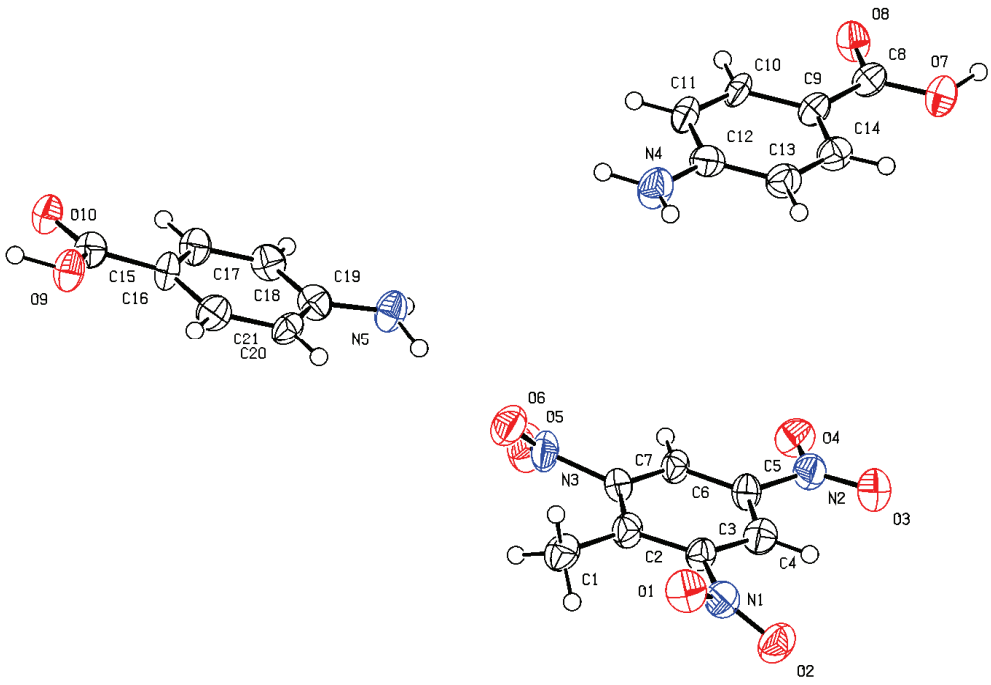

Figure A1.28 ORTEP diagram of TNT/4-aminobenzoic acid 1:2 cocrystal with thermal ellipsoids of 50% probability.

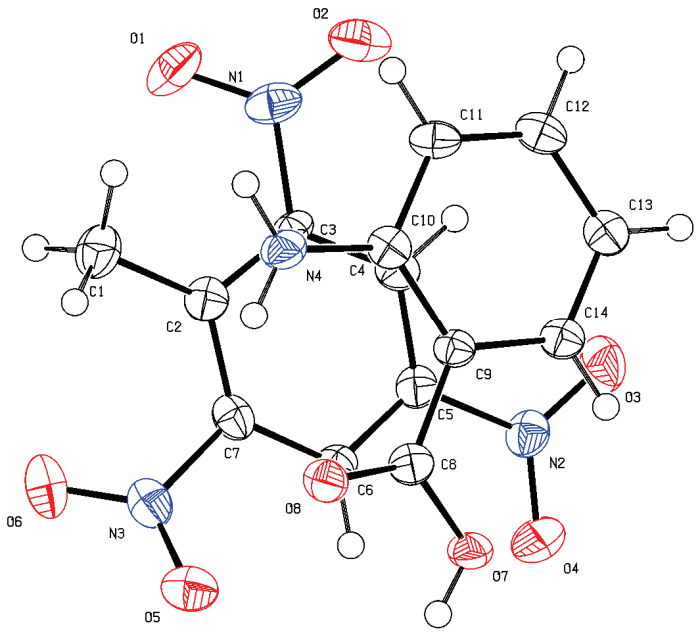

Figure A1.29 ORTEP diagram of TNT/anthranilic acid 1:1 cocrystal with thermal ellipsoids of 50% probability.

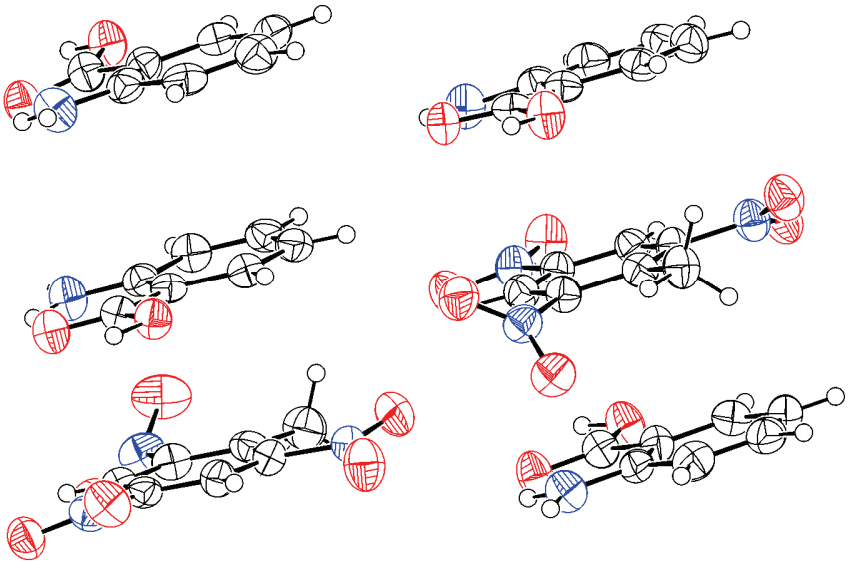

Figure A1.30 ORTEP diagram of TNT/anthranilic acid 1:2 cocrystal with thermal ellipsoids of 50% probability.

A1.3 PXRD Patterns for TNT Cocrystals

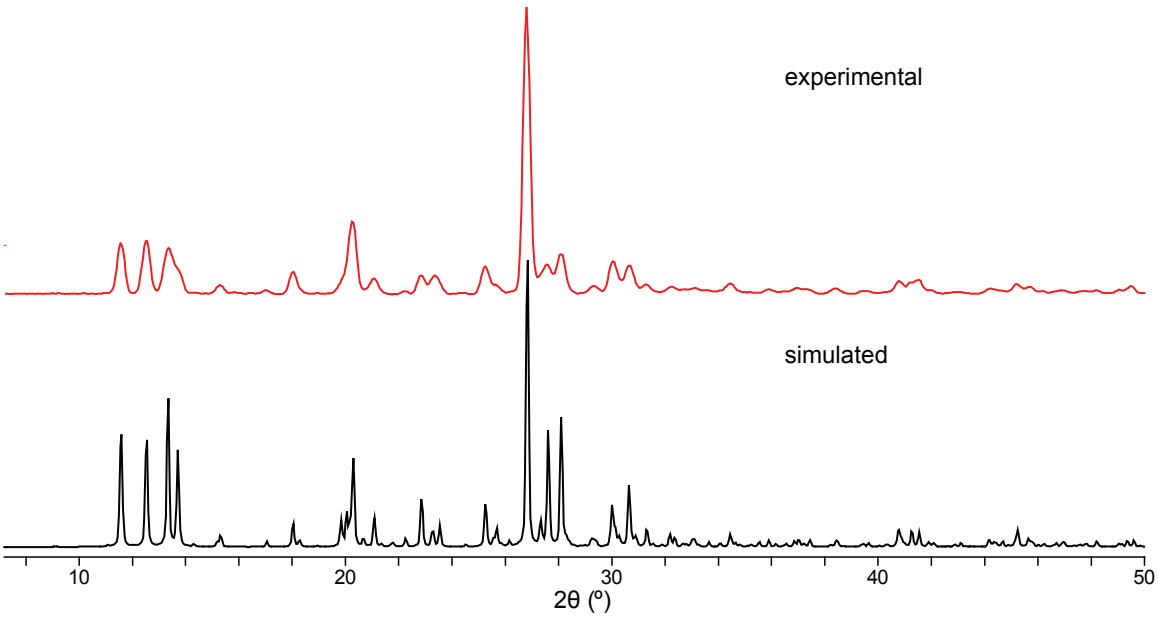

Figure A1.31 Simulated and experimental PXRD patterns for the TNT/naphthalene cocrystal at 95 K.

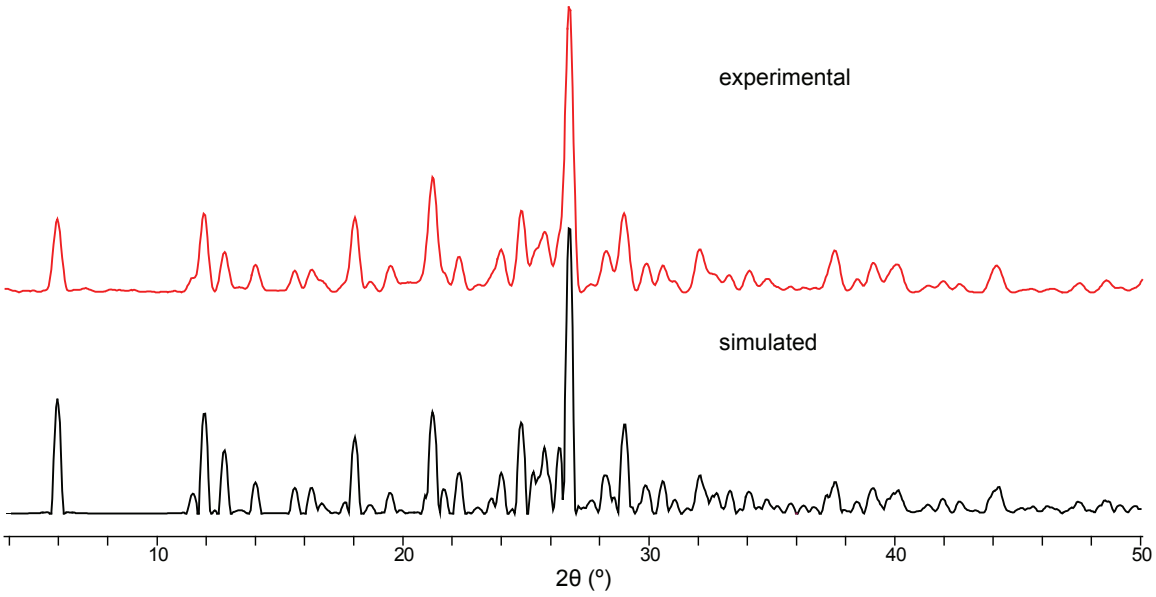

Figure A1.32 Simulated and experimental PXRD pattern for the TNT/1-bromonaphthalene cocrystal at 95 K.

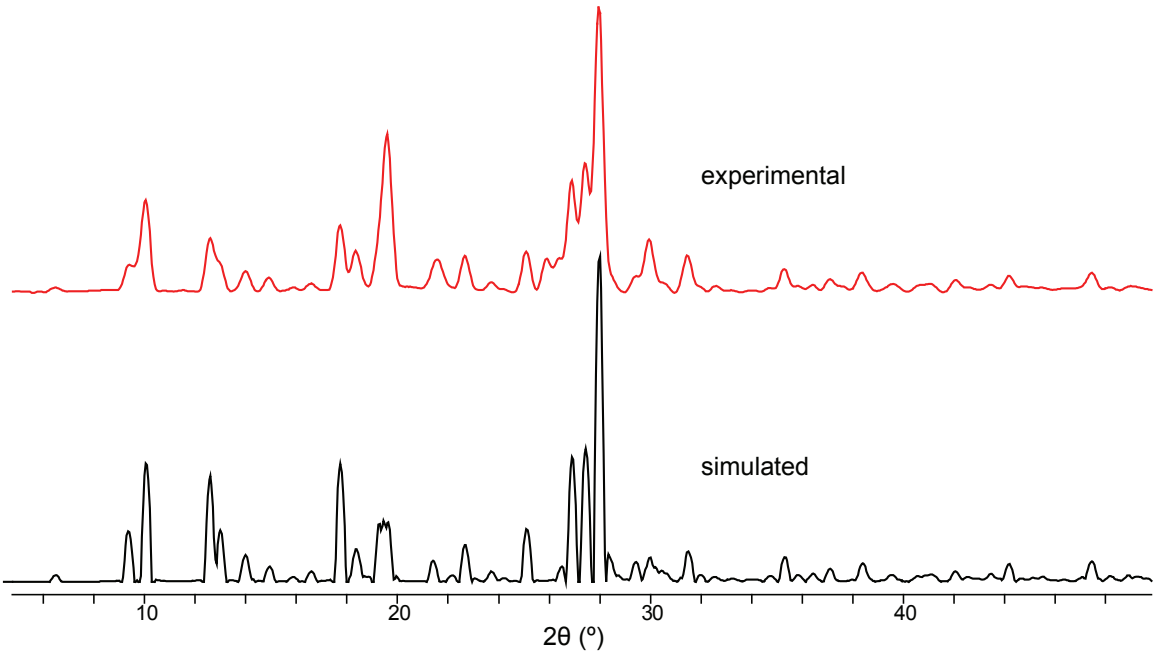

Figure A1.33 Simulated and experimental PXRD pattern for the TNT/anthracene cocrystal at 95 K.

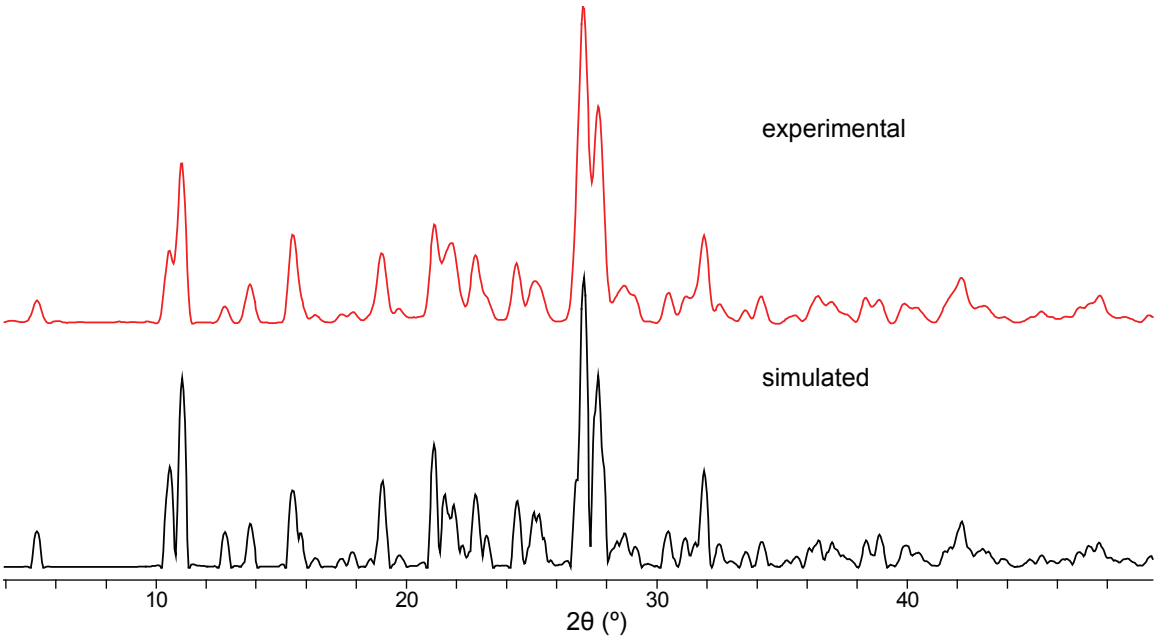

Figure A1.34 Simulated and experimental PXRD pattern for the TNT/9-bromoanthracene cocrystal at 95 K.

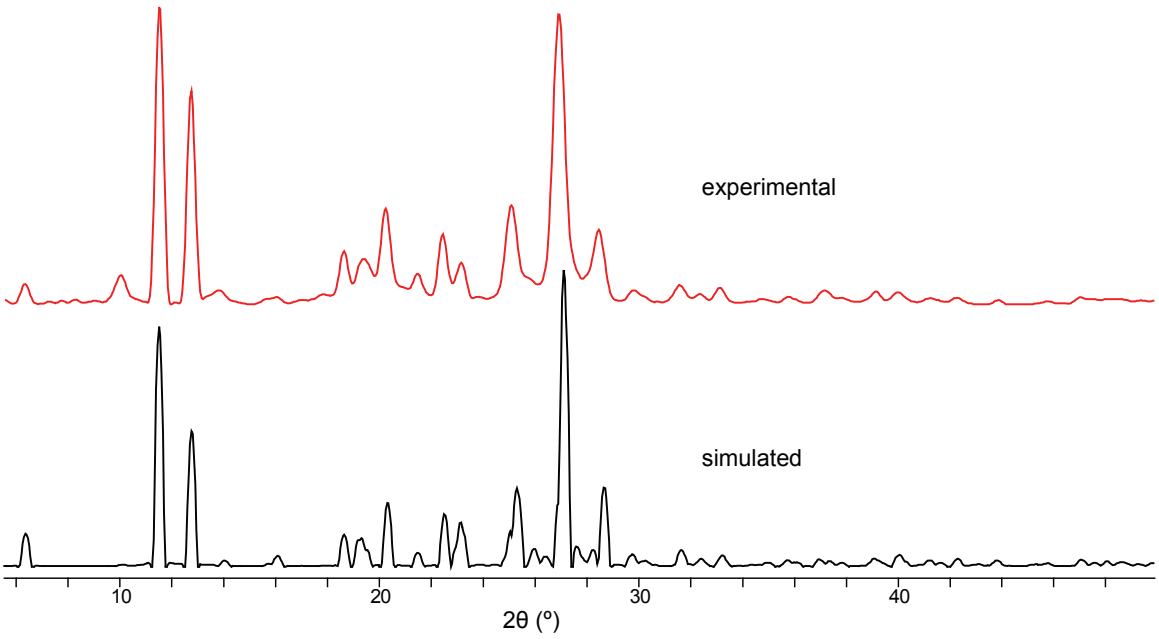

Figure A1.35 Simulated and experimental PXRD pattern for the TNT/phenanthrene cocrystal at 95 K.

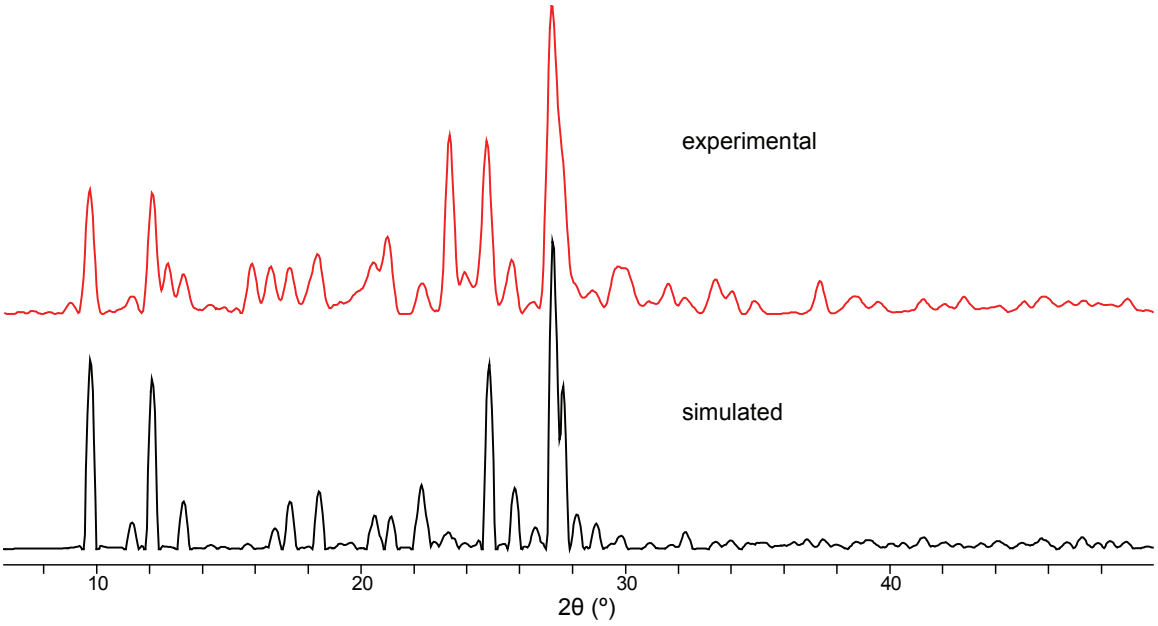

Figure A1.36 Simulated and experimental PXRD pattern for the TNT/perylene cocrystal at 95 K.

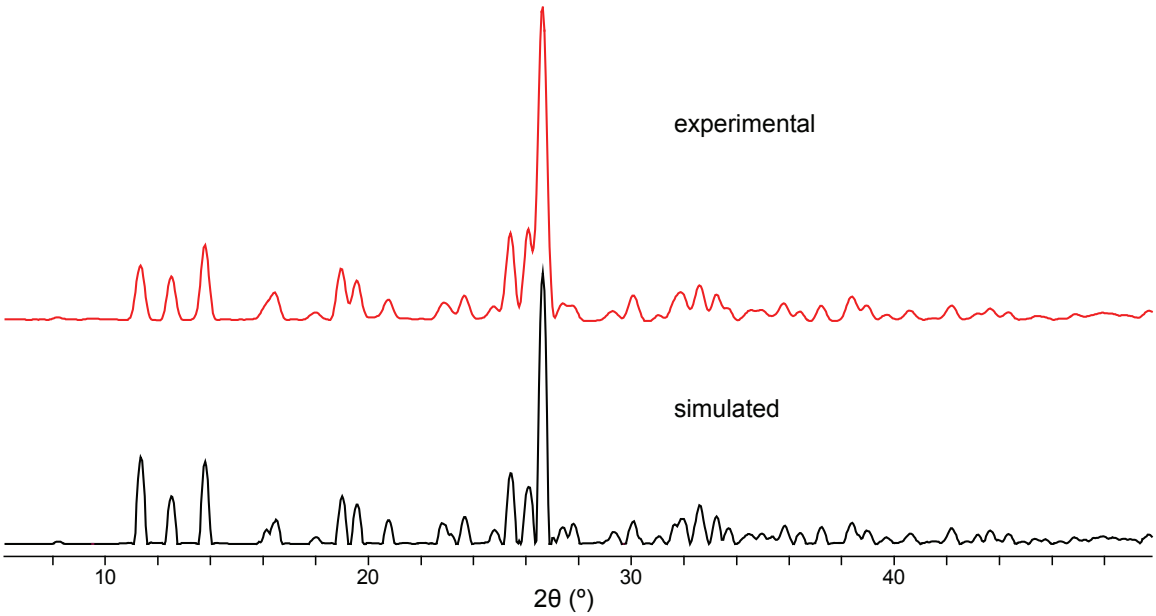

Figure A1.37 Simulated and experimental PXRD pattern for the TNT/tetrathiafulvalene cocrystal at 95 K.

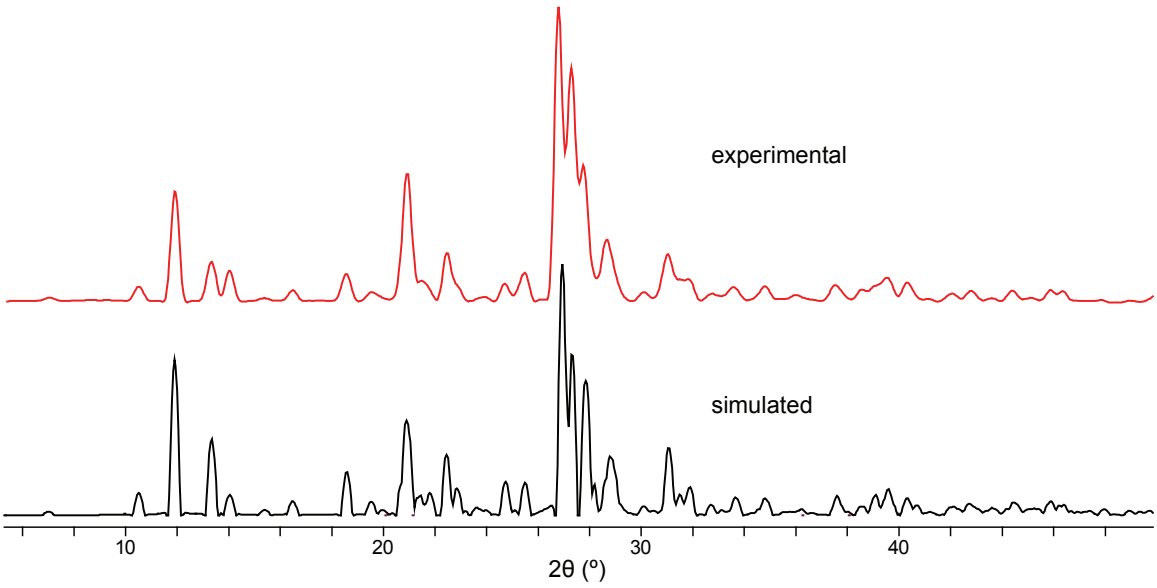

Figure A1.38 Simulated and experimental PXRD pattern for the TNT/thieno[3,2-*b*]thiophene cocrystal at 95 K.

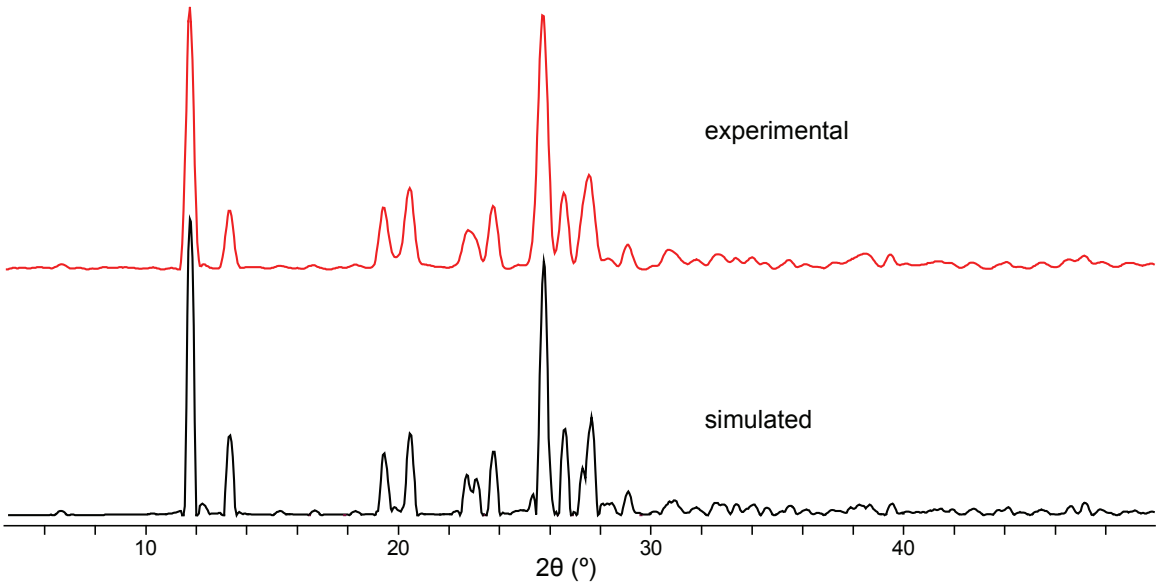

Figure A1.39 Simulated and experimental PXRD pattern for the TNT/phenothiazine cocrystal at 95 K.

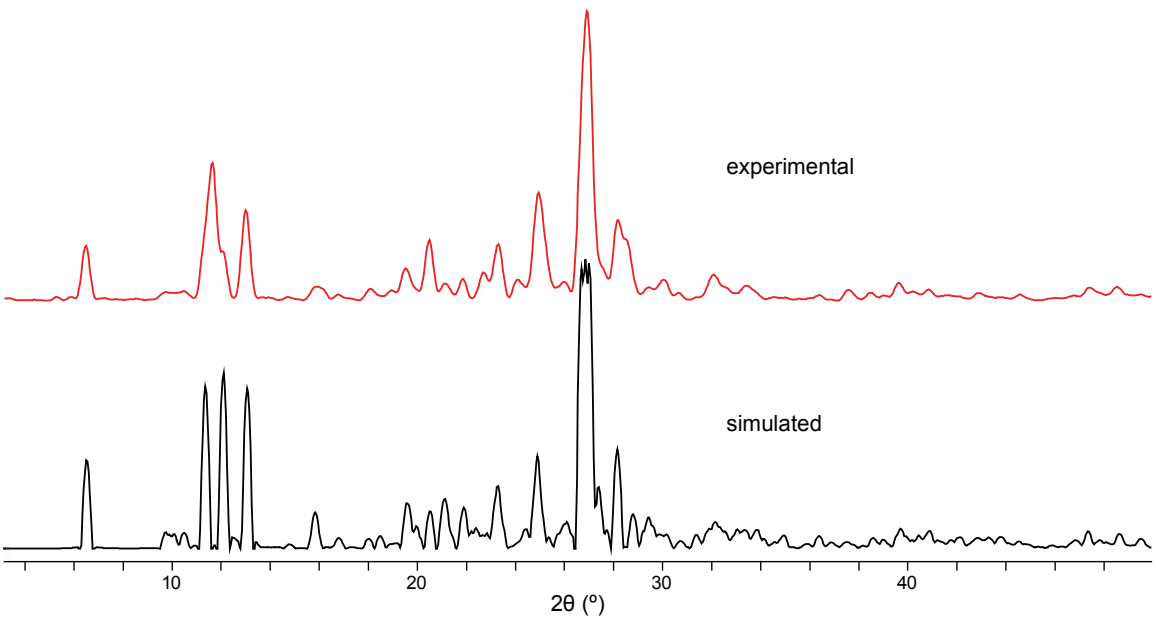

Figure A1.40 Simulated and experimental PXRD pattern for the TNT/dibenzothiophene cocrystal at 95 K.

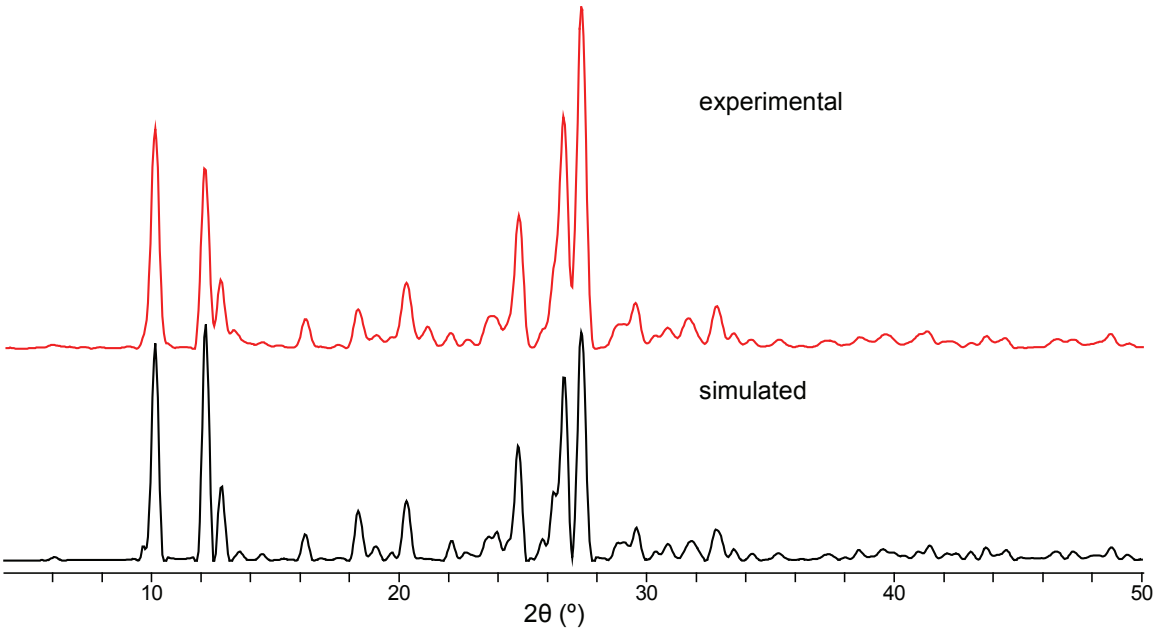

Figure A1.41 Simulated and experimental PXRD pattern for the TNT/4,6-dimethyldibenzothiophene cocrystal at 95 K.

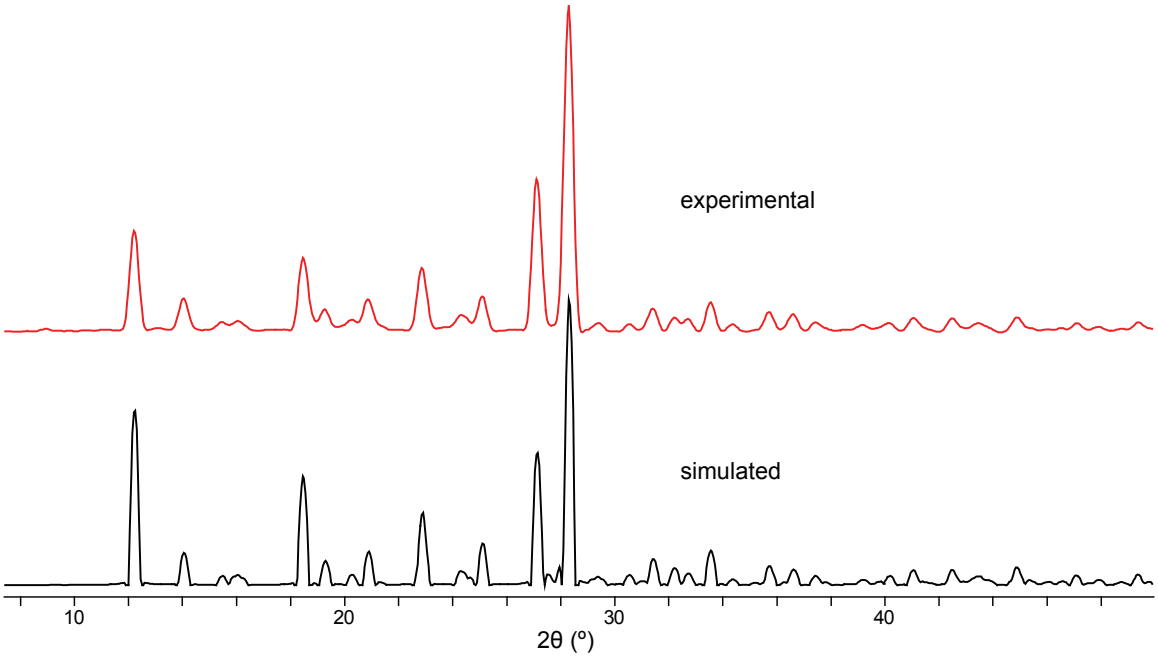

Figure A1.42 Simulated and experimental PXRD pattern for the TNT/1,2-phenylenediamine cocrystal at 95 K.

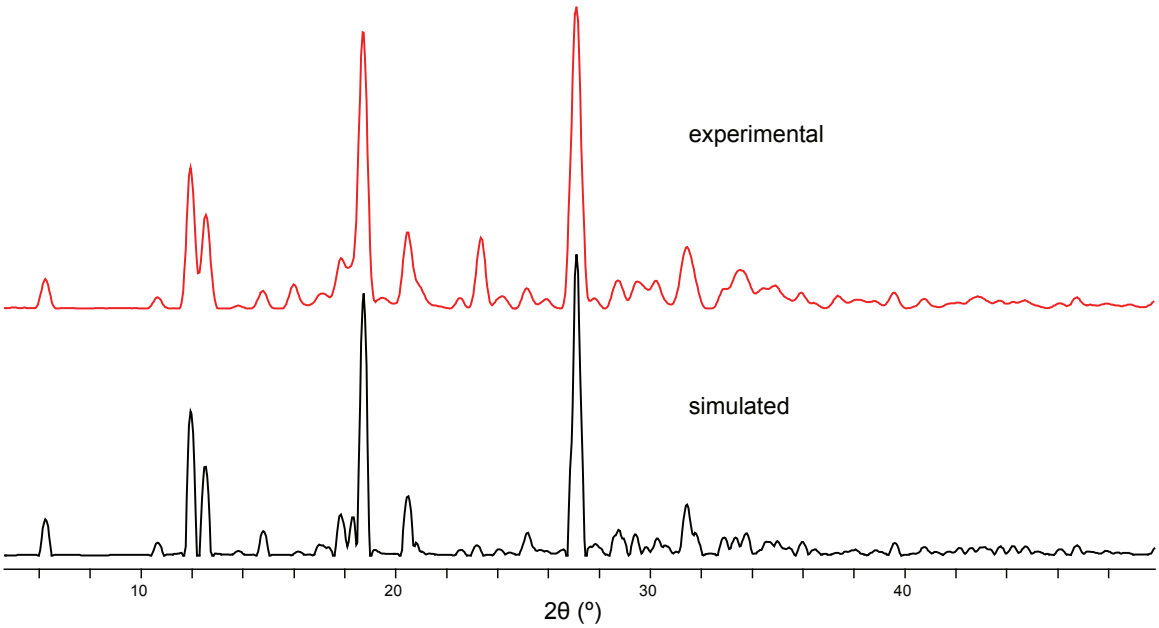

Figure A1.43 Simulated and experimental PXRD pattern for the TNT/1,4-dimethoxybenzene cocrystal at 95 K.

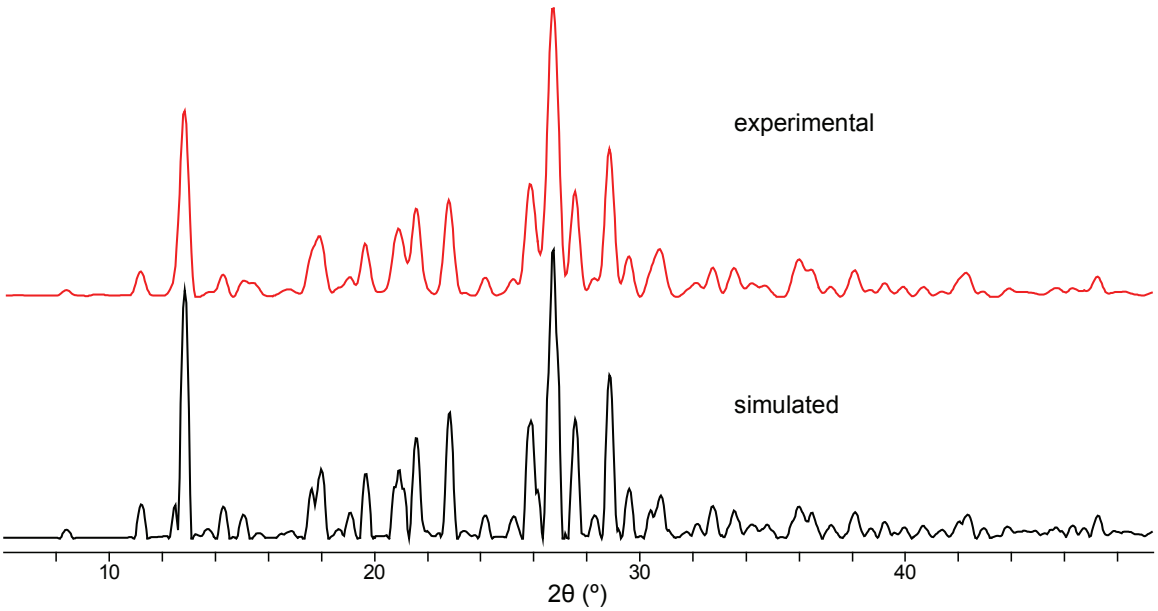

Figure A1.44 Simulated and experimental PXRD pattern for the TNT/4-aminobenzoic acid 1:1 cocrystal at 95 K.

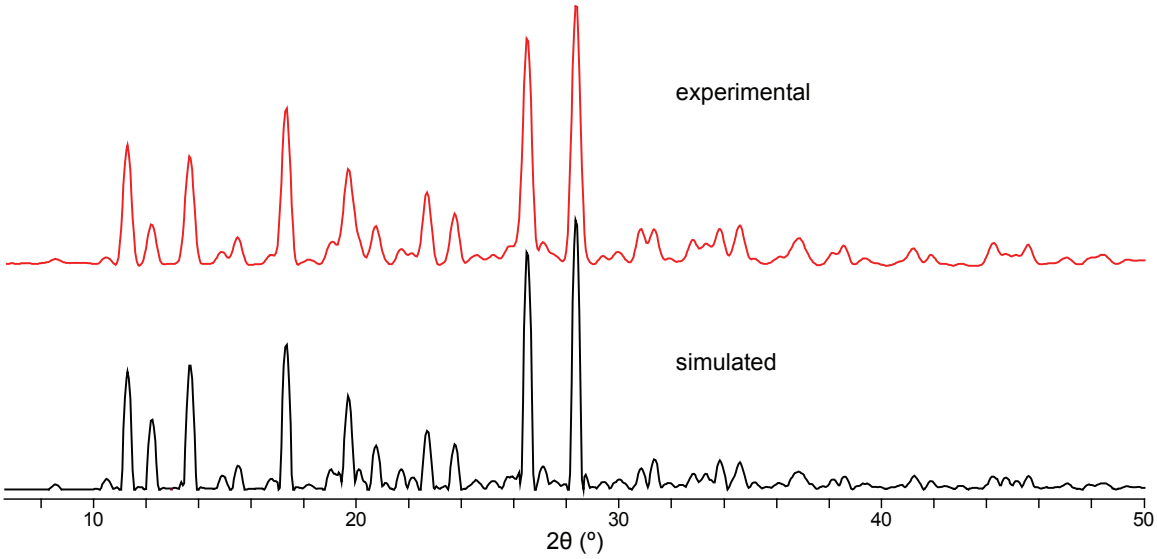

Figure A1.45 Simulated and experimental PXRD pattern for the TNT/4-aminobenzoic acid 1:2 cocrystal at 95 K.

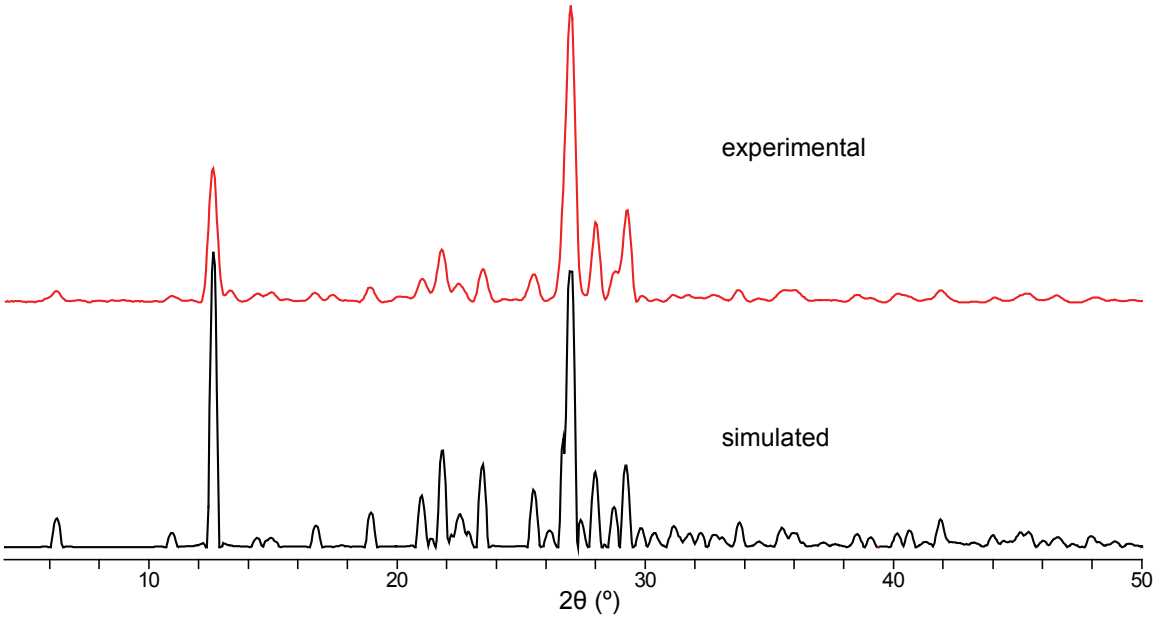

Figure A1.46 Simulated and experimental PXRD pattern for the TNT/anthranilic acid 1:1 cocrystal at 95 K.

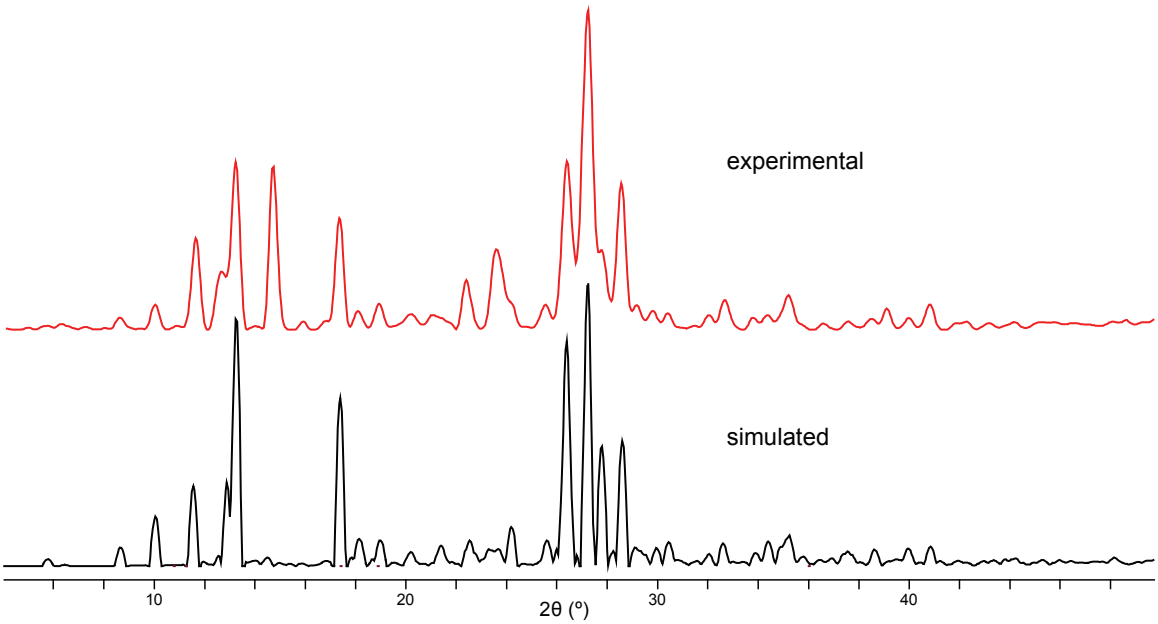

Figure A1.47 Simulated and experimental PXRD pattern for the TNT/anthranilic acid 1:2 cocrystal at 95 K.

Table A1.3 Experimental PXRD peak positions (°) and the relative intensity (%) of TNT cocrystals **1-9**.

1		**2**		**3**		**4**		**5**		**6**		**7**		**8**		**9**	
2θ	**I/I_0**	**2θ**	**I/I_0**	**2θ**	**I/I_0**	**2θ**	**I/I_0**	**2θ**	**I/I_0**	**2θ**	**I/I_0**	**2θ**	**I/I_0**	**2θ**	**I/I_0**	**2θ**	**I/I_0**
11.56	18.9	5.95	25.6	9.43	8.9	5.25	2.0	6.35	6.9	9.74	37.7	11.34	17.8	11.92	37.7	11.75	100
12.51	19.2	11.89	27.6	10.01	32.0	10.90	51.3	10.04	9.2	11.29	6.7	12.51	14.3	13.35	13.3	13.33	22.4
13.38	16.5	12.76	13.9	12.66	19.0	12.20	7.4	11.52	100	12.15	38.6	13.79	24.6	14.03	10.2	19.44	23.7
15.29	3.2	14.00	9.1	13.99	7.0	12.75	3.6	12.75	71.7	13.32	14.0	16.40	8.9	18.56	9.2	20.43	31.2
18.04	8.2	15.61	6.9	14.90	4.9	13.80	2.6	13.78	4.5	14.32	4.5	18.99	16.5	20.94	42.6	22.82	15.0
20.24	26.5	16.34	7.7	17.76	23.1	15.50	11.0	17.81	3.3	15.89	17.8	19.53	12.3	22.53	16.0	23.75	24.3
22.88	7.1	18.04	26.2	18.35	14.2	16.05	5.9	18.63	18.0	16.61	17.5	20.75	5.9	25.45	9.1	25.72	97.3
23.34	6.9	19.53	9.1	19.56	55.3	17.35	12.6	19.41	15.3	17.29	17.7	22.90	4.8	26.90	100	26.55	29.3
25.27	10.5	21.21	40.2	21.56	10.7	19.05	7.0	20.24	32.4	18.33	23.4	23.68	6.5	27.27	79.1	27.52	36.0
26.80	100	22.29	12.3	22.67	12.2	19.75	2.2	21.47	10.3	20.47	21.8	25.39	24.5	27.82	45.8	29.08	9.5
27.61	6.5	23.96	14.8	25.09	14.3	21.10	15.8	22.46	23.8	20.94	29.9	26.17	27.2	28.69	20.3	30.75	7.5
28.09	12.7	24.83	28.4	25.90	11.8	21.80	11.4	23.12	14.0	22.32	15.7	26.62	100	31.08	14.1	31.79	3.8
30.07	10.7	25.71	21.1	26.87	39.1	22.85	23.9	25.10	33.6	23.37	60.6	27.49	4.5	31.72	5.0	32.68	5.8
30.64	9.9	26.74	100	27.94	100	24.45	7.6	26.92	98.2	24.74	59.2	30.09	7.7	39.48	5.5	34.03	4.6
34.45	3.2	28.30	14.2	29.94	18.4	24.90	18.5	28.44	25.2	25.67	20.6	31.86	7.3	50.89	3.1	38.46	6.1
36.99	1.8	28.98	27.5	31.48	13.1	25.35	11.5	29.83	4.7	27.30	100	32.60	7.9	53.10	2.7	39.50	5.7
40.83	3.9	29.91	9.9	35.31	8.0	27.05	100	31.57	6.4	29.84	12.8	33.31	6.0	53.68	5.4	41.40	3.2
41.47	4.9	30.57	9.3	37.14	4.5	27.65	22.4	33.11	5.5	31.62	7.3	34.60	2.8			44.03	2.8
45.24	2.7	32.10	15.0	38.36	6.8	28.56	2.6	37.17	4.6	32.26	4.3	35.81	4.6			46.58	3.9
45.65	1.9	33.27	6.0	40.99	3.0	29.50	9.5	37.76	2.2	33.46	11.3	37.23	5.0			47.12	5.3
49.47	2.6	34.10	7.4	42.10	4.2	30.45	2.1	40.00	3.9	33.93	7.7	38.41	7.8			48.93	2.5
54.87	2.8	34.83	4.7	44.19	5.1	31.13	1.5			34.92	5.4	38.88	4.6			50.40	3.7
		37.54	13.8	47.43	5.8	31.90	14.6			37.33	10.1	42.17	4.5			51.80	2.0
		39.16	9.6	50.30	3.9	33.45	5.3			52.06	5.8	43.63	3.5			52.69	3.0
		40.06	9.8	54.56	5.7	33.95	4.1					52.43	3.3				
		41.43	2.3			35.35	5.0										
		41.94	3.8			37.30	4.4										
		44.13	9.4			38.34	2.1										
		48.63	4.1			38.95	3.9										
		50.20	5.8			40.30	4.4										
		51.14	4.3			42.35	7.4										
		55.19	3.7			43.86	0.9										
		57.33	3.2			45.10	2.2										
		60.11	1.9			46.55	2.3										
						47.60	2.8										
						48.99	0.9										
						49.66	2.2										
						51.80	2.2										
						52.80	1.4										
						53.45	1.4										
						54.50	2.2										
						57.20	1.9										

Table A1.4 Experimental PXRD peak positions (°) and the relative intensity (%) of TNT cocrystals **10-17**

10		**11**		**12**		**13**		**14**		**15**		**16**		**17**	
2θ	**I/I_0**	**2θ**	**I/I_0**	**2θ**	**I/I_0**	**2θ**	**I/I_0**	**2θ**	**I/I_0**	**2θ**	**I/I_0**	**2θ**	**I/I_0**	**2θ**	**I/I_0**
6.48	19.0	10.14	64.4	12.21	30.5	6.25	9.7	11.19	8.3	11.29	46.5	12.59	45.0	10.04	7.7
9.83	2.9	12.18	52.7	14.05	9.6	11.97	46.4	12.83	65.2	12.22	15.7	14.45	2.8	11.65	28.7
10.39	3.2	12.80	20.0	16.03	3.0	12.53	30.9	14.27	8.1	13.66	42.0	14.91	3.3	12.70	18.2
11.63	48.0	13.43	5.0	18.48	22.2	14.78	5.8	15.15	5.3	14.94	4.7	18.94	5.0	13.21	52.5
13.01	31.6	16.24	8.5	19.26	6.4	16.01	7.3	17.89	19.7	15.48	10.4	21.02	8.3	14.74	51.0
15.93	4.6	18.39	11.5	20.27	3.1	17.86	13.5	19.08	5.3	17.33	60.8	21.80	18.1	17.36	36.2
19.57	13.7	19.04	3.9	20.86	9.3	18.71	87.0	19.65	15.9	19.06	9.2	22.51	6.5	18.14	7.3
20.49	24.2	20.30	19.3	22.87	19.1	20.49	23.6	20.92	20.9	19.72	38.1	23.47	11.2	18.95	10.1
21.19	8.6	21.15	6.4	24.36	4.7	23.34	22.7	21.55	28.4	20.75	16.1	25.50	9.2	20.20	7.9
21.85	9.3	22.07	4.5	25.07	10.7	25.16	6.9	22.80	33.0	21.75	6.8	26.97	100	21.12	8.0
22.72	10.3	23.78	9.4	27.12	46.3	25.89	2.8	24.17	6.2	22.69	28.4	28.00	26.9	22.42	18.5
23.25	19.2	24.81	38.9	28.29	100	27.09	100	25.88	38.3	23.75	19.2	29.24	31.1	23.63	27.2
24.13	6.2	26.64	67.9	31.39	7.0	28.71	7.6	26.73	100	26.51	85.0	31.74	2.2	25.53	7.6
24.97	36.2	27.36	100	32.28	4.2	29.55	5.9	27.55	35.9	28.37	100	35.69	3.9	26.41	52.6
26.90	100	29.01	7.1	32.64	3.8	30.18	7.2	28.86	49.4	29.46	3.0	40.26	2.7	27.24	100
28.27	27.2	29.50	13.4	33.55	8.9	31.46	19.7	29.61	11.0	29.95	4.3	41.91	3.9	28.55	46.0
30.02	7.4	30.83	6.1	35.71	6.0	33.02	4.4	30.72	16.7	30.90	12.6	45.37	2.8	29.83	5.9
32.13	9.9	31.71	8.8	36.58	5.3	33.50	9.5	32.15	4.4	31.30	12.6			32.06	4.5
33.45	6.5	32.85	12.3	41.08	4.3	34.88	3.8	32.73	8.6	32.83	8.6			32.66	9.2
36.38	3.4	33.49	4.4	42.52	4.1	38.17	1.7	33.54	7.7	33.82	13.0			34.34	4.4
37.60	5.2	37.35	2.2	43.46	2.8			34.22	4.2	34.61	12.4			35.18	10.7
39.67	7.5	38.64	3.2	44.91	4.5			36.02	12.8	36.85	10.0			39.08	6.5
40.90	5.1	39.65	4.1	47.10	2.7			36.38	9.5	38.24	4.6			40.81	7.8
42.92	3.5	41.28	5.0	49.40	3.0			38.08	8.5	38.51	7.3			45.28	2.3
47.46	3.6	43.78	3.6	55.05	4.9			39.24	3.5	41.19	6.4			48.14	2.5
		44.40	3.0	60.41	2.0			42.27	7.9	44.26	6.8			48.58	2.8
		46.63	2.7					47.24	5.6	45.58	6.2			49.79	3.5
		47.17	2.6							48.41	3.6			53.72	7.1
		48.71	4.2							56.28	4.3				
		51.94	5.6												
		52.78	3.3												
		55.36	5.1												

Appendix 2 Cocrystals of HMX

A2.1 ORTEP Diagrams for HMX Cocrystals

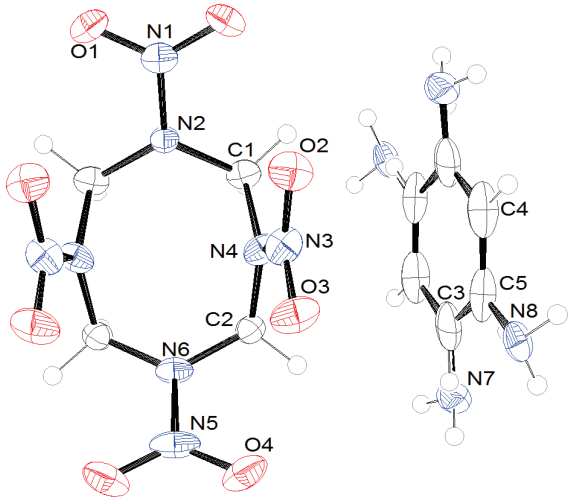

Figure A2.1 ORTEP diagram of HMX/1,2-phenylenediamine with thermal ellipsoids of 50% probability.

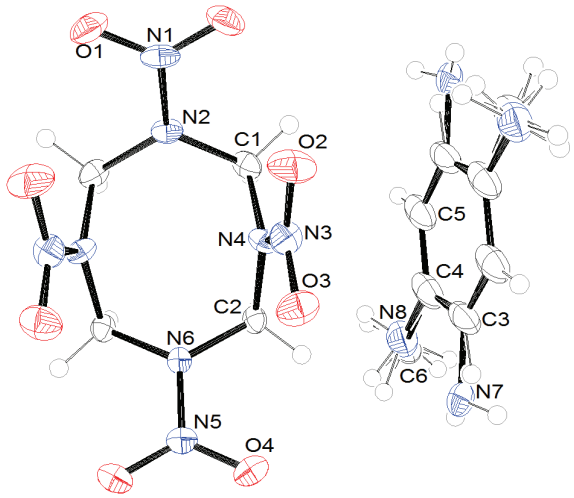

Figure A2.2 ORTEP diagram of HMX/3,4-diaminotoluene with thermal ellipsoids of 50% probability.

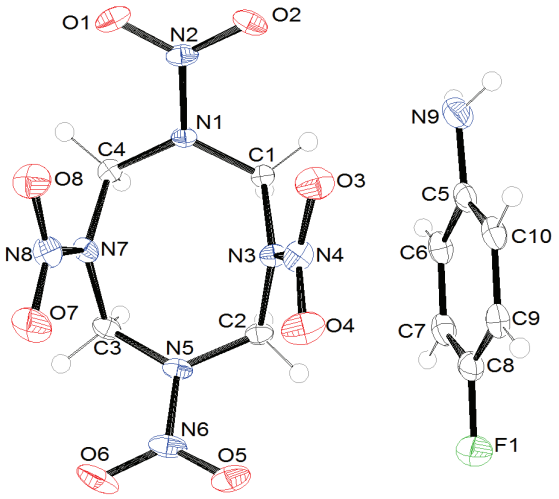

Figure A2.3 ORTEP diagram of HMX/4-fluoroaniline with thermal ellipsoids of 50% probability.

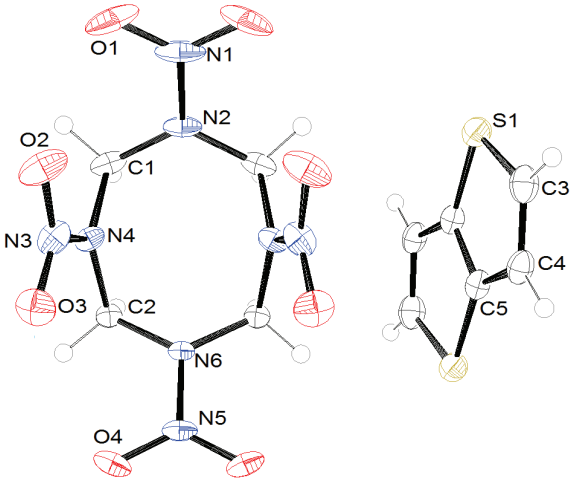

Figure A2.4 ORTEP diagram of HMX/thieno[3,2-*b*]thiophene with thermal ellipsoids of 50% probability.

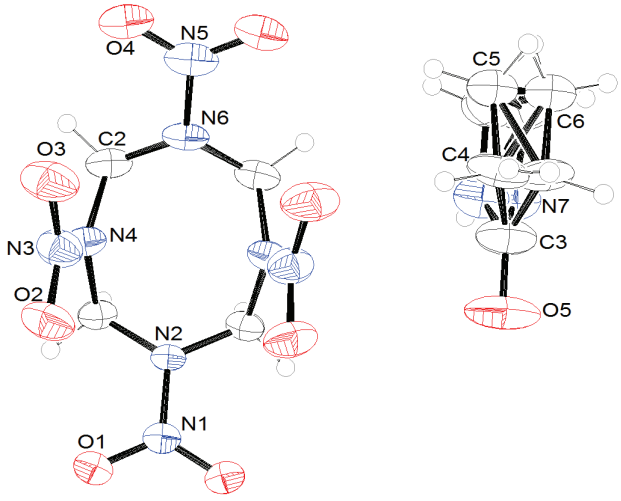

Figure A2.5 ORTEP diagram of HMX/2-pyrrolidone with thermal ellipsoids of 50% probability.

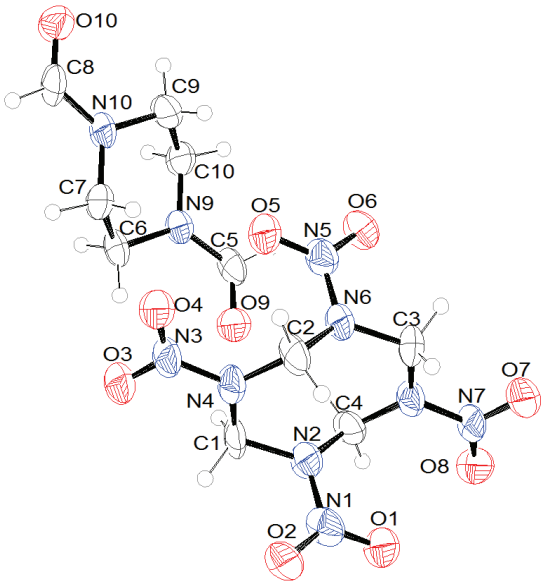

Figure A2.6 ORTEP diagram of HMX/1,4-piperazinedicarboxaldehyde with thermal ellipsoids of 50% probability.

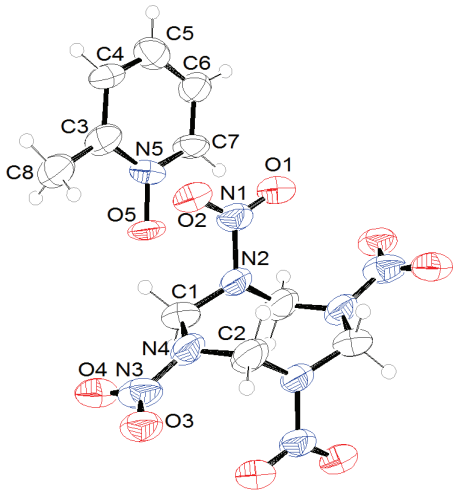

Figure A2.7 ORTEP diagram of HMX/2-picoline-*N*-oxide 1:2 with thermal ellipsoids of 50% probability.

A2.2 Raman Spectra for HMX Cocrystals

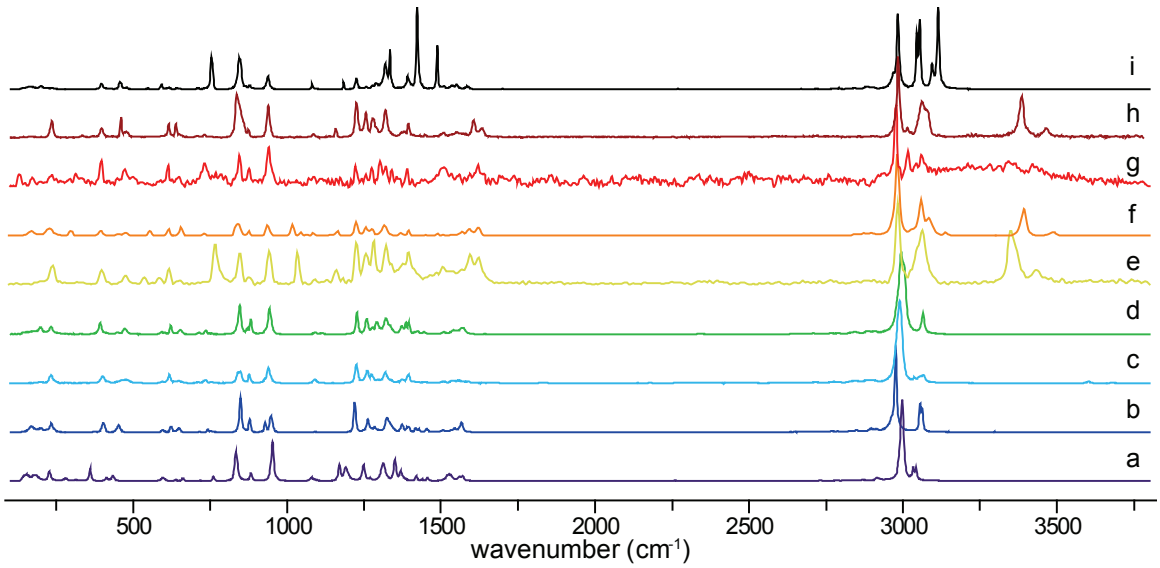

Figure A2.8 Raman spectra comparison among polymorphs of HMX and the *chair-chair/layered* cocrystals: a) β-HMX b) α-HMX c) γ-HMX d) δ-HMX e) HMX/1,2-phenylenediamine f) HMX/2-bromoaniline g) HMX/3,4-diaminotoluene h) HMX/4-fluoroaniline i) HMX/thieno[3,2-*b*]thiophene.

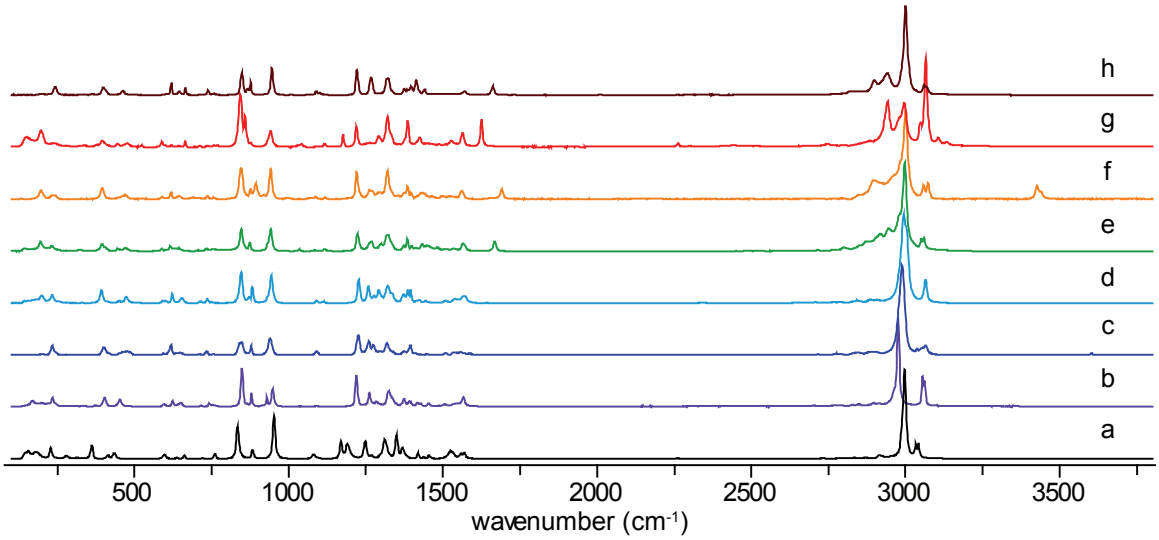

Figure A2.9 Raman spectra comparison among polymorphs of HMX and the *chair-chair/pocket* cocrystals: a) β-HMX b) α-HMX c) γ-HMX d) δ-HMX e) HMX/*N*-methyl-2-pyrrolidone f) HMX/2-pyrrolidone g) HMX/4-picoline-*N*-oxide h) HMX/DMF.

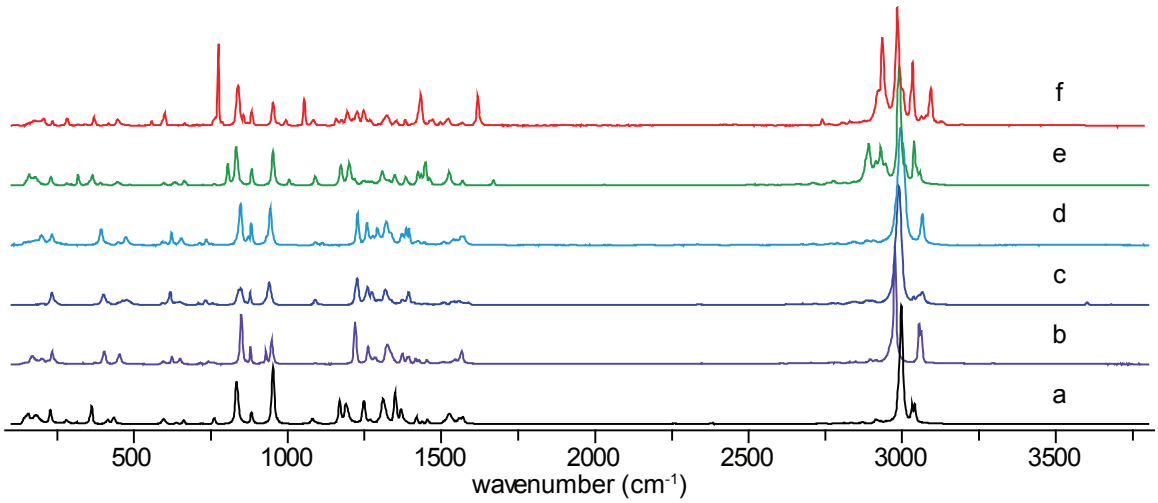

Figure A2.10 Raman spectra comparison among polymorphs of HMX and the *chair/layered* cocrystals: a) β-HMX b) α-HMX c) γ-HMX d) δ-HMX e) HMX/1,4-piperazinedicarboxaldehyde f) HMX/2-picoline-*N*-oxide.

A2.3 Powder X-Ray Diffraction Pattern Comparison for HMX Cocrystals

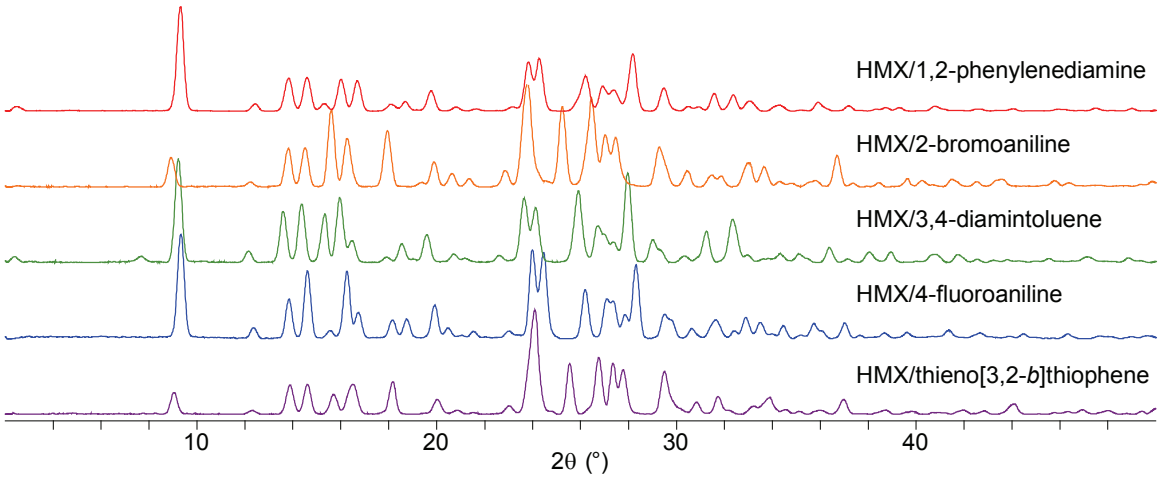

Figure A2.11 PXRD patterns for HMX cocrystals in the *chair-chair/layered* motif.

Table A2.1 Experimental PXRD peak positions and relative intensity (%) of *chair-chair/layered* HMX cocrystals.

HMX/1,2-phenylenediamine		HMX/2-bromoaniline		HMX/3,4-diaminotoluene		HMX/4-fluoroaniline		HMX/thieno[3,2-*b*]thiophene	
2θ(°)	**I/I_0**	**2θ(°)**	**I/I_0**	**2θ(°)**	**I/I_0**	**2θ(°)**	**I/I_0**	**2θ(°)**	**I/I_0**
2.464	4.5	8.929	29.3	2.396	5.4	9.336	100.0	9.049	20.6
9.316	100.0	12.242	4.7	7.674	6.0	12.397	8.5	12.318	3.6
12.434	7.1	13.809	36.4	9.228	100.0	13.843	37.8	13.886	28.0
13.827	29.8	14.511	35.2	12.157	11.0	14.611	82.2	14.61	28.6
14.599	29.6	15.611	73.2	13.599	49.4	15.541	8.1	15.704	19.0
16.012	28.8	16.271	45.7	14.371	56.8	16.244	49.0	16.503	28.7
16.692	28.3	17.944	55.8	15.327	47.2	16.711	29.0	18.167	31.2
18.689	8.3	19.398	3.9	15.96	63.2	18.159	16.8	20.02	14.2
19.77	18.6	19.892	23.6	16.451	21.4	18.758	14.9	20.841	3.6
20.8	3.8	20.645	11.6	17.928	5.4	19.912	39.4	23.018	7.9
23.834	46.6	21.363	7.4	18.558	18.3	21.54	6.7	24.089	100.0
24.279	49.0	22.861	14.2	19.594	26.7	24.012	74.0	24.852	2.7
26.207	30.9	23.782	100.0	20.719	8.4	24.425	51.0	25.555	48.2
26.937	19.2	25.242	76.1	22.615	7.0	26.202	47.9	26.761	54.5
27.375	14.1	26.449	71.2	23.658	62.2	27.118	23.2	27.361	49.0
28.186	50.8	27.042	44.7	24.114	53.1	27.881	20.2	27.779	42.7
29.474	22.2	27.459	33.9	25.912	69.6	28.302	44.6	29.506	41.0
30.508	4.0	29.301	38.9	26.74	35.3	29.508	24.6	30.843	11.4
30.91	3.2	30.445	15.1	27.363	19.8	29.788	17.1	31.737	17.1
31.583	15.7	31.485	11.8	27.976	86.5	30.636	7.3	32.188	3.4
32.374	13.7	31.86	10.7	29.031	22.2	31.586	16.9	33.228	7.4
33.063	8.1	33.017	23.1	29.351	11.7	32.401	5.8	33.882	15.9
34.312	5.9	33.668	16.2	30.34	6.3	32.881	16.7	34.562	4.3
35.916	8.4	34.326	4.1	31.25	30.4	33.509	14.3	35.116	2.4
37.189	4.8	35.798	6.0	32.362	41.8	34.462	12.5	35.995	3.3
38.724	3.5	36.703	30.9	32.951	7.4	35.739	10.7	36.978	13.9
39.308	2.8	38.44	4.2	34.336	8.8	36.061	6.8	38.717	3.9
40.779	4.5	39.615	7.7	35.118	8.4	37.015	12.7	39.838	2.6
44.05	2.4	40.258	6.1	36.382	14.7	38.676	5.0	41.946	3.9
47.511	2.6	41.505	7.2	38.063	10.3	39.624	5.7	42.835	3.1
48.996	2.5	42.54	4.7	38.944	10.3	41.35	7.1	44.077	9.9
		43.57	7.0	40.717	7.9	42.669	5.2	46.925	4.3
		45.763	5.4	41.76	7.7	44.463	4.8	48.01	3.4
		49.85	5.1	47.142	5.7	46.313	4.6		

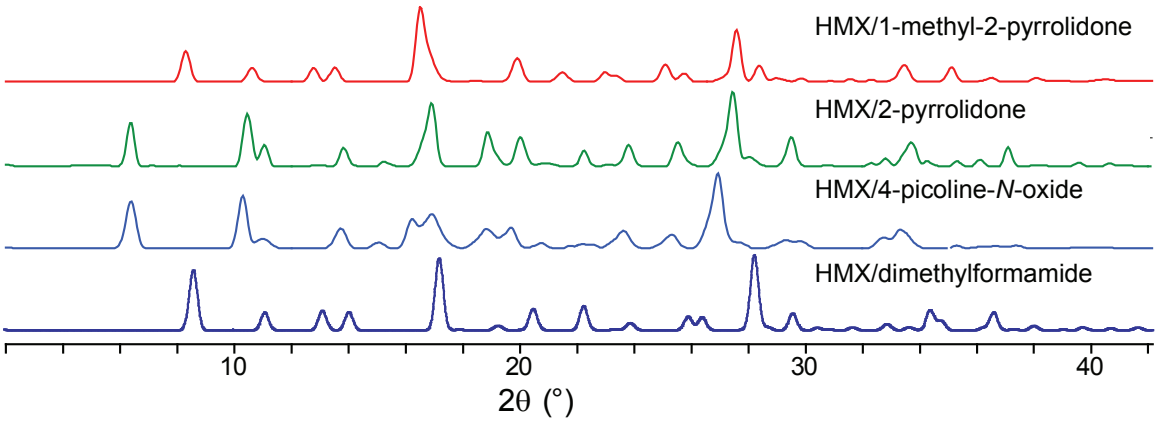

Figure A2.12 PXRD patterns for HMX cocrystals in the chair-chair/pocket motif.

Table A2.2 Experimental PXRD peak positions and relative intensity (%) of *chair-chair/pocket* HMX cocrystals.

HMX/1-methyl-2-pyrrolidone		HMX/2-pyrrolidone		HMX/4-picoline-*N*-oxide		HMX/DMF	
2θ(°)	**I/I_0**	**2θ(°)**	**I/I_0**	**2θ(°)**	**I/I_0**	**2θ(°)**	**I/I_0**
8.296	41	6.363	57.1	6.377	61.4	8.566	79.7
10.621	18.3	10.459	69.8	10.304	69.5	11.068	23.5
12.783	18.2	11.029	28.3	10.986	12.4	13.083	25.6
13.506	18.9	13.828	23.7	12.766	1.1	14.005	23.7
16.547	100	15.27	6.1	13.707	25.7	17.173	95.3
19.895	31.2	16.881	84.6	15.073	8.0	19.223	6.1
21.485	12.3	18.908	45.2	16.284	38.9	20.461	28.1
23.044	12.3	20.012	38.3	16.879	44.9	22.232	31.8
25.103	23.4	20.891	3.5	18.827	24.1	23.859	9.5
25.71	11	22.245	21.9	19.625	25.8	25.898	17.8
27.585	70.2	23.23	3.9	20.731	7.2	26.37	17.2
28.378	21.7	23.793	29.4	22.231	6.7	28.213	100.0
28.966	4.6	25.549	32.5	23.576	22.9	29.557	22.4
29.838	3.8	27.443	100.0	25.302	17.8	30.413	3.3
31.582	3.1	28.09	12.2	26.911	100.0	31.64	3.5
32.283	2.4	29.497	38.1	27.835	10.1	32.844	7.7
33.456	22.2	32.367	4.3	29.336	12.6	33.613	3.1
35.112	19.2	32.798	10.3	32.768	15.0	34.368	26.5
36.48	4.8	33.68	32.6	33.318	25.0	34.739	12.5
38.125	5.1	34.23	7.5	35.277	5.6	36.588	23.7
39.042	1.4	35.312	7.3	36.279	4.6	37.994	5.8
40.549	2.9	36.119	9.1	37.402	5.1	39.697	3.8
		37.102	25.7			40.685	2.5
		39.585	5.6			41.628	3.5
		40.663	4.4			42.928	3.3
		41.235	2.3			53.241	5.0

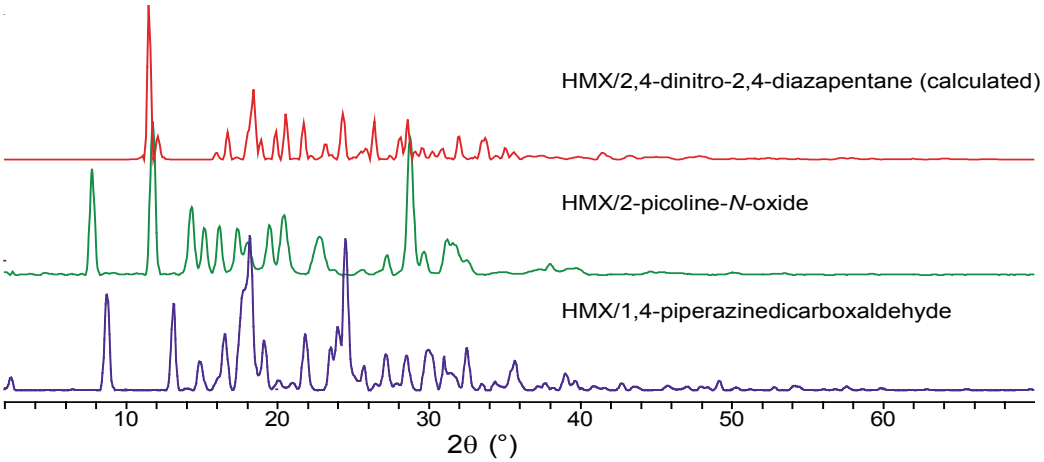

Figure A2.13 PXRD patterns for HMX cocrystals in the *chair/layered* motif.

Table A2.3 Experimental PXRD peak positions and relative intensity (%) of *chair/layered* HMX cocrystals.

HMX/1,4-piperazinedicarboxaldehyde		HMX/2-picoline-*N*-oxide	
2θ(°)	**I/I_0**	**2θ(°)**	**I/I_0**
2.378	6.4	7.759	68.8
8.731	61.7	11.754	100.0
13.102	56.1	14.302	44.2
14.892	18.1	15.16	30.2
16.493	36.0	16.152	31.7
17.768	64.4	17.383	30.1
18.102	100.0	17.976	20.7
19.092	32.0	19.458	32.1
20.066	6.1	20.406	38.7
20.958	4.5	22.774	24.8
21.825	36.1	27.193	12.4
23.495	27.7	28.762	88.6
24.46	98.5	29.656	14.5
25.662	15.7	31.254	22.3
26.494	4.4	32.527	9.7
27.153	23.6	37.962	6.0
28.508	23.4	39.679	4.2
29.948	27.6		
31.06	23.7		
31.463	12.5		
32.497	29.0		
33.464	4.6		
34.414	5.5		
35.623	19.0		
37.663	4.2		
39.032	10.9		
39.605	6.1		
42.726	5.3		
49.137	6.1		

Table A2.4 Experimental PXRD peak positions and relative intensity (%) of HMX cocrystals. Based on the PXRD comparisons these cocrystals seem likely to adopt the *chair-chair/pocket* structural motif.

HMX/δ-valerolactam		HMX/pyridine-*N*-oxide	
2θ(°)	**I/I_0**	**2θ(°)**	**I/I_0**
6.256	62.7	6.29	62.9
10.401	31.8	10.489	38.6
10.808	23.7	10.878	16.0
12.532	8.0	12.616	12.3
13.621	12.8	13.777	10.3
16.633	100.0	16.753	100.0
18.635	19.4	18.77	27.0
19.856	8.1	20.257	13.3
21.05	15.6	21.029	5.8
21.84	18.8	21.83	32.9
23.332	9.4	23.601	14.9
25.25	9.6	24.404	5.9
25.967	21.6	25.575	8.2
26.698	38.8	26.67	57.6
27.284	15.0	27.781	40.2
28.206	15.8	29.112	39.0
28.944	32.6	30.393	3.8
32.835	8.6	31.929	12.0
34.68	4.9	33.112	11.4
35.416	4.3	33.935	9.9
36.367	7.3	35.667	13.8
38.794	4.4	36.676	10.7
		39.058	8.0

Appendix 3 Cocrystals of Diacetone Diperoxide

A3.1 Raman Spectra of DADP Cocrystals

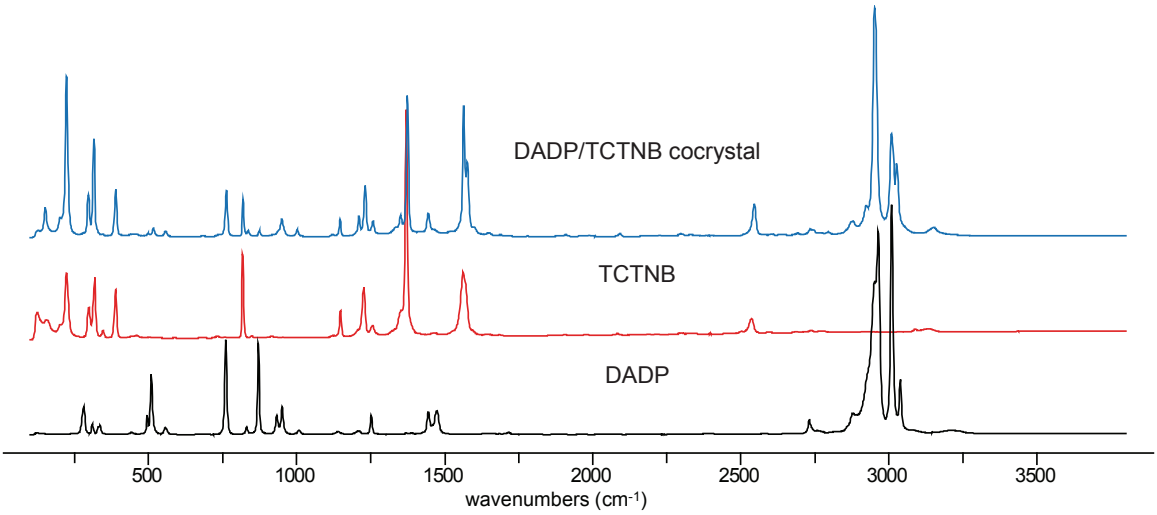

Figure A3.1 Raman spectra of the DADP/TCTNB cocrystal, TCTNB and DADP

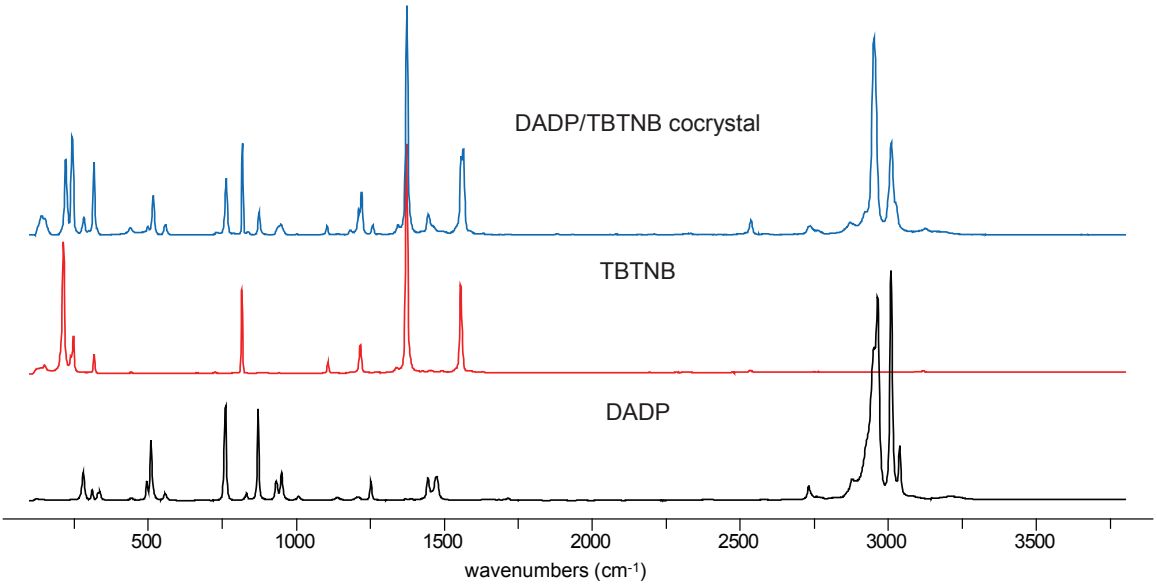

Figure A3.2 Raman spectra of the DADP/TBTNB cocrystal, TBTNB and DADP

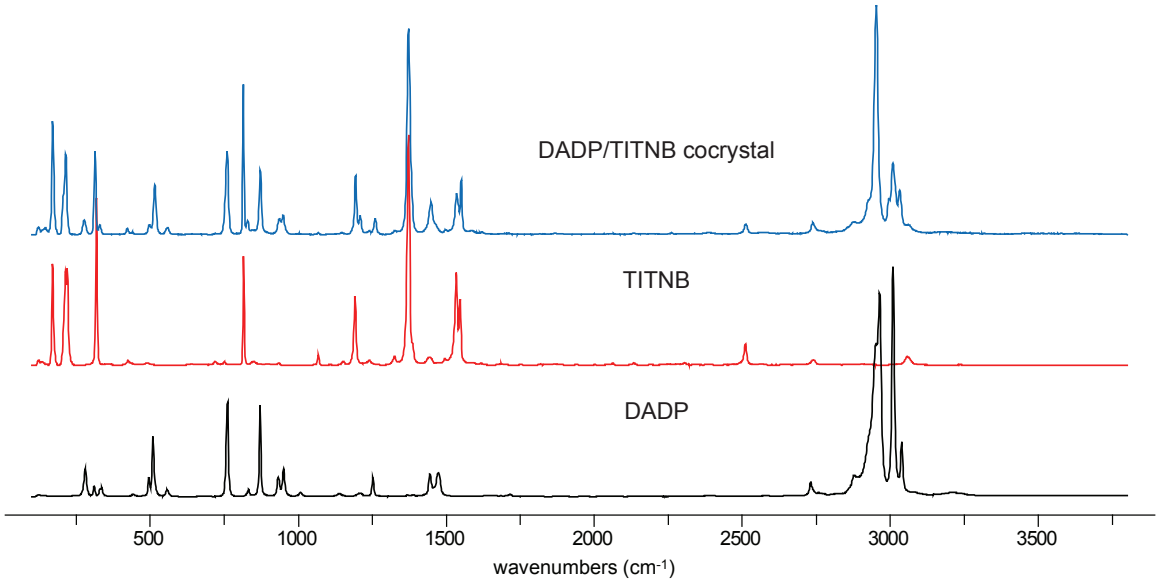

Figure A3.3 Raman spectra of the DADP/TITNB cocrystal, TITNB and DADP

Table A3.1 Frequency of Raman vibrational modes (cm^{-1}) of DADP, trihalogenated trinitrobenzenes and DADP cocrystals with the trihalogenated trinitrobenzenes.

DADP	TCTNB	TBTNB	TITNB	DADP/TCTNB cocrystal	DADP/TBTNB cocrystal	DADP/TITNB cocrystal
280.14	155.28	149.45	122.7	151.08	140.9	122.8
311	222.61	212.58	133.93	222.61	150.72	145.25
330.64	298.36	246.24	170.4	296.96	222.26	170.49
336.25	318	317.78	213.88	315.19	243.3	213.98
442.85	346.05	442.62	220.89	346.05	282.58	277.1
494.75	389.53	725.97	319.09	389.53	316.24	313.57
508.78	459.67	817.14	424.29	455.46	439.68	329
556.47	817.35	1107.51	718.86	498.94	498.6	421.58
761.26	849.61	1183.25	751.13	517.18	516.83	497.33
831.39	1148.38	1216.92	815.65	556.45	557.51	515.56
870.67	1226.93	1338.95	1068.14	762.65	763.71	559.05
932.39	1256.39	1372.62	1152.31	818.75	818.42	718.95
950.62	1353.17	1452.57	1191.58	836.99	874.53	759.63
1008.13	1370.01	1554.97	1240.68	874.86	948.87	814.34
1139.98	1465.39	2534.06	1326.24	949.2	1104.58	828.37
1210.12	1562.17	3117.59	1372.53	1002.5	1183.13	871.85
1252.2	2535.63		1444.07	1146.98	1211.18	936.37
1444.36	2737.62		1495.97	1211.5	1221	949
1473.82	3089.69		1533.85	1231.14	1258.88	1068.23
2730.62	3133.18		1546.47	1257.79	1344.44	1146.78
2877.9			2511.55	1351.77	1373.9	1194.47
2952.24			2740.19	1374.21	1446.84	1209.9
2963.46			3057.21	1444.35	1557.66	1260.4
3009.75				1564.98	1564.67	1326.33
3039.21				1576.2	2536.76	1372.62
				2545.45	2737.36	1448.36
				2734.81	2870.61	1497.46
				2877.89	2921.11	1535.33
				2950.83	2951.97	1550.76
				3009.74	3010.89	2513.02
				3026.57	3125.91	2738.86
				3151.41		2877.73
						2953.47
						3009.58
						3032.03
						3062.89

A3.2 PXRD Patterns for DADP Cocrystals

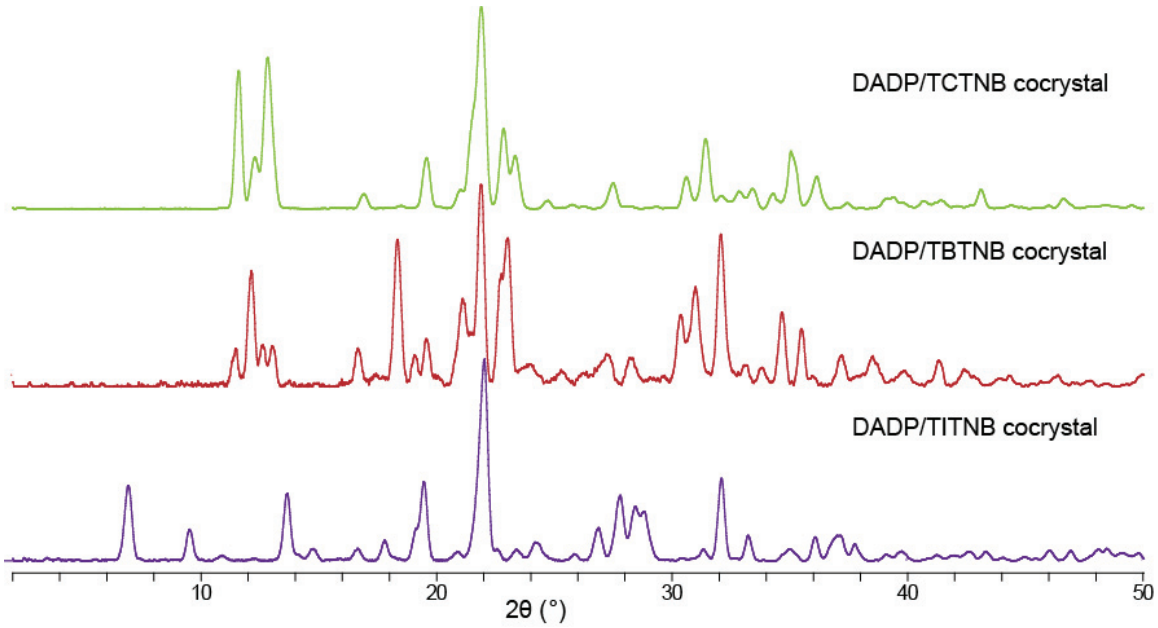

Figure A3.4 PXRD patterns at room temperature for the three DADP cocrystals: DADP/TCTNB, DADP/TBTNB and DADP/TITNB.

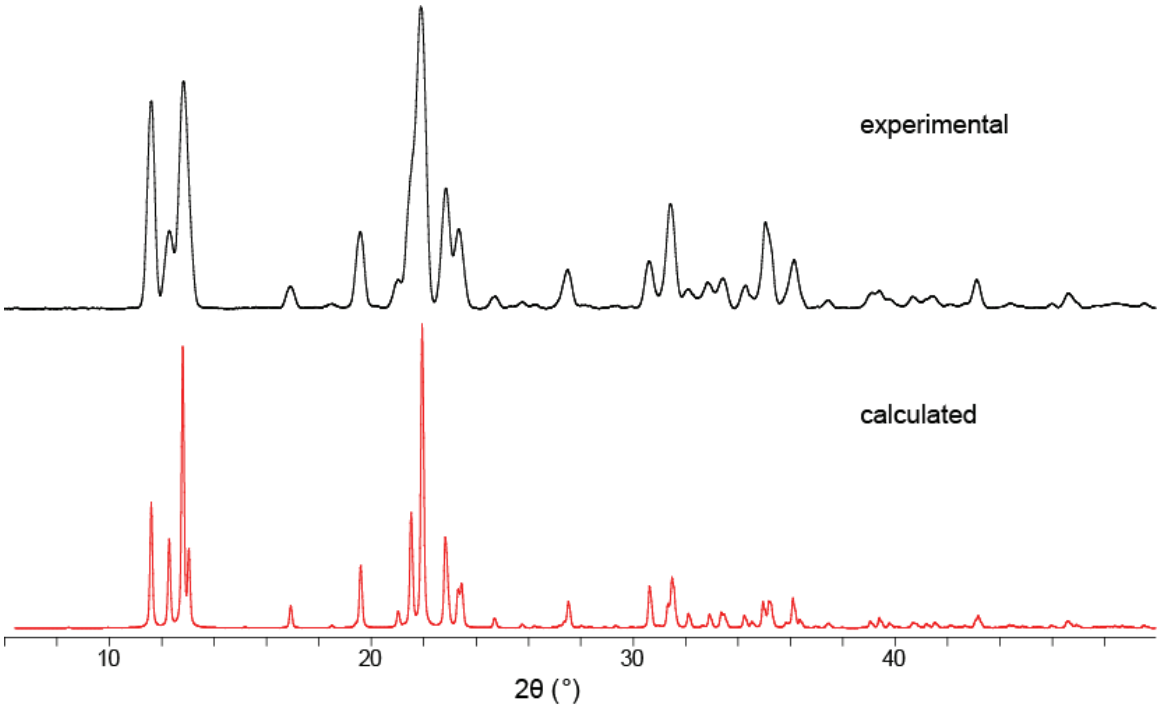

Figure A3.5 Comparison of experimental and calculated PXRD patterns for DADP/TCTNB at room temperature

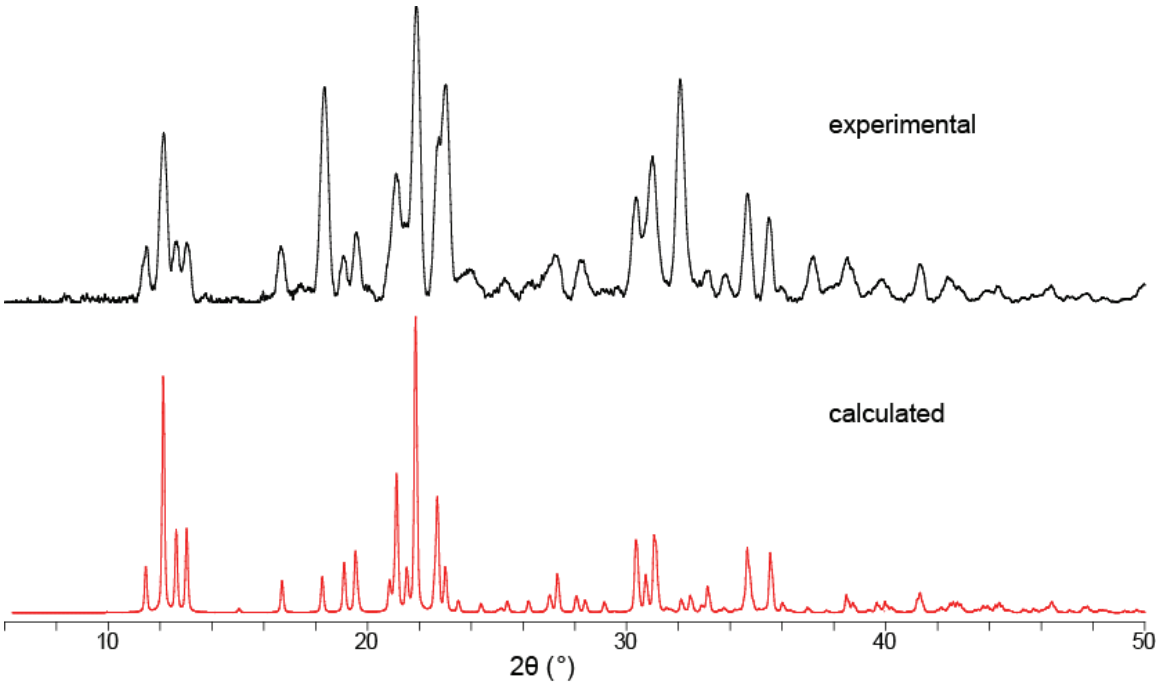

Figure A3.6 Comparison of experimental and calculated PXRD patterns for DADP/TBTNB at room temperature

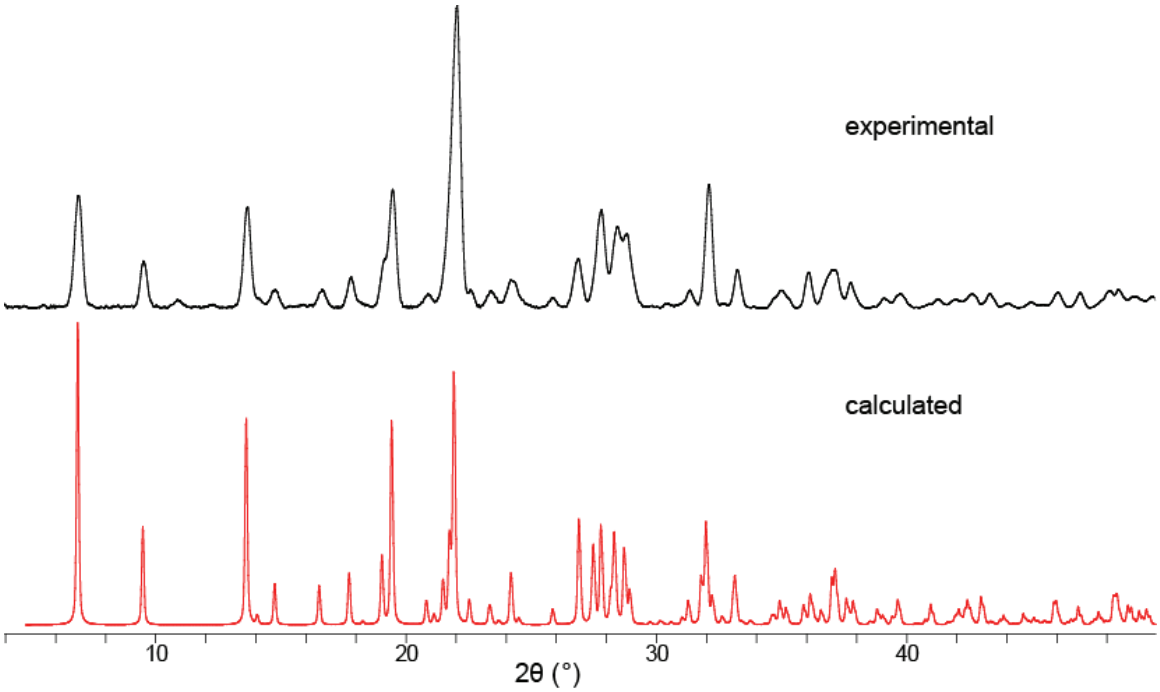

Figure A3.7 Comparison of experimental and calculated PXRD patterns for DADP/TITNB at 95 K

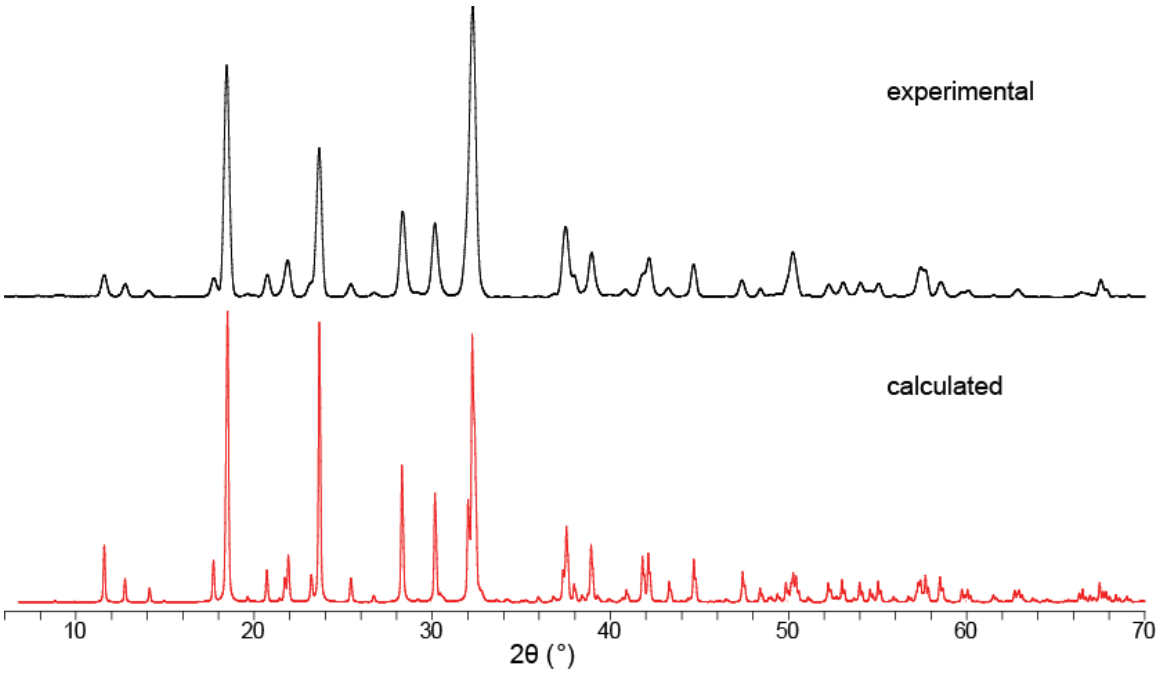

Figure A3.8 Comparison of experimental and calculated PXRD patterns for TBTNB at 95 K

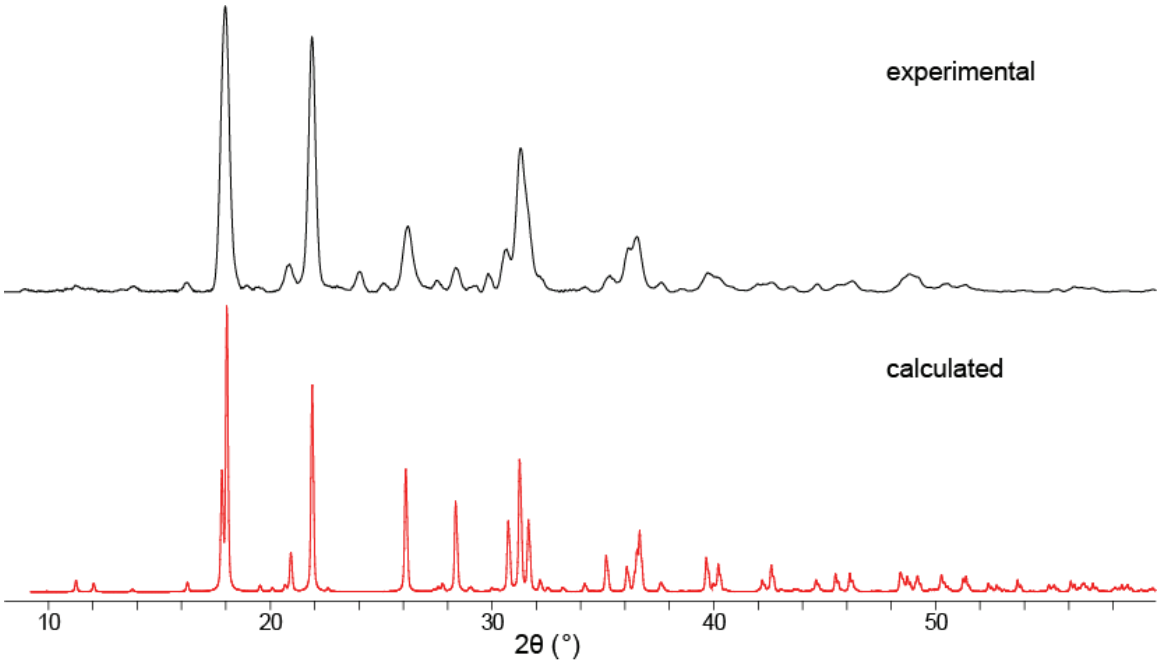

Figure A3.9 Comparison of experimental and calculated PXRD patterns for TITNB at room temperature

Table A3.2 Experimental PXRD peak positions (°) and the relative intensity (%) of DADP cocrystals with the trihalogenated trinitrobenzenes and TBTNB and TITNB

DADP/TCTNB cocrystal[a]		DADP/TBTNB cocrystal[a]		DADP/TITNB cocrystal[b]		TBTNB[b]		TITNB[a]	
2θ (°)	**I/I_0**	**2θ (°)**	**I/I_0**	**2θ (°)**	**I/I_0**	**2θ (°)**	**I/I_0**	**2θ (°)**	**I/I_0**
11.61	65.9	11.46	19.1	6.90	37.0	11.59	7.8	11.22	2.2
12.28	21.2	12.14	58.8	9.51	15.4	12.78	4.5	13.82	2.0
12.83	73.5	12.64	20.9	10.88	2.6	17.75	5.1	16.24	3.2
16.92	7.3	13.03	20.2	13.67	33.2	18.47	84.3	17.98	100
19.59	25.3	16.66	18.3	14.77	5.9	20.74	7.8	18.99	2.1
21.50	43.0	17.34	4.8	16.65	6.1	21.89	12.3	20.87	7.5
21.90	100	18.34	73.8	17.81	10.1	23.66	52.6	21.89	87.7
22.85	38.1	19.08	14.9	19.10	15.1	25.44	4.5	24.02	7.0
23.34	25.4	19.57	23.7	19.47	39.0	28.34	30.3	25.09	3.0
24.74	4.0	21.11	24.9	20.87	4.4	30.15	25.6	26.22	22.9
27.50	12.7	21.89	100	22.04	100	32.27	100	27.50	3.8
30.61	12.7	22.72	52.1	22.59	5.7	37.48	21.3	28.37	8.3
31.43	30.7	23.03	72.7	23.40	5.4	38.95	14.9	29.30	2.1
32.12	2.6	24.00	9.3	24.21	8.8	42.17	11.0	29.83	6.4
32.84	6.0	25.29	7.6	25.83	3.4	43.25	2.7	30.65	14.9
33.43	8.7	26.25	6.1	26.88	16.4	44.67	11.7	31.29	50.4
34.30	5.6	27.31	15.0	27.81	32.5	47.39	6.0	31.60	30.3
35.05	26.3	28.22	13.5	28.45	26.9	48.42	2.8	32.21	5.0
36.14	15.2	29.08	3.4	28.81	24.5	50.24	15.3	35.27	5.4
37.46	2.7	30.37	34.3	31.34	5.4	52.26	3.8	36.14	15.4
40.66	2.5	31.00	48.6	32.10	40.3	53.07	4.3	36.54	19.3
43.11	9.2	32.07	75.3	33.23	12.1	54.04	3.8	37.64	3.3
46.62	4.9	33.07	9.0	34.98	5.8	55.07	3.7	39.74	6.3
		33.83	7.7	36.09	11.8	57.42	9.1	40.20	4.7
		34.66	36.6	37.15	12.5	57.67	7.3	41.98	2.3
		35.49	29.0	37.76	8.4	58.55	5.1	42.61	2.9
		35.99	4.8	39.11	3.2	67.53	5.6	44.64	2.4
		37.21	15.5	39.76	4.8			45.60	1.9
		38.52	15.2	41.24	3.0			46.23	3.5
		39.83	7.8	41.95	2.7			48.83	5.9
		41.31	12.9	42.63	4.5			49.18	4.9
		42.39	8.6	43.35	4.6			50.54	2.6
		42.88	4.3	46.04	5.1			51.36	2.1
		43.87	3.6	46.93	5.0			56.26	1.7
		44.37	5.2	48.10	5.6				
		46.39	5.2	48.45	6.0				
		47.76	2.8	49.04	3.6				
		49.97	6.0	49.80	3.8				
				53.18	2.7				
				54.08	4.4				
				55.19	3.2				
				56.56	4.5				

[a] room temperature [b] 95 K

A3.3 ORTEP Diagrams for DADP Cocrystals

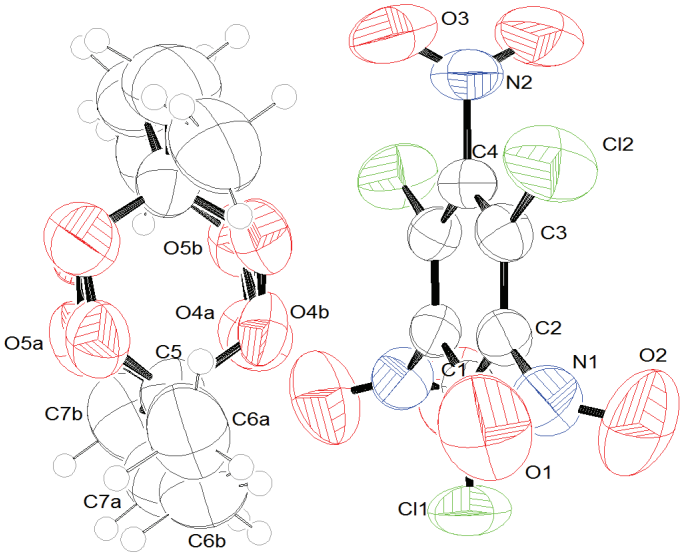

Figure A3.10 ORTEP diagram for the DADP/TCTNB cocrystal collected at room temperature with thermal ellipsoids of 50% probability.

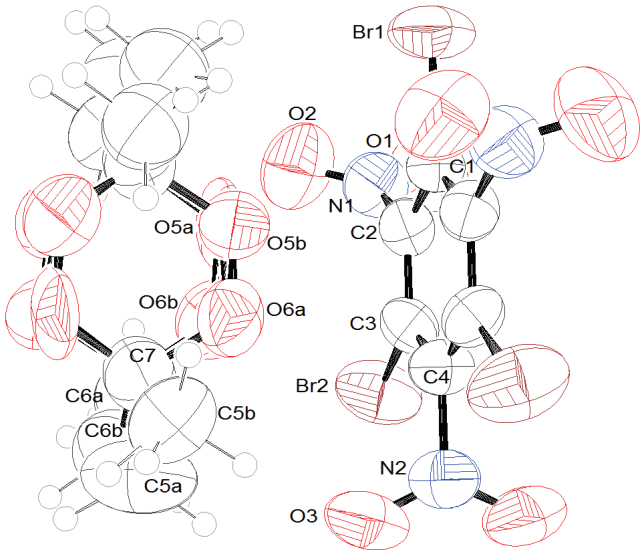

Figure A3.11 ORTEP diagram for the DADP/TBTNB cocrystal collected at room temperature with thermal ellipsoids of 50% probability.

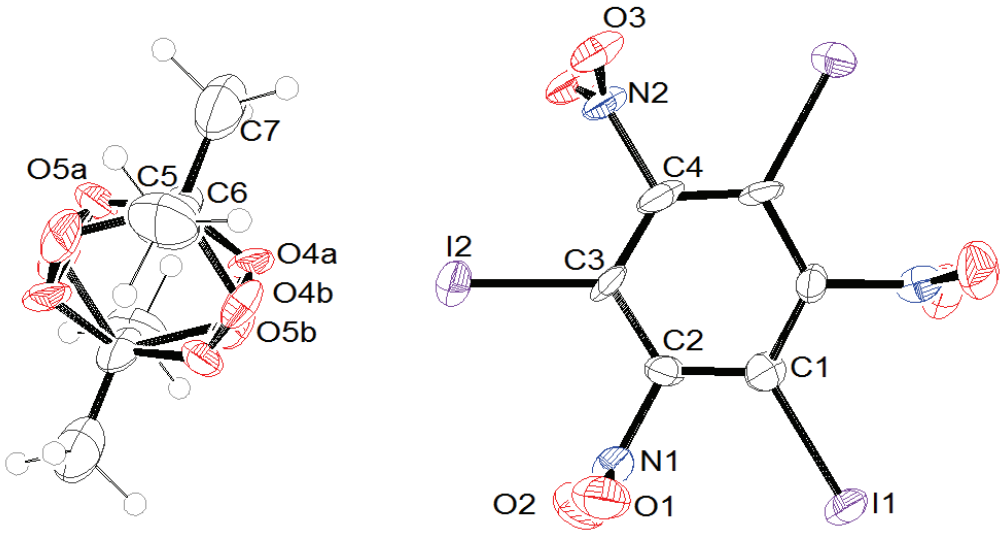

Figure A3.12 ORTEP diagram for the DADP/TITNB cocrystal collected at 95 K with thermal ellipsoids of 50% probability.

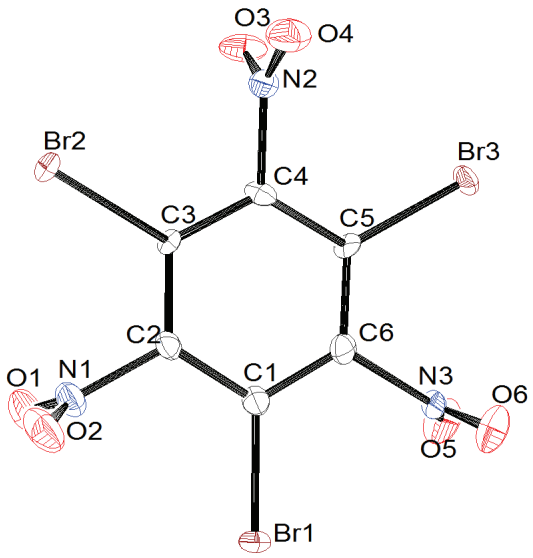

Figure A3.13 ORTEP diagram for the TBTNB cocrystal collected at 95 K with thermal ellipsoids of 50% probability

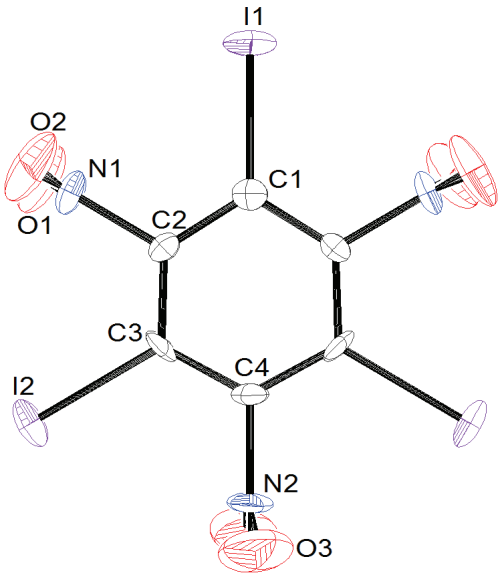

Figure A3.14 ORTEP diagram for the TITNB cocrystal collected at room temperature with thermal ellipsoids of 50% probability

A3.4 Dissolution of the DADP/TBTNB Cocrystal in Cocrystal Former Saturated Solvents

DADP/TBTNB cocrystal was formed from cyclohexane and isolated before transformation could occur. Before addition of solvents saturated with both TBTNB and DADP were added a picture was taken. As soon as solvent was added pictures were taken at a rate of 1 every 0.5 s. The pictures below show a) the initial picture and b) the time at which the cocrystal disappeared entirely from view of the camera. The results were repeatable and within some margin of error allowing for the amount of cocrystal and the speed of mixing. All solvents except for methanol, ethanol, cyclohexane and water showed transformation in less than a minute. Cocrystals took 2 minutes and 6 minutes to fully dissolve in methanol and ethanol respectively. In cyclohexane dissolution was within 50 minutes and in water dissolution took over two weeks. Care was taken not to move the vials except in the case of water.

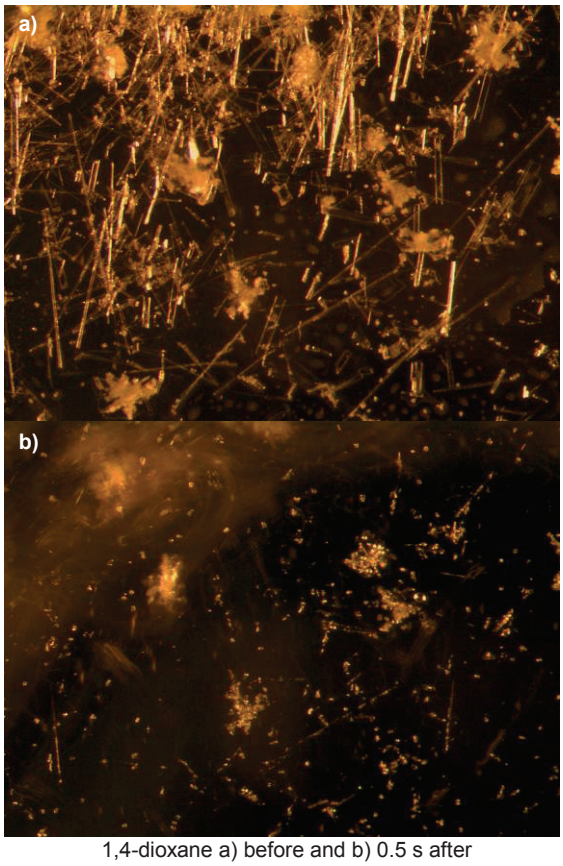

1,4-dioxane a) before and b) 0.5 s after

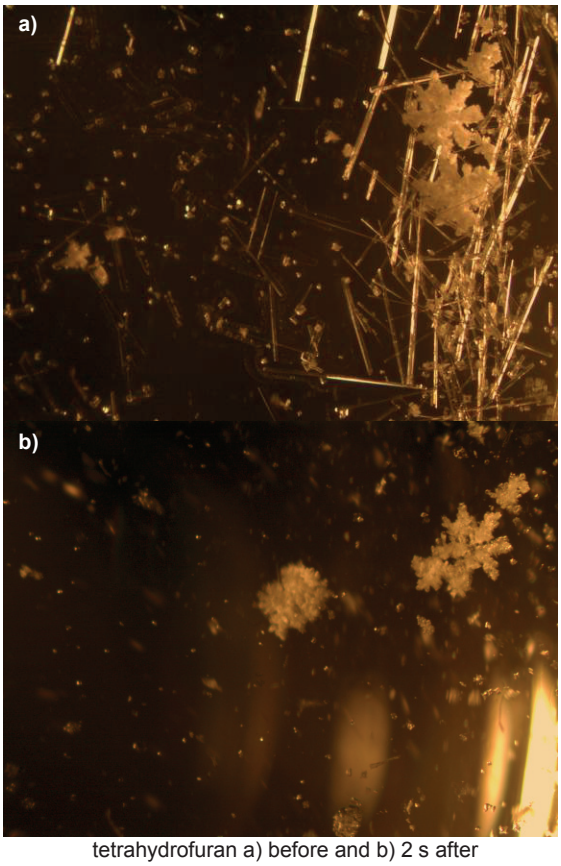

tetrahydrofuran a) before and b) 2 s after

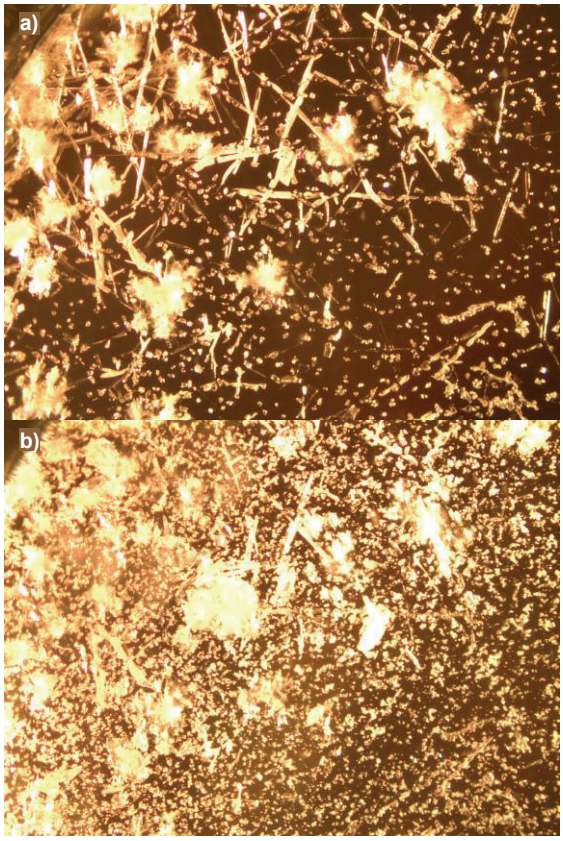

acetonitrile a) before and b) 6 s after

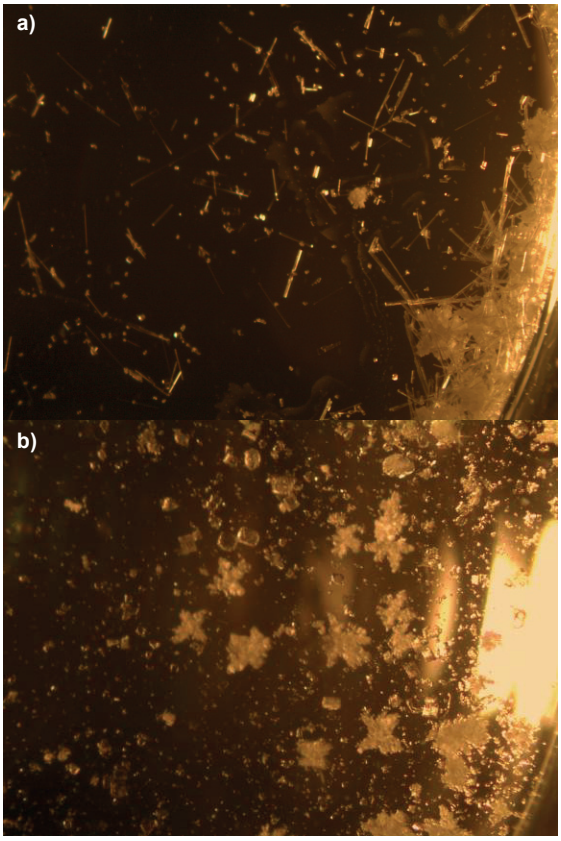

ethyl acetate a) before and b) 15 s after

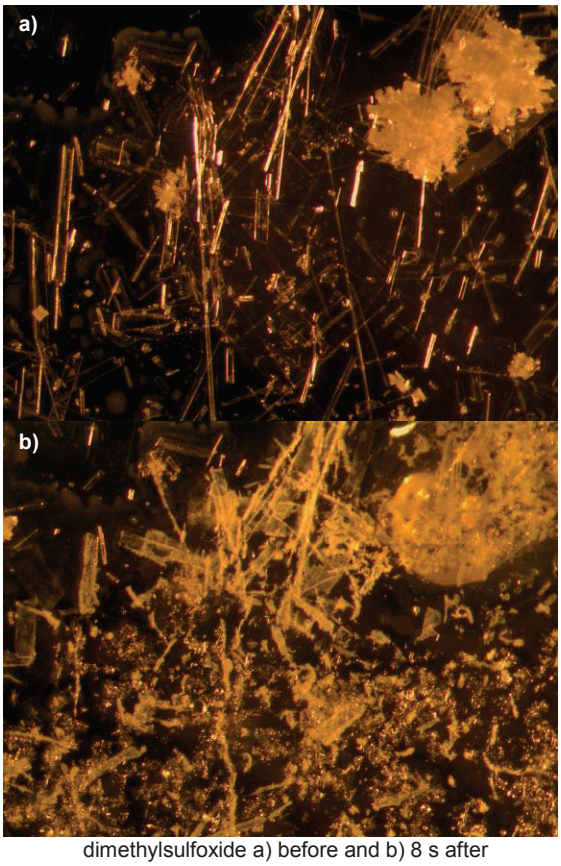

dimethylsulfoxide a) before and b) 8 s after

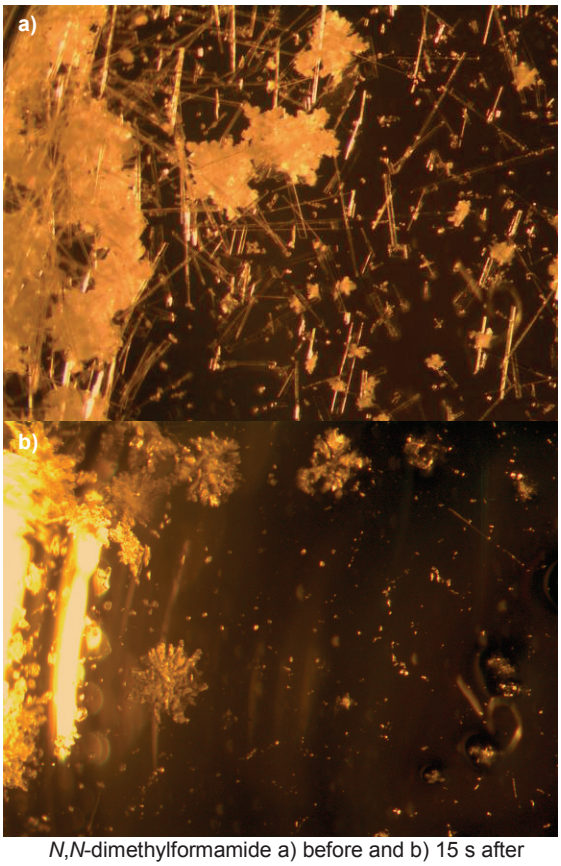

N,*N*-dimethylformamide a) before and b) 15 s after

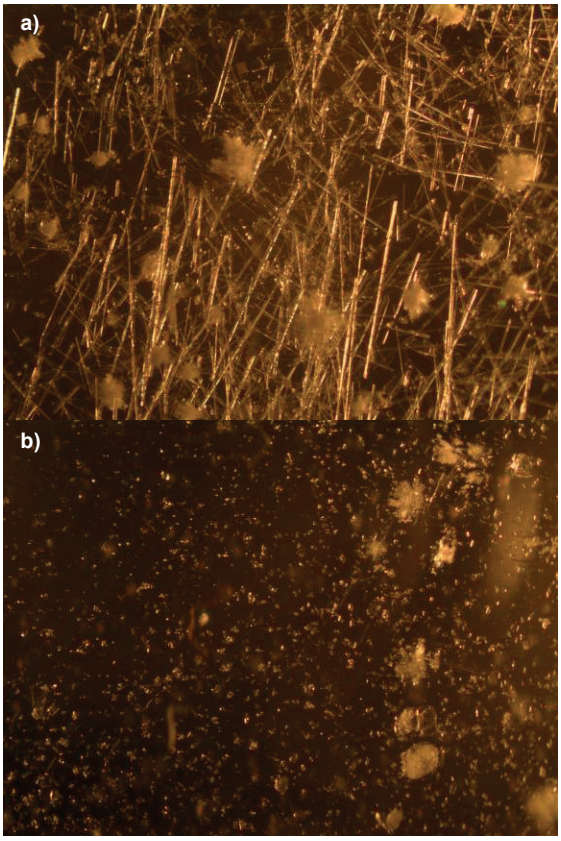

chloroform a) before and b) 30 s after

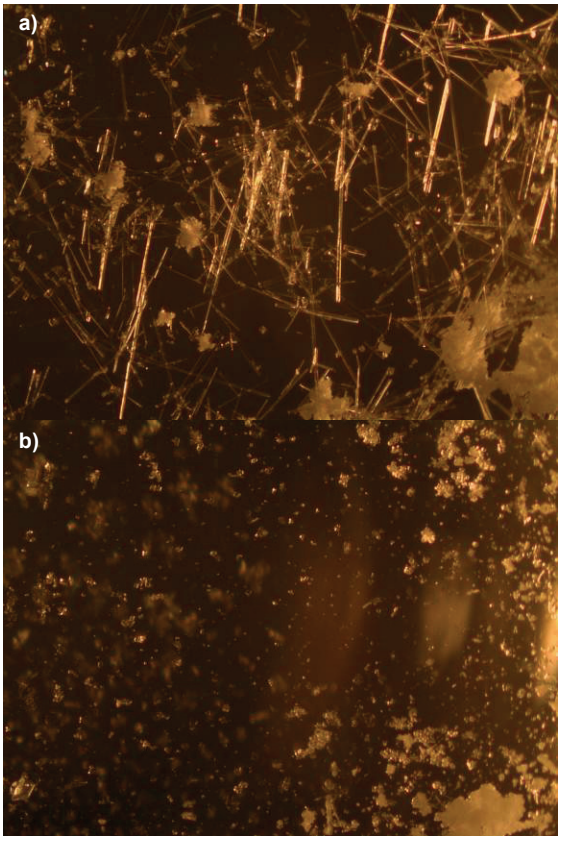

diethyl ether a) before and b) 30 s after

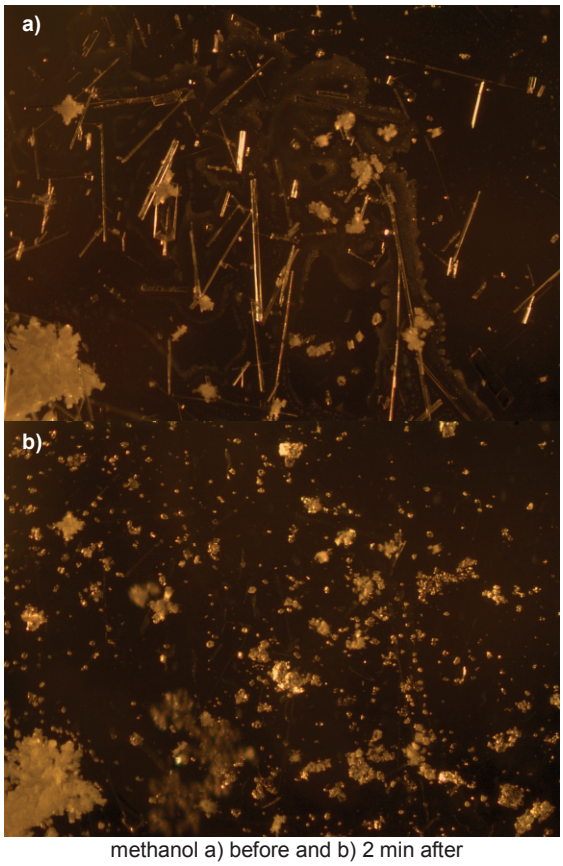

methanol a) before and b) 2 min after

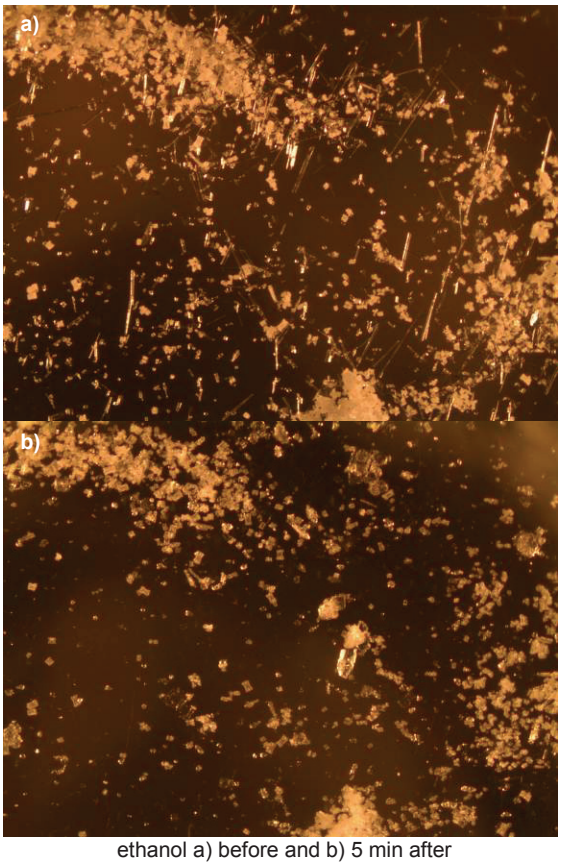

ethanol a) before and b) 5 min after

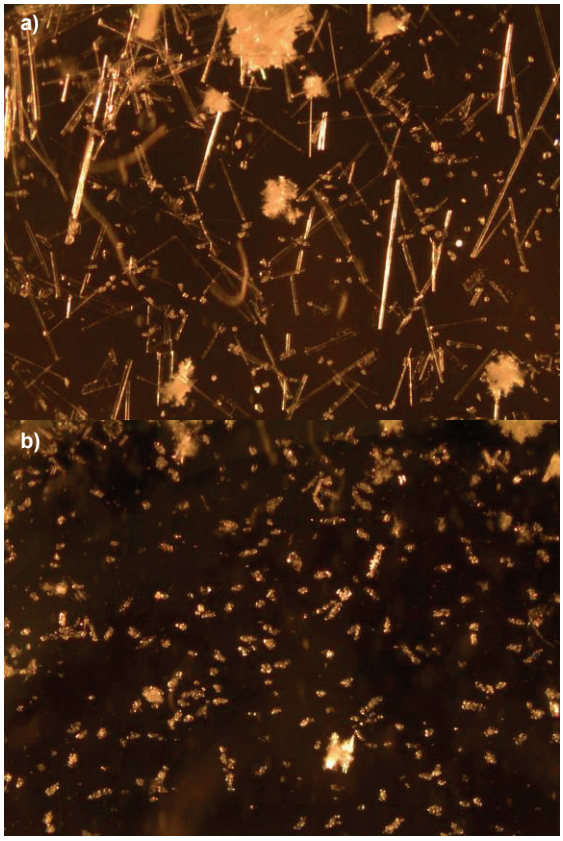

cyclohexane a) before and b) 1 hr after

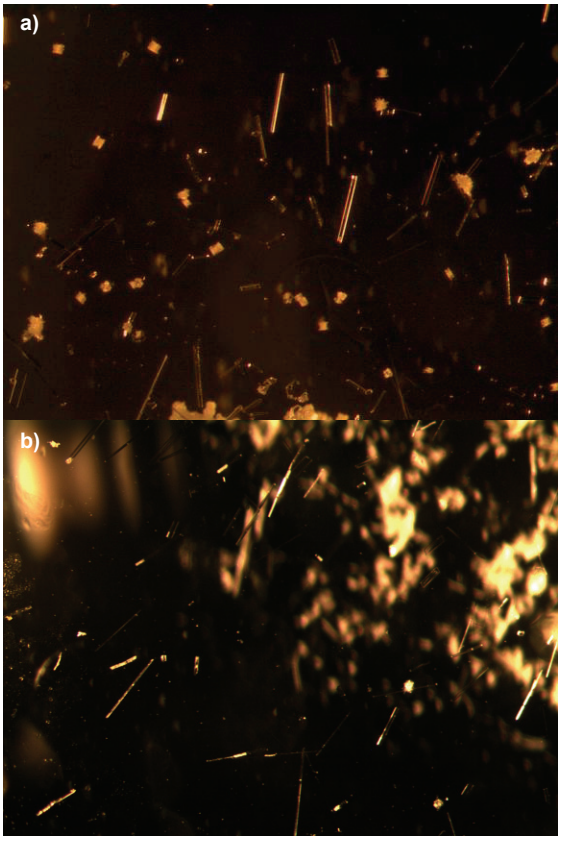

water a) before and b) 1 week after